LBL-23717

Lawrence Berkeley Laboratory
UNIVERSITY OF CALIFORNIA

EARTH SCIENCES DIVISION

HEAT AND MASS TRANSFER IN THE KLAMATH FALLS, OREGON, GEOTHERMAL SYSTEM

R.H. Prucha
(M.S. Thesis)

May 1987

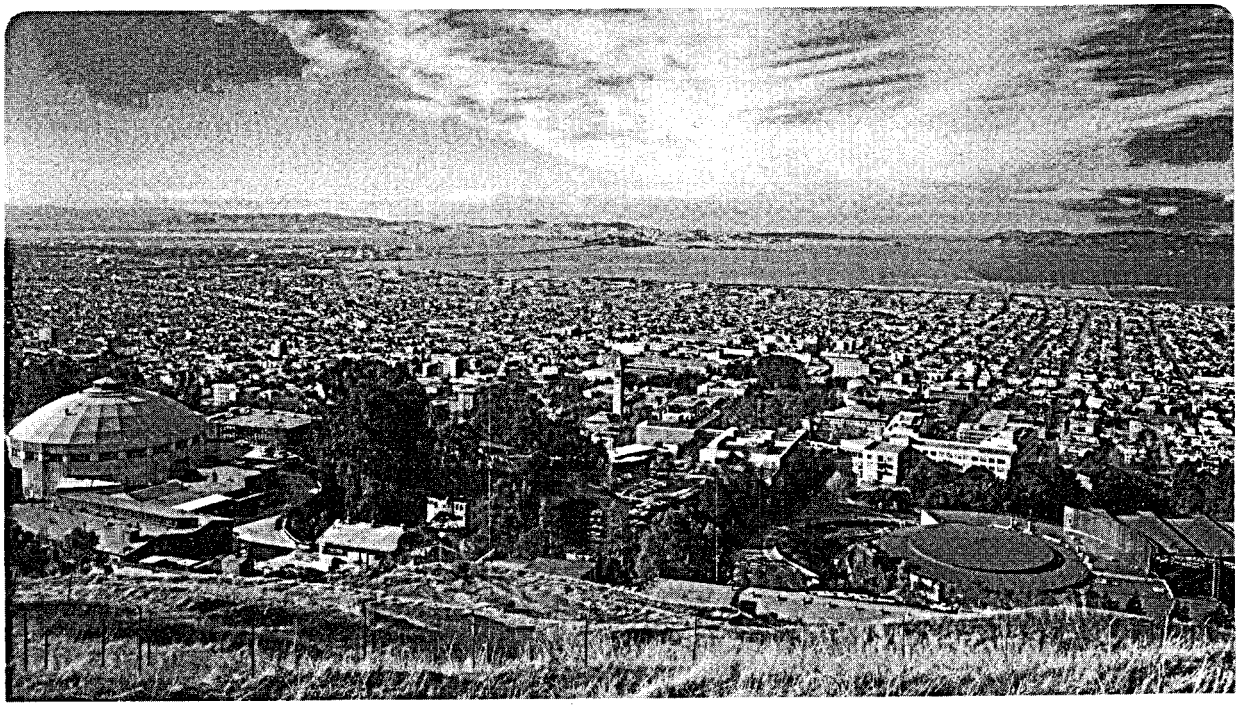

Prepared for the U.S. Department of Energy under Contract DE-AC03-76SF00098

DISCLAIMER

LBL--23717

DE87 014676

HEAT AND MASS TRANSFER IN THE KLAMATH FALLS, OREGON, GEOTHERMAL SYSTEM

Robert H. Prucha

Earth Sciences Division, Lawrence Berkeley Laboratory
University of California, Berkeley, California 94720 USA

May 1987

Master's Thesis

Table of Contents

LIST OF FIGURES iii

LIST OF TABLES viii

NOMENCLATURE ix

ACKNOWLEDGMENTS x

1.0 INTRODUCTION 1

2.0 DATA EVALUATION 8

2.1 Geology 8

2.2 Geothermal Aquifer 14

2.1.1 Well Testing 22

2.3 Geochemistry 26

2.4 Geophysics 27

2.5 Temperature Data 27

2.5.1 Methodology 30

2.5.2 Fault Locations 38

3.0 CONCEPTUAL MODEL 40

4.0 QUANTITATIVE ANALYSIS 46

4.1 Fault-Charged System 47

4.2 Lumped-Parameter method 56

4.3 Distributed-Parameter method 59

4.4 Grid Size Analysis 63

4.5 Average Reservoir Properties 66

5.0 THREE-DIMENSIONAL NUMERICAL MODEL 72

5.1 Three-Dimensional Mesh 74

5.2 Material Properties 79

5.3 Boundary Conditions 89
5.4 Initial Conditions 108
5.5 Results 108
5.5.1 Temperature and Pressure Distributions 109
5.5.2 Heat and Mass Recharge Estimates 130
5.5.3 Sensitivity Study 143
6.0 SUMMARY AND CONCLUSIONS 146
REFERENCES 152
APPENDIX A 156

LIST OF FIGURES

Figure 1.	Location map for Klamath Falls, Oregon.	2
Figure 2.	Map showing topography, trace of main normal fault and the effective area for the Klamath Falls, Oregon, KGRA.	3
Figure 3.	Typical heat exchanger at Klamath Falls	4
Figure 4.	Regional Fault trends in the Klamath Basin area (taken from Kiele et al., 1981).	10
Figure 5.	Three types of models possible in the Basin and Range, (taken from Stewart 1979).	11
Figure 6.	Stratigraphic column for the Klamath Falls area (taken from Stark et al., 1980).	13
Figure 7a.	Lithologic column from the YMCA-2 borehole in the geothermal area at Klamath Falls (taken from M. O'Brian and S. Benson, 1980).	15
Figure 7b.	Lithologic column from the CW-1 borehole in the geothermal area at Klamath Falls (taken from M. O'Brian and S. Benson, 1980).	16
Figure 7c.	Lithologic column from the CW-2 borehole in the geothermal area at Klamath Falls (taken from M. O'Brian and S. Benson, 1980).	17
Figure 8.	Correlation between YMCA-2, CW-1 and CW-2 lithologies from the Klamath Falls geothermal area.	18
Figure 9.	Regional groundwater levels and boundary used in numerical simulation (water levels taken from Sammel, 1980).	20
Figure 10.	Monthly mean air temperature and heating days for the years 1969-76 (taken from Sammel et al., 1984).	21
Figure 11.	Location map of wells used in aquifer tests and temperature analysis. Lines for the temperature cross-secional profiles are also shown. Shaded areas indicate once active artesian springs.	24
Figure 12.	Locations of wells used in aquifer test by Nork Inc., 1986. These wells are located in the OIT campus area.	25
Figure 13.	Typical temperature profiles from Klamath Falls, Oregon.	29
Figure 14a.	Cross-sectional temperature profiles parallel to the main normal fault. Well numbers appear above the isotherms. Lithologic columns are shown for several wells.	31

Figure 14b.	Cross-sectional temperature profiles perpendicular to the main normal fault. Well numbers appear above the isotherms. Lithologic columns are shown for several wells.	32
Figure 14c.	Cross-sectional temperature profiles perpendicular to the main normal fault. Well numbers appear above the isotherms. Lithologic columns are shown for several wells.	33
Figure 15.	Fault locations inferred form the cross-sectional temperature profiles and temperature contour plots. Solid lines indicate a higher degree of certainty.	35
Figure 16a.	Temperature contour plots drawn at elevations 3600 ft, 3700 ft and 3800 ft a.s.l.	36
Figure 16b.	Temperature contour plots drawn at elevations 3900 ft, 4000 ft and 4100 ft a.s.l.	37
Figure 17.	Two-dimensional conceptual model proposed for the Klamath Falls geothermal system.	41
Figure 18.	Three-dimensional conceptual model proposed for the Klamath Falls geothermal system. This model is used as a basis for the numerical mesh.	43
Figure 19.	Fault-charged model showing important parameters (taken from Bodvarsson et al., 1982).	48
Figure 20a.	Calculated and actual field data comparison for the fault-charged model.	51
Figure 20b.	Calculated heat losses from the aquifer using the fault-charged model.	55
Figure 21.	Lumped-parameter volume showing heat flows into and out of the system.	57
Figure 22.	Permeable layer system indicating geometry and important parameters (modified from Bodvarsson, 1982).	64
Figure 23.	Comparison between different degrees of discretization for the permeable layer study, using 4, 11 and 21 vertical nodes and 10 horizontal nodes.	67
Figure 24.	Comparison between semi-analytic and numerical solutions for the permeable layer study, using velocities of 0.1 m/day and 100.0 m/day.	68
Figure 25.	Relation between heterogenous, anisotropic system and homogenous isotropic system.	69
Figure 26.	Two-dimensional mesh used as a basis for the three-dimensional mesh. This vertical section is viewed from the northwest towards the southeast. Mesh is oriented perpendicular to the main normal fault, represented by elements 1, 9, 17, 25 and 31.	76

Figure 27.	Final three-dimensional mesh used in numerical analysis of the Klamath Falls geothermal system. The mesh views the system from the northeast towards the southwest. The numbering scheme for the mesh is seen at the base of each vertical section (1, 100, 200, 300,.....1200, 1300).	77
Figure 28.	Inferred subsurface geology for the three-dimensional model.	81
Figure 29a.	Final permeability distribution key to Figures 29b-e.	83
Figure 29b.	Final permeability distribution for vertical cross-sections perpendicular to the main normal fault, 1, 100, 200 and 300.	84
Figure 29c.	Final permeability distribution for vertical cross-sections perpendicular to the main normal fault, 400, 500, 600 and 700.	85
Figure 29d.	Final permeability distribution for vertical cross-sections perpendicular to the main normal fault, 800, 900, 1000 and 1100.	86
Figure 29e.	Final permeability distribution for vertical cross-sections perpendicular to the main normal fault, 1200, 1300.	87
Figure 30.	Boundary conditions for three-dimensional numerical model.	90
Figure 31.	Conceptual model of possible flow regimes within the geothermal system. Arrows indicate direction of both cold and hot water as described in text. System is viewed from the northwest looking towards the southeast.	92
Figure 32a.	Southwestern Boundary pressure distribution (Bars).	95
Figure 32b.	Southwestern Boundary temperature distribution ($^{\circ}$C).	96
Figure 33.	Qualitative representation of convective flow induced by differences in temperature dependant densities. Two columns are shown on the right are dependant upon temperatures determined by a geothermal gradient.	99
Figure 34a.	Bottom Boundary pressure distribution (Bars).	101
Figure 34b.	Bottom Boundary temperature distribution ($^{\circ}$C).	102
Figure 35a.	Southeastern Boundary pressure distribution (Bars).	104
Figure 35b.	Southeastern Boundary temperature distribution ($^{\circ}$C).	105
Figure 36a.	Northwestern Boundary pressure distribution (Bars).	106
Figure 36b.	Northwestern Boundary temperature distribution ($^{\circ}$C).	107

Figure 37.	Temperature and pressure distribution sections. Each section includes the entire set of connected nodes in the plane created by the arrows.	110
Figure 38.	Actual temperature data at 3800 feet a.s.l. with horizontal grid overlay for comparison with the numerical results. Temperatures are in °C	112
Figure 39a.	Temperature distribution for horizontal section, HZ33. Temperatures are in (°C).	113
Figure 39b.	Pressure distribution for horizontal section, HZ33. Pressures are in (Bars).	114
Figure 40a.	Temperature distribution for horizontal section, HZ25. Temperatures are in (°C).	115
Figure 40b.	Pressure distribution for horizontal section, HZ25. Pressures are in (Bars).	116
Figure 41a.	Temperature distribution for horizontal section, HZ17. Temperatures are in (C).	118
Figure 41b.	Pressure distribution for horizontal section, HZ17. Pressures are in (Bars).	119
Figure 42.	Temperature distribution for vertical sections VSP1, parallel to the main normal fault. Temperatures are in (°C).	120
Figure 43.	Temperature distribution for vertical sections VSP2, parallel to the main normal fault. Temperatures are in (°C).	121
Figure 44.	Temperature distribution for vertical sections VSP5, parallel to the main normal fault. Temperatures are in (°C).	122
Figure 45.	Temperature distribution for vertical sections VSP6, parallel to the main normal fault. Temperatures are in (°C).	123
Figure 46.	Temperature distribution for vertical section, VS200, perpendicular to the main normal fault. Temperatures are in (°C).	125
Figure 47.	Temperature distribution for vertical section, VS500, perpendicular to the main normal fault. Temperatures are in (°C).	126
Figure 48.	Temperature distribution for vertical section, VS900, perpendicular to the main normal fault. Temperatures are in (°C).	127
Figure 49.	Temperature distribution for vertical section, VS600, perpendicular to the main normal fault. Temperatures are in (°C).	128
Figure 50.	Temperature distribution for vertical section, VS1300, perpendicular to the main normal fault. Temperatures are in (°C).	129

Figure 51.	Mass flux plots for vertical section, VSP1, parallel to main normal fault. Mass flux is in ($kg/m^2 \cdot s$).	131
Figure 52.	Mass flux plots for vertical section, VSP5, parallel to main normal fault. Mass flux is in ($kg/m^2 \cdot s$).	132
Figure 53.	Mass flux plots for vertical section, VS600, perpendicular to main normal fault. Mass flux is in ($kg/m^2 \cdot s$).	133
Figure 54.	Mass flux plots for vertical section, VS500, perpendicular to main normal fault. Mass flux is in ($kg/m^2 \cdot s$).	135
Figure 55.	Mass flux plots for vertical section, VS900, perpendicular to main normal fault. Mass flux is in ($kg/m^2 \cdot s$).	136
Figure 56.	Mass flux plots for horizontal section, HZ33. Mass flux is in ($kg/m^2 \cdot s$).	137
Figure 57.	Mass flux plots for horizontal section, HZ25. Mass flux is in ($kg/m^2 \cdot s$).	139
Figure 58.	Heat flux plots for horizontal section, HZ33. Heat flux is in ($J/m^2 \cdot s$).	140
Figure A1.	Numbering scheme for Southwestern Boundary condition.	161
Figure A2.	Numbering scheme for Bottom Boundary condition.	162
Figure A3.	Numbering scheme for Northwestern Boundary condition.	163
Figure A4.	Numbering scheme for Southeastern Boundary condition.	164

LIST OF TABLES

Table 1.	Average Reservoir Parameters	22
Table 2.	Reservoir Parameters	23
Table 3.	Parameters used in Fault-Charged Model	52
Table 4.	Parameters for Lumped-Parameter Analysis al., 1981).	59
Table 5.	Rock Densities for 3-Dimensional Model	80
Table 6.	Parameters used in 3-Dimensional Model	82
Table 7.	Boundary Mass Flow Rates	141
Table 8.	Boundary Heat Flow Rates	141
Table 8.	Sensitivity Simulations	144
Table 9.	Mass Flow Rate Comparison	149

NOMENCLATURE

ρ_w	-	Density of water, (kg/m^3)
λ	-	Thermal conductivity, ($J/m \cdot s \cdot ^\circ C$)
c_w	-	Specific heat of water, ($J/kg \cdot ^\circ C$)
$\rho_a \cdot c_a$	-	Aquifer volumetric heat capacity, ($J/m^3 \cdot ^\circ C$)
b	-	Thickness of aquifer, (m)
B	-	Thickness of bedrock, (m)
D	-	Thickness of caprock, (m)
s	-	Laplace variable
A	-	Area, (m^2)
Q	-	Heat flux, (J/s)
T_f	-	Temperature of recharge water, ($^\circ C$))
T_b	-	Temperature ground surface, ($^\circ C$)
ϕ	-	Porosity
$\dot{m}$	-	Mass flow rate, (kg/s)
ρ_r	-	Density of rock, (kg/m^3)
c_r	-	Specific heat of rock, ($J/kg \cdot ^\circ C$)
V	-	Volume, (m^3)
$\frac{\delta T}{\delta x}$	-	Temperature gradient, ($^\circ C/m$)
U	-	Total internal energy, (J)
G_f	-	Mass source or sink, ($kg/m^3 \cdot s$)
G_h	-	Heat source or sink, ($J/m^3 \cdot s$)
k	-	Permeability, (m^2)
g	-	Gravitational acceleration, (m/s^2)
μ	-	Viscosity, ($kg \cdot s/m$)
q	-	Mass flow rate per unit length of fault, ($m^3/m \cdot s$)
d	-	Thickness of permeable bed, (m)
P	-	Pressure, (Pa)
P_o	-	Atmospheric pressure, (Pa)
t	-	Time (s)

Acknowledgements

I would like to thank Sally Benson for her patience, guidance and very helpful suggestions during this study. Special thanks are given to Amanda L. Spencer for her support and help during throughout this work. I would especially like to thank Dr. Paul A. Witherspoon, my advisor, for his overall supervision and support, and valuable insights.

I am indebted to Kent Colahan of Klamath Falls, and both Gene Culver and Paul Lineau (OIT campus) for supplying crucial data needed for this report. Thanks are also due M. Lippman, N.E. Goldstein, and S. Halfman for critical review of the first part of this paper.

This work was supported through U.S. Department of Energy Contract No. DE-AC03-76SF00098 by the Assistant Secretary for Conservation and Renewable Energy, Office of Renewable Technology, Division of Geothermal Technology.

ABSTRACT

Over the last 50 years significant amounts of data have been obtained from the Klamath Falls geothermal resource. To date, the complexity of the system has perplexed researchers, leading to the development of only very generalized hydrogeologic and geothermal models of the area. Recently, the large quantity of available temperature data have been re-evaluated, revealing new information on subsurface heat flow and locations of faults in the system. These inferences are supported by borehole, geochemical, geophysical, and hydrologic data. Based on re-evaluation of all available data, a detailed conceptual model for the Klamath Falls geothermal resource is proposed.

A comprehensive 3-dimensional numerical model, based on the proposed conceptual model is also presented. This numerical model incorporates all of the main reservoir characteristics. Hot water recharge flows from depth, along a large normal fault, and flows into near surface permeable strata where it loses heat to surrounding beds and to mixing with cold regional groundwaters introduced from the north. By matching calculated and measured temperatures and pressures, hot and cold water recharge rates and the permeability distribution for the geothermal system are estimated. A semi-analytic solution and simple lumped parameter methods are also compared to the numerical analysis.

Results suggest that the flow patterns within the geothermal system at Klamath Falls are complex and intimately associated with the permeability distribution and the pressures and temperatures at depth, within the faults. Temperature and pressures match well for the 3-dimensional model and the calculated hot water recharge rate is in the range of 0.1 - 10.0 x 10^{-6} kg/m·s with enthalpies of approximately 504.0 KJ/kg. Permeabilities within the main reservoir are within the range of 100.0 - 700.0 md. A sensitivity study on the final 3-dimensional numerical model for the system indicate that these hot water recharge rates are reasonable.

1.0 INTRODUCTION

The Klamath Falls KGRA (Known Geothermal Resource Area), located in south-central Oregon, is a low- to moderate-temperature resource (Figure 1). The approximately 2 square mile shallow thermal anomaly is associated with an adjacent, steeply dipping normal fault, shown in Figure 2. This principle normal fault acts as a conduit for upwelling hot waters which intersect near surface permeable strata. The hot waters then flow through the permeable strata where heat is lost to the confining beds.

Over 500 wells have been drilled in the area, ranging in depth from 90 to 1900 ft. Most temperatures encountered in these wells range from 70 to 120 °C. Temperatures in one well have been measured as high as 140 °C, but this data is somewhat suspect (Gene Culver, personal communication). The geothermal resource has been used for space heating for some 70 years; special uses include heating greenhouses and swimming pools, snow melting, and milk pasteurization. The local use of the geothermal resource has proven to be one of the most successful systems for such space heating in the United States. The most popular type of heat extraction system is the closed loop down-hole heat exchanger, shown in Figure 3.

Several investigators have obtained and evaluated data from the Klamath Falls geothermal area and the surrounding region, in an effort to better understand the reservoir characteristics and to examine the possibilities for further exploitation. Moore (1937) was the first to describe the rocks of the greater Klamath region. Meyers and Newcomb (1952) and Newcomb (1958) were the first to describe the geology and evaluate the groundwater resources in the adjacent Yonna Valley, shown in Figure 3. Peterson and McIntyre (1970) investigated the economic potential of eastern Klamath and western Lake Counties by reconnaissance geology methods, and proposed a conceptual model for the Klamath Falls geothermal system. These authors postulate that the heat source is a shallow, igneous dike or sill-like body of Pliocene-Pleistocene age, intercalated in lacustrine deposits which transform cold flowing groundwater into steam that rises along fault zones and heats the surrounding reservoir rock.

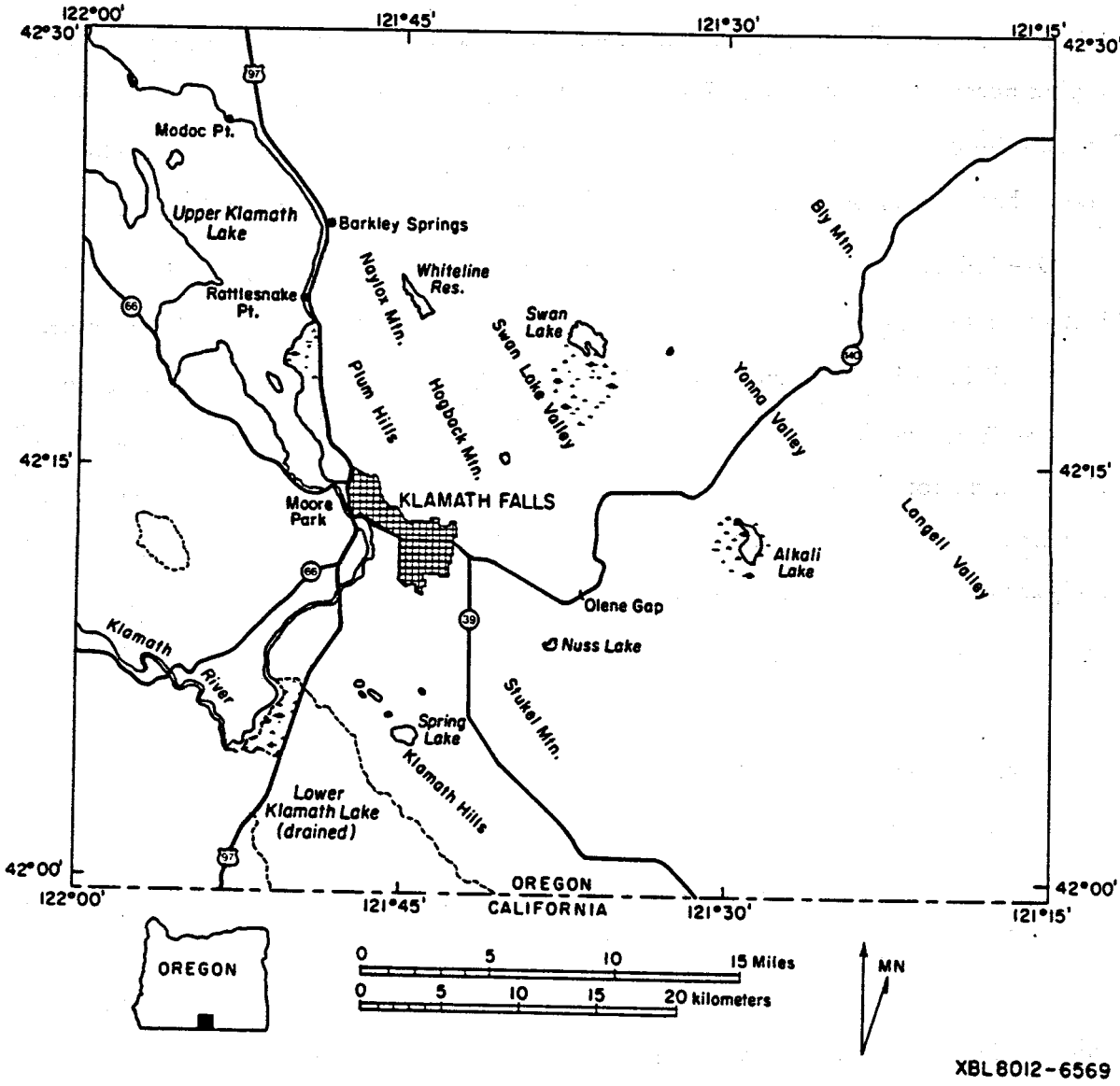

Figure 1. Location map for Klamath Falls, Oregon.

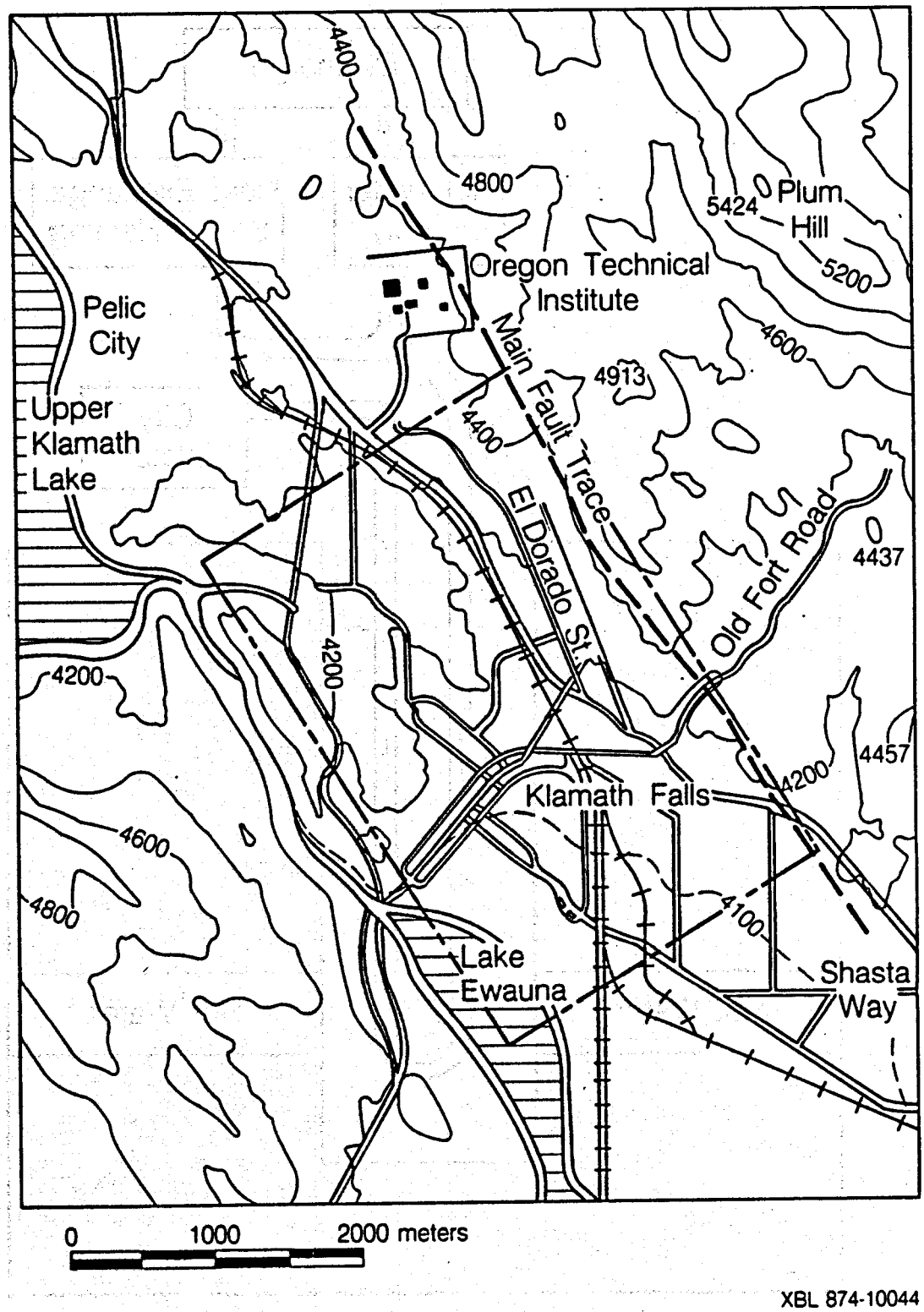

Figure 2. Map showing topography, trace of main normal fault and the effective area for the Klamath Falls, Oregon, KGRA.

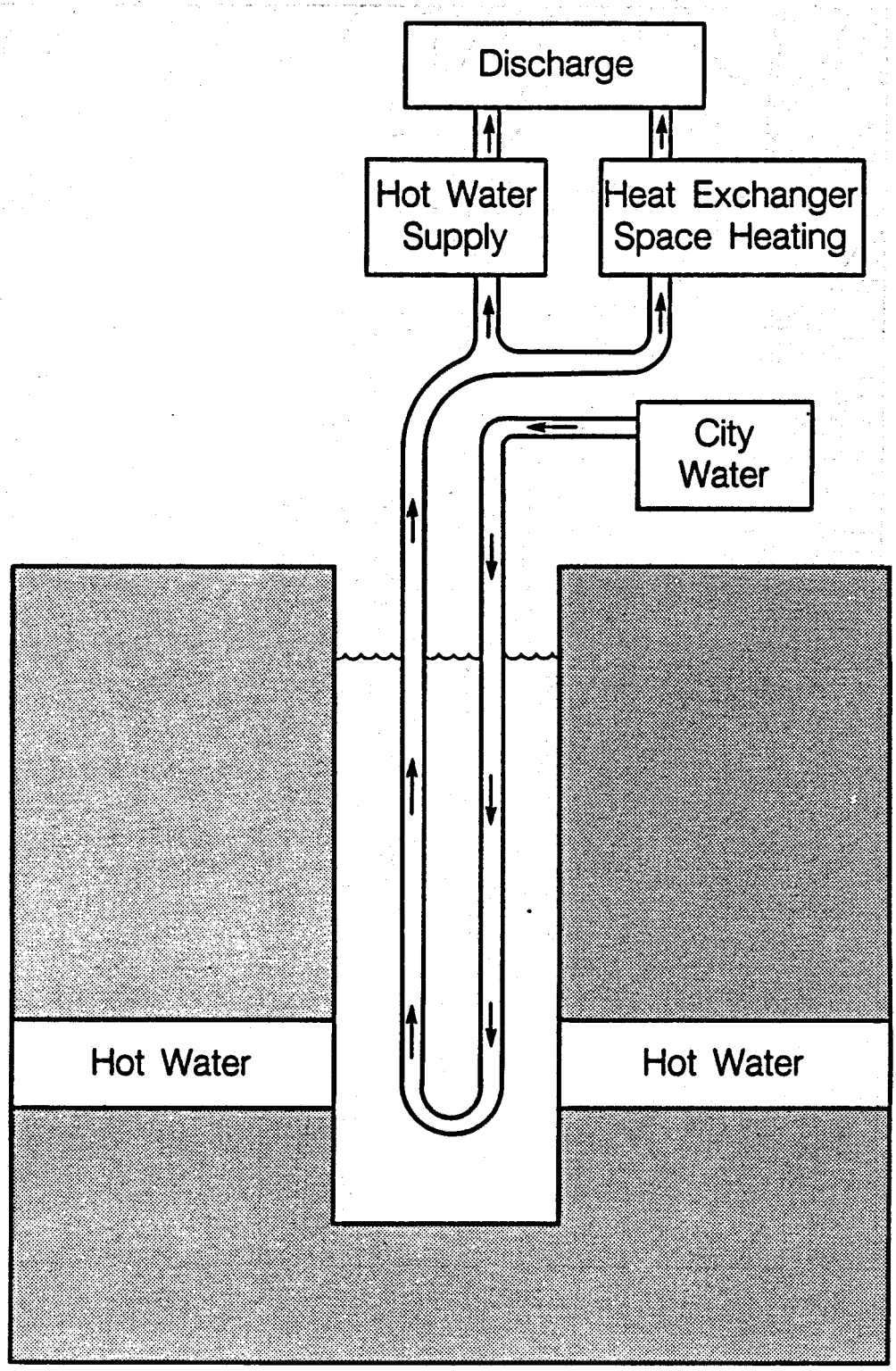

Figure 3. Typical heat exchanger at Klamath Falls

In the mid-late 70's the oil and gas crisis diverted a great deal of funds into research for alternative means of energy. Because geothermal energy offered a viable alternative, a good deal of research has been devoted to the field. Hence, it was at about this time that an increased effort was made to determine what KGRA's where exploitable and where these KGRAs were located. Aside from the KGRA in the town of Klamath Falls, two others have been identified in the Klamath Basin: a) Olene Gap KGRA, southeast of the town, and b) Klamath Hills KGRA south of the town. The KGRA in Klamath Falls is a much larger system and reaches temperatures significantly greater than the other two.

In 1974, a hot-water well study was done on the various private and commercial heating systems in the town of Klamath Falls (Culver et al., 1974). Lund et al. (1978) constructed several maps in a study of the geothermal hydrology and geochemistry of Klamath Falls.

The USGS was interested in the hydrologic assessment of the geothermal area near Klamath Falls (Sammel and Peterson, 1976). A study on heat flow data for the Klamath Basin was conducted by Sass and Sammel (1976) in an effort to characterize the mean thermal conductivity and to provide some constraints on a possible magma chamber beneath the graben. In 1980, Sammel (1980) assessed the regional hydrogeology of the Klamath Falls area and presents an alternate conceptual model for the Klamath Falls geothermal system. He proposes that water is circulated to great depths along faults, where it is heated to rock temperatures corresponding to a 30°C/km gradient. The hot water then rises to shallow depths through conduits closely associated with major faults, until it begins to flow laterally towards the southwest through horizontal permeable strata.

Sammel (1980) also performed a regional geochemical analysis in the Klamath Falls area. Janik et al. (1985), recently published a paper on the chemistry of the geothermal reservoir and proposed a conceptual model for the system described in the geochemistry section.

Working with the USGS and Oregon's Department of Geology and Mineral Industries (DOGAMI), in 1979 and 1980 Stark et al. (1979, 1980) studied the geophysical characteristics of the Klamath Basin. They found no direct evidence to either support or refute the possible existence of an igneous heat source, or the concept of deep circulation along fault zones penetrating a hotter-than-average crust.

In 1983, Lawrence Berkeley Laboratory, Stanford University, Oregon Institute of Technology (OIT), and the U.S. Geological Survey collaborated in pumping and injection tests at Klamath Falls (Sammel et al. 1984). The hydrologic data confirm the highly-fractured and faulted nature of the system as indicated by the high degree of connectivity between wells and high transmissivity of the aquifer. A four month operation of the city's geothermal heating system was studied to provide information on the effects of the operation (D.C. Long Energyman, Inc., 1984). Among some of the data collected were water levels, temperatures, average daily ambient air temperatures, and seasonal water level graphs. A recent well test near OIT also indicates a high transmissivity for the reservoir (Nork, Inc., 1986).

This study reviews all the available data accumulated to date, and considers a new model for the Klamath Falls geothermal system based on recent interpretations. This model includes a detailed conceptual model for the geothermal system and also provides a quantitative analysis of the system. By analyzing the temperature distribution in detail, it is possible to detect the locations of several subsidiary faults to the large northwest-trending normal fault identified in previous reports. The existence of these faults is verified by high-altitude infrared photographs of the area. A detailed conceptual model that emphasizes the role of subsidiary faults has been developed.

The quantitative analysis applies three different methods for calculating the hot water recharge rate into the system and include a semi-analytic approach for a generalized model of the Klamath Falls geothermal system, a lumped-parameter analysis, and a detailed three-dimensional numerical model. The first two methods are used to obtain initial 'order of magnitude' type estimates for the hot water recharge rates. Estimates of the heat loss from the aquifer, total stored energy within the Klamath

Falls system, and times necessary to reach steady state are also estimated. The numerical model employees an integrated finite difference code, PT, developed by Bodvarsson (1982).

The main portion of the quantitative analysis for the geothermal system concentrates on the three-dimensional numerical model. The motivation behind this type of analysis is to incorporate the main features of the geothermal system (spatial variations of properties) that can not be considered using the simple methods above. The three-dimensional model can also give some indication of the credibility of the proposed conceptual model. The degree to which the numerical model is unique can be determined from relative sensitivities of the principal variables for the geothermal system. Estimates of the hot water recharge and the permeability distribution for the system are presented.

The numerical approach provides a unique way to evaluate complicated geothermal system such as Klamath Falls. This numerical model, sets the framework for further modeling studies that might include a rigorous exploitation strategy and future reservoir predictions. A problem such as the 1 ft/year water level declines in the reservoir might also be answered using this model.

2.0 DATA EVALUATION

To begin any type of quantitative analysis of a geothermal reservoir, a complete knowledge and understanding of all current data and their previous interpretations is essential. A large amount of data has be collected and analyzed for the Klamath Falls geothermal area. In this study, all of the available data for the geothermal system has been reviewed and in some cases re-evaluated to construct a detailed conceptual model. Previous conceptual models have only been very generalized, offering simple models to explain the geothermal phenomenon. These conceptual models have also been reviewed and combined into the new conceptual model.

A conceptual model is perhaps the most vital stage in geothermal modeling, because it sets up the basic framework necessary for any type of quantitative analysis. The conceptulization of the physical processes and characteristics of the geothermal reservoir is a step that must be re-evaluated and updated every time new data is collected and analyzed. Data used in developing a conceptual model is derived from several sources:

- Geology
- Well Testing
- Geophysics
- Geochemistry
- Temperature Data

These data groups are discussed in the following sections, from which a conceptual model is developed.

2.1 Geology

The Klamath Falls geothermal area, east of the Cascade Range and north of the Medicine Lake Highlands, California, is situated in a horst and graben structure typical of the Basin and Range province. The Klamath graben complex extends some 80 km, from Lower Klamath Lake, to as far north as Crater Lake, trending approximately N40W. Faulting in the area is believed to have commenced during the late Pliocene

and continued well into the Pleistocene. Steeply dipping normal faults with vertical throws up to 1600 ft flank either side of the graben complex and trend N25-35W. On the western shore of Upper Klamath Lake the large fault blocks dip towards the southwest, while on the eastern shore they dip to the northeast, suggesting that the axis of the graben complex passes through the lake.

The two types of faulting occurring in the immediate region are NW-trending normal faults and NE-trending, strike-slip cross-faults. Figure 4 shows the regional fault trends associated with the Klamath Basin (Kienle et al., 1981). Donath (1962) describes these two sets of faults as being contemporaneous, originally developing as conjugate strike-slip shears in a stress system with a north-south maximum principal stress and an east-west minimum principal stress. The system forms what Donath refers to as a rhombic fracture pattern. Lawrence (1976) interprets the Basin and Range faulting in Oregon as being separated by four strike-slip zones trending WNW. The fault blocks between these strike slip fault zones exhibit the rhombic fracture pattern suggested by Donath (1962). Lawrence (1976) suggests that the rhombic pattern of normal faulting in the region is a result of the interaction of extensional faulting between the fault zones and right-lateral strike-slip motion at the edges of the blocks.

It is worth noting an interesting pattern described by Peterson and McIntyre (1970) regarding the fault block movements. The fault blocks on the western shore of Upper Klamath Lake are tilted to the southwest and on the eastern shore they are tilted towards the northeast. This particular type of feature has been identified in other areas of the Basin and Range province and has been the subject of several studies. Stewart (1979) describes three types of general models proposed for the Basin and Range structures. Figure 5 shows three types of horst and graben structures. According to Stewart (1983), the tilting of these fault blocks can be most easily accommodated by the listric fault and the bouyant block models.

The geology of the area has been mapped and described by Peterson and McIntyre (1970). Four dominant rock units occur in the immediate Klamath Falls area, identified by outcrops and borehole data (Newcomb, 1958). These rock units are, from

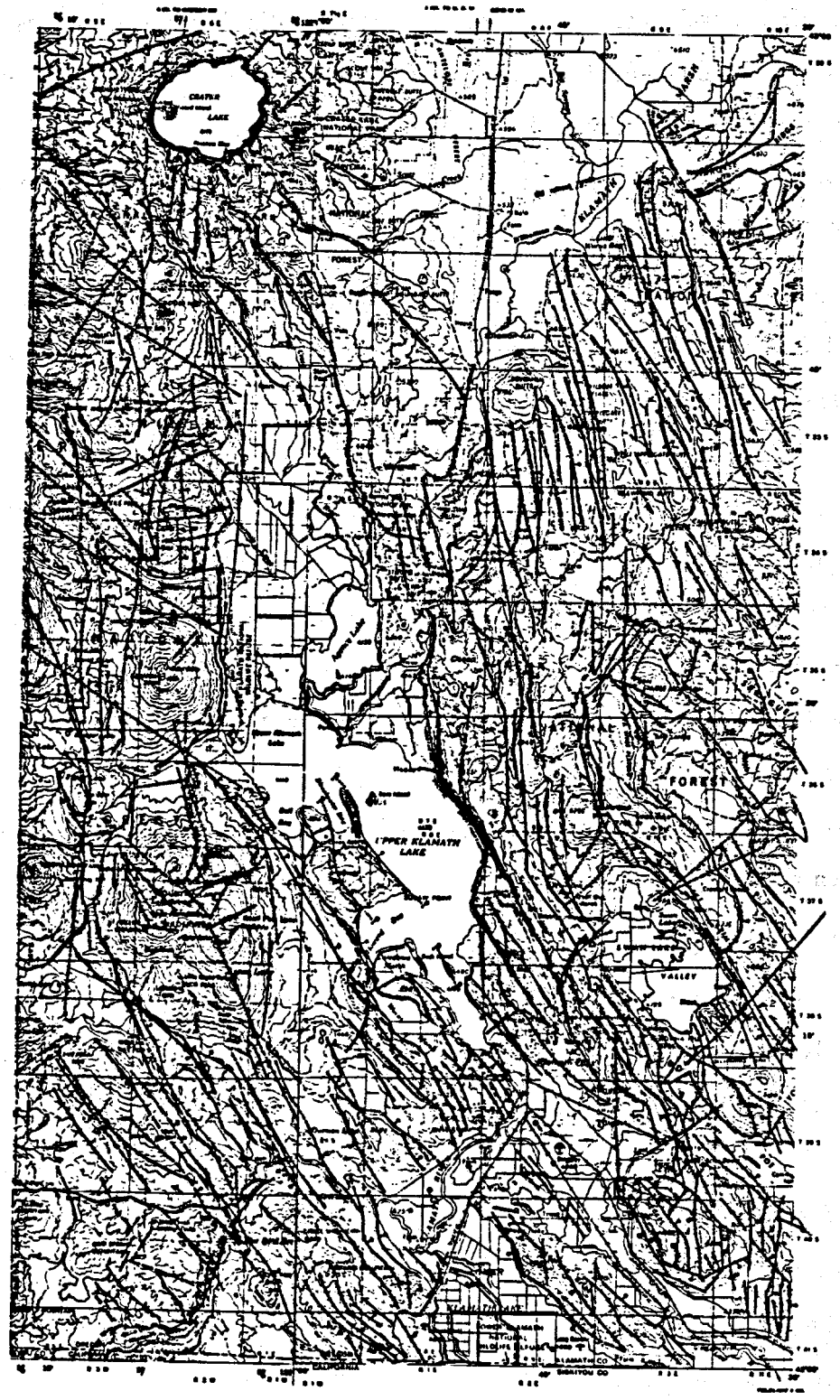

XBL 871-100

Figure 4. Regional Fault trends in the Klamath Basin area (taken from Kienle et al., 1981).

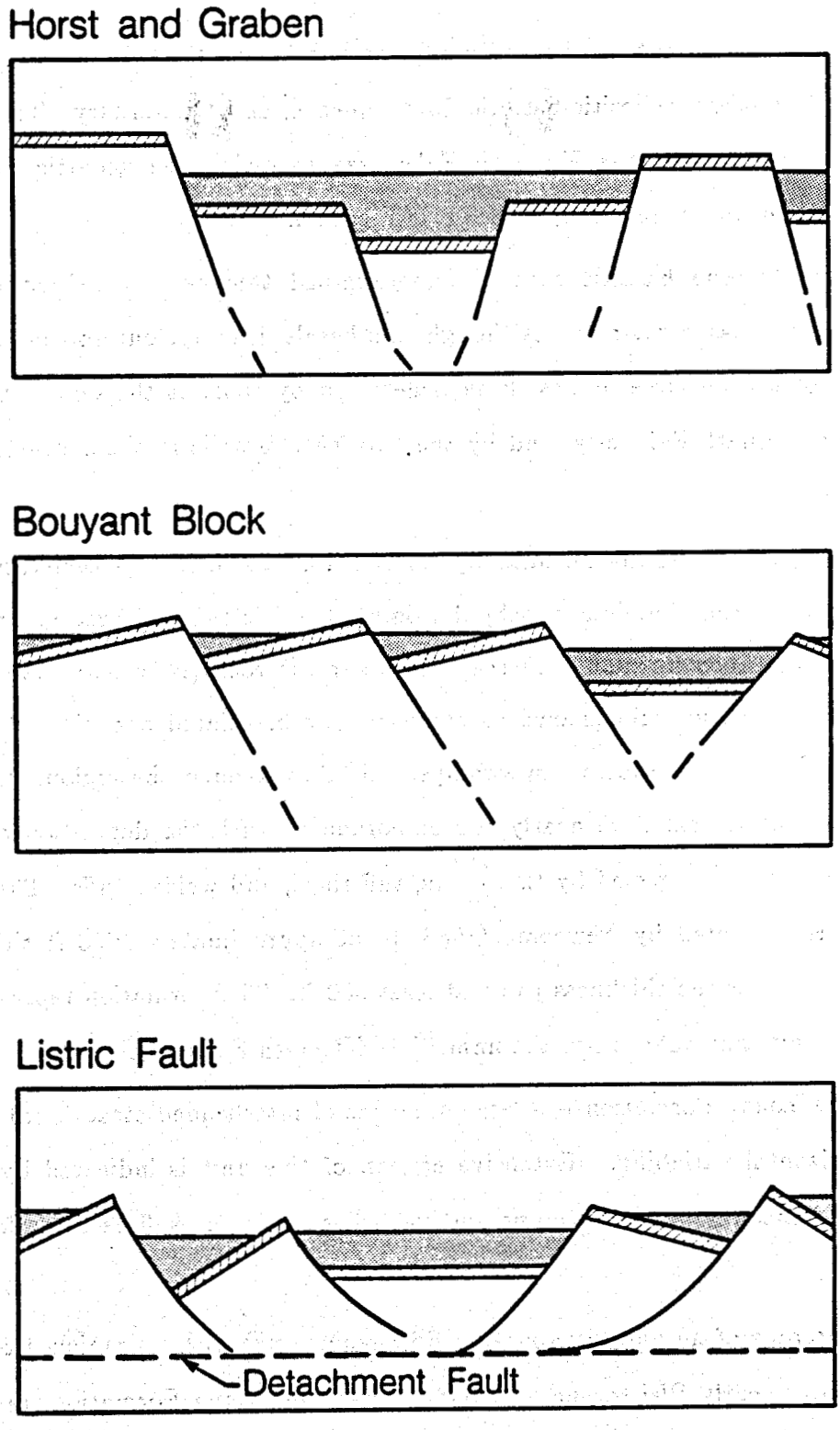

Figure 5. Three types of models possible in the Basin and Range, (taken from Stewart 1979).

earliest to most recent, a Pliocene basement basalt, the thick Pliocene Yonna Formation, a Pleistocene andesitic-basaltic flow sequence, and Quaternary alluvium. A stratigraphic column for the Klamath Falls area following the geologic description by Peterson and McIntyre (1970) is shown in Figure 6.

The Pliocene basaltic rock of undetermined thickness is defined by Newcomb (1958) as the basement rock. Although this basalt does not outcrop in the immediate vicinity of the resource, it has been penetrated by wells at the OIT campus, 2 miles north of Klamath Falls city, and by the two YMCA wells in the southern part of the resource.

The Pliocene Yonna Formation, comprised of a sequence of lacustrine and fluvial tuffaceous siltstone, sandstone, ashy diatomite, basaltic tuff and breccia, and a few thin basalt flows, uncomformably overlies the basement rock (Newcomb, 1958). This formation is primarily subaqueous, as evidenced by brecciated and altered basalt flows, deposited during a period when swamps and lakes covered the region. Explosive and quiescent volcanisms were nearly contemporaneous with the deposition of the Yonna Formation, as is suggested by the maars, tuff rings, and welded tuffs. The Yonna Formation is estimated by Newcomb (1958) to be approximately 1000 ft thick. Sammel (1980) estimates the thickness to be at least 850 ft. This formation represents the oldest rock unit that outcrops in the immediate Klamath Falls geothermal area.

The Yonna Formation is a large sequence of interbedded strata with high vertical and horizontal variability. Extensive erosion of this unit is indicated by the varying thickness encountered in outcrops and in driller's logs, as well as unconformable rock contacts.

Outcrops of an andesitic-basaltic flow sequence(s) with volcaniclastic interbeds of late Pliocene-early Pleistocene age, lying above the Yonna Formation, range in thickness from 0-180 ft. Just north of the immediate Klamath Falls geothermal area, on the southeast shore of Upper Klamath Lake, Peterson and McIntyre (1970) mapped several basalt eruptive centers. Newcomb (1958) describes several dikes which cut through or into sedimentary Tertiary rocks in the area surrounding the geothermal

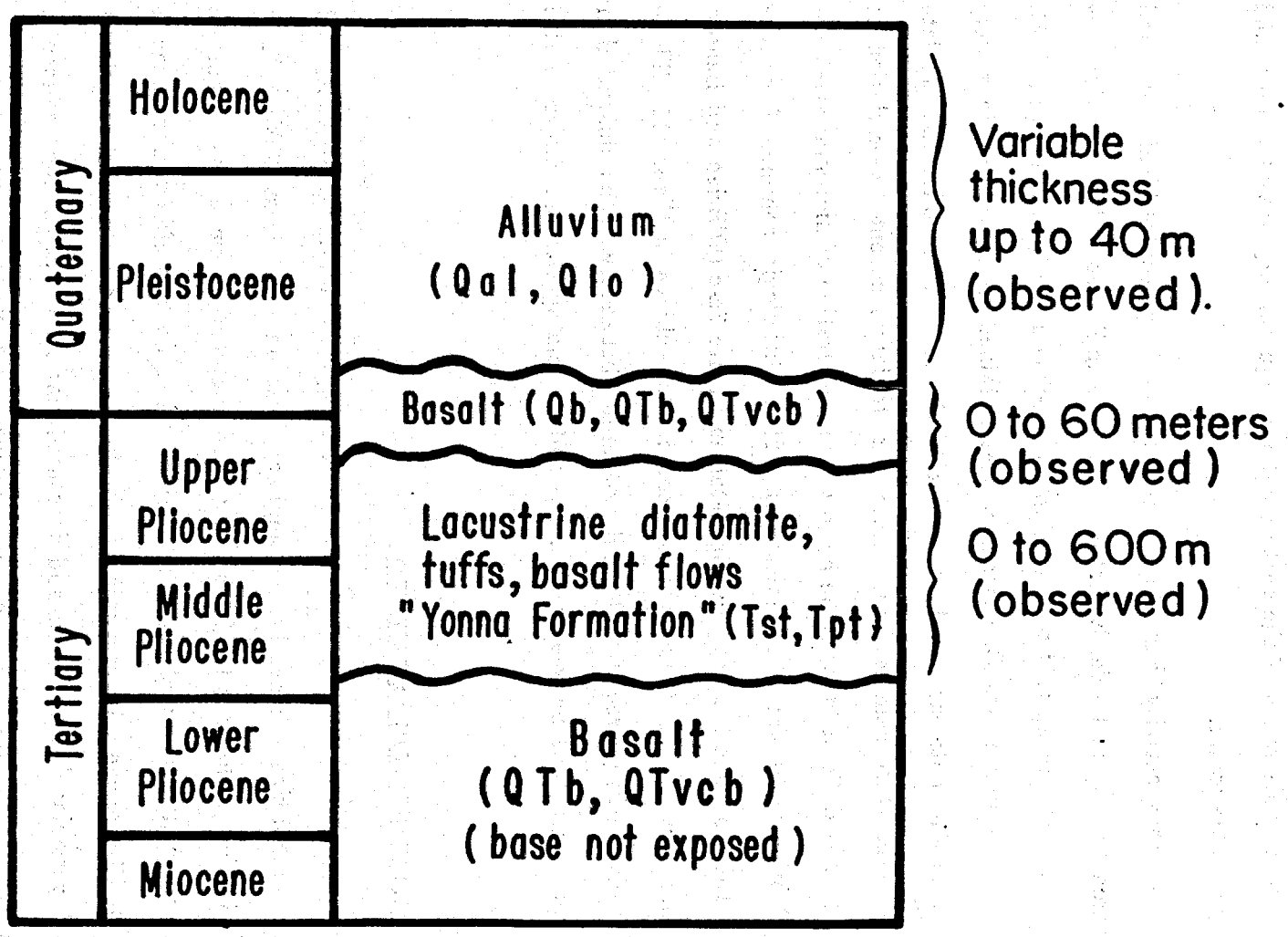

XBL 7810-6540

Figure 6. Stratigraphic column for the Klamath Falls area (taken from Stark et al., 1980).

anomaly. These igneous features are considered to be contemporaneous with the Pliocene-early Pleistocene basalt flow sequence.

Much of the lower valleys in the Klamath Basin are covered by Quaternary alluvium. To the immediate south of the geothermal area, Quaternary fluvial terraces and lacustrine deposits are found.

Nearby volcanic activity has been dated by both paleontological data and potassium/argon (K/Ar) methods. K/Ar methods have indicated volcanic activity as recent as 1.9 m.y.b.p. and up to 4 to 5 m.y.b.p., for rocks on the KGRA periphery (M. O'Brian, personal communication). Diatom species obtained from well cuttings were used to correlate and date strata. It was concluded that surface outcrops are late Pliocene while subsurface samples range from mid to late Pliocene. Correlation of lithologic strata was difficult, due to the hydrothermal alteration of diatomaceous sediments (M. O'Brien, personal communication). Three lithologic columns from the immediate geothermal area are described in detail in Figure 7a-c (O'Brien and Benson 1980). The map locations for these lithologic columns are shown in Figure 11. These lithologies exhibit a high degree of geologic discontinuity between wells as illustrated in Figure 8. Poor correlations between rock types and diatom species are shown in this figure.

2.2 THE GEOTHERMAL AQUIFER

Based on logs from a well drilled at the OIT campus, Sammel (1980) concluded that the rocks comprising the geothermal aquifer to extend to at least 2000 ft. The flow of water in the geothermal aquifer has not been confined to one specific lithologic unit. Within the units that make up the aquifer, water flows preferentially through strata consisting of volcanic breccia (cinders, broken lava, porous lava, etc.), jointed and fractured vesicular basalt flows, and fractured, indurated lacustrine sediments. These strata range in thickness from one to a few feet and have high vertical and areal variability. The permeable strata are interspersed with layers of lacustrine and tuffaceous sediments and diatomite, from 30 to 150 ft thick. Fluid flows from the

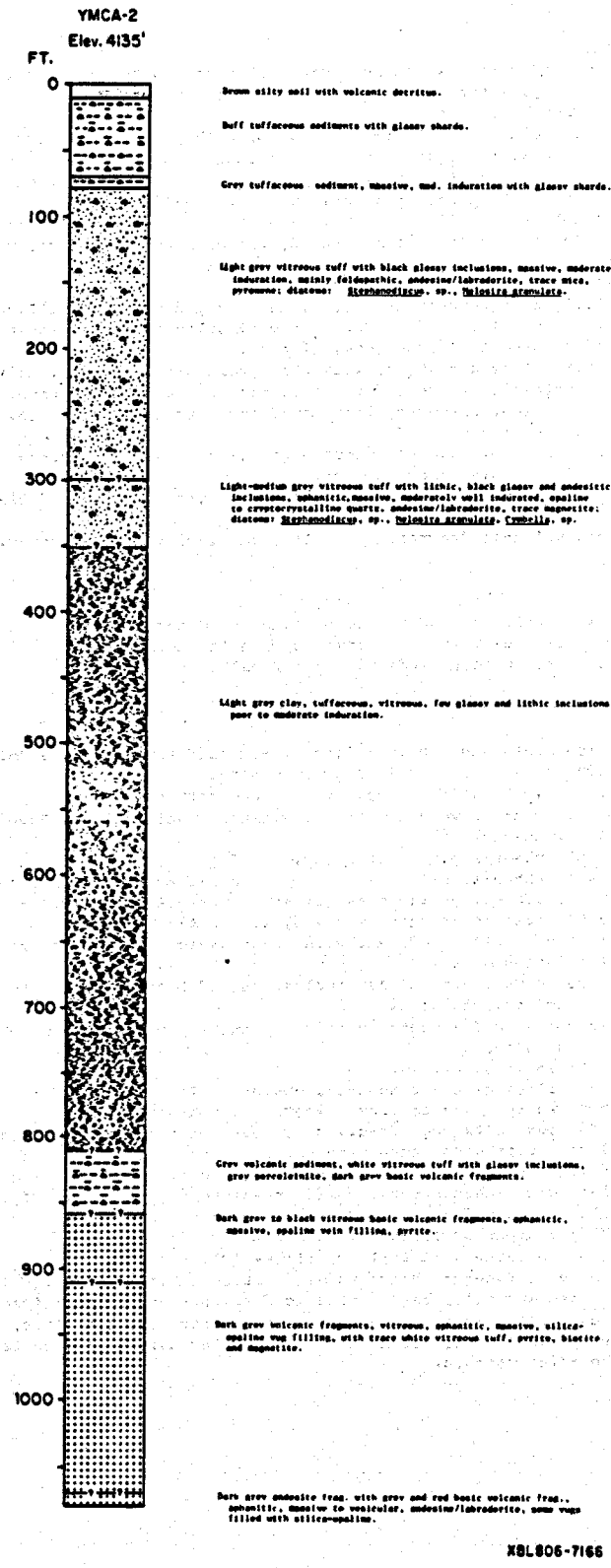

Figure 7a. Lithologic column from the YMCA-2 borehole in the geothermal area at Klamath Falls (taken from M. O'Brian and S. Benson, 1980).

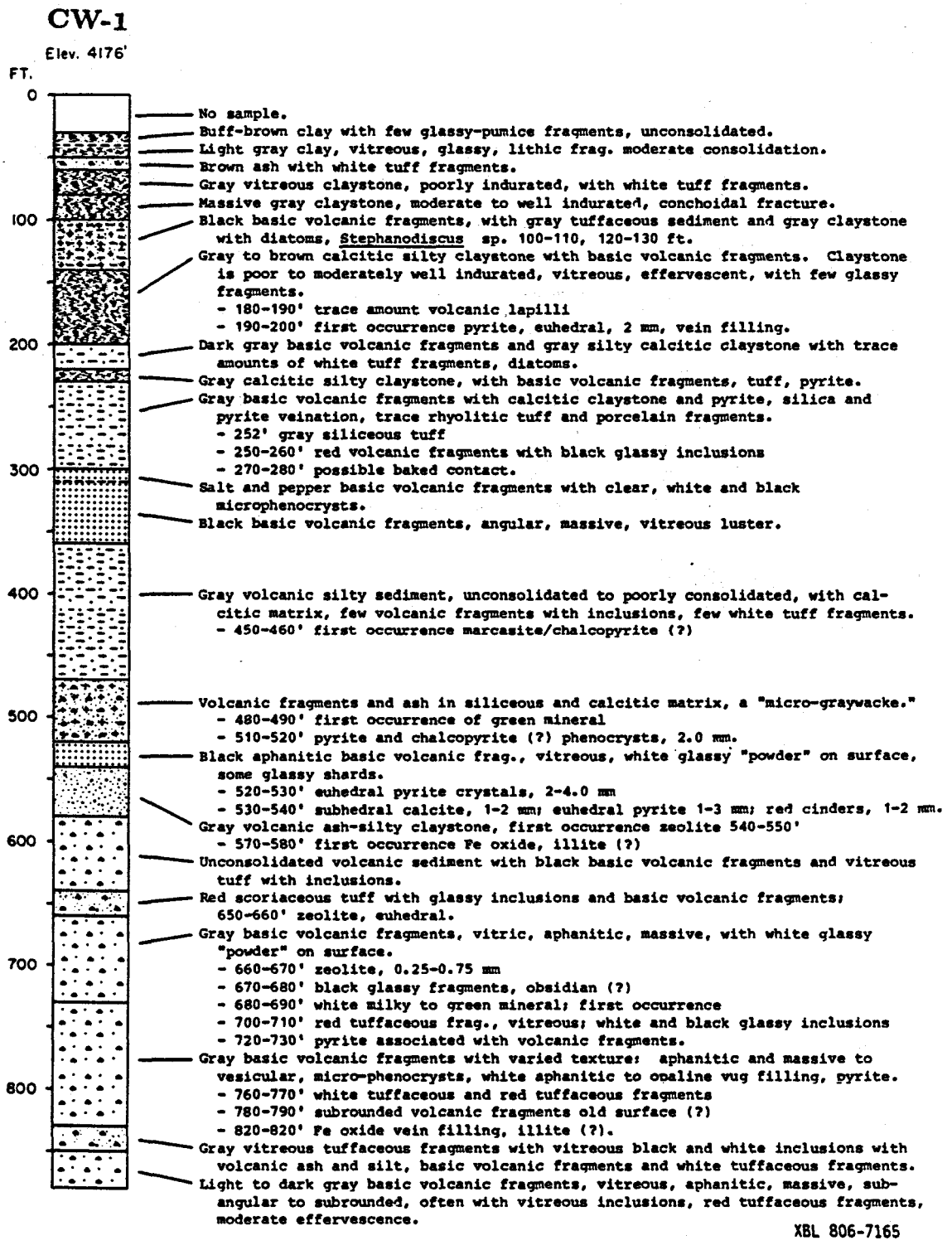

Figure 7b. Lithologic column from the CW-1 borehole in the geothermal area at Klamath Falls (taken from M. O'Brian and S. Benson, 1980).

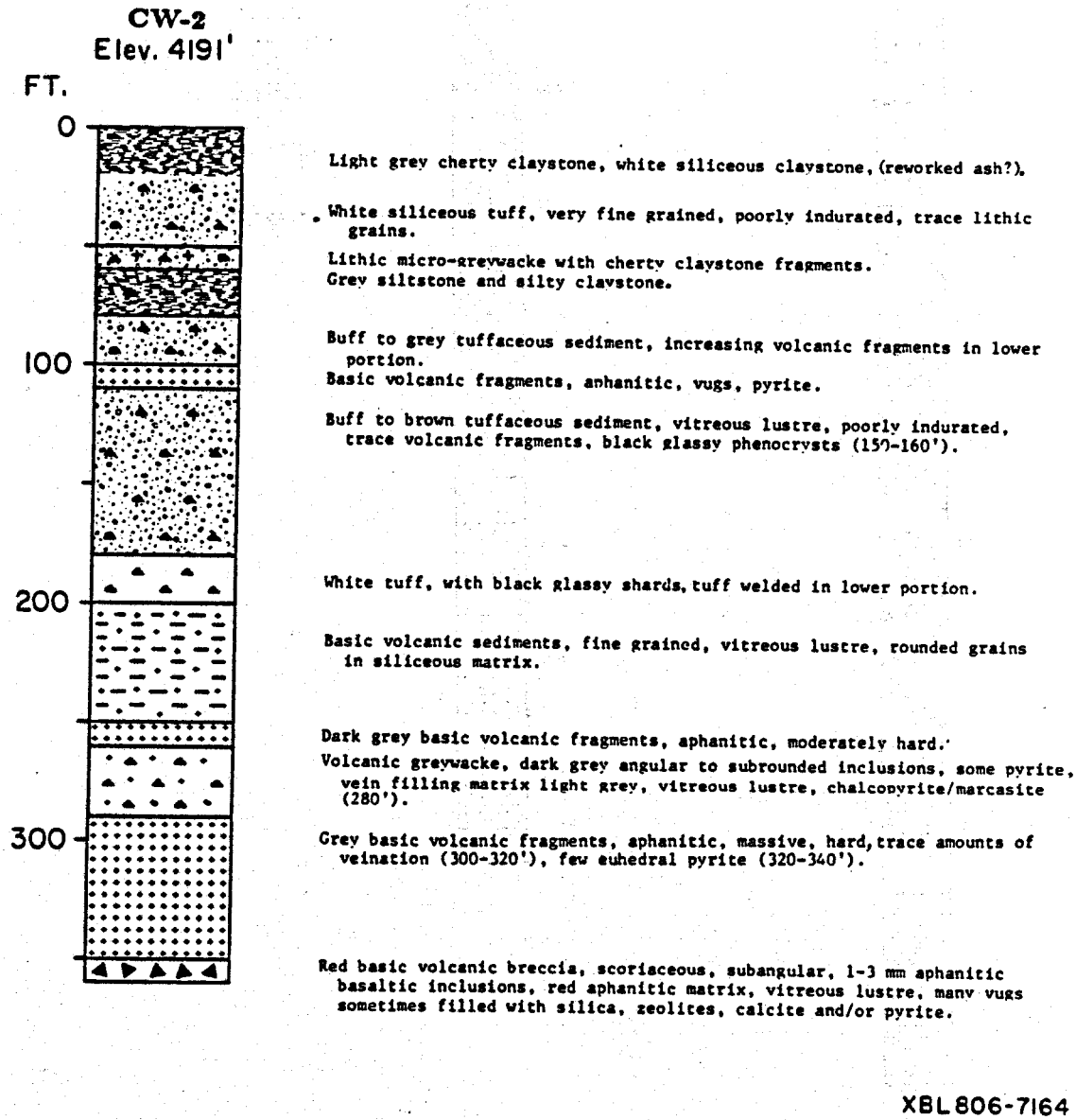

Figure 7c. Lithologic column from the CW-2 borehole in the geothermal area at Klamath Falls (taken from M. O'Brian and S. Benson, 1980).

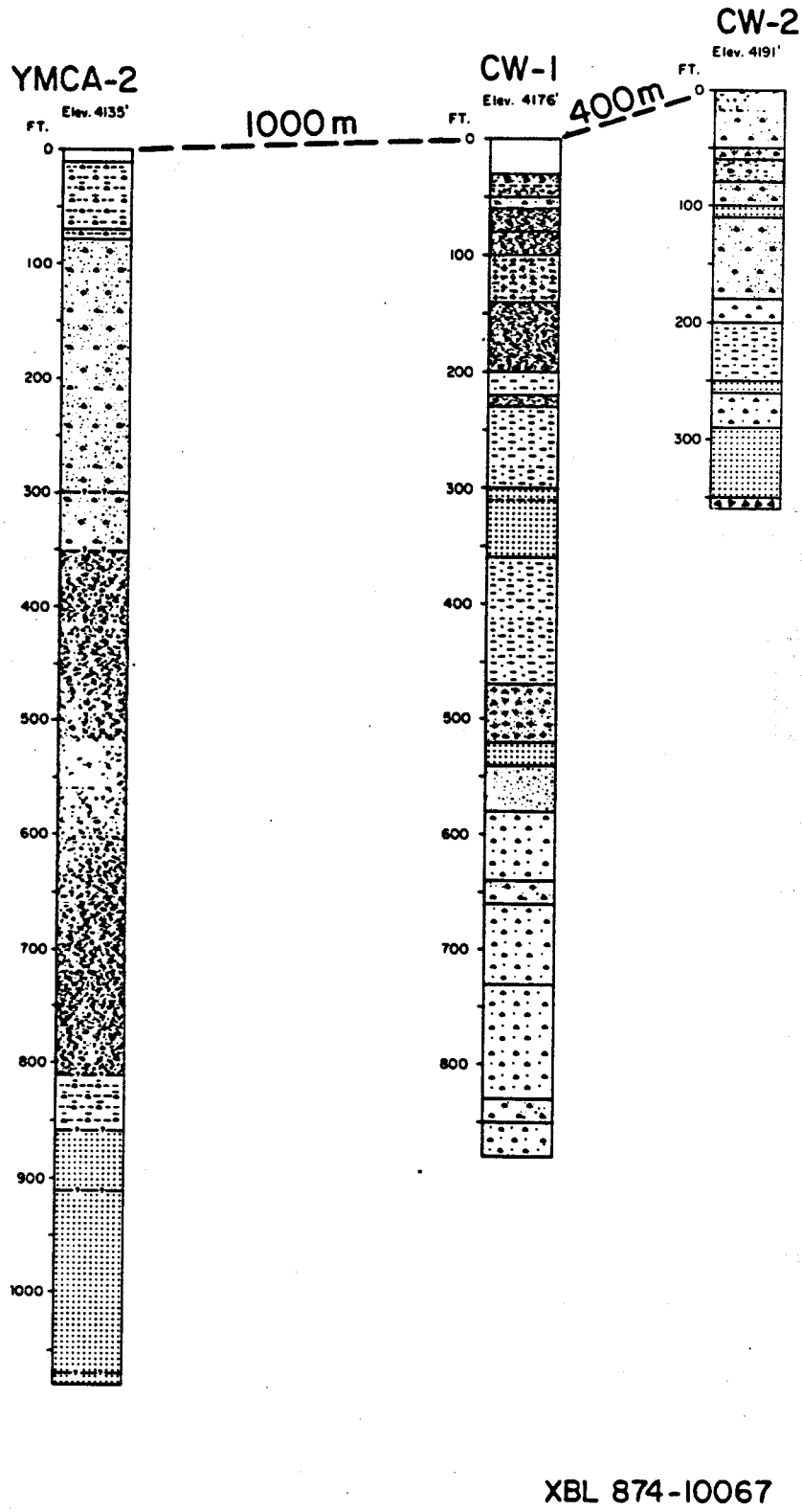

Figure 8. Correlation between YMCA-2, CW-1 and CW-2 lithologies from the Klamath Falls geothermal area.

main fault zone toward the southwest, following the general surface topography, as indicated by static water level maps drawn by Lund (1978) and Sammel et al. (1984). The regional groundwater levels are shown in Figure 9 (Sammel, 1980).

Among some of the data collected to date, are seasonal water level declines and average ambient air temperatures. These data have been plotted on a graph shown in Figure 10 in which a good correlation can be seen between the seasonal water level declines and the average daily temperatures (Sammel et al., 1984). The reason for this good correlation is in part due to the different heating demands placed on the reservoir during the year. However the degree to which the production of the geothermal fluids influences the seasonal water level declines has not been established. The actual seasonal water levels cannot be determined yet without knowing the undisturbed water levels.

The problem of a declining water level at approximately 1 ft/yr at this point in time has only been a matter of speculation. This problem might be explained by: a) the increased rate of production on the system overwhelming the recharge rate into the system, b) a decreasing rate of recharge into the system, c) subsidence and its associated decrease in effective permeability, d) lower permeabilities associated with precipitation. Further investigation into these possibilities is needed to determine the cause of this decline.

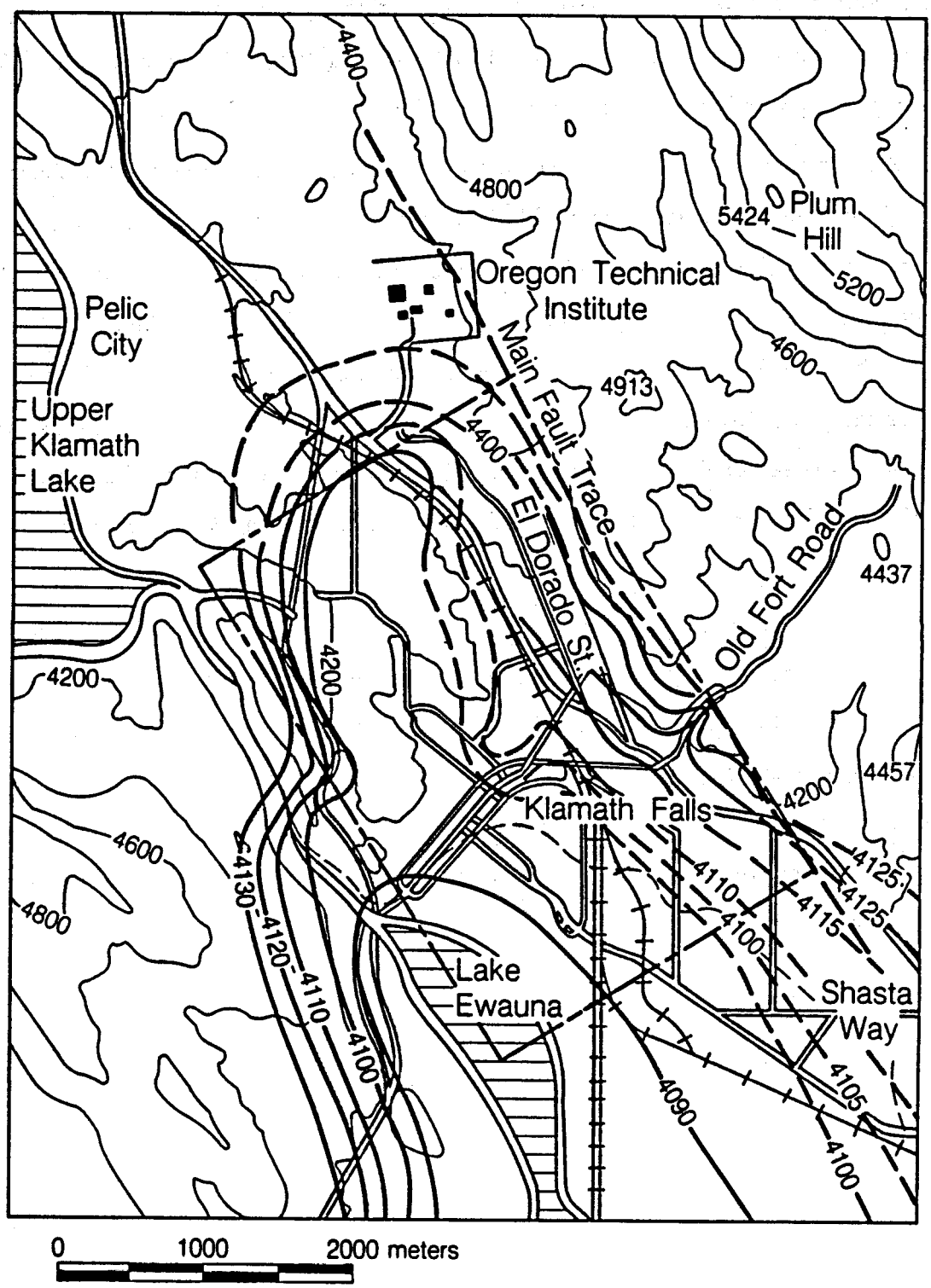

Figure 9. Regional groundwater levels and boundary used in numerical simulation (water levels taken from Sammel, 1980).

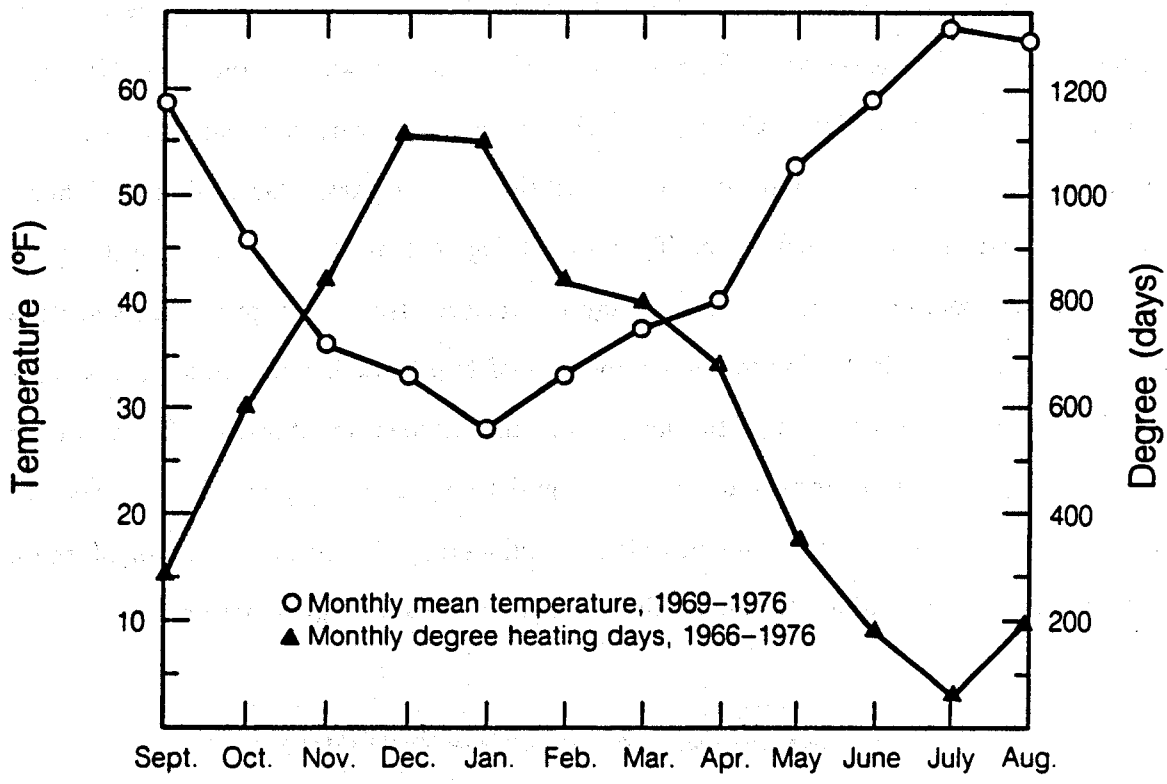

XBL 874-10053

Figure 10. Monthly mean air temperature and heating days for the years 1969-76 (taken from Sammel et al., 1984).

2.1.1 WELL TESTING

Numerous interference tests have been conducted within the Klamath Falls KGRA. From these tests, the hydrological parameters of the reservoir (transmissivity, kb/μ and storage coefficient, $\phi c_t b$) have been estimated and the nature of the thermal aquifer has been investigated. The transmissivity is actually defined by Kb (the hydraulic conductivity times the aquifer thickness), however, because the water is non-isothermal the density depends on the location of the particular well test. Therefore, the transmissivity is defined as $T/\rho g$ or $Kb/\rho g$ in this study. The storativity is defined as the volume of water than an aquifer releases from storage per unit surface area of aquifer per unit decline in the component of hydraulic head normal to that surface (Freeze and Cherry, 1979). In the petroleum engineering literature the term for the storativity S is given by $\phi c_t b$ which is equal to $S/\rho g$ or $S_s b/\rho g$. The storativity term used in this study uses the petroleum engineering definition. Results of these tests, summarized in Tables 1. and 2., show the aquifer to be highly permeable.

Table 1. Average Reservoir Parameters

Well Location	Transmissivity (kb/μ) x 10^{-6} $m^3/Pa \cdot s$	Storativity ($\phi c_t b$) x 10^{-6} m/Pa	Source
south central area	2.192	0.102-1.02	Lund, 1978
south central area	1.096	0.102-1.02	Sammel, 1980
south central area	4.21-4.51	0.106-.345	Benson et al., 1980
south central area	3.0-9.03	0.039-0.088	Benson, 1982a.
south central area	6.017	—	Benson, 1982b.
south central area	1.955	0.0301	Benson, 1983
OIT area	.498-7.48	0.0408-1.02	Nork Inc., 1986
south central area	2.11	0.0221	Sammel et al., 1984

Table 2 is a list of all of the values to date, for storativity and transmissivity of the reservoir from several drawdown/buildup tests.

Table 2. Reservoir Parameters

Obs. Well	Active Well	Transmissivity (kb/μ) x $10^{-6}m^3/Pa \cdot s$	Storativity ($\phi c_t b$) x $10^{-6}m/Pa$	Source
FS 3	Museum	2.522	8.16	Lund, 1978
GC 9	Museum	3.618	0.204	Lund, 1978
HD 7	Museum	3.069	0.204	Lund, 1978
MW 5	Museum	9.868	—	Lund, 1978
KU 1	Museum	5.263	0.102	Lund, 1978
LJ 4	Museum	5.482	0.510	Lund, 1978
24	CW-1	2.617	0.225	Sammel, 1984
4	CW-1	2.95	1.33	Sammel, 1984
3	CW-1	2.287	1.45	Sammel, 1984
101	CW-1	2.090	0.42	Sammel, 1984
203	CW-1	2.015	0.42	Sammel, 1984
177	CW-1	2.617	2.90	Sammel, 1984
200	CW-1	2.045	2.92	Sammel, 1984
101	Museum	1.760	0.269	Sammel, 1984
3	Museum	19.10	0.102	Sammel, 1984
203	Museum	2.030	0.141	Sammel, 1984
24	Museum	1.435	0.181	Sammel, 1984
177	Museum	2.153	0.323	Sammel, 1984
39	Museum	1.715	0.049	Sammel, 1984
123	Museum	1.925	0.265	Sammel, 1984
YMCA 1	YMCA 2	1.676	—	O'Brien, 1981
4	CW-2	6.017	0.044	Benson, 1981
4	CW-1	10.23	0.177	Benson, 1981
HermosaApts.*	Museum	0.6017	0.663	Benson, 1981
HermosaApts.**	Museum	2.74	0.221	Benson, 1981
125	Museum	6.017	—	Benson, 1981
127	CW-2	0.156	0.049	Benson et al., 1980
4	CW-2	0.102	0.0062	Benson et al., 1980
101	CW-2	0.198	0.04	Benson et al., 1980
CIP-2	CIP-1	4.625	7.648	Nork Inc., 1986
CIP-3	CIP-1	3.172	3.569	Nork Inc., 1986
OIT-3	CIP-1	1.222	1.530	Nork Inc., 1986
OIT-5	CIP-1	2.445	4.079	Nork Inc., 1986
La Vista Motel	CIP-1	6.278	3.977	Nork Inc., 1986
N. Entrance Motel	CIP-1	2.445	1.36	Nork Inc., 1986
JELD-WEN	CIP-1	16.850	21.41	Nork Inc., 1986
N. Entrance Motel	Jeld-Wen2	13.55	6.118	Nork Inc., 1986
JELD-WEN	Jeld-Wen2	13.55	1.02	Nork Inc., 1986

(* build-up, ** drawdown)

Location maps for each of these wells are shown in Figures 11 and 12.

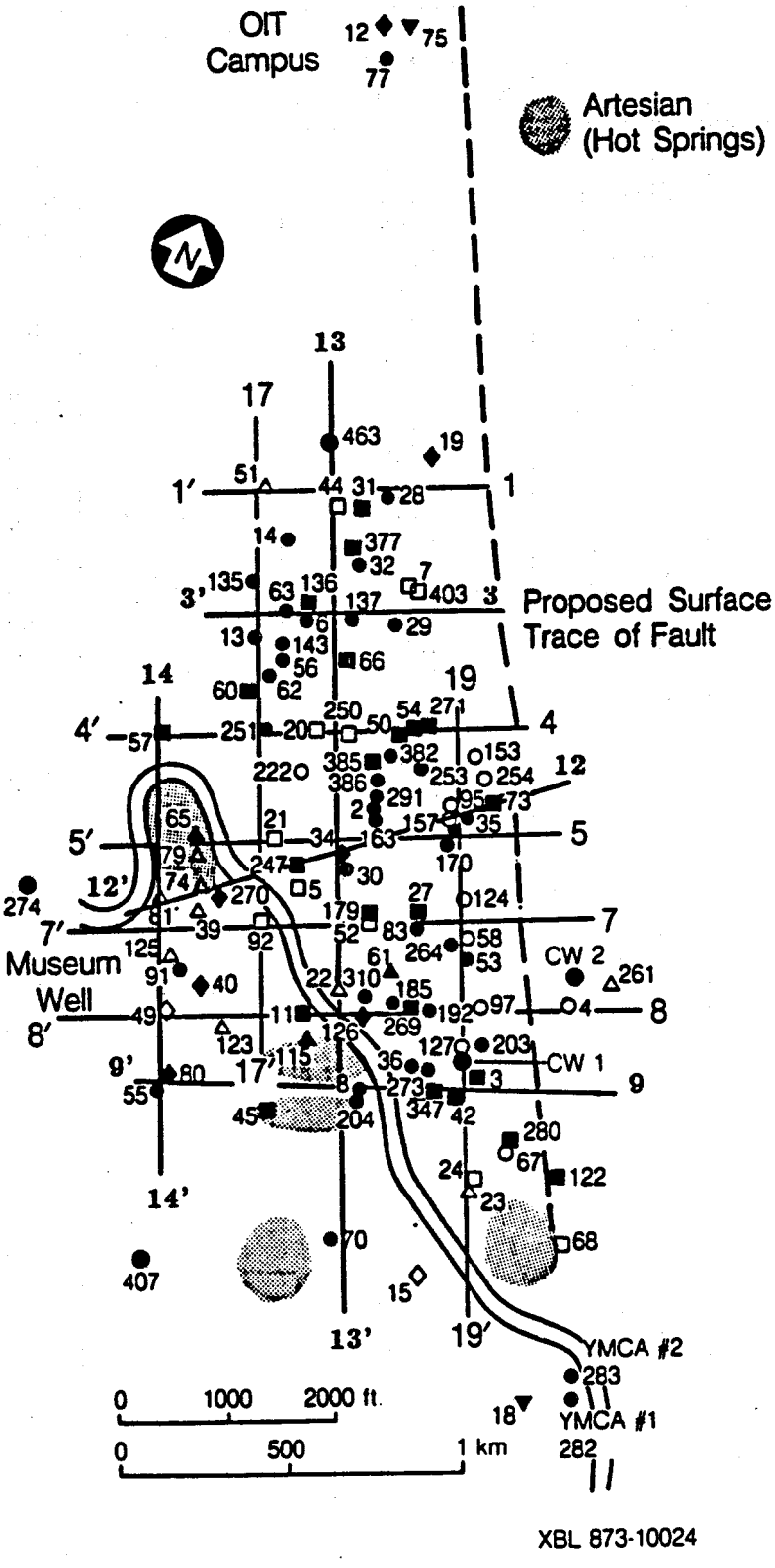

Figure 11. Location map of wells used in aquifer tests and temperature analysis. Lines for the temperature cross-secional profiles are also shown. Shaded areas indicate once active artesian springs.

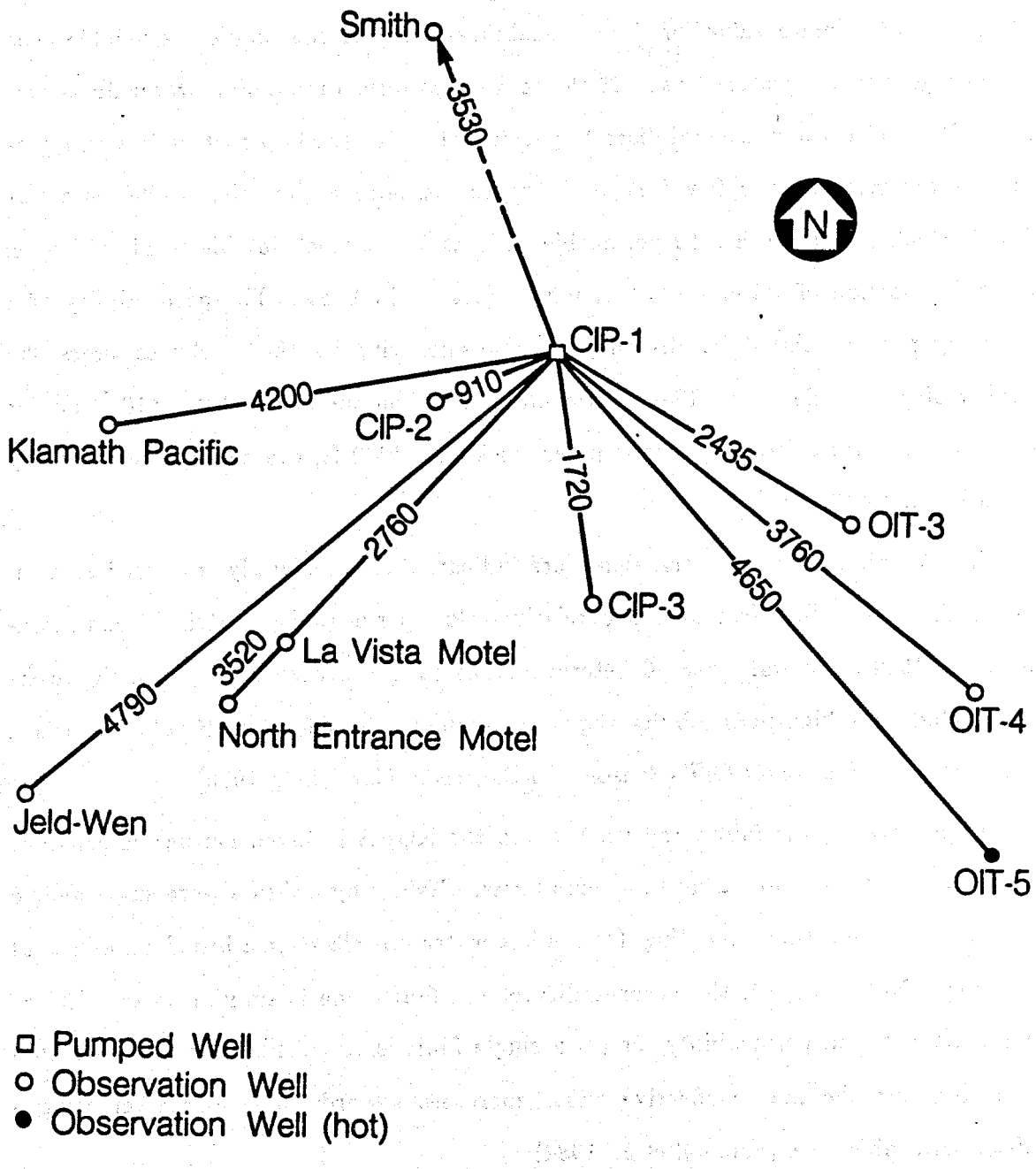

Figure 12. Locations of wells used in aquifer test by Nork Inc., 1986. These wells are located in the OIT campus area.

Using an average value of 1.40×10^{-6} $m^3/Pa \cdot s$ for the transmissivity, one can calculate an approximate value for the permeability of one of the smaller permeable beds in which geothermal waters flow. Of the rocks that form the aquifer, water flows preferentially only through several discrete permeable beds usually a foot or less and generally never more than a few feet in thickness. Assuming that the aquifer is about 2000 ft thick and there are 10 permeable beds at 5 feet thick in this total thickness, the major portion of water flows through 50 feet of thickness. The permeability of a single layer is calculated by dividing the transmissivity by the thickness times the number of permeable beds. These permeabilities are on the order of 2.8×10^{-11} m^2 for the individual beds. For the total aquifer thickness, 2000 ft, the average permeability would be 7.00×10^{-13} m^2.

In general, the pressure transients are indicative of a naturally fractured system, with high permeability fractures and relatively low permeability matrix blocks (Sammel et al, 1984). Several localized heterogeneities have also been detected in the reservoir, including a high-permeability region centered in the Old Fort Road area and a semi-permeable fault near OIT (Benson and Lai, 1986; Nork, Inc., 1986).

Unexpectedly, the faults and fractures in the KGRA behaved neither as constant potential boundaries, nor as no-flow boundaries. Several hypotheses were suggested to explain this observation, including: (1) the hot water upwells over a broad zone instead of a single fault zone, (2) the permeability of the fault zone is similiar to that of the near surface strata permeability, or (3) a single fault is responsible for the deep fluid upwelling, but the fault's effective width increases towards the surface, creating a diffuse permeable zone (Sammel et al, 1984).

2.3 GEOCHEMISTRY

Geochemical data contributes valuable information regarding maximum reservoir temperatures, mixing of thermal waters, fluid residence times and possible sources of recharge. Janik et al. (1985) used tritium data to determine the cold water residence time in the aquifer to be at least 30 years, and that of the thermal waters to be at

least 60 years. From tritium and deuterium data they were also able to conclude that the cold water recharge probably does not originate from the modern Klamath Lake (Sammel, 1980). The tritium data also leads Janik et al. (1985) to suspect two cold water sources—a very shallow one containing tritium and a deeper one that is tritium-free. Geothermometry and mixing models indicate a maximum source-water temperature of 190 ° C.

Janik et al. (1985) developed a conceptual model consisting of a shallow 70-100 ° C thermal aquifer, caused by the mixing of 100-120 ° C and 20 ° C waters. The hot water may be derived from a deeper source where mixing of older tritium-free hot and cold water occurs. Although the maximum source-water temperature has not been encountered yet, geothermometry indicates temperatures of 150 to 190 ° C somewhere in the system.

2.4 GEOPHYSICS

Peterson and McIntyre (1976) prepared a Bouger gravity map for the Klamath Basin. He estimated the thickness of the valley fill in the graben structure to be on the order of 3000 ft southeast of Klamath Falls, and 6000 ft southwest of Klamath Hills. Stark et al. (1980) employed various geophysical methods to investigate the geothermal system in the Klamath Basin. Based on the results of remote sensing, gravity, geology, aeromagnetic and resistivity survey data, they conclude that the shallow hydrothermal circulation is related to the intersection of northeast-trending cross-faults and northwest-trending normal faults. These surveys did not reveal any new information on the heat source; however, they did suggest that either the conceptual model proposed by Peterson and McIntyre (1970) or Sammel et al (1984) could be correct.

2.5 TEMPERATURE DATA

Temperature data are very important to the understanding of a hydrothermal system and the transfer of heat throughout the system. The temperature data used in

this study were obtained primarily from drillers' logs and are derived from over 100 of the wells in the geothermal reservoir. These wells are shown in Figure 13. Temperatures in most cases were measured using a maximum reading thermometer or a simple thermistor apparatus. A few studies (Lund, 1978; Sammel and Peterson, 1976; and Sammel, 1980; Sass and Sammel, 1976) also recorded independent temperature data for the Klamath Falls geothermal area. According to Sass and Sammel (1976), temperature profiles in the Basin and Range province are classified into four distinct types:

1. near-isothermal temperature profiles, indicating hydrologic recharge;
2. quasi-conductive temperature profiles;
3. convex-upward profiles with elevated temperatures, indicating areas of discharge;
4. temperature profiles exhibiting varied types of curvature, implying a combination of upward and downward flow.

As shown in Figure 13, profiles from Klamath Falls exhibit all four types of patterns; however, most temperature profiles show a combination of conductive and convective heat flow.

The most detailed temperature profiles of the system appear to be measured during the drilling process, as opposed to waiting until the borehole is cased and in operation. Before analyzing the temperature data in any detail it is necessary to realize the limitations of the recorded data. For this study, the desired measurement is the formation equilibrium temperature (the formation temperature in its undisturbed state).

Several problems are associated with obtaining accurate equilibrium formation temperatures and this is strongly dependent on when the measurement takes place. Many downhole temperatures are measured while drilling to obtain the most accurate temperatures, however if the temperatures are measured too quickly after drilling intervals, significant errors in measurement are caused by the circulating drilling mud. This problem has been studied by many investigators who have shown that a certain amount of time must be allowed for the system to return to its equilibrium state before any measurements are taken. Bullard (1947) estimated that in order to obtain

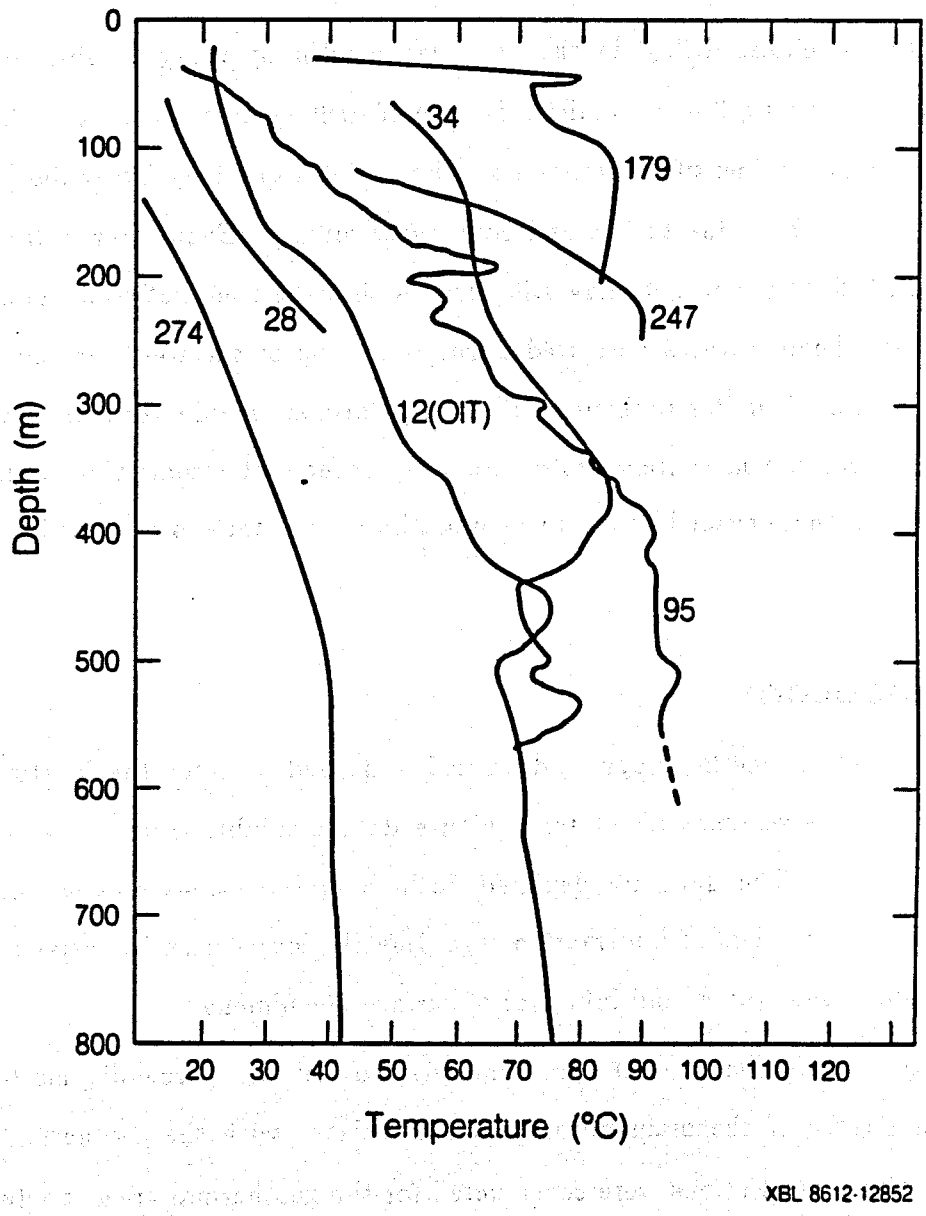

Figure 13. Typical temperature profiles from Klamath Falls, Oregon.

temperatures within 1 percent of equilibrium, the system must be left alone for up to 10 to 20 times that of the actual drilling time.

Most of the boreholes drilled in the area were drilled by using a cable tool rig which does not use drilling fluids. While this type of drilling does not require drilling fluids, it is important to identify intraborehole circulation caused by hydraulic potentials, and bouyancy effects due to hot and cold water mixing. Even after well casing has been installed, fluid circulation may still occur within the zone between the casing and the borehole. Temperatures measured during pumping of the well were not used in this study because of similar problems. The temperatures recorded during pumping do however give accurate measurements of the temperatures of intersecting feedzones in the borehole and there exact locations which are important factors to consider while drilling.

2.5.1 METHODOLOGY

In this section the methodology is discussed and used to infer the locations of faults from the extensive amounts of temperature data available from the Klamath Falls geothermal area. The data are depicted both in cross-sections and as contour plots. Both offer a good deal of information regarding the location and relative size of faults, magnitude of the system and influence of surface phenomena.

Cross-sections were constructed approximately parallel and perpendicular to the proposed surface trace of the main normal fault associated with the geothermal system. Twenty such cross-sections were constructed for the geothermal area; twelve are shown in Figures 14a, b and c and their map locations are shown in Figure 11. Since relatively little temperature data exist east of the normal fault, no cross-sections or horizontal contour maps were constructed for that area.

Figure 14a shows four cross-sections parallel to the main normal fault, while Figures 14b and 14c show eight cross-sections essentially perpendicular to the fault. Both sets of cross-sections show thermal features which can only be explained by complex convection heat transfer mechanisms. Cross-section 13, which is parallel to the fault,

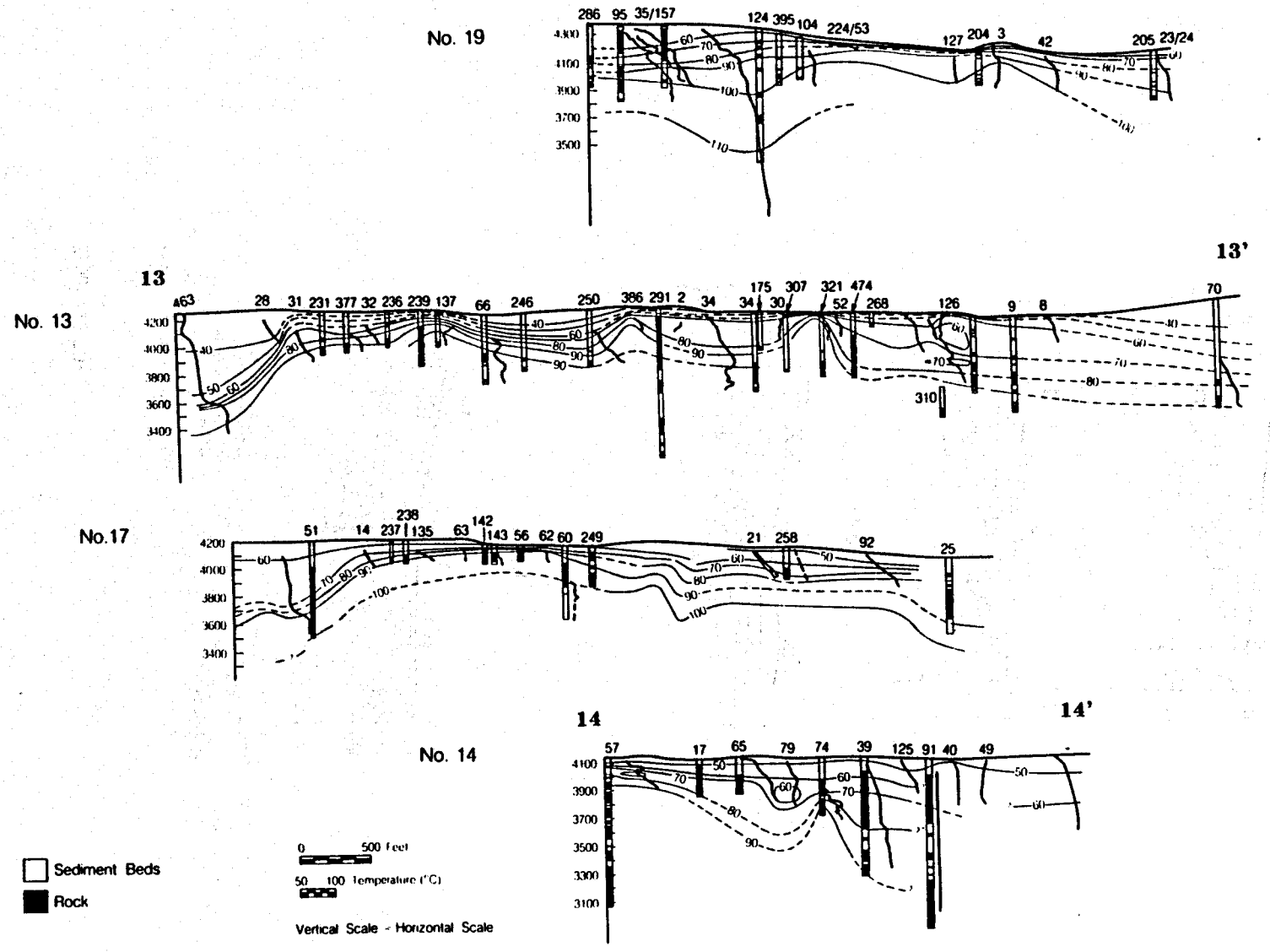

XBL 874-10070

Figure 14a. Cross-sectional temperature profiles parallel to the main normal fault. Well numbers appear above the isotherms. Lithologic columns are shown for several wells.

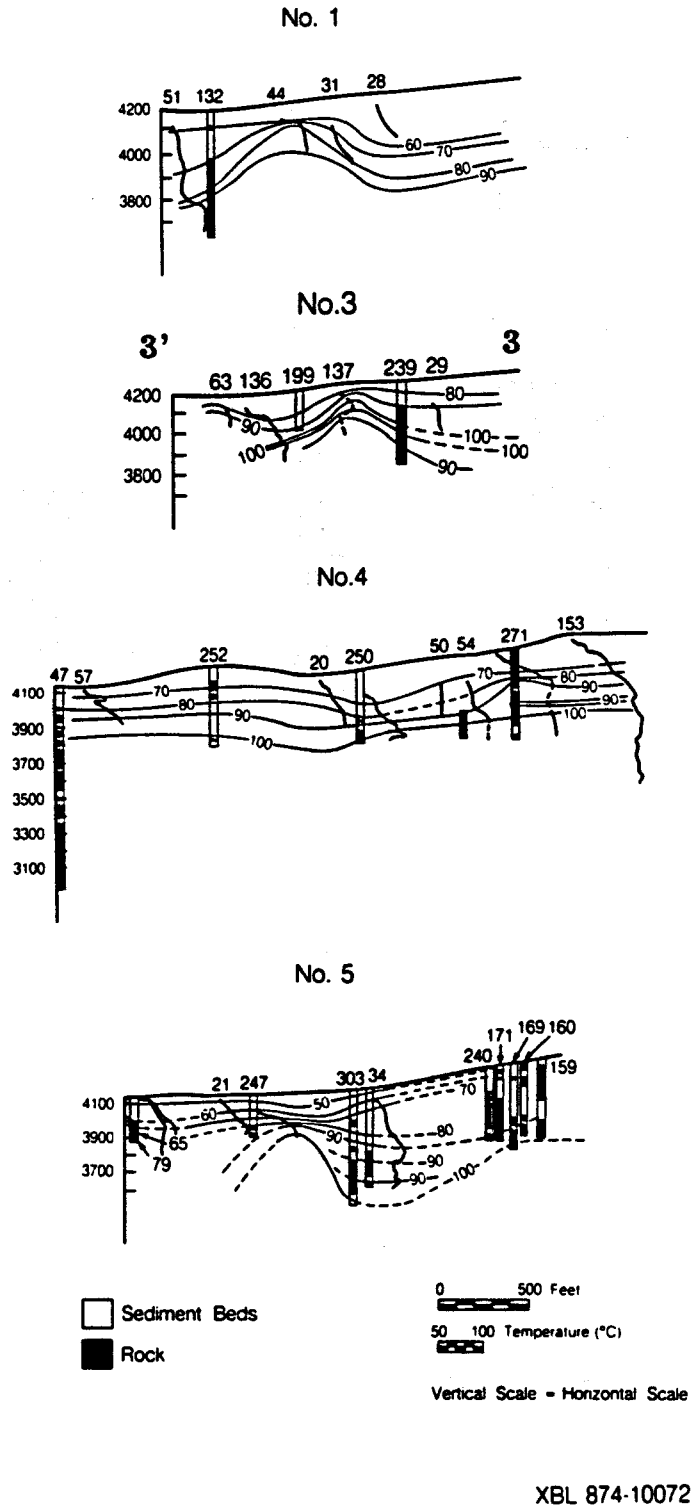

Figure 14b. Cross-sectional temperature profiles perpendicular to the main normal fault. Well numbers appear above the isotherms. Lithologic columns are shown for several wells.

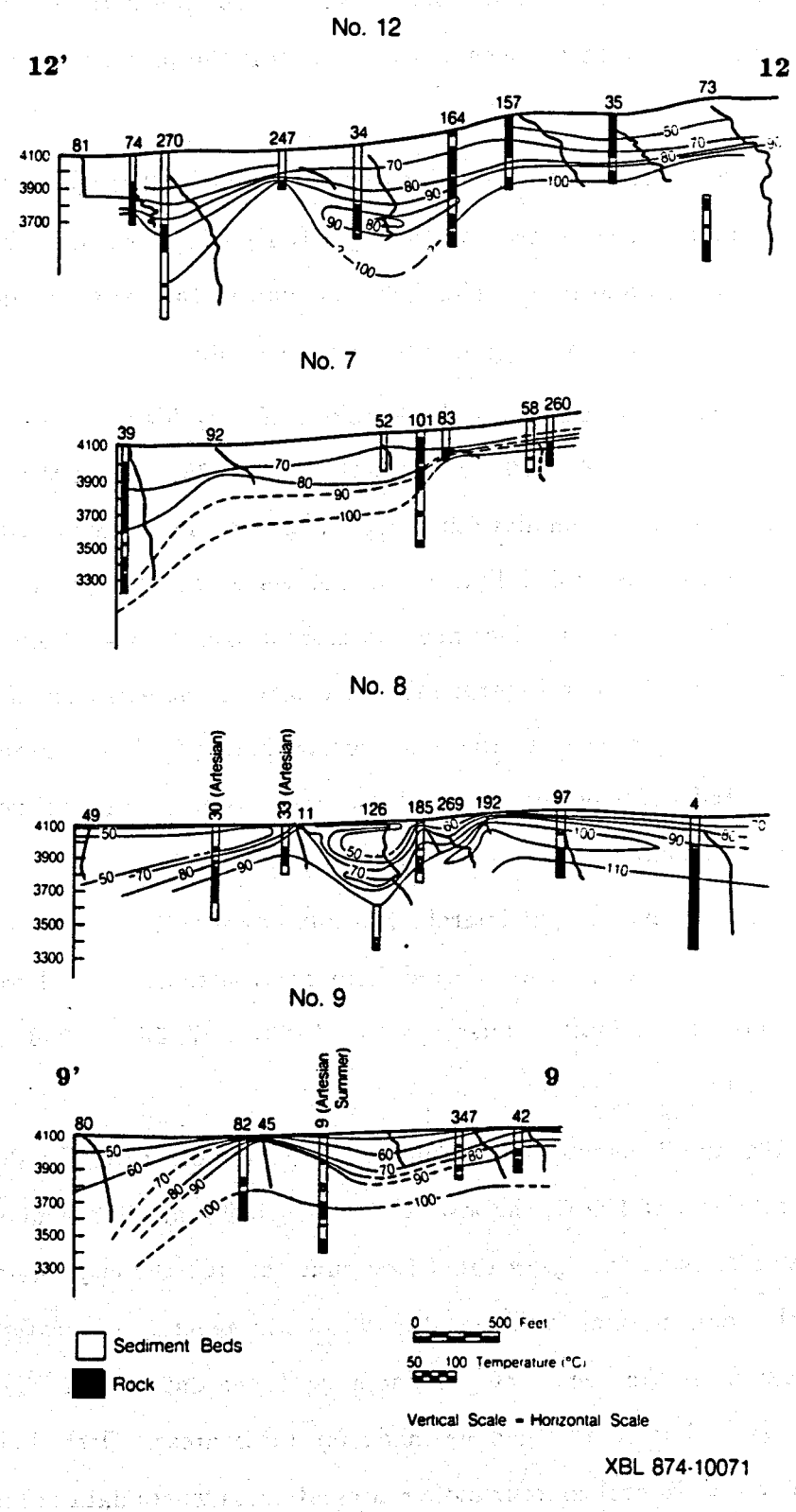

Figure 14c. Cross-sectional temperature profiles perpendicular to the main normal fault. Well numbers appear above the isotherms. Lithologic columns are shown for several wells.

shows temperatures at both ends of the anomaly decreasing rapidly. We propose that northeast-trending cross-faults limit the northern and southern extension of the resource, and that the region between wells 31 and 9 is the primary zone of hot water recharge.

In cross-sections drawn perpendicular to the normal fault (Figures 14b and c), a higher thermal gradient zone is seen on the right (NE) side, most likely indicating the location of the main normal fault. This helps to confirm the existence and define the location of this normal fault, as suggested in previous studies.

Both sets of cross-sections show the locations of very high, near-surface thermal gradients (see wells 31, 44, 386, 179, 137, 74, 247, 45, 192, 25). When the cross-sections are aligned these thermal anomalies fall along lineaments, interpreted in this study as faults (see Figure 15). Several 3-dimensional models using these cross-sections were constructed revealing these fault lineaments in more detail. Cross-sections perpendicular to the main normal fault in Figures 14b and c suggest the existence of a subsidiary normal fault (Fault 1b) parallel to the main normal fault (Fault 1a) intersecting wells 45, 11, 247, 137 and 44. The northern and southern extent of this subsidiary normal fault cannot be determined from the available data.

The locations of several right lateral strike-slip cross-faults, roughly perpendicular to the main normal fault are also inferred from cross-sections parallel to the normal fault (Figure 14a). These faults intersect wells, 31, 237, 137, 56, 57, 386, 179 and 224, as seen in Figure 15.

Figures 16a and b shows contour maps of the temperature distribution at six elevations at intervals of 100 ft, the lowest elevation being at 3600 ft above sea level. The locations of artesian springs, a canal that runs through the city, main roads, and the trace of the main normal fault are also shown. In general, at greater depths and larger distances from the center of the anomaly, fewer data are available. Consequently, only general inferences can be made for these areas. Dashed lines in both cross-sections and horizontal contour plots represent areas where data are limited.

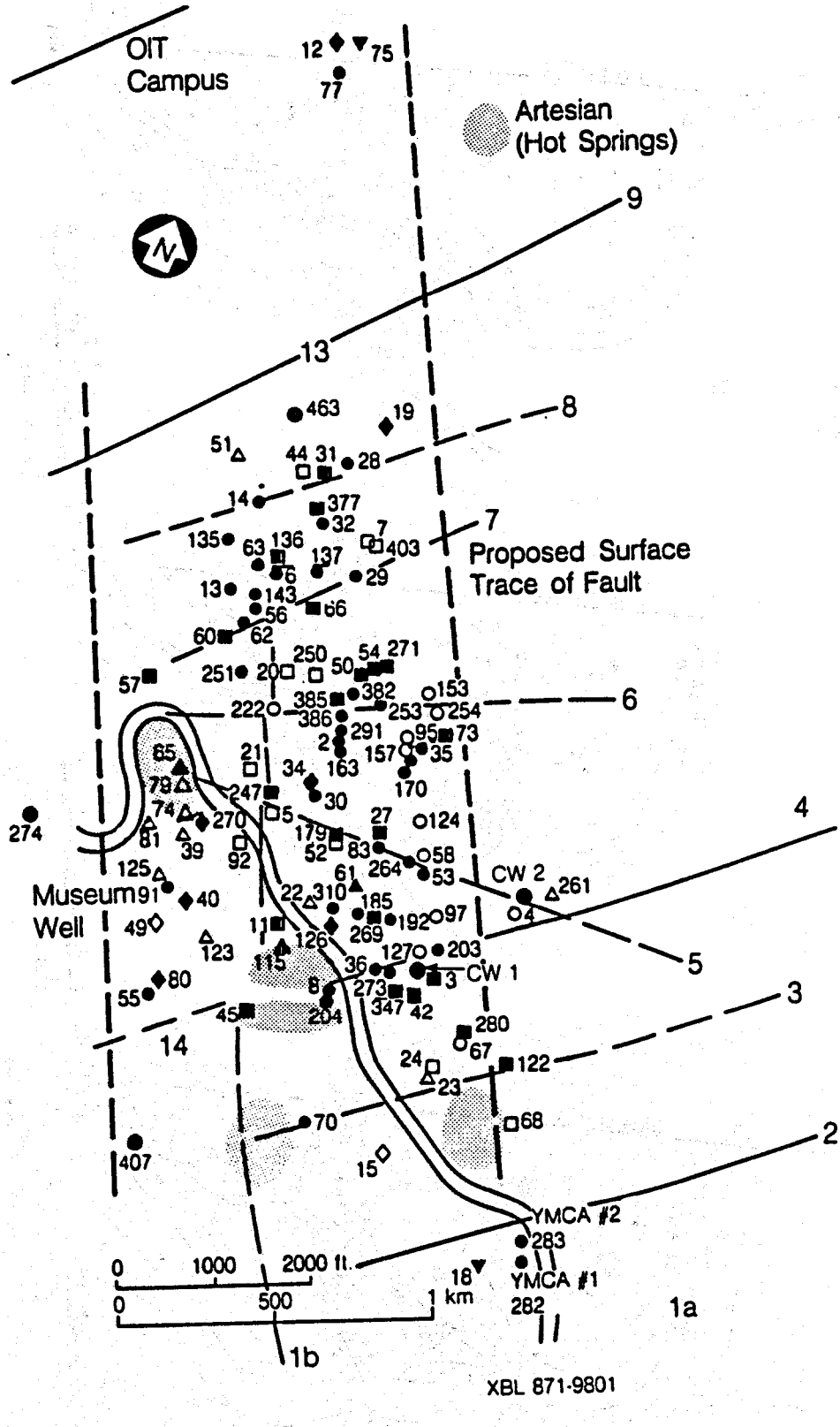

Figure 15. Fault locations inferred form the cross-sectional temperature profiles and temperature contour plots. Solid lines indicate a higher degree of certainty.

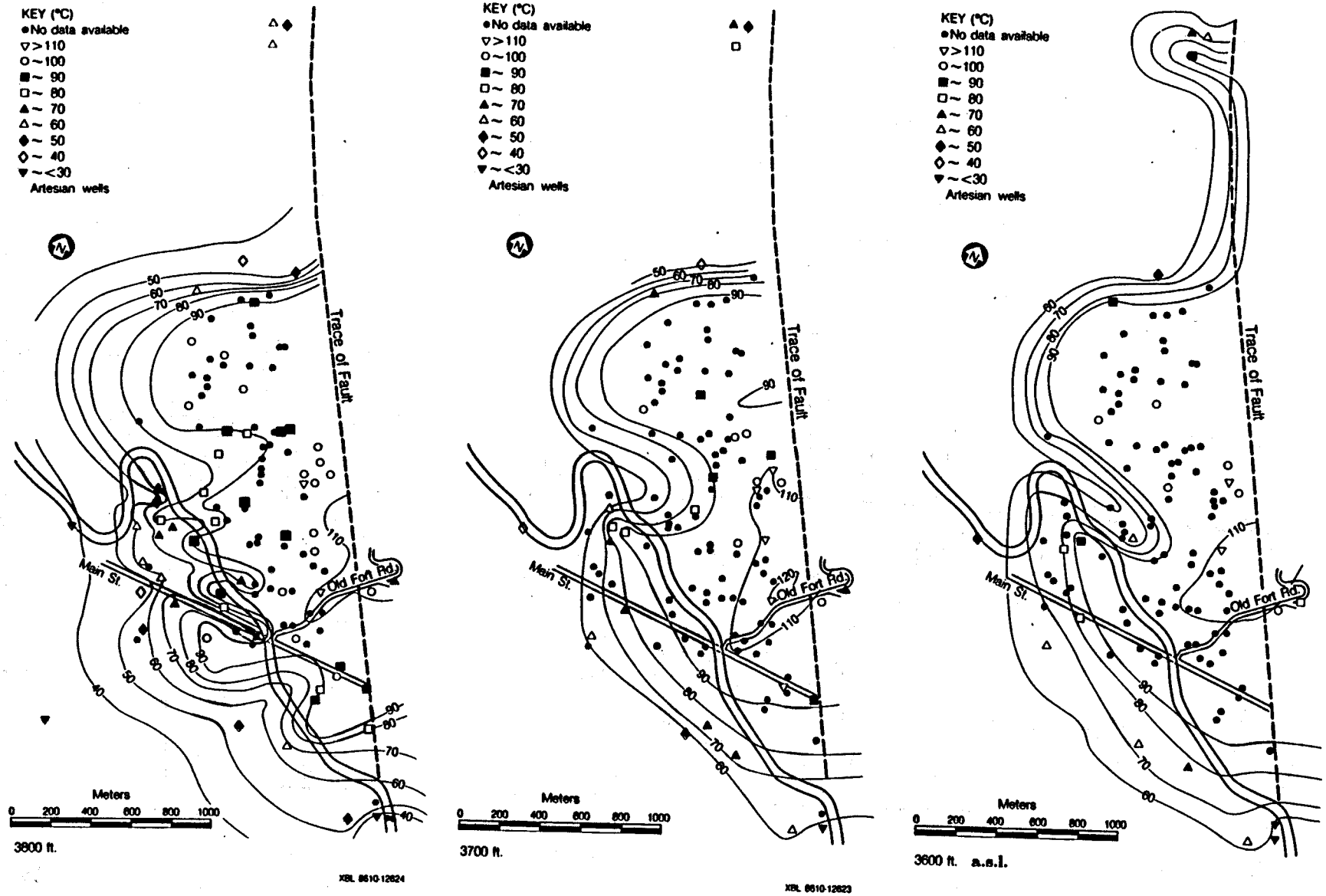

Figure 16a. Temperature contour plots drawn at elevations 3600 ft, 3700 ft and 3800 ft a.s.l.

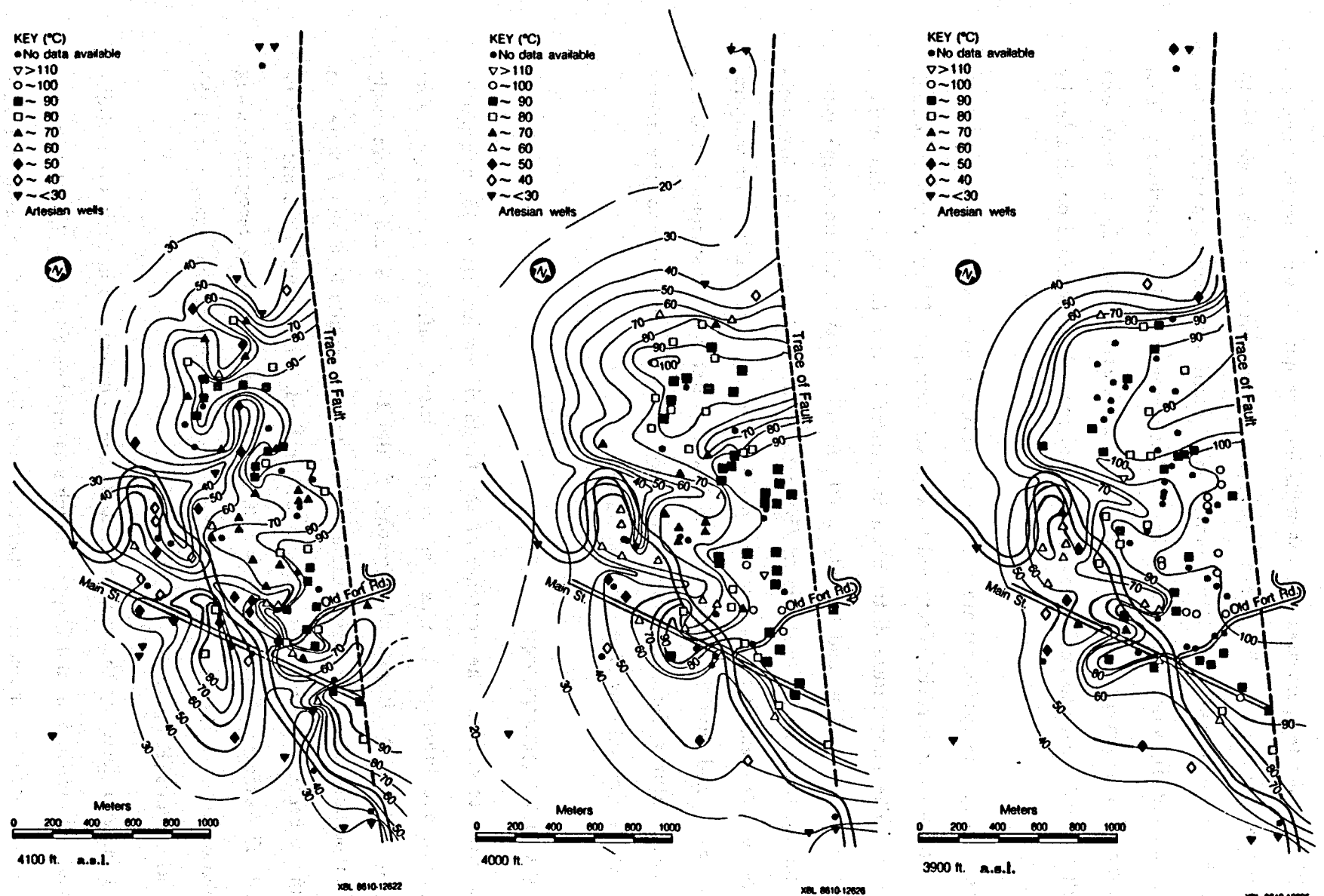

Figure 16b. Temperature contour plots drawn at elevations 3900 ft, 4000 ft and 4100 ft a.s.l.

Although the temperatures in most wells increase quickly with depth, temperatures to the southwest of the artesian springs seem to increase much more slowly. This might be explained by a third normal fault (Fault 1c) trending northwest (see Figures 16a and b), which impedes the flow of hot water toward the southwest. This same characteristic feature is seen in wells located southeast of Fault 2, and northwest of Fault 8, which seems to imply that the thermal anomaly is bounded on all sides by large faults.

Near surface temperatures are much more variable, as seen in Figure 16b. This can be attributed to surficial effects and to a greater amount of data available at shallow depths. The temperature distribution is correlated with faults, artesian springs, regional groundwater flow, and the city canal. At all depths maximum temperatures are associated with the faults shown in Figure 15, while at shallow depths, high temperatures are also related to the artesian springs. On the other hand, cooler temperatures are associated with the canal, which leaks cold water into the surrounding formation. Temperatures decrease towards the southwest in response to the south-southwesterly regional flow of cold groundwater.

2.5.2 FAULT LOCATIONS

In order to confirm the existence of the faults shown in Figure 15, hydrologic, geophysical, and lithologic data as well as high altitude infrared photographs were analyzed. From high altitude photographs, Faults 1a, 2, 3, 4, 8 and 9 were easily identified because of their clearly visible surface traces. Faults 5, 6 and 7 were less pronounced because their traces tend to be localized, while fault 1b could not be detected. The exact locations of Faults 2, 3, and 9 were more easily recognized using areal photographs, as their traces were found to extend well into the region east of the main normal fault (Fault 1a).

The ease of detecting the various faults is due to differences in their size and displacement. Faults 1b, 5, 6, and 7 appear much smaller than Faults 1a, 2, 3, 4, 8, and 9, in view of the size of their relative temperature disturbance. All of the faults in Figure

conform to the regional fault pattern, which trends either northwest or northeast.

Lithologic data were re-examined with the intention of confirming the existence of the newly-proposed faults; however, this proved more difficult than anticipated. Poor lithologic correlations were found between nearby wells, both within the fault blocks and across fault block boundaries. This is partly due to the poor quality of the drillers' logs, and the complexity of the sedimentation and erosion processes. However, the system most likely experienced faulting concurrently with erosion and deposition of sediments, resulting in the highly complex subsurface geologic structure.

Well testing in Klamath Falls is also supportive of the proposed fault locations. The geothermal reservoir appears to have a high degree of transmissivity and connectivity between wells, implying a highly fractured and faulted medium. The results of the many well tests conducted in the area can be interpreted within the framework of a fault and fracture dominated hydrologic regime. The normal faults, cross-faults and contacts between lithologic layers act as high-permeability conduits. Low permeability strata within the fault blocks provide a large storage volume for the thermal fluids. The double-porosity behavior reflected by the well test data support this interpretation (Benson and Lai, 1986).

The data interpretation for one of the well tests suggest the existence of an approximately cylindrical region with a permeability 7.5 times higher than the rest of the reservoir. This high permeability region coincides with the proposed intersections of Faults 1a, 4 and 5.

Local regions with higher permeability are expected at each intersection of two or more faults. Although data to support this hypothesis at Klamath Falls are not yet available, the locations of once-active artesian hot springs generally coincide with the intersection of the strike-slip and normal faults (see Figure 15). This suggests that higher permeability regions are associated with the intersections of two or more faults throughout the KGRA.

The regional geophysical data suggests that the whole Klamath Basin graben has been offset along northeast-trending cross-faults. Although these cross-faults are

indicated only on a regional scale, it was suggested that the shallow hydrothermal circulation is related to the intersection of northeast trending cross-faults and the northwest trending normal faults (Stark et al., 1980).

3.0 CONCEPTUAL MODEL

Figure 17 shows the 2-dimensional conceptual model developed in this study of the Klamath Falls geothermal area. The reservoir consists of a shallow and a deep aquifer. For the sake of simplicity, three permeable layers represent the shallow aquifer zone. The deep aquifer is inferred from geochemical data, although it has not been penetrated by wells. The two aquifers are connected through the main normal fault and possibly by the two subsidiary normal faults. Although upflow occurs along fault planes, it is proposed that the most permeable zones occur at the intersections of the normal and cross-faults as described in the previous section.

The dominant normal fault and two subsidiary normal faults indicate downthrows toward the southwest. This displacement might explain the successively lower temperatures encountered at greater distances from the main normal fault.

Hot water recharge may be derived from two possible sources. It is possible that thermal waters flow into the geothermal system from the upthrown block (mountainous region to the east of the main normal fault). Hot water could also be recharged from the west indicating a possible connection to a deep aquifer within the Klamath Falls graben. At depth, it is unclear whether hot water from the deep aquifer is driven up individual faults, or whether the main normal fault recharges the two subsidiary normal faults at a shallower depth.

At shallow depths thermal waters spread laterally through permeable strata, and mixes with colder regional groundwater. Mixing also occurs along the faults. As the thermal water flows toward the southwest, temperatures are cooled to regional groundwater temperatures.

An age of 2 to 4 million years is estimated for the geothermal system. Silicified palagonitic tuff, found at elevations up to several hundred feet above the present

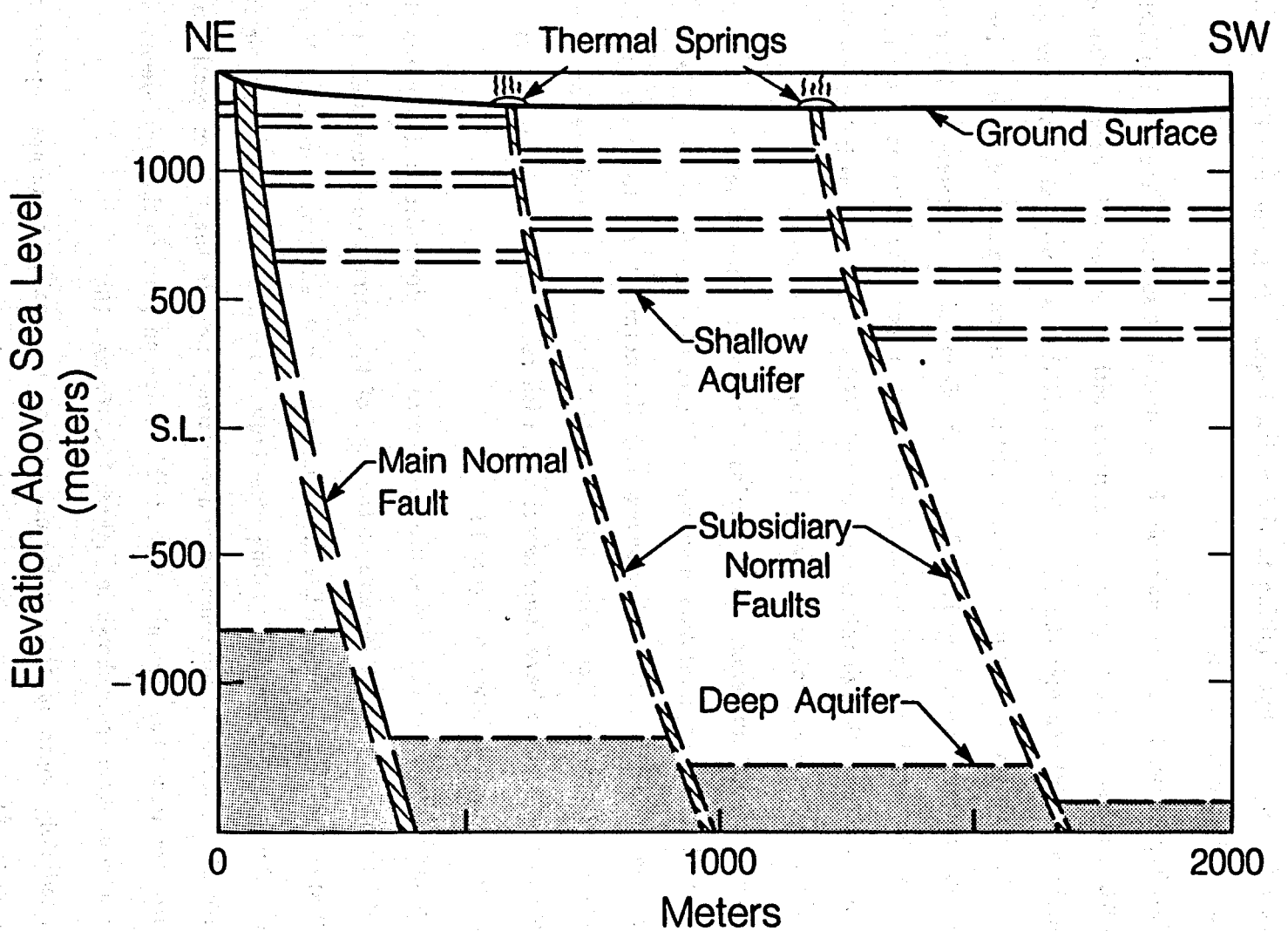

Figure 17. Two-dimensional conceptual model proposed for the Klamath Falls geothermal system.

XBL 873-10023

geothermal system suggests that the system was associated with early fault displacements (Sammel, 1980). The fresh appearance of the normal fault scarps in the area indicates recent fault displacements. Paleontological dates and the age of recent volcanic activity suggest that faulting in the region began during the late Pliocene and continued well into the Holocene.

Two hypotheses have been made on the possible heat source. Peterson and McIntyre (1970) suggest the heat source is associated with a cooling dike or sill. Sammel and Peterson (1976) consider the Klamath Falls KGRA as a normal geothermal gradient system. This would require a fault zone that extends to nearly 6 km in order to reach temperatures approaching 190°C at depth. Sammel and Peterson (1976) point out that no noticeable surficial volcanic manifestations or dike intrusions are found within the KGRA. Although this is true for the KGRA, geologic maps indicate a high degree of relatively recent volcanic activity in the surrounding area.

A 3-dimensional numerical interpretation of the subsurface structure used in the 3-dimensional computer simulation is shown in Figure 18. This figure is similar to the 2-dimensional model in Figure 17 showing only the normal fault displacements, but also includes relative displacements along cross-faults within the study region. Only faults which appeared to have some association with recharge or discharge within the geothermal system are shown in Figure 18.

Displacements along the cross-faults are shown to be down-dropped towards the southeast and the northwest because of the lack of the permeable strata seen in the hot well area and also because of the increased amount of sedimentary rock at depth, relative to the hot well area. Bounding cross-faults on either end of the reservoir are suggestive of significant displacements and effectively impede the flow of geothermal fluids into this area. The reasoning behind this is due, in part, to the rapid decline of temperatures in these areas shown in Figures 14a, 16a and 16b.

Immediately south of the geothermal system, the graben structure appears to widen considerably into a region which contains primarily alluvium. From the geophysical gravity anamolies, the depth of these sediments to some type of basement rock in

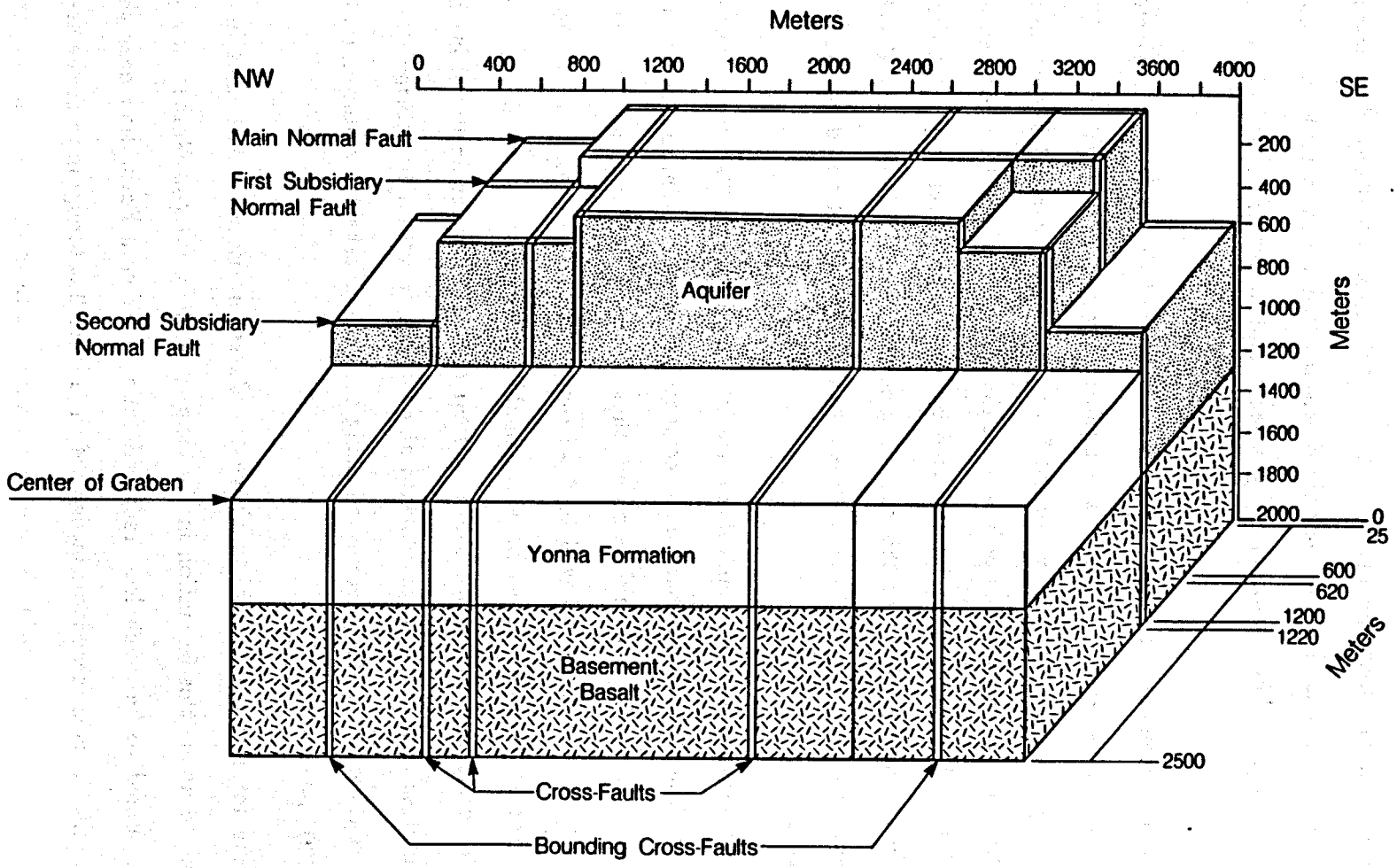

Figure 18. Three-dimensional conceptual model proposed for the Klamath Falls geothermal system. This model is used as a basis for the numerical mesh.

this area is on the order of almost 2000 meters. For this reason the aquifer in the southeast end of the 3-dimensional model in Figure 18 is shown at a considerably lower elevation than its neighboring sections towards the northwest. The Bounding Faults act as the mechanism by which the aquifer section in this area is displaced downwards. The northwestern section is also considerably down-dropped which is reasonable considering the significantly lower geothermal gradients and water levels found in this immediate area.

No major displacements are assumed near the center of the graben as suggested by the relatively flat surface topography and uniform temperature distribution. The displacement along the first subsidiary normal fault shown in Figure 18 is seen to be greater than the two center cross-faults but is considerably less than the second subsidiary normal fault. This assumption is supported by the comparatively rapid temperature declines in the neighborhood of this second subsidiary normal fault. The depths to the basement basalt is assumed to be between 3000 and 6000 feet based on the geophysical evidence.

The normal faults and cross-faults in Figure 18 were drawn at 90- degree angles to the surface bedding. The associated displacements are shown as sharp discontinuities in the bedding surface. It should be noted, that although the faults are not actually completely vertical and are believed to dip from 60-80- degrees from the horizontal, the 90-degree angle appeared to be a reasonable assumption as it aided in the simplification of designing a mesh for the numerical model (described in detail in the quantitative analysis chapter). Displacements along the first subsidiary normal fault are probably on the order of 150 meters and along the second subsidiary normal fault, greater than 400 meters.

The Yonna formation lies directly above the Basement Basalt. Although little can be ascertained about this formation in the vicinity of the Center of Graben in Figure 18, it is assumed to be much less fractured than the Yonna Formation near the main normal fault. This is reasonable in light of the rather flat topography in the area of the graben axis. Because faulting is believed to have begun in the region during the

Late Pliocene and well into the Pleistocene, and because most of the Yonna formation was in place before this faulting took place, the formation is probably fairly consistent in its lateral and vertical distribution. Its original depositional environment would have required a relatively flat region to accommodate the extensive marshy type conditions implied by the types of rock found in the Yonna Formation.

It is believed that interbedded sandstones, gravels, siltstones claystones and thin basalt flows overlie the Yonna Formation near the center of the graben, while the Yonna Formation almost outcrops near the surface in the region adjacent to the normal fault. The interbedded sedimentary rock overlying the Yonna Formation near the center of the graben are most likely derived from the adjacent uplifted blocks.

Additional deep drilling is needed to further characterize the source recharging the Klamath Falls geothermal system. Further work is still needed to identify and describe the actual fault systems in the area and determine the role of the different faults in the development and dynamics of the geothermal reservoir.

4.0 QUANTITATIVE MODELING

Once a conceptual model has been developed that considers all of the important physical processes and current knowledge about the geothermal system, it is possible to begin a quantitative analysis. In order to quantify the heat and mass transfer in the system, an adequate mathematical model must be chosen which can satisfactorily reproduce the temperature and pressure distributions observed in the field. If reservoir performance evaluations and future behavior predictions are desired, more complicated models are necessary.

The purpose of this section is to describe the methods employed in calculating estimates of heat and mass flow rates for the system using lumped-parameter method, and a semi-analytic method. A rough estimate for the stored energy (volumetric approach) is also determined. The later part of this section provides a general background for the distributed parameter approach to modeling and describes the numerical code PT. A small study was performed, comparing results from the code, PT, to a simple semi-analytic solution for flow through a set of permeable beds. The discretization necessary for flow in a set of permeable beds was also considered.

Other methods, such as, decline curve analysis and lumped parameter methods are available to the reservoir engineer to evaluate the reservoir performance and predict future behavior. These methods, however, are useful only if the system has well-monitored pressure and enthalpy declines. They are generally applied when a geothermal system is under exploitation and significant quantities of fluid are being pumped from the system. At Klamath Falls, the idea of large-scale exploitation of the system has not been attempted primarily because many private wells were thought to be at risk of losing their heat supplies. As a consequence of this situation, a lack of detailed, long term pressures and temperatures which are necessary in these types of analysis has resulted.

4.1 Fault-Charged Model

The geothermal system at Klamath Falls has been classified as a fault-charged system. A fault-charged system is described by hot water flowing up a fault zone until it intersects permeable strata where it flows out laterally, losing heat to the confining beds. Several geothermal systems are characterized by vertical fault zones charged with hot water, such as East Mesa and Susanville both of which are in California, the Roosevelt Hot Springs, and Monroe hydrothermal systems both found in Utah, and Wairakei, in New Zealand.

Several authors have studied the temperature distribution in fault-charged geothermal reservoirs, including Goyal and Narasimhan (1982), Goyal and Kassoy (1981). Goyal and Narasimhan (1982) impose a constant pressure boundary condition at the bottom of the reservoir, while Goyal and Kassoy (1980) consider a constant flux boundary condition at the bottom of the fault and apply their solution to the East Mesa field in California. The solution techniques involve boundary layer theory, numerical methods and a combination of perturbation methods. Kassoy and Zebib (1978) use the same basic solution techniques as Goyal and Narasimhan (1982), however, they consider only a fault zone. Pritchett and Garg (1979) studied a fault-charged reservoir by numerically simulating mass and energy transport in the aquifer, while neglecting bedrock heat losses. Kilty et al. (1978) used a finite difference numerical model to study the heat transfer in the fault-charged geothermal system at Monroe, Utah.

Bodvarsson et al. (1982) developed a semi-analytic solution for the temperature distribution in a fault-charged system and applied it to the hydrothermal system at Susanville, California. Figure 19 shows the important parameters and the geometry used in this study. By finding a suitable match between the measured and the calculated temperature distributions, the hot water recharge into the system can be determined. The main advantage in using the semi-analytic solution is that it does not require the use of large computers and produces immediate results. This solution has been used to obtain an initial estimate of hot water recharge into the Klamath Falls system. Therefore, the assumptions, governing equations, and the solution are

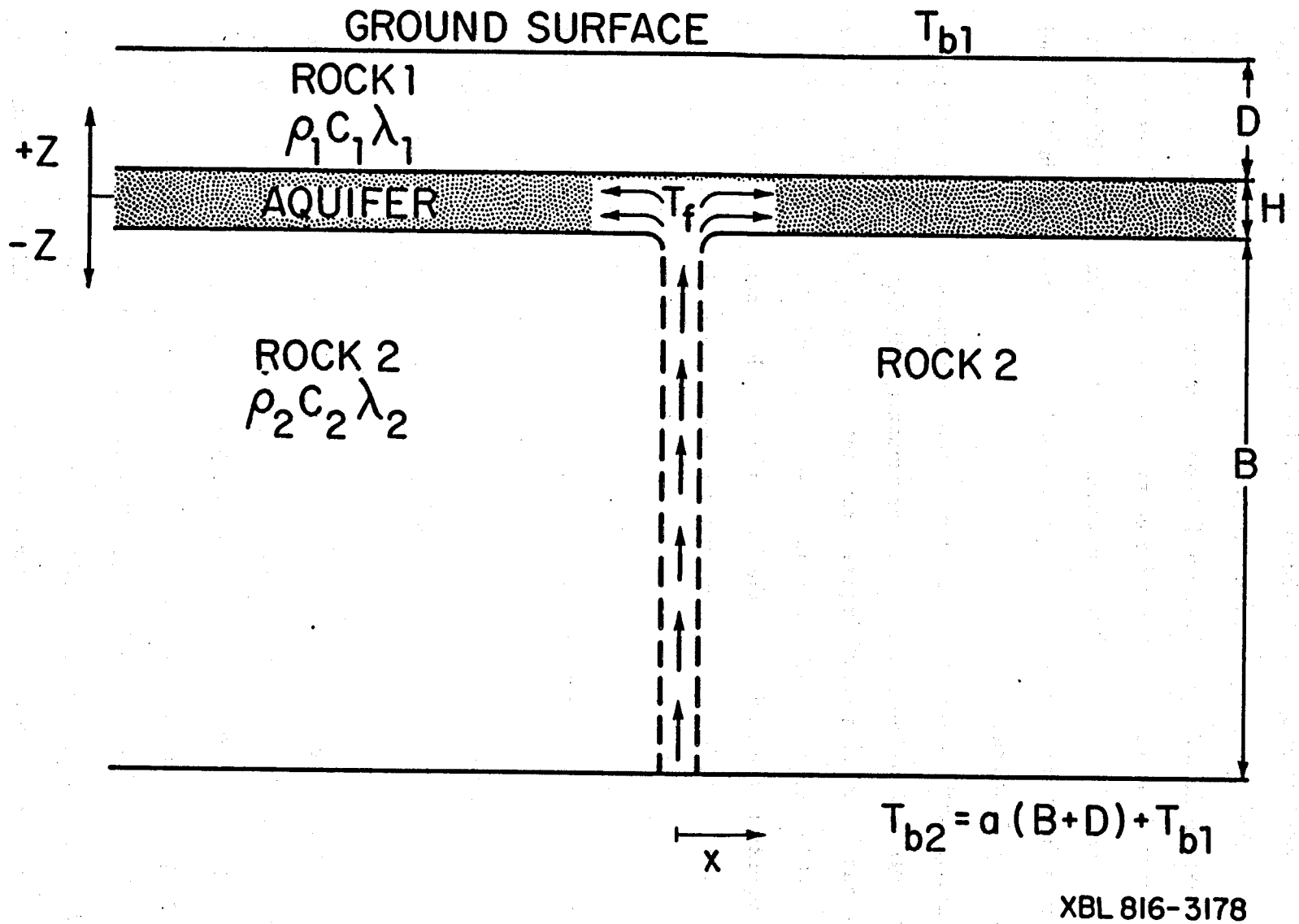

Figure 19. Fault-charged model showing important parameters (taken from Bodvarsson et al., 1982).

described below.

Several assumptions are made in this model (Bodvarsson, 1982), including no heat loss from the fault, and constant thermal parameters for the liquid and rock. Only vertical heat conduction is considered in the rock above and below the aquifer. Within the aquifer the mass flow rate is constant, horizontal conduction is neglected, temperatures are uniform in the vertical direction of the relatively thin aquifer and there is instantaneous thermal equilibrium between solid and fluid. This solution has been used to obtain an initial estimate of hot water recharge into the Klamath Falls geothermal system.

The governing equation for the temperature distribution in the aquifer, (slightly modified from Bodvarsson, 1982) which was derived by performing an energy balance on a control volume within the aquifer is given by

$$\frac{\lambda_1}{b}\frac{\delta T_1}{\delta z}\bigg|_{z=0} - \frac{\lambda_2}{b}\frac{\delta T_2}{\delta z}\bigg|_{z=0} - \frac{\rho_w c_w q}{H}\frac{\delta T_a}{\delta x} - \rho_a c_a \frac{\delta T_a}{\delta t} = 0. \qquad (1)$$

where the subscripts 1, 2 and a, indicate the caprock, bedrock and aquifer, respectively. A simple one-dimensional heat conduction equation governs the temperature distribution in the caprock and bedrock and is given as

$$\text{for } z > 0: \quad \lambda_1 \frac{\delta^2 T_1}{\delta z^2} = \rho_1 c_1 \frac{\delta T_1}{\delta t} \qquad (2)$$

$$\text{for } z < 0: \quad \lambda_2 \frac{\delta^2 T_2}{\delta z^2} = \rho_2 c_2 \frac{\delta T_2}{\delta t} \qquad (3)$$

where λ, ρ and c represent the thermal conductivity, the density, and the heat capacity, respectively.

To simplify the equations and their solution, several dimensionless parameters were introduced. The resulting partial differential equations were solved for the temperature distribution by using a Laplace transform. This semi-analytic solution for the temperature in the aquifer is given as

$$T_s = \frac{1}{s}(1 - T_g)\exp-\left[\theta_1 s + \frac{\sqrt{s}}{\tanh\sqrt{s}} + \kappa\frac{\sqrt{(\frac{\gamma}{\kappa})s}}{\tanh\frac{B}{D}\sqrt{(\frac{\gamma}{\kappa})s}}\right]\xi_1 + \frac{T_g}{s}, \qquad (4)$$

where κ, θ, T_g, ξ, γ, τ and s are the dimensionless parameters for thermal conductivity, dimensionless energy potential, dimensionless thermal gradient, dimensionless distance, heat capacity ratio, dimensionless time and the inverted Laplace variable (time), respectively. These are defined as

$$\kappa = \lambda_1/\lambda_2$$

$$\theta = b/D\cdot\rho_s c_s/\rho_1 c_1$$

$$T_g = a\cdot D/T_f - T_b$$

$$\xi = \lambda_1\cdot x/\rho_w c_w q D$$

$$\gamma = \rho_2 c_2/\rho_1 c_1$$

$$\tau = \lambda_1 t/\rho_1 c_1 D^2$$

The equation for the dimensionless heat loss from the aquifer can be calculated from

$$Q_D = (1 - T_g)\left[1 + \frac{\kappa}{\sigma}\right]\exp - (1 + \frac{\kappa}{\sigma})\xi_1, \qquad (5)$$

and the actual heat loss is determined from,

$$Q = \frac{Q_D A\lambda_1(T_f - T_b)}{D.} \qquad (6)$$

The term T_f and T_b refer to the recharge water temperature and the surface temperature.

The procedure for calculating the hot water recharge rate is to find a best match between the field temperatures and the calculated temperatures. When a good match is found, the recharge rate used in the calculation is chosen as a best estimate for the system. To determine real values for the solution which is given in the Laplace domain, a numerical algorithm is used (Stehfast, 1970).

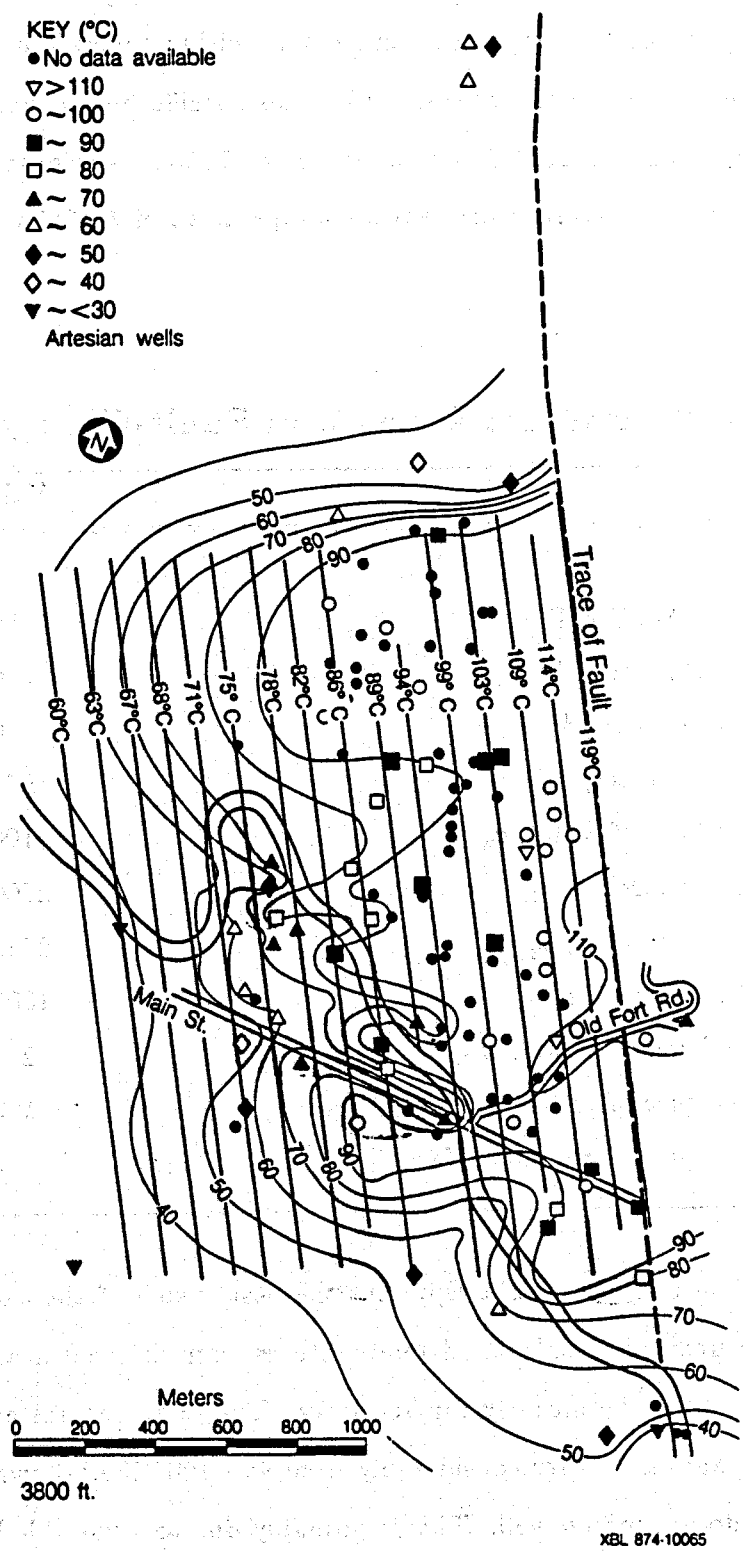

Figure 20a. Calculated and actual field data comparison for the fault-charged model.

The values for the reservoir properties used in the calculation are given in Table 3. An average value for the water temperature within the system was assumed to be 80 °C to determine average water densities and specific heat capacities. A hot water recharge temperature of 120 °C was based on the hottest waters found in the geothermal system. A mean average ambient air temperature of 7.9 °C was used for the surface temperature.

Table 3. Parameters used in Fault-Charged Model

Parameter	Value
Depth to Aquifer, D	50. m
Aquifer thickness, b	600. m
Aquifer porosity, ϕ	0.2
Density of water, ρ_w	970. kg/m^3
Specific heat of water, c_w	4100. J/kg· °C
Density of Rock 1, ρ_1	2500. kg/m^3
Density of Rock 2, ρ_2	2650. kg/m^3
Specific heats, c_1, c_2	1000. J/kg· °C
Thermal conductivities, λ_1, λ_2	2. J/m·s· °C
Temperature of recharge water, T_f	120. °C
Temperature of ground surface, T_b	7.9 °C

The results shown in Figure 20a represent the best match of the calculated and measured temperatures. The calculated temperatures compare well nearest the fault zone and appear to differ significantly further away. The temperatures along the main normal fault also appear to vary considerably from 95 - 120 °C as shown in Figure 20, and consequently do not match well. This is probably due to a variable hot water recharge rate along the length of the normal fault.

The calculated recharge rate per unit meter of the fault is 2.0×10^{-5} m^3/m·s, which is slightly higher than the recharge rate calculated for the Susanville geothermal

system (9.0×10^{-6} $m^3/m \cdot s$) (Bodvarsson, 1982). The calculated heat flows plotted against the distance from the fault are shown in Figure 20b. These show a maximum heat loss of 107.0 HFU near the fault and a minimum value 2500 meters away of 30.0 HFU. No detailed heat flow data has been determined yet for the geothermal area and therefore no direct comparisons can be made. These heat flow values represent maximum heat losses for the system.

The semi-analytic model estimates that steady state is approached within approximately 30,000 years. Because this is a relatively short time period in comparison to geologic time, and because geothermally altered rock has been found at much higher elevations than the present system, a steady state or slow transient state seems to be a reasonable assumption. This geothermally altered rock is located near the OIT campus towards the northern end of the geothermal system.

Although this method of analysis provides a good, quick, initial estimate of the recharge rate, the model has several limitations that limit the applicability of the model to a system as complex as at Klamath Falls. First, the semi-analytic model neglects cold water recharge near the center of the graben which most likely causes the rapid cooling near the second subsidiary normal fault. It also assumes a continuous, symmetrical geometry for the aquifer and only conductive heat transfer within the caprock and bedrock. In reality the system indicates downward displacement along subsidiary normal faults towards the center of the graben. The fault-charged model is not capable of considering the role of cross-faults which probably provide significant hot water recharge to the near surface permeable aquifer. The aquifer itself is not a single, uniformly-permeable feature, but is permeable only in small discrete layers.

Conductive heat loss from the main normal fault to the surrounding bedrock is neglected, however, this appears to play an important role in the steady state temperature distribution and should not be neglected (i.e., the temperature contours near the aquifer are horizontal, while near the fault zone they are vertical). The geothermal system is also assumed to have reached a steady state, while it may in fact be possible for the system to be in a transient state. This might explain why temperatures

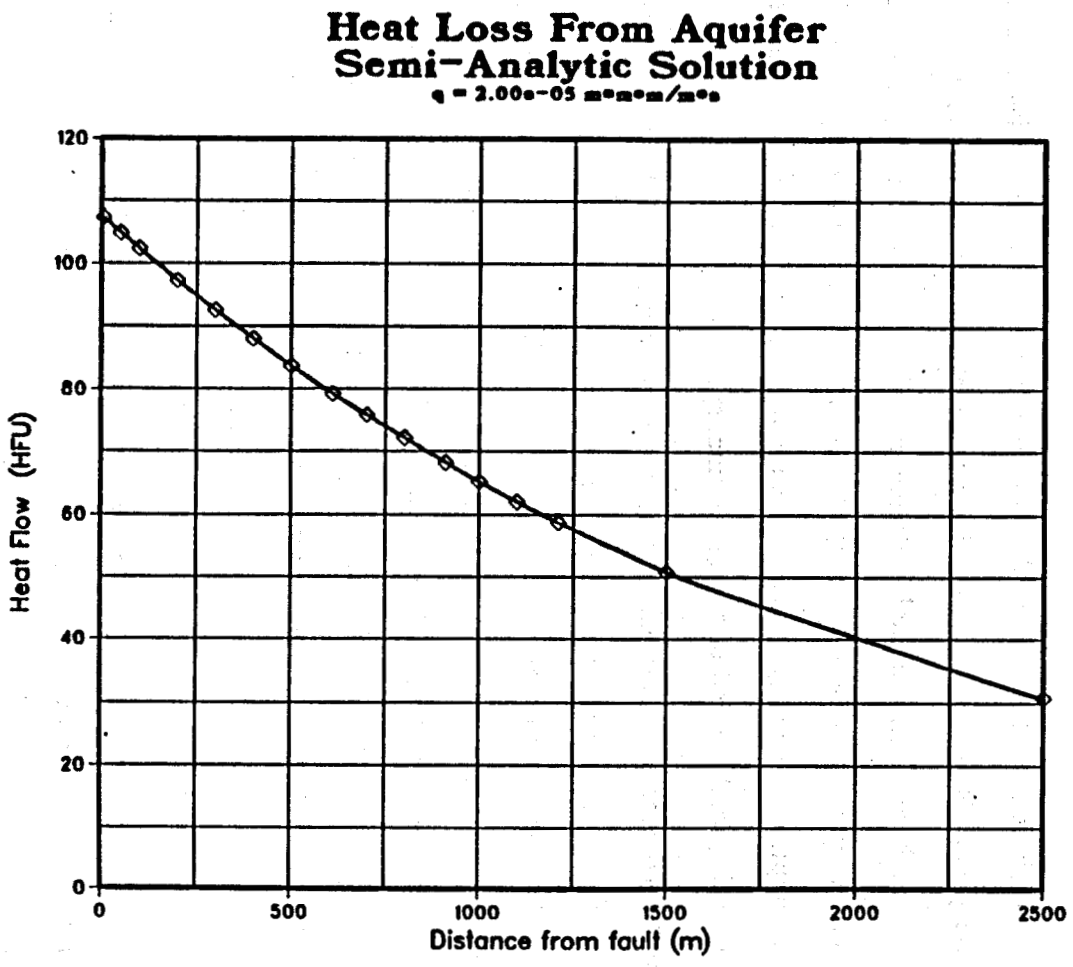

Figure 20b. Calculated heat losses from the aquifer using the fault-charged model.

decrease so rapidly, further from the main normal fault (i.e. the rock at further distances from the main normal fault would not have heated up to its steady state values).

4.2 Lumped Parameter Methods

As an alternate approach to first-cut estimates of the hot water recharge for the Klamath Falls system, a lumped parameter analysis can be performed. In the lumped parameter analysis the entire geothermal system is considered as one large block (shown in Figure 21), which experiences heat and mass transfer into and out of the system through each face. This block is found within the study area shown in Figure 9. Internal conditions need not be considered for this type of analysis, however, the internal properties must be averaged over the entire block before being used in the mass and energy balance equations.

Heat is convectively transferred into the system and is given by q_{in} in Figure 21. Heat is both convected and conducted out of the system as indicated by q_{out} and q_{cond}. One way the hot water recharge rate can be calculated is by assuming that the steady state conductive heat flow out of the caprock is equal to the heat lost from the aquifer. This is done by equating the conductive heat loss q_{cond} out the top of the block, to the convective heat loss by the aquifer. The recharge rate can be determined from

$$q_{cond} = \lambda A \frac{\Delta T}{\Delta x} = c_w \Delta T \dot{m}. \tag{7a}$$

Another method of determining a hot water recharge rate is to use the hydraulic head at the surface to calculate a Darcy velocity. This Darcy velocity can be multiplied by the average water density and the cross-sectional area to estimate the hot water recharge rate. The equation used for this calculation is given by

$$\dot{m} = \rho_w g H \frac{k}{\mu} \frac{\delta h}{\delta x} \tag{7b}$$

A rough estimate of the total energy stored in the system can also be calculated using the following equation given by

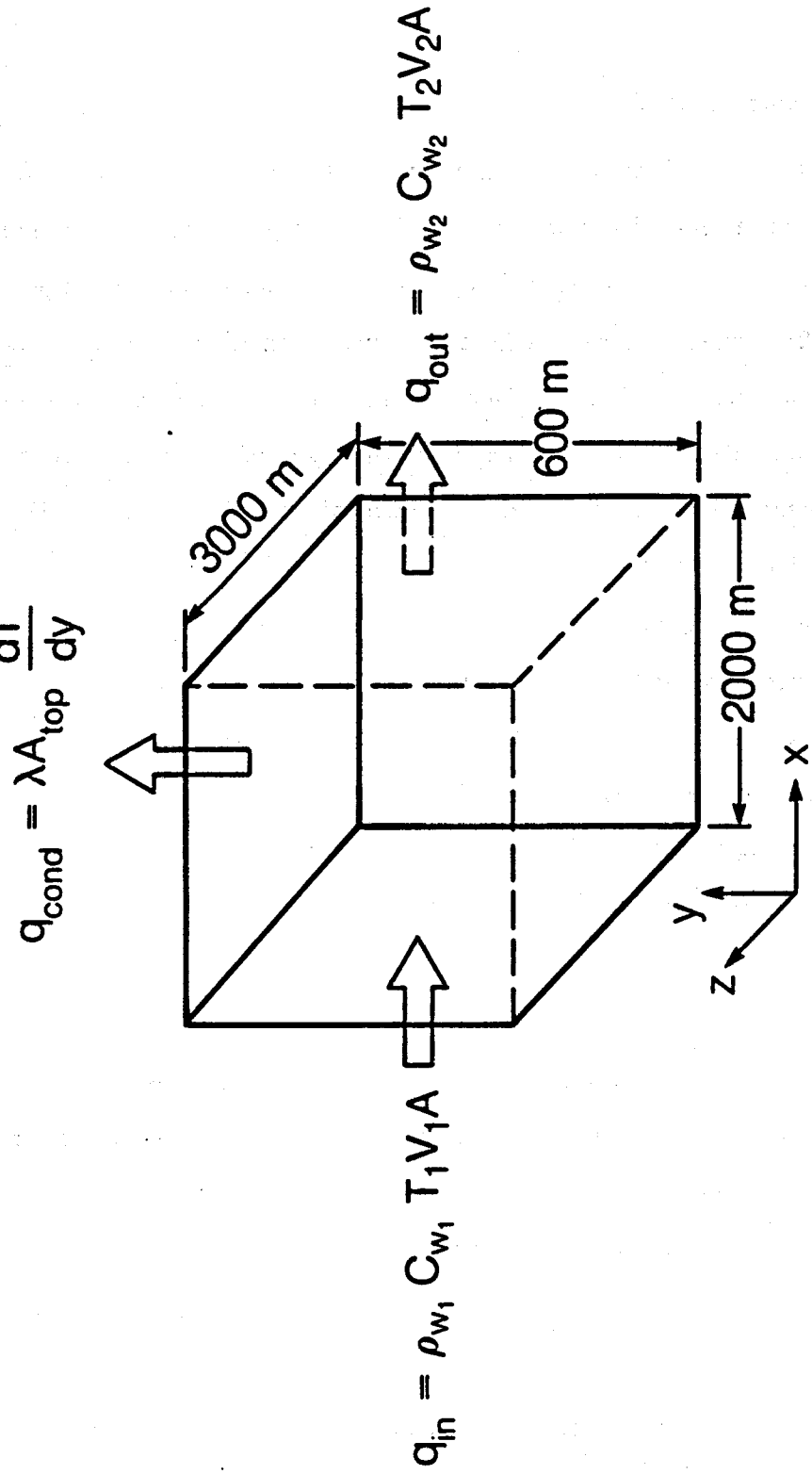

XBL 874-10128

Figure 21. Lumped-parameter volume showing heat flows into and out of the system.

$$U = T_{avg}V[(1-\phi)\rho_r c_r + \phi\rho_w c_w] \quad (8)$$

The parameters used in these calculations are given in Table 4. An average reservoir temperature of 80°C was used to determine the average temperature dependent fluid properties c_w, ρ_w, and μ. The hot water decreases in temperature across the x direction (2000.0 meters), from 120°C to 40°C. All of the other reservoir parameters are assume average values for the system within the block shown in Figure 21.

For a surface area of approximately 6 km^2, a conductive heat loss of approximately 7.2×10^6J/s was calculated. From this value the hot water recharge rate per unit meter along the length of the fault is calculated to be approximately 7.5×10^{-6} $m^3/s\cdot m$. A hot water recharge rate of 6.6 x 10^{-5} $m^3/s\cdot m$ was calculated using equation 7b. The total stored heat within the block was calculated to be on the order of 9.4 x 10^{17} Joules.

These hot water recharge rates compare well to the results of the semi-analytic solution. The lumped parameter methods are very useful in determining initial order of magnitude estimates with only a hand calculator. They also serve as a basis for comparison against the numerical and the semi-analytic solution. The variations in recharge rates are expected because of the average values used in these calculations. The largest uncertainties associated with the first method include a single average temperature gradient assigned over the entire study area, and that it is assumed that the total heat lost from the aquifer is equal to the heat lost through the caprock. The greatest uncertainty in the second method is that it is appropriate to assign a single average permeability over the entire study volume. Both methods neglect the recharge of cold water into the system.

Table 4. Parameters for Lumped-Parameter Analysis

Parameter	Value
Volume, V	4.20×10^9 m^3
Average Temperature, T_{avg}	80 °C
Change in water temperature across block, ΔT	80 °C
Water density, ρ_w	970.0 kg/m^3
Rock density, ρ_r	2500.0 kg/m^3
Specific heat of water, c_w	4100.0 J/kg· °C
Specific heat of rock, c_r	1000.0 J/kg· °C
Average porosity ϕ	0.20
Average temperature gradient, $\frac{\Delta T}{\Delta y}$	60 °C/100 m
Average thermal conductivity, λ	2.0 J/m·s· °C
Total depth, H	700.0 m
Hydraulic head gradient, $\Delta h/\Delta x$	12.0 m/ 1700.0 m
Average water viscosity, μ	3.55×10^{-4} Pa·s
Aquifer permeability, k	5.0×10^{-13} m^2

4.3 Distributed Parameter Method

When a more detailed analysis of the geothermal system is desired, a distributed parameter model which, is capable of handling spatial variations in the system's hydrogeologic properties is required. The region of interest is divided into subregions to adequately describe the variability of the system. Each of these subregions behaves much in the same way as the large block in the lumped parameter model (Figure 21). The lumped parameter model is essentially a coarse discretization (usually one or two blocks) of the same system that neglects spatial variations. Distributed-parameter models are capable of incorporating the entire set of available field data and determining reasonable values for reservoir properties.

For geothermal systems, distributed-parameter models are solved by coupling mass, momentum and energy conservation equations which are tailored to

accommodate the desired dynamic and thermodynamic processes that occur in the system of interest. The solution of these coupled equations involve various numerical techniques because of the complex nonlinearities that arise. A general heat and mass balance equation described by Bodvarsson et al. (1985) is written as

$$\frac{\delta}{\delta t} \int_{V_n} M^{(\kappa)} \delta V = \int_{\Gamma_n} F^{(\kappa)} \cdot \underline{n}\, \delta \Gamma + \int_{V_n} q^{(\kappa)}\, \delta V. \qquad (9)$$

The accumulation term on the left hand side of the equation $M^{(\kappa)}$ represents the amount of component κ present in a unit volume for a given domain V_n. The right hand side of equation (9) gives the change in M in response to flow across the boundary Γ_n given by the flux term F, and to sinks and sources with volumetric rate q for a domain V_n. The flux term F includes conduction and convection heat transfer and the source term q can include injection and production as well as recharge and discharge zones.

A distributed parameter model uses a network of specifically arranged nodal points to describe the system being studied. Nodal points usually occur at the center of each block in the grid and represent the point at which temperatures and pressures are calculated. The spatial grid allows one to model complicated geometries, which are not possible, or require many simplifying assumptions in an analytic approach. The heat and mass balance equations are solved at each individual node and allow for transient and steady state analysis of the system.

Material properties used in the mass and energy equations are assigned to each node and are assumed to be uniform over the entire elemental volume. Simple temperature and pressure gradients are set up between each node. By increasing the number of nodes for a given system, a higher degree of accuracy can be obtained.

Boundary and initial conditions are prescribed for each system. The boundary conditions are extremely important in determining the final temperature and pressure distributions as well as the fluxes through the system. The three possible types of boundary conditions can be imposed on the system, including: insulated, constant temperature and pressure, and constant heat and mass fluxes.

Numerical simulators were originally developed for single-phase liquid water transport, and only within the last 10 years for two-phase liquid-gas systems. Finite difference techniques are most frequently used in modeling geothermal reservoirs. Several models using the integrated finite difference method have been developed which allow for direct discretization of the conservation integrals and more flexibility in defining a grid mesh. Finite element methods have been developed to study both natural state and forced convection.

Distributed parameter modeling is an accepted means of evaluating geothermal systems. A few of the most well-documented and successful models are listed below. Several papers have been presented on numerical simulations of natural convection in geothermal systems (e.g., Cheng, 1978; Donaldson; 1970). Only more recently have numerical codes been developed to address exploitation problems. Some of these authors are Faust and Mercer (1975); Sorey (1975); Garg et al. (1975); Coats (1977).

THE NUMERICAL CODE

The Klamath Falls geothermal system is characterized by low to moderate temperatures and is predominantly liquid dominated. It was decided that the computer code PT developed by Bodvarsson (1982) which uses a single-phase three-dimensional integrated-finite difference method would be sufficient for modeling the system. PT was modified from the code CCC (Lippmann et al., 1977), which has been used for many years in solving geothermal, energy storage and waste isolation problems. The code has been successfully used in a modeling study of the natural state of the Heber geothermal field in California (Lippmann and Bodvarsson, 1983), an exploitation study of the Susanville geothermal system in California (1981), and also in a seasonal aquifer thermal energy storage field experiment near Mobile, Alabama in a joint project by the University of Auburn, Alabama and Lawrence Berkeley Laboratory (Tsang, et al. 1981, 1985, Buscheck, et al. 1983)

The governing equations for the model are mass and energy balances given in integral form. The mass balance is given as

$$\int_V \frac{\delta}{\delta t}(\phi\rho)dV = -\int_A \rho\vec{v}_d \cdot \vec{n}dA + \int_V G_f dV, \qquad (10)$$

where any control volume V and surface area A, containing solids and/or liquid water is applicable. The energy balance is given as

$$\int_V \frac{\delta}{\delta t}(\rho e_f)dV = \int_A \lambda\vec{\nabla}T \cdot \vec{n}dA - \int_A \rho c_f \delta T\vec{v}_d \cdot \vec{n}dA + \int_V G_h dV, \qquad (11)$$

where the term on the left hand side is an accumulation term for internal energy e_f. The first two terms on the right hand side of equation 11 represents the conductive and the convective terms, respectively. The third term is for sources or sink terms. Fluxes are calculated using Darcy's law given as

$$\vec{v}_d = -\frac{k}{\mu}(\vec{\nabla}P - \rho\vec{g}). \qquad (12)$$

The complex equations can be solved in the form of a set of linear equations. Temperatures and pressures at the interfaces between nodes are evaluated using an upstream weighting criterion. The matrix permeability and conductivity however, are determined using a harmonic mean. The code uses an efficient sparse matrix solver to solve the set of nonlinear equations. Array dimensions in the computer the code, PT, were increased to allow for larger numbers of material properties and greater numbers of elements used in the 3-dimensional numerical model of Klamath Falls. The code allows for heterogeneity and anisotropy within a system and has optional gravitational effects.

The fluid properties that are considered in PT, include the density, dynamic viscosity, compressibility, specific heat and thermal expansivity. The fluid density is calculated both, as a function of the temperature and pressure. The fluid viscosity and the thermal expansivity are both calculated as a function of temperature, while the fluid compressibility is calculated as a function of pressure.

4.4 Grid Size Analysis

Before performing any computer simulations it is helpful to consider the consequences of averaging the material properties for the reservoir. Since the Klamath Falls reservoir is very heterogeneous and anisotropic, properties for each element in the mesh for the system must be appropriately averaged.

Therefore, a small study was conducted to investigate the accuracy of the numerical code PT, and to determine the degree of discretization necessary to simulate the mass and heat transfer. This was done by using a semi-analytic model, similar to the fault-charged model, that considers only the heat and mass transfer in a set of permeable layers capped above and below by impermeable rock. This simple case was used because it considers only the most basic thermodynamic and dynamic processes for a system like Klamath Falls.

Derivation of the mass and energy balance equations was done following the approach taken by Lauwerier (1955), who studied the transport of heat in an oil layer caused by the injection of hot fluid. Bodvarsson (1982) developed a similar solution to this problem in radial coordinates to study injection into fractured geothermal wells. The semi-analytic solution used in this study is based upon the same method used by Bodvarsson and Lauwerier but uses cartesian coordinates. Figure 22 shows a permeable bed of thickness b, and a caprock of thickness D, which is part of a large system of layered permeable beds capped above and below by impermeable rock. Hot water flows through the permeable bed from left to right, losing heat to the impermeable rock. Heat is transferred vertically through the impermeable rock by conduction. Because of the symmetry of the model, the datum is defined at $y = 0$. The governing equations are similar to equations 1 and 2 for the fault-charged system except that, due to symmetry, only the caprock is considered for heat loss. The governing equation for the aquifer is given by

$$b\rho_a c_a \frac{\delta T_a}{\delta t} + b\rho_w c_w V_w \frac{\delta T_a}{\delta x} - k_1 \frac{\delta T_1}{\delta y}\bigg|_{y=b} = 0, \qquad (13)$$

and for the caprock:

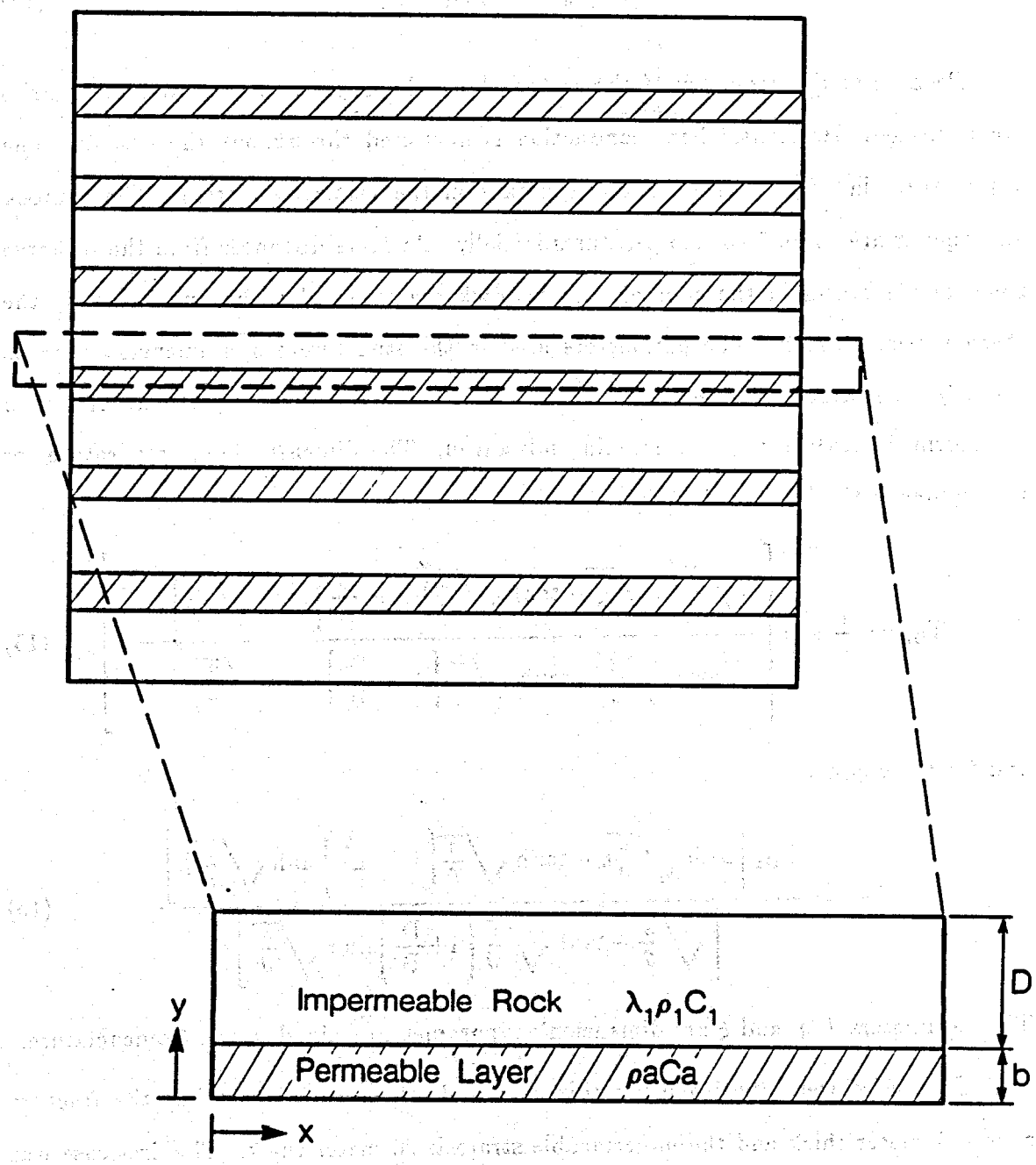

Figure 22. Permeable layer system indicating geometry and important parameters (modified from Bodvarsson, 1982).

$$k_1 \frac{\delta^2 T_1}{\delta y^2} = \rho_1 c_1 \frac{\delta T_1}{\delta t} \tag{14}$$

Because of the geometry of the system, both the upper and the lower boundaries are insulated. Horizontal heat conduction is neglected throughout the system. The temperature in the fracture remains constant in the vertical direction. The caprock and aquifer are at uniform temperatures initially. At large distances from the recharge zone, temperatures in the caprock and bedrock are assumed to be unaffected by the thermal perturbation. The parameters used in the study were nondimensionalized to simplify the differential equation. The resulting differential equations are then transformed into the Laplace domain and solved. The dimensionless temperature for the aquifer in the Laplace domain is given as

$$T_{Da} = \frac{1}{s} \exp \left[\frac{\sqrt{\frac{s}{\theta}} \left(\sqrt{\frac{s}{\theta}} - \tanh \sqrt{\frac{s}{\theta}} \left(1 + \frac{D}{B} \right) \cosh \sqrt{\frac{s}{\theta}} \right)}{\cosh \sqrt{\frac{s}{\theta}} - \tanh \sqrt{\frac{s}{\theta}} \left(1 + \frac{D}{B} \right) \sinh \sqrt{\frac{s}{\theta}}} - s \right] \xi \tag{15}$$

and for the caprock:

$$T_{Dr} = \frac{T_{Da} \left[\cosh \sqrt{\frac{s}{\theta}} \eta - \tanh \sqrt{\frac{s}{\theta}} \left(1 + \frac{D}{B} \right) \sinh \sqrt{\frac{s}{\theta}} \eta \right]}{\left[\sqrt{\frac{s}{\theta}} - \tanh \sqrt{\frac{s}{\theta}} \left(1 + \frac{D}{B} \right) \sinh \sqrt{\frac{s}{\theta}} \right]} \tag{16}$$

The parameters θ, η, and ξ are dimensionless parameters defined in the Nomenclature.

Two cases were studied using this model. Both cases assume that the fracture zone is 1 meter thick and the impermeable strata is 20 meter thick. The first case was done to compare different degrees of mesh refinement for the same system. The three different discretizations include using 4, 11 and 21 vertical nodes and 10 nodes in the horizontal distance (1000.0 meter), all equally spaced. The location at which the temperature is compared for each case is 15 m from the interface between the permeable and the impermeable beds and 250 m from the hot water recharge point. A 30.0 m/day hot water velocity was used. The second case compares the results of the

semi-analytic solution for the permeable layer problem(in Figure 22) to the numerical results for the same problem, at two different velocities, 0.1 and 100.0 m/day. The numerical grid uses 21 vertical nodes and 10 horizontal nodes to describe the system.

Figures 23 and 24 represent the results from this study. Figure 23 indicates the results of the discretization comparison and shows that the difference in the mesh arrangements is very small, implying that the discretization in the vertical sense does not necessarily require large numbers of nodes to accurately describe this type of system. Figure 24 shows the comparison between the semi-analytic permeable layer solution and the numerical solution. The results of this comparison indicate a fairly good match between the two methods at velocities of 0.1 m/day and 100. m/day, suggesting that the numerical solution is reasonably accurate at this scale.

4.5 Average Reservoir Properties

Averaging of reservoir properties is a necessary and important step in detailed modeling of a geothermal reservoir. Since there is a limitation on the money and computer time available, it is important to use as few nodes as possible to describe the physical processes of the reservoir. Initially, a simple, but finely discretized two-dimensional model for the Klamath Falls geothermal system was used to determine the regions where several smaller elements could be appropriately averaged and represented by one larger element, thereby reducing the total number of nodes necessary for the simulation.

The methods for averaging several of these material properties (i.e. permeability, thermal conductivity and the volumetric capacity) for a generalized layered system are shown below. Freeze and Cherry (1979) described the relationship between layered heterogeneity and anisotropy. Figure 25 shows a layered system, where each layer is isotropic and homogeneous, with permeabilities k_1, k_2,....k_n, thermal conductivities λ_1, λ_2,....λ_n, and volumetric capacities $\rho_1 c_1$, $\rho_2 c_2$,....$\rho_n c_n$, thicknesses d_1, d_2,... d_n and total thickness d. When the whole system acts as a homogeneous anisotropic layer (i.e. at steady state), average values for the permeability (k_x,k_y), thermal conductivity (λ_x, λ_y)

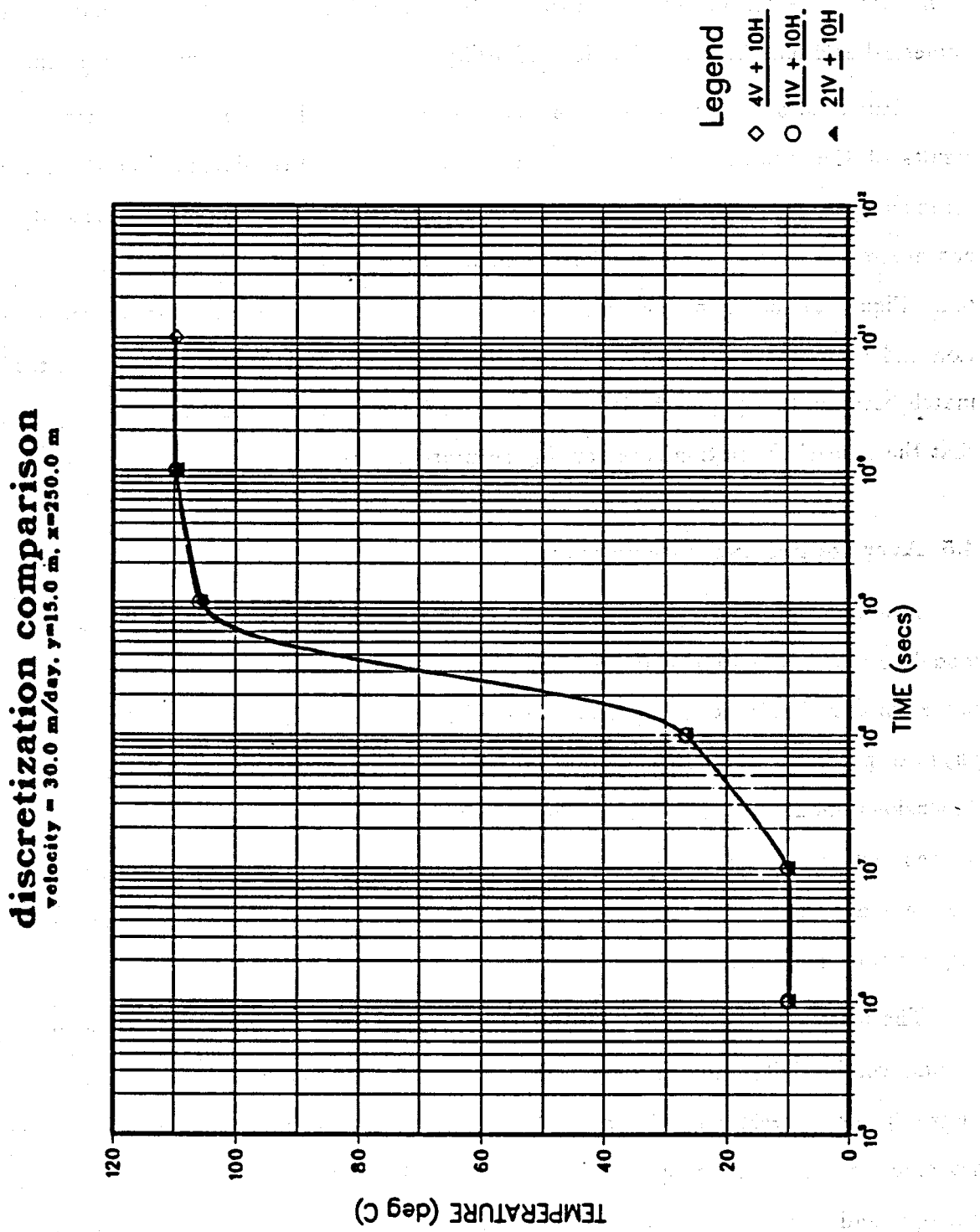

Figure 23. Comparison between different degrees of discretization for the permeable layer study, using 4, 11 and 21 vertical nodes and 10 horizontal nodes.

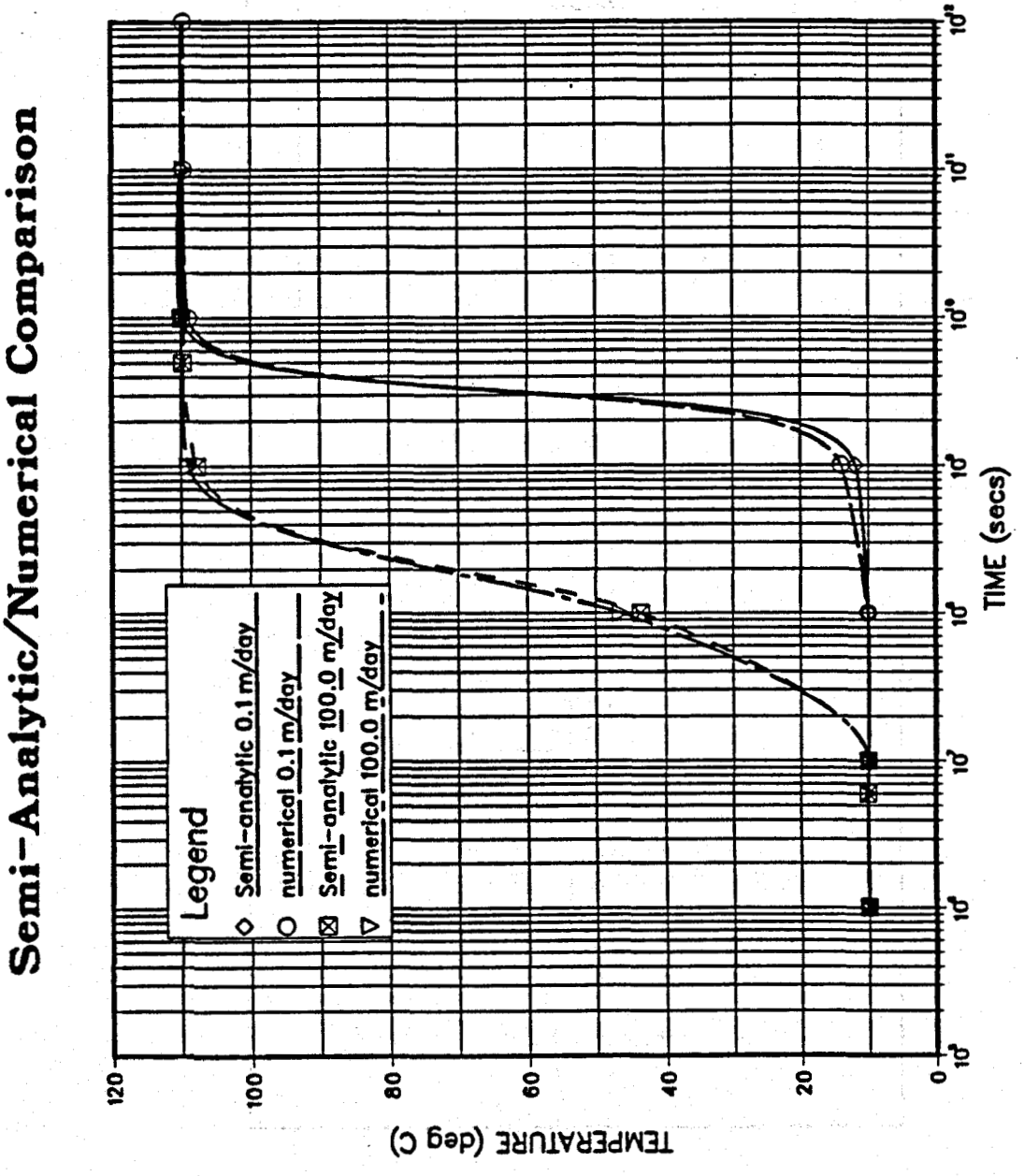

Figure 24. Comparison between semi-analytic and numerical solutions for the permeable layer study, using velocities of 0.1 m/day and 100.0 m/day.

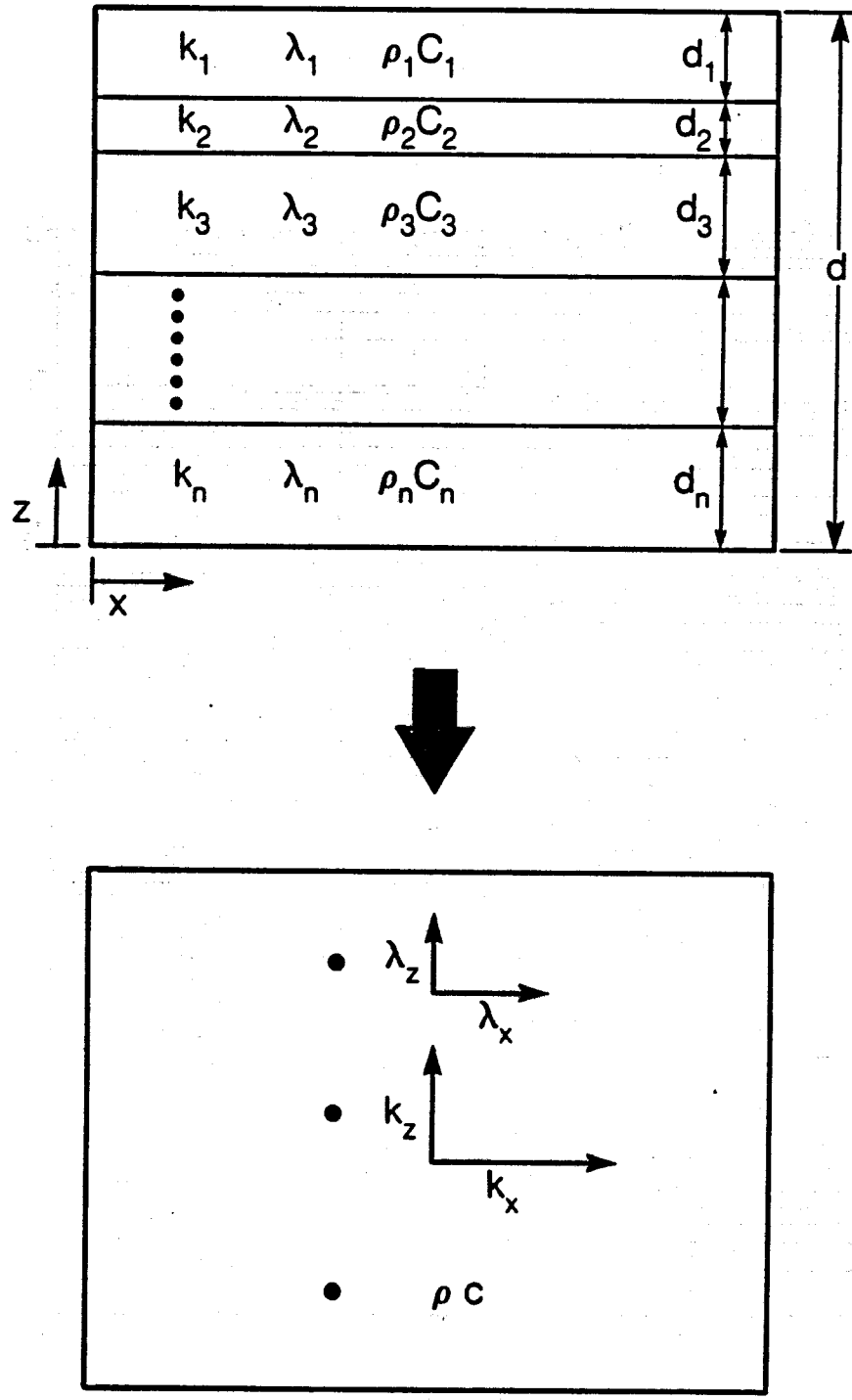

XBL 874-10051

Figure 25. Relation between heterogenous, anisotropic system and homogenous isotropic system.

and volumetric capacity (ρC) can be determined. The appropriately averaged permeability and thermal conductivity in the numerical simulations are derived in an analogous manner.

For flow perpendicular to the surface of the layers and for a constant specific discharge υ throughout the system, the total head loss across the layered system is given by $\Delta h = \Delta h_1 + \Delta h_2 + ... + \Delta h_n$, where Δh_1 represents the head drop across the first layer, and so on. From Darcy's law,

$$\upsilon = \frac{k_1 \Delta h_1}{d_1} = \frac{k_2 \Delta h_2}{d_2} = \cdots = \frac{k_n \Delta h_n}{d_n} = \frac{k_z \Delta h}{d}, \tag{17}$$

where k_z is the average permeability for the layered system. By rearranging terms and solving for k_z, one obtains the following relation:

$$k_z = \frac{d}{\sum_{i=1}^{n} \frac{d_i}{k_i}}. \tag{18}$$

A similar approach yields an equation for flow parallel to the layers:

$$k_x = \sum_{i=1}^{n} \frac{k_i d_i}{d}, \tag{19}$$

where n in the summation term represents the number of layers in the system.

The thermal conductivity can be derived in a similar fashion using Fouriers law of heat conduction. Steady state heat transfer is assumed, where the heat in equals the heat out of the layered system. For the heat flow in a direction perpendicular to the layered system, the average thermal conductivity is given by λ_z. The equation for λ_z is given as

$$\lambda_z = \frac{d}{\sum_{i=1}^{n} \frac{d_i}{\lambda_i}}, \tag{20}$$

and the average thermal conductivity parallel to the layers is given by

$$\lambda_x = \sum_{i=1}^{n} \frac{\lambda_i d_i}{d}. \tag{21}$$

To determine the equivalent volumetric capacity for the layered system, steady state is assumed and both the total internal energy and the temperatures of the layered system and the averaged system are also assumed to be equal. By equating the total internal energies of the layered and the averaged system, and canceling the temperatures the following equation results:

$$\sum_{i=1}^{n} V_i\left(\rho_{r_1}c_{r_1}(1-\phi_i) + \rho_w c_w \phi_i\right) = V_2\left(\rho_{r_2}c_{r_2}(1-\phi_2) + \rho_w c_w \phi_2\right) \qquad (22)$$

The subscript (i) in the summation refers to the individual layers in the layered system, while the subscript (2) represents the averaged system. The porosities, ϕ_i and ϕ_2 indicate the individual layers in the layered and averaged system, respectively.

5.0 THREE-DIMENSIONAL NUMERICAL MODEL

A detailed three-dimensional numerical analysis of the Klamath Falls, Oregon geothermal system is presented in this section. The principal reservoir characteristics from the three-dimensional conceptual model in Figure 18 are transformed into an equivalent numerical representation. This step involves, determining an adequate three-dimensional spatial discretization for the conceptual model, assigning appropriately averaged material properties for each element in the mesh, and imposing initial and boundary conditions for the system. These factors are discussed in detail in this section along with the results from the final three-dimensional numerical simulations.

The study area for the 3-dimensional numerical simulations is shown by the rectangular box drawn over the topography map in Figure 9. This particular area is chosen because it encompasses the entire thermal anomaly, and because it is assumed that the vertical boundaries were far enough away from this anomaly that they would not dominate the heat and mass transfer within the system. The area also considers an area large enough to allow for cross-flow of cold regional water recharge which is an important feature in the 3-dimensional model. The actual scales in each dimension are shown in the 3-dimensional mesh shown in Figure 27.

As a basis for the numerical simulations, several 2-dimensional models were used to understand the more fundamental flow patterns and, temperature and pressure distributions that might develop in such a system as Klamath Falls. The two dimensional models served as useful, quick and inexpensive methods of generating an adequately discretized three-dimensional mesh for describing the system. They were oriented perpendicular to the main normal fault and extend in a southwest direction. These 2-dimensional simulations are useful in familiarizing oneself with the relative sensitivities to imposed boundary conditions and the reservoir parameters. The permeability distribution and boundary conditions appear to govern the temperature and pressure distribution within the system.

Although the two-dimensional models are useful in many respects, there are several limitations with this approach. First, they neglect recharge of cold regional

groundwater that flows perpendicular to the two-dimensional cross-sections, towards the south, in the central graben area (area shown in Figure 18). In order to maintain cooler temperatures near the vicinity of the second subsidiary normal fault, the 2-dimensional models required significant displacements along the first and second subsidiary normal faults to divert the hot waters downwards. This causes the near surface sediments, at distances further from the main normal fault, to remain cooler. However, these displacements would have been on the order of 400-500 meters within short horizontal distances of 600 meters. This is considerably larger than the local topography indicates.

Another limitation of the 2-dimensional models is that they do not adequately resolve the problem of hot water discharge from the system. The effects of cross-faults could not be considered and therefore only generalized vertical mesh arrangements could be used. These are constructed perpendicular to the main normal fault. The two-dimensional models also neglect the lateral flow of hot waters in the normal faults, cross-faults and the aquifer.

The geothermal system at Klamath Falls is governed by 3-dimensional features and therefore only a 3-dimensional model could be used to sufficiently replicate the temperature and pressure distributions within the study area. The 3-dimensional natural state model of the system assumes a steady state, and estimates the permeability distribution, recharge and discharge rates for the system, and the associated heat flows. When a suitable match is found between the actual field data and the numerical results, the proposed conceptual model, although not necessarily a completely unique solution, represents a plausible model for the Klamath Falls system. By a suitable match, it is meant that calculated temperature and pressure distributions from each numerical simulation compare well to the actual temperatures and pressures measured in the geothermal system. The degree of uniqueness for the final numerical solution can be determined by varying the most sensitive parameters. The degree to which these parameters influence the state of the system is indicative of the solution's uniqueness. Several simulations using the final model are discussed at the end of this section.

5.1 Three-Dimensional Mesh

The design of the numerical mesh plays an important role in determining the resulting temperature and pressure distributions, as well as the heat and mass flows within the system. It is essential to construct a 3-dimensional mesh which conforms to the proposed conceptual model shown in Figure 18, and which also uses a sufficient number of elements to adequately account for both the local and large scale dynamic and thermodynamic processes that influence the system. The geological structure of the geothermal system must be incorporated into the mesh showing relative offsets of major faults, and reasonable extents and thicknesses of beds and fault zones.

Although there are no definite limits on the maximum number of elements that can be used in the computer code PT, the simulation time, storage facilities and financial constraints are all factors which must be considered when designing a mesh with large numbers of elements. Because the computer uses a sparse matrix solver to solve the series of heat and mass balance equations, doubling the number of elements in the mesh increases the number of calculations by n^2 or 4 times the original number of nodes. Efficient numerical modeling of complex geothermal systems such as Klamath Falls, requires the use of a fairly large number of nodes to satisfactorily simulate the reservoir and its thermodynamic processes (i.e. 1000 plus elements).

The final three-dimensional mesh used in this study was based on an understanding of the system developed by studying the results of two-dimensional simulations (Fig. 26). These are used to obtain a reasonable compromise between geological structure, average properties for individual elements, and the total number of nodes. The 2-dimensional mesh is viewed from the northwest looking towards the southeast, along the trace of the main normal fault in the geothermal system. The vertically oriented main normal fault and the two subsidiary normal faults are seen as a series of thin elements. The main normal fault is represented by elements 1,9,17,25 and 33, and the two subsidiary normal faults are represented by elements 3,11,19,27,35 and 5,13,21,29,37. Permeable strata usually occurs in elements 20,26,28,34, and 36. In areas where significant quantities of heat and mass transfer occur, and where

temperatures and pressures change rapidly, such as near faults, or permeable beds, a finer discretization was necessary to generate a more accurate temperature and pressure distribution within the system.

Because of the inefficiency (time and money) of using large numbers of elements (+1000) in the computer simulations, only a given number of elements are permitted in each of the three dimensions. The 2-dimensional mesh shown in Figure 26, is somewhat coarse near zones of large heat and mass flows, however this allows for a better discretization in the 3rd dimension, along the main normal fault. This discretization along the main normal fault allows for the influence of the cross-faults and accounts for the notable variation of temperatures in this direction (Figures 16a and 16b). It is conventional in numerical modeling, to compare a coarse discretization to a much finer mesh, to determine how accurately the coarse mesh will represent the system being investigated. The 2-dimensional mesh in Figure 26 exhibited negligible differences when compared to a finer representation of the same system. This suggests that the 2-dimensional mesh in Figure 26 is sufficiently discretized to accurately describe the temperature and pressure distributions.

The 3-dimensional mesh illustrated in Figure 27, shows the entire volume of the reservoir used in the simulation. A total volume of 2.0×10^{10} m^3 is used as indicated by the three scales drawn. A depth of 2000 meters, a length of 4000 meters along the normal fault, and a 2500 meter distance perpendicular to the main normal fault were assumed. The particular 2-dimensional mesh in Figure 26 was duplicated along the length of the main normal fault to generate the 3-dimensional mesh, for two reasons. The first reason was to maintain simplicity in the 3-dimensional mesh and the second was that this particular mesh allowed a sufficient amount of flexibility in describing the various geological structures within the 3-dimensional system.

The advantage of maintaining simplicity in every aspect of a 3-dimensional numerical simulation becomes evident as one begins to, interpret the results, plot temperature and pressure distributions, and consider the complexities associated with equilibrating the system and assigning various properties and boundary conditions.

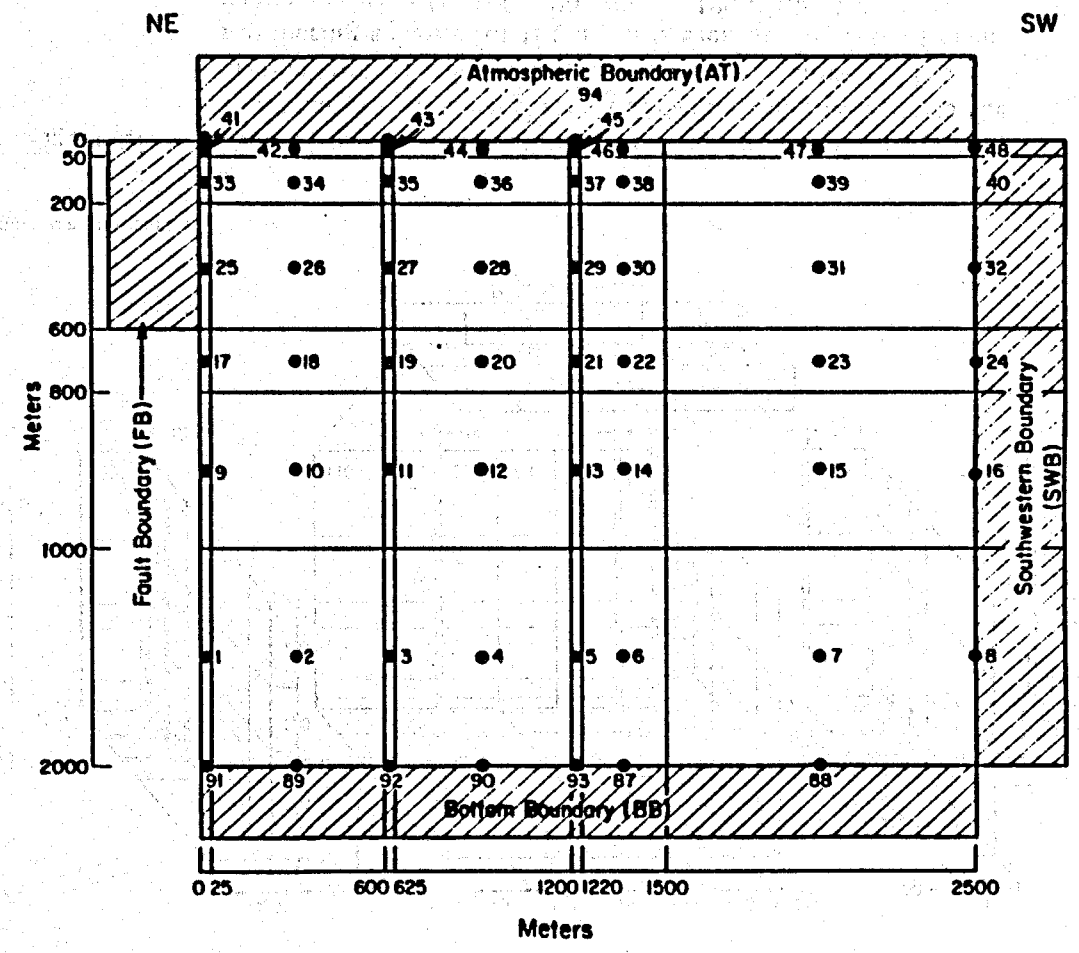

XBL 874-10058

Figure 26. Two-dimensional mesh used as a basis for the three-dimensional mesh. This vertical section is viewed from the northwest towards the southeast. Mesh is oriented perpendicular to the main normal fault, represented by elements 1, 9, 17, 25 and 31.

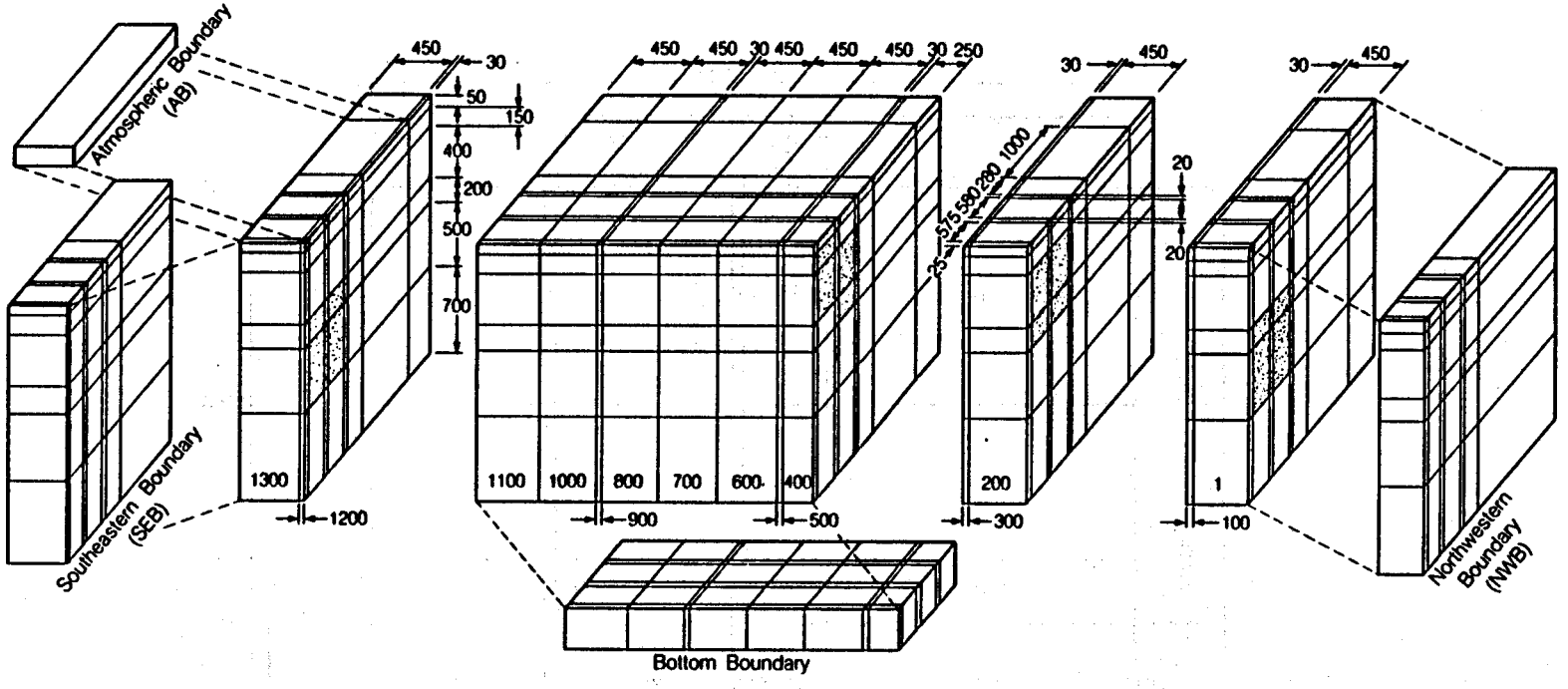

All dimensions in meters

XBL 874 10043

Figure 27. Final three-dimensional mesh used in numerical analysis of the Klamath Falls geothermal system. The mesh views the system from the northeast towards the southwest. The numbering scheme for the mesh is seen at the base of each vertical section (1, 100, 200, 300,.....1200, 1300).

Although the computer code PT can accommodate any type of mesh arrangement desired, it is found that a simple rectangular coordinate grid is sufficient for the study and offered results that were easily interpreted.

Figure 27 represents the 3-dimensional discretization of the subsurface geothermal system with relative displacements as indicated. Fourteen vertical sections were drawn and are labeled as shown in Figure 27 from section 1 to 1300. For each vertical section perpendicular to the main normal fault, the numbering scheme is exactly the same as described in Figure 26, except that the section number (100,200,...1300) is added to each node number. This 3-dimensional mesh was developed from Figure 18 described in the conceptual model section. The faults are all assumed to be vertical and vary from 20 - 30 meters in thickness. This is reasonable, considering the steepness of the normal faults in the area (60° - 80°).

Along the length of the main normal fault, 5 cross-faults are shown by sections 100,300,500,900, and 1200, which correspond to faults 9, 8, 7, 4 and 2 respectively (Figure 15). These cross-faults were selected based on their inferred relative magnitudes and their possible association with recharge and/or discharge in the system. The cross-faults are all assigned the same thickness of 30 meters. The 20 - 30 meter thicknesses (actually considered to be fault zones) were determined by the relative widths of the thermal contours which outline the faults with depth in the cross-sectional temperature profiles (Figures 14a, 14b and 14c). In Figure 27, the cross-faults are seen transecting the main normal fault at 90°. These cross-faults actually form acute angles with the main normal fault ranging from 15-20° as shown in Figure 15. This is a particular limitation with the rectangular mesh used, however it was believed that this would not effect the recharge rates. Bedding is assumed to be a horizontally oriented, planar feature.

5.2 Material Properties

Both fluid and rock properties must be assigned for each element before each new simulation. The rock material properties that are used in the simulation include: permeability, porosity, density, thermal expansivity, compressibility, specific heat, and thermal conductivity. Specific heats, thermal conductivities and permeabilities are dependant on temperature. Their changes with temperature can be prescribed in the numerical code. Furthermore, since the thermal conductivities and the permeabilities usually show significant variations between the vertical and horizontal axes in nature, the degree of anisotropy can also be prescribed for each element. The fluid properties that may be assigned include the density, viscosity, compressibility, specific heat and the expansivity. The specific heat was chosen to be constant at 4200 J/kg °C. The fluid density is calculated both as a function of the temperature and pressure. The fluid viscosity and the expansivity are both calculated as a function of temperature, while the fluid compressibility is calculated as a function of pressure.

Due to the complexity of this system, and the general assumptions associated with the subsurface geology and the 3-dimensional mesh, only the permeabilities and the boundary conditions are varied. The two-dimensional simulations show that the thermal conductivity, porosity, specific heat and so on, have second order effects on the system. Of the reservoir properties, the permeability is the most important because it controls the rate of flow of the geothermal fluids into and out of the system. The degree of anisotropy and temperature dependence in the permeability is not well defined at Klamath Falls and is therefore, considered isotropic and constant with temperature. The thermal conductivity and the heat capacity of the rock are also kept isotropic and invariant with temperature. Densities are better documented for several rock formations such as the basalt, the impermeable layer (clays, mudstones) and the sedimentary rock. These particular rock formations are assigned densities according to Table 5.

Table 5. Rock Densities

Rock Formation	Density ρ kg/m^3
Basement Basalt	2650.00
Impermeable surface layer	1700.00
Sedimentary Rock	1850.00
Yonna Formation	2000.00

The Sedimentary Rock refers to the rock found in the center of the graben, overlying the Yonna Formation. The Caprock represents the top 50 meters of the 3-dimensional model. Since the densities of the faults were not known, the aquifers and the remaining formations were assigned an average density.

Since no wells greater than approximately 2000 feet deep have been drilled in the immediate hot well area of Klamath Falls, only general inferences can be made of the subsurface geology. Figure 28 displays the rock formations consistent with the 3-dimensional conceptual model shown in Figure 18. This figure acts as a general guide for assigning material properties to each node shown in Figure 27. Table 6 lists the average material properties assigned, based on inferences made about the type of subsurface geology in the geothermal system (see Figure 28).

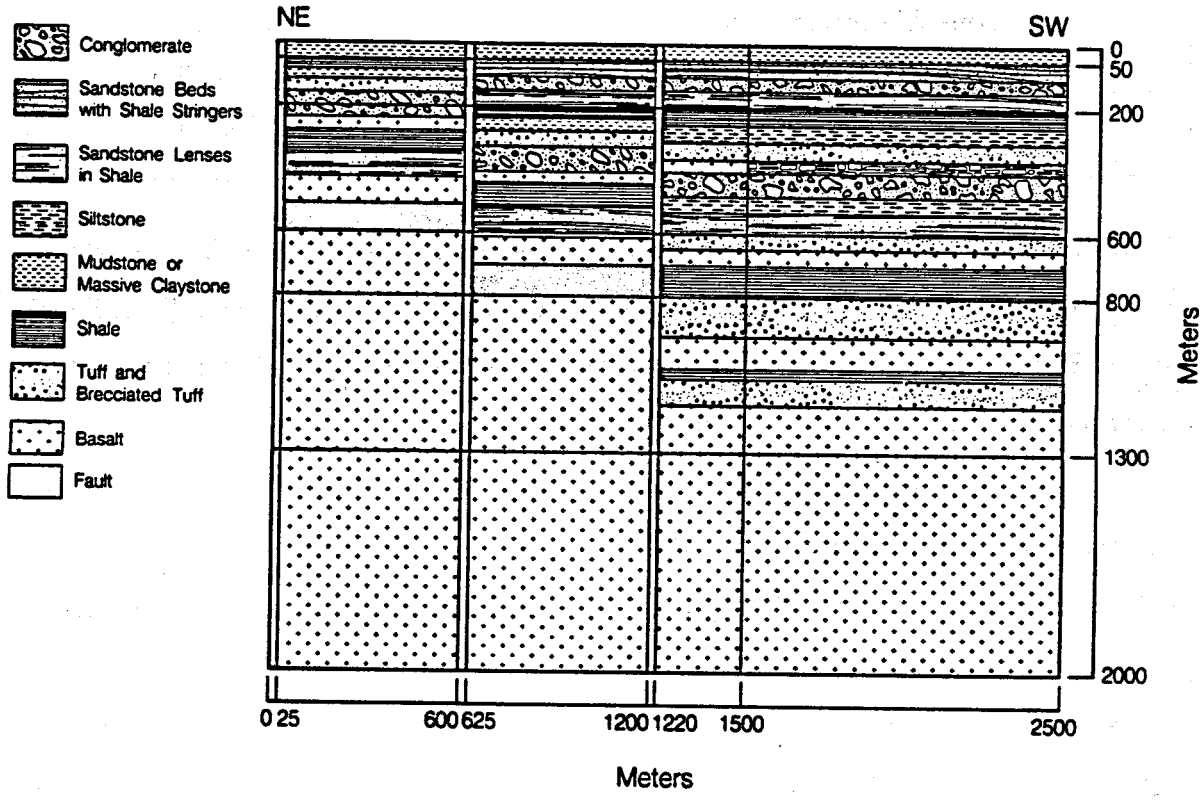

Figure 28. Inferred subsurface geology for the three-dimensional model.

Table 6. Constant Rock Properties

Rock Property	Value
Porosity	0.19
Heat Capacity	1000.00 J/kg C
Thermal Conductivity	2.00 J/s·m C
Compressibility	1.00×10^{-9} Pa^{-1}
Expansivity	1.00×10^{-19} C^{-1}
Permeability	see Figures 29a,b,c,d,e

The highest permeabilities were assigned the main normal fault and the two subsidiary normal fault elements. The second subsidiary normal fault is assigned a high permeability to allow more cold recharge to mix with the hot waters. This is done as a means of controlling the temperatures at the second subsidiary normal fault where temperatures appear to decline rapidly, suggesting some type of cooling or downflow. The fault permeability is crucial in determining the quantity of hot water recharge to the system. These permeabilities are not well known, but are believed to be at least as high as the permeable aquifer they intersect (Sammel, 1984). The northern and southern ends of the normal faults (sections 1, 100, 1200 and 1300) were assigned relatively low permeabilities because no hot water recharge is seen in these areas.

The permeabilities for the aquifer, near the Museum well in Figure 11, are well constrained An average aquifer permeability for this area of 6.000×10^{-13} m^2, is based on the transmissivities determined from well tests done in the area. An almost circular region near the intersection of the main normal fault and the cross-fault represented by the vertical section 900 (in Figure 27), has permeabilities almost 7.5 times that of the values near the Museum Well (Benson, 1983). The intersections defined by cross sections 500 and 900 are assumed to add significant hot water recharge to the system. This can be shown by the temperature contour plots in Figures 16a and 16b, where the highest temperature contours appear to be located near these two fault intersections. These two intersections are represented by elements, 501, 509, 517, 525, 533 and 901, 909, 917, 925, and 933 in Figure 27. Relatively high permeabilities are therefore

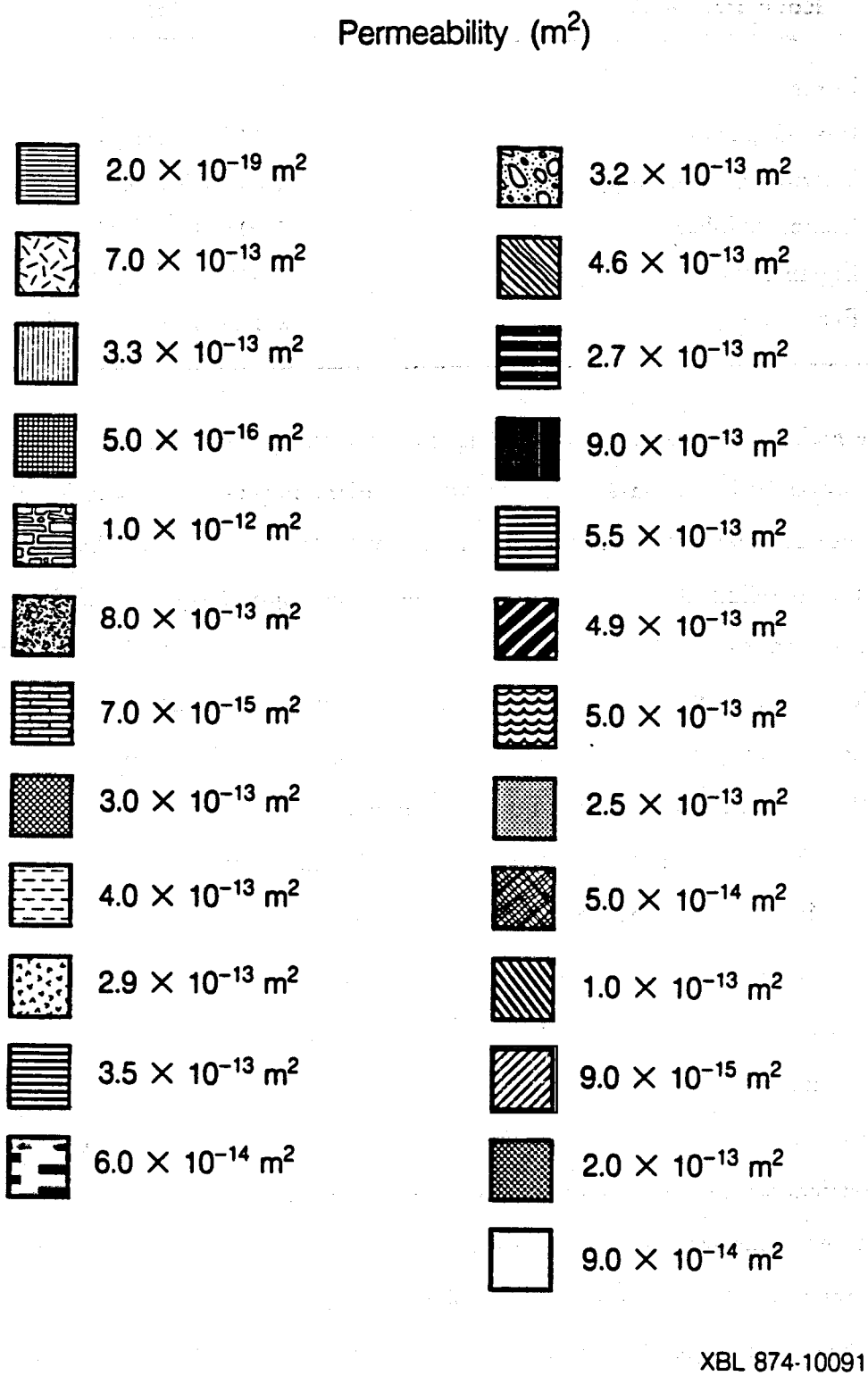

Figure 29a. **Final permeability distribution key to Figures 29b-e.**

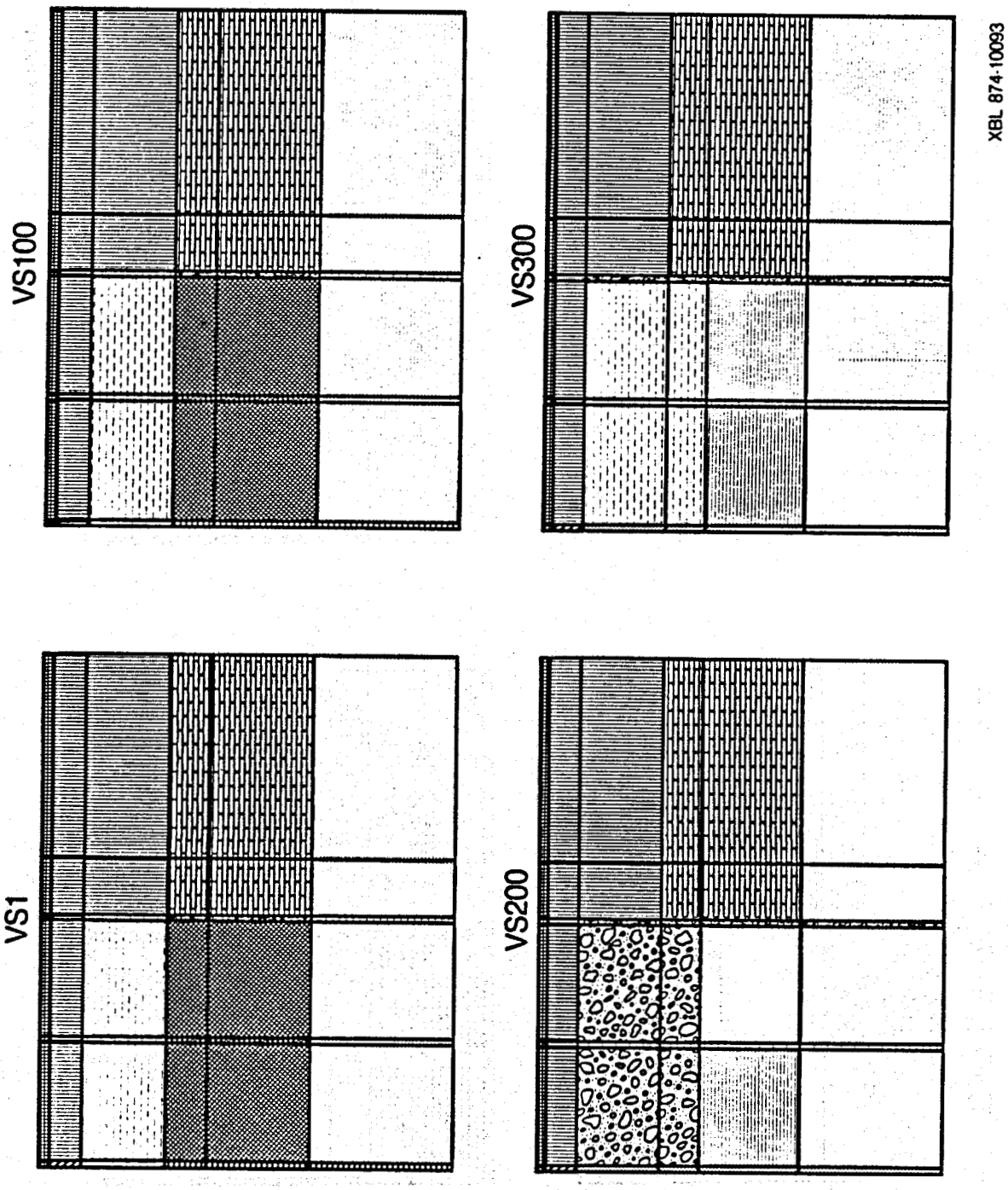

Figure 29b. Final permeability distribution for vertical cross-sections perpendicular to the main normal fault, 1, 100, 200 and 300.

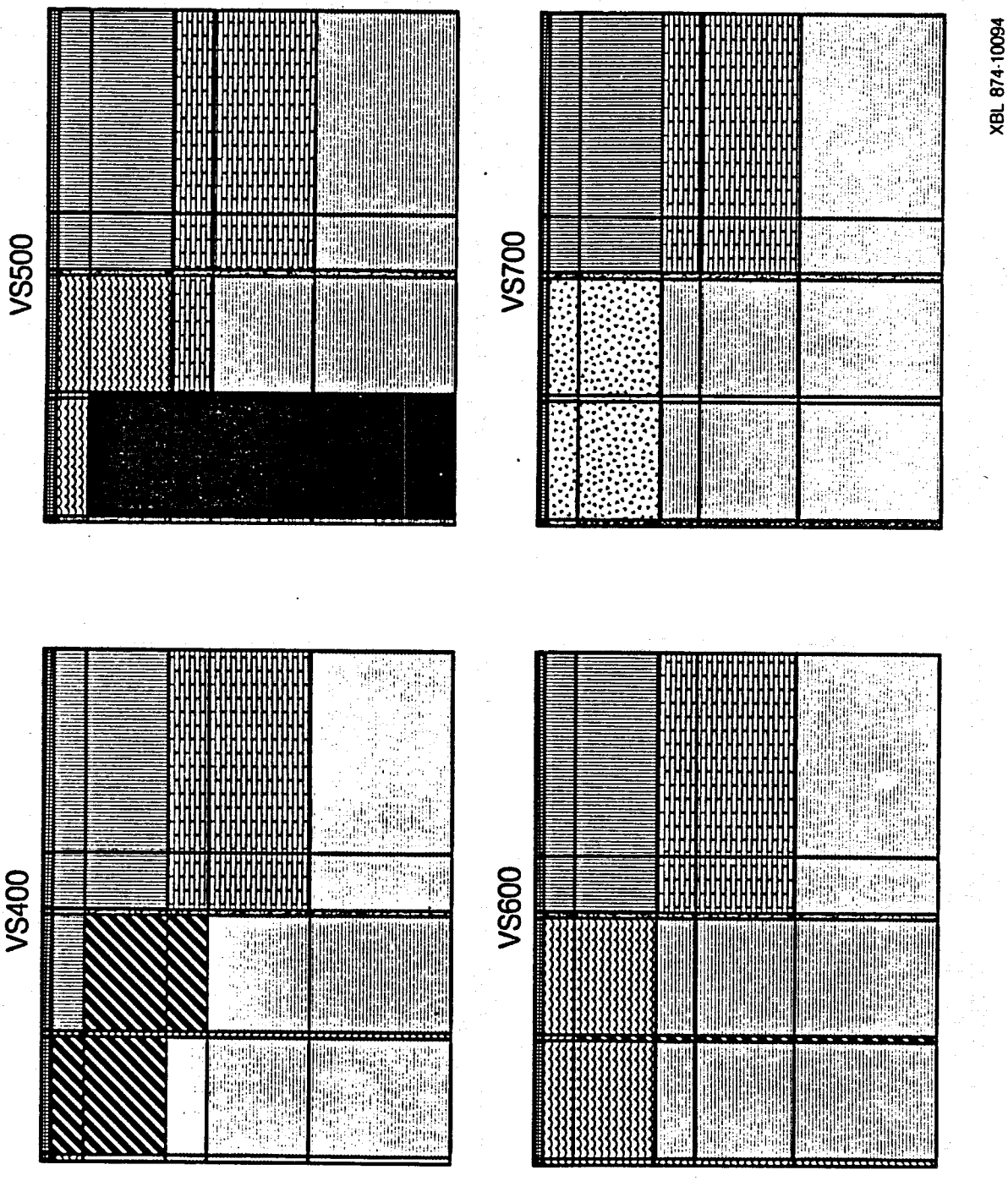

Figure 29c. Final permeability distribution for vertical cross-sections perpendicular to the main normal fault, 400, 500, 600 and 700.

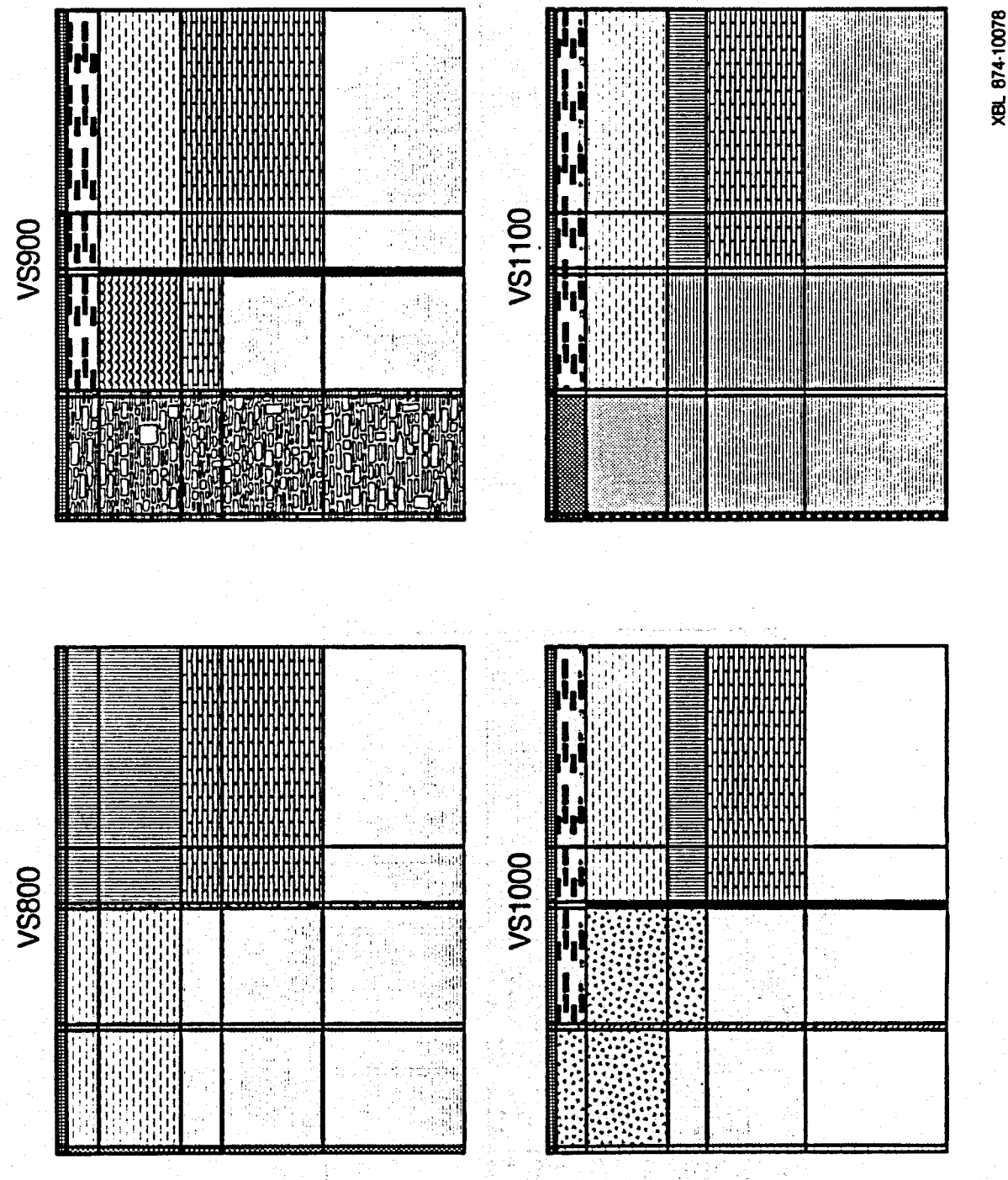

Figure 29d. Final permeability distribution for vertical cross-sections perpendicular to the main normal fault, 800, 900, 1000 and 1100.

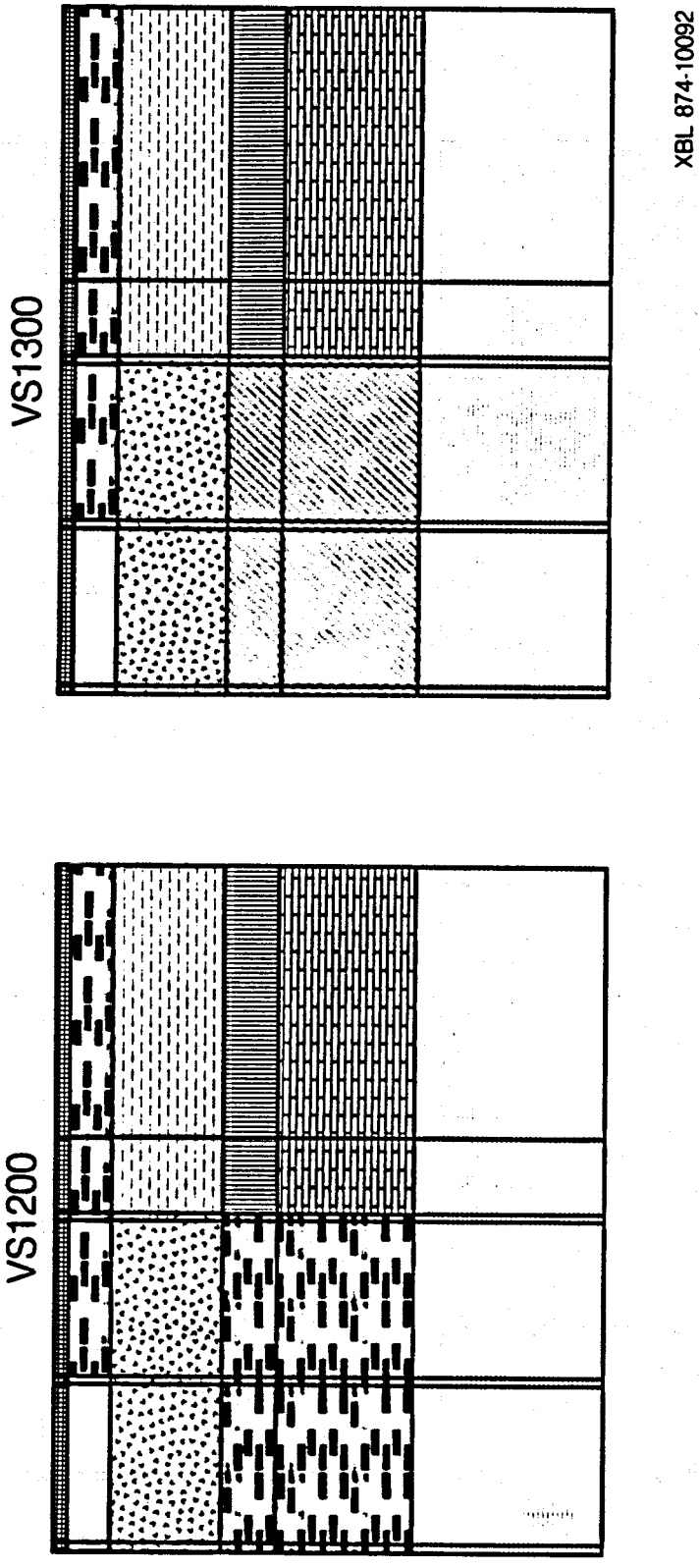

Figure 29e. Final permeability distribution for vertical cross-sections perpendicular to the main normal fault, 1200, 1300.

assigned to these cross-faults.

Permeabilities for the aquifer and the fault are relatively high for most geothermal systems and is attributed to the highly fractured nature. In general, vertical sections further from cross-sections 500 and 900 (north and south) were assigned progressively lower permeabilities because of the notable decline of temperatures in these directions. The temperature profiles near the ends of the cross sections shown in Figure 14a appear to be dominated by more conductive heat transfer or cold water recharge. Based on inferences made about the subsurface geology near the central graben, the upper sedimentary strata are assigned moderately high permeabilities. The depths to these strata are estimated to be from 200 to 800 meters.

The area near Klamath Falls is believed to have experienced significant localized faulting and fracturing which resulted in large topographic variations over short distances. High rates of erosion are also believed to have accompanied this highly variable topography. Initially the eroded rock fragments are expected to have short travel times and consequently are described by larger, coarser material. These coarser rocks are therefore expected to be more permeable than finer sediments that cap them.

Very low permeabilities were assigned to the basement basalt and for the very top 50 meter thick section (referred to as the caprock). The basalts near the main normal fault zone might have actually been assigned a higher permeability due to the apparently high degree of fracturing. As the uplifted fault blocks become more rounded by erosional processes, increasingly finer sediment is deposited. A considerable amount of clays, muds and silts are therefore envisioned in the upper sediments. These sediments have very low permeabilities and act as effective impediments to vertical groundwater flows.

South of cross-fault 4 in Figure 15, the topography suggests that a substantial downwards displacement occurs. This would suggest that the permeable beds within the Yonna Formation, and the overlying coarse grained strata, might be found at much lower depths than other parts of the central graben area. For this reason the permeabilities at lower depths south of vertical section 900 are higher than more

northern areas.

It should be noted that the permeabilities shown in Figures 29a, b, c, d, and e represent the final permeability distribution for the 3-dimensional model. The 2 and 3-dimensional numerical simulations that preceded the present 3-dimensional model, were used to determine successively better approximations for the permeabilities within the system. They were assigned initial order of magnitude type values based on the rationale just described and are varied directly in conjunction with the boundary conditions to produce an acceptable match between the temperature and pressure distribution.

5.3 Boundary Conditions

The boundary conditions are crucial in determining the final temperature and pressure distributions within the system, and therefore require some explanation. Constant temperatures and pressures were imposed at the boundaries as opposed to constant heat and mass fluxes. This is because the temperatures and pressures are known down to depths of almost 2000 feet from borehole measurements, whereas no indication of the heat and mass fluxes at this depth are known.

The 3-dimensional numerical mesh can be visualized as a single, large element with 6 different boundaries that influence the internal heat and mass transfer of the system. The 6 boundaries imposed on the study area are shown in Figure 30. The different boundaries are labeled as follows: Atmospheric Boundary (AB), Bottom Boundary (BB), Northwestern Boundary (NWB), Southeastern Boundary (SEB), Southwestern Boundary (SWB), and the Fault Boundary (FB).

To numerically represent these six boundary conditions, large volumes are assigned to each respective element in the boundary condition. This is to ensure that the pressures and temperatures specified at the boundaries remain constant throughout the simulation. By connecting the boundary node exactly at the interface of the adjacent element as shown in Figure 26, the material properties of the large boundary elements do not affect the calculations.

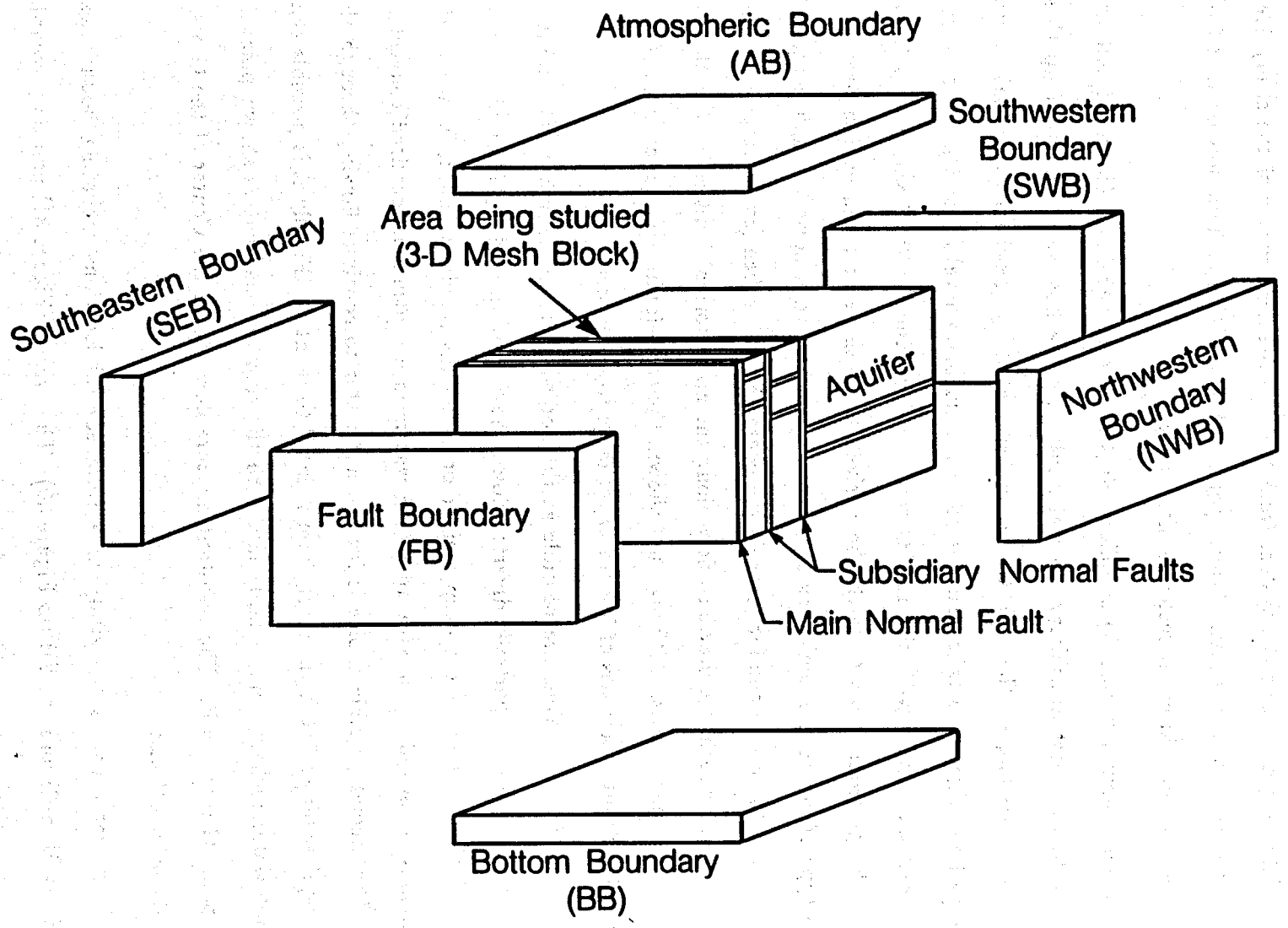

XBL 874-10041

Figure 30. Boundary conditions for three-dimensional numerical model.

Before describing these boundaries in detail it is helpful to envision the various flow patterns that might develop within the geothermal system. Figure 31 illustrates the basic flow patterns that might occur within the geothermal system at Klamath Falls. The diagram views the system from the northwestern corner of the study area, looking towards the southeast. Arrows point in the direction of fluid flow derived from both the hot and cold water recharge into the system.

A deep aquifer (point A) supplies 190°C water to the Main Normal Fault and possibly to the First Subsidiary Normal Fault. As the hot water is driven up these faults some cooling of the 190°C waters (estimated by geochemistry data) occurs. This cooling might also take place at some intermediary level (B or C), where a cold water recharge mixes with the 190°C water and produces 120°C water at point D. The recharge from point C might be derived from the east (uplifted fault-block) if some type of permeable aquifer existed here. The water then flows through permeable sediments in the upper aquifer towards the center of the graben (southwest). At point D the hot water recharge may also flow along the main normal fault as well as the two subsidiary normal faults. Although not shown, the cross-faults are also capable of supplying significant quantities of hot water recharge to the system.

Three flow directions are possible as the hot water recharge approaches point F. First, the flow may be partially diverted down the Second Subsidiary Normal Fault, to eventually recirculate to the deep aquifer or to an intermediary point, E, where the water may be mixed again with upflowing waters in a continuous localized convection cell. The second possible choice is for the hot water to continue flowing through the same aquifer (cross-hatch shading), from point F to point G. Finally it is possible that the hot water recharge may simply mix with the cold regional waters shown pointing from point G towards F. The resultant mixture flows down the Center of the Graben towards the southeast.

Cold water enters the study area from several locations including boundaries, NWB, SWB, SEB and the FB (in Figure 30). The arrows (Figure 31) pointing towards the uplifted block near the Center of the Graben (from point G towards F) represent

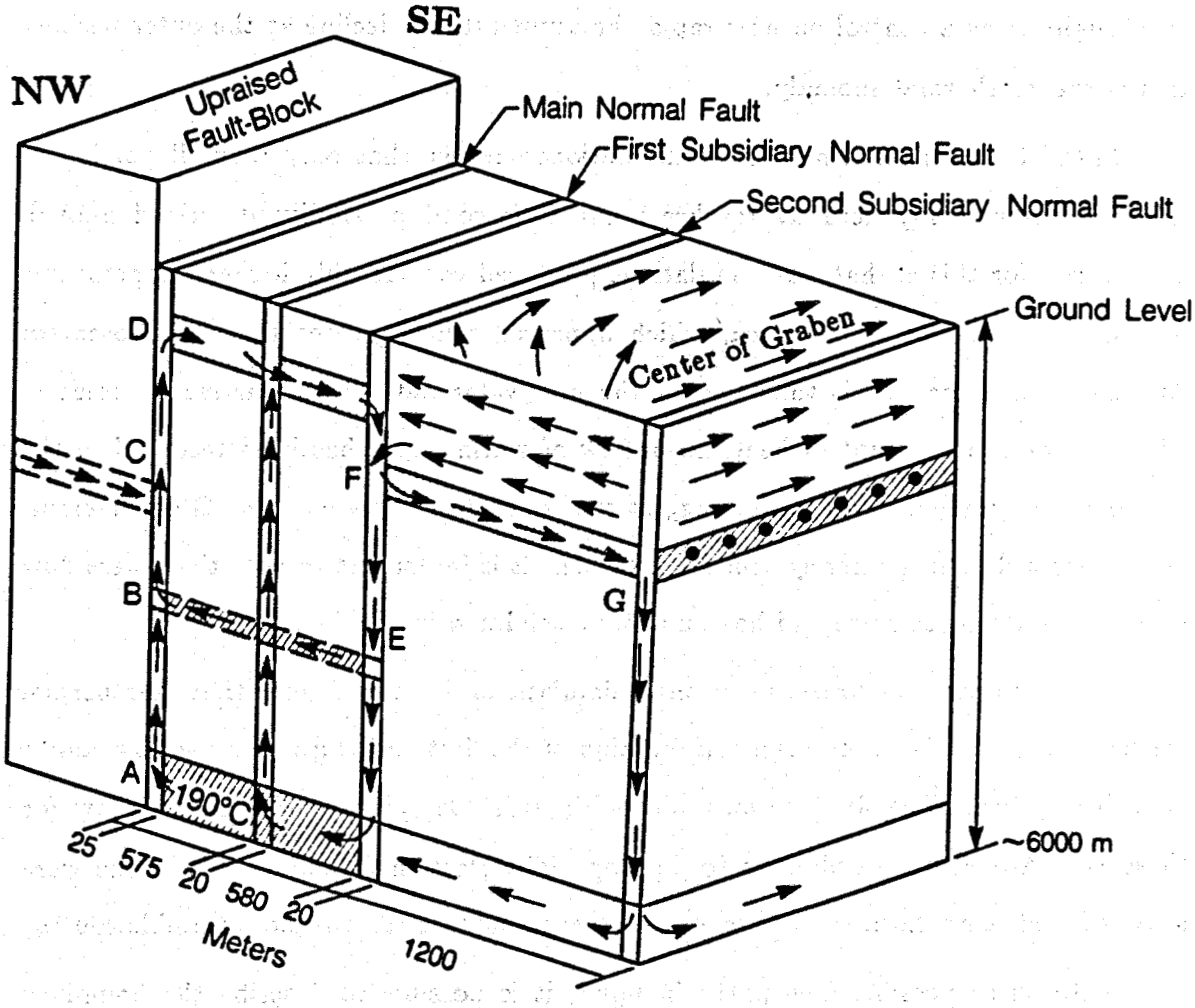

Figure 31. Conceptual model of possible flow regimes within the geothermal system. Arrows indicate direction of both cold and hot water as described in text. System is viewed from the northwest looking towards the southeast.

the flow of cold waters from the SWB. Although not shown, cold recharge enters from eastern portions of both the Northwestern and Southeastern Boundaries. At the very southern end of the Fault Boundary, cold water also enters the system (flowing towards the southwest) and mixes with hot waters flowing towards the south, from the hot well area. In general, the cold water recharge mixes with thermal waters and can be thought of as a control on how rapid the temperatures decline at the outer perimeters of the geothermal anomaly.

Initial 3-dimensional numerical simulations suggest that only a small portion of the hot water if any actually reaches point G (second possibility described above). One reason for this is that, the simulations produced considerably higher temperatures in the center of the graben area, which appeared much greater than the observed. Another reason for this is that even if the hot water did actually arrive at point G with a significant amount of heat, no upflow of warm water has been recorded in the center of the graben. This would suggest that only down-flow at point G and recirculation into a deeper aquifer system are possible. It is important to note that these flow routes are only speculative and have not been validated in the field.

From numerous three-dimensional simulations it was found that geothermal discharge most likely occurs as a combination of the first and third possible flow routes described above. The final permeabilities (Figures 29a-e) were assigned to allow for these two flow route possibilities to develop. The Bottom Boundary conditions were also assigned temperatures and pressures to accommodate the two flow possible routes.

With these possible flow paths in mind, it is possible to describe the boundary conditions in detail. It is assumed that no heat or mass is transferred across the Fault Boundary and it is therefore treated as an insulated boundary. This boundary represents the plane of the main normal fault. Also included in the Fault Boundary is a cold water recharge at the southeastern corner of the study area (attached to sections 1200 and 1300 in Figure 27, and connected to elements 17, 25, and 33 as shown in Figure 26). A 12 meter hydraulic head is imposed at this boundary which is determined from the water levels shown in Figure 9.

For the Atmospheric Boundary, an average ambient air temperature of 7.9°C and a pressure of approximately 1 bar were imposed. The flow of water from the atmospheric boundary into the system is effectively impeded by the low permeabilities of the caprock (5.00×10^{-18} m^2). The atmospheric boundary condition is seen in both Figure 26 and Figure 27.

Along the Southwestern Boundary a linear temperature gradient of 30°C/1000 m and a pressure distribution consistent with the water levels shown in Figure 9 were imposed. The temperature gradient imposed on this boundary was based on the assumption that the outer regions of the study area remain cool due to the flux of cold regional groundwaters towards the south. The pressures assigned to this condition take into account the variation of density with temperature and are calculated using:

$$P = \rho(T) \cdot g \cdot h + P_o \qquad (23)$$

where $\rho(T)$ is the average density as a function of temperature, P_o is the atmospheric pressure, and h is the height of the water column above the point where the pressure is measured. The temperatures and pressures assigned to the SWB condition are shown in Figures 32a and 32b. The exact values for the temperatures and pressures and temperatures for each of the boundaries, SEB, SWB, BB, NEB and FB are given in the appendix and include figures of each boundary condition with corresponding numbers (Figures A1 - A4).

Along the northern portion of the Southwestern Boundary, cold regional groundwater flows towards the east, against the flow of hot waters being discharged from the main normal fault, while at the southern end of the SWB, waters are directed more towards the south. This can be seen in the water levels shown in Figure 9. The water levels near Lake Ewauna are approximately at an elevation of 4090 feet above sea level, representing the lowest water level measured within the study area.

The temperatures and pressures in the Bottom Boundary fault elements are the least known characteristics in the model, and yet together with the permeability distribution, are the most responsible for the resultant temperature and pressure distributions and hot water recharge rates within the system. The main concern in assigning

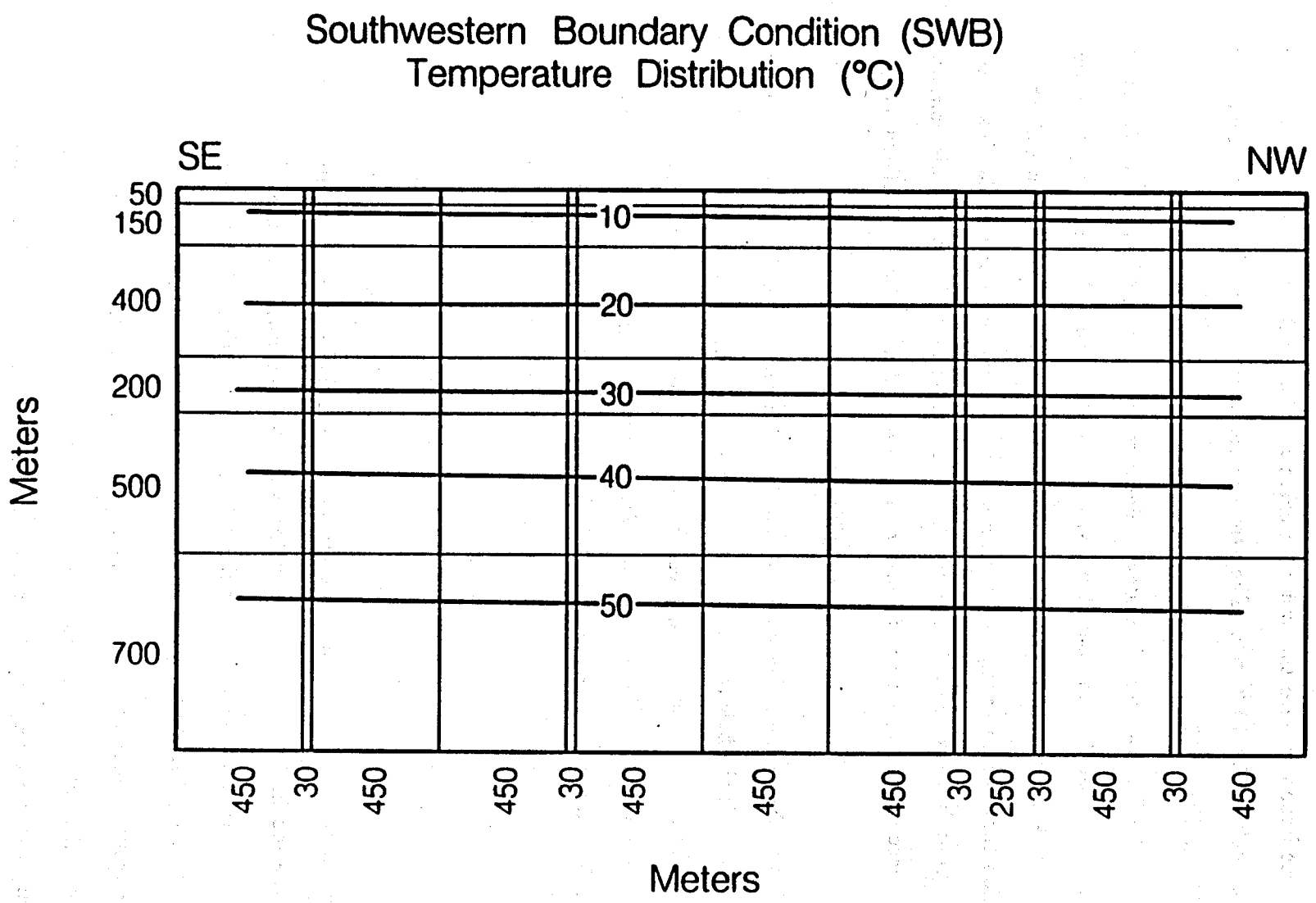

Figure 32a. **Southwestern Boundary pressure distribution (Bars).**

XBL 874-10099

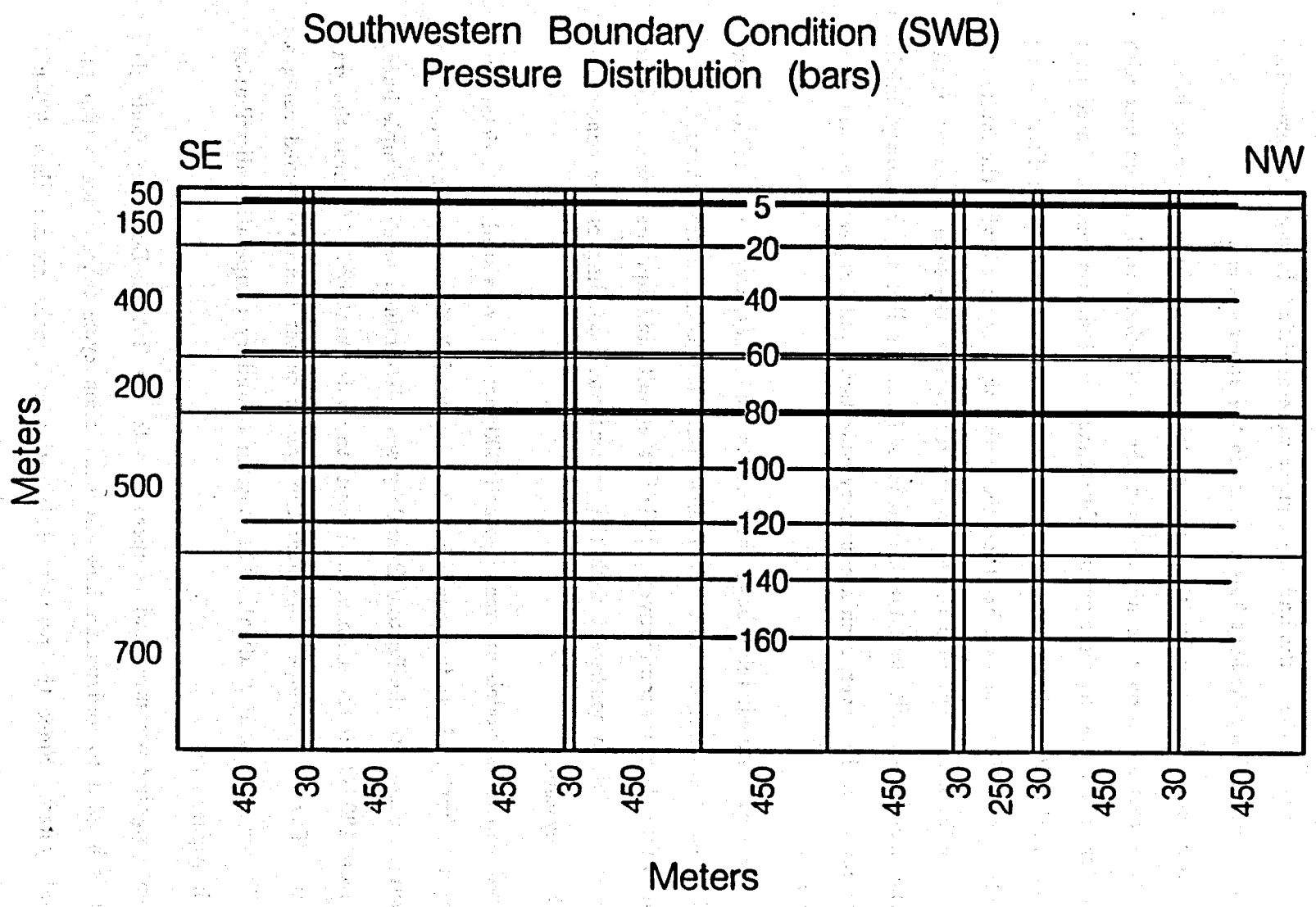

XBL 874-10100

Figure 32b. Southwestern Boundary temperature distribution (°C).

the Bottom Boundary fault elements was to use pressures and temperatures that would allow the upper system to equilibrate to the observed conditions in the field. The permeabilities for the faults and the aquifer were modified during each simulation as a means of controlling the heat flow patterns in the upper system.

A depth of 2000 meters for the Bottom Boundary was chosen because it was assumed that this elevation was higher than the point where cold waters mix with 190°C waters from the deeper aquifer. Two-dimensional simulations indicated that this depth would allow the upper system to equilibrate by itself with little or no influence from the BB elements other than those directly associated with the faults. A boundary condition that supplied the hot water recharge at the same elevation as the aquifer (i.e. from the Fault Boundary), instead of from the Bottom Boundary, might have been imposed. However, such a boundary condition would neglect heat flow from the fault zones.

The elements immediately above the Bottom Boundary, were assigned low permeabilities (basalt matrix), except for fault elements. Heat is transferred through these low permeability elements conductively, while in the faults and aquifers it is dominated by convection. This is consistent with the present understanding of the conceptual model for the system.

Two-dimensional models at great depths (6000 meters) were studied to determine an appropriate bottom boundary condition at a depth of 2000 meters. In general the temperatures assigned to the Bottom Boundary were determined using a simple linear gradient from 120°C (at the main normal fault) to approximately 70°C (near the graben center). The 70°C temperature near the graben center was determined using a 30°C/1000 meter thermal gradient. The Bottom Boundary temperature distribution is shown in Figure 34b.

When assigning pressures and temperatures to the Bottom Boundary fault elements, it is helpful to understand how the convection cycle takes place within the geothermal system. Since the pressure distribution at depths greater than 300-400 meters has not been measured for Klamath Falls, the appropriate values for the

pressures in the boundary fault elements must be determined iteratively, along with the permeabilities. The main normal fault is assumed to remain at a constant temperature of 120°C with depth, while the temperature distribution along the Southwestern Boundary varies according to the 30°C/1000 m geothermal gradient. If hydrostatic pressures are assigned with this temperature distribution to both the hot and cold ends of the Bottom Boundary, the pressures in the hot end (fault zone) will be less than the cold end (SWB). These pressures are estimated to be on the order of,

$$P_{hot} = (2012\text{m} \times 9.81\text{m/s}^2 \times 950.0\text{kg/m}^3) + P_{atm} = 1.89 \times 10^7 \text{ Pa},$$

$$P_{cold} = (2000\text{m} \times 9.81\text{m/s}^2 \times 990.0\text{kg/m}^3) + P_{atm} = 1.95 \times 10^7 \text{ Pa},$$

which would indicate that cold water at this depth would flow from the cold to the hot end if some type of permeable conduit existed. Measured values of the water levels in the near surface aquifer indicate that there is a higher fluid potential in the hot well area than in the southern corner of the study area shown in Figure 9, suggesting that the water flows from the hot area towards the cold area. No groundwater is believed to flow into the hot well area from the upthrown fault block (main normal fault). Consequently the entire hydraulic head of 12 meters seen in the hot well area is assumed to be caused by the bouyant forces of the upwelling thermal waters along the main normal fault.

Figure 33 shows a qualitative interpretation of the fundamental nature for the continuous convective cell produced by the bouyant force of the upwelling thermal waters. Two columns, one hot and one cold, and a diagram showing a qualitative pressure variation with depth in the hot and cold columns are illustrated. Only the isostatic condition is considered in which no flow occurs between the hot and cold columns.

The pressures in the hot column near the surface are greater than the pressures in the cold column at the same elevations and remains so until one drops down to point A, where the pressures in both columns are equal. Below point A, the cold pressures are larger than the hot pressures. If the conduits at C were open, cold waters would flow towards the hot column, and hot waters would flow through the conduit at A

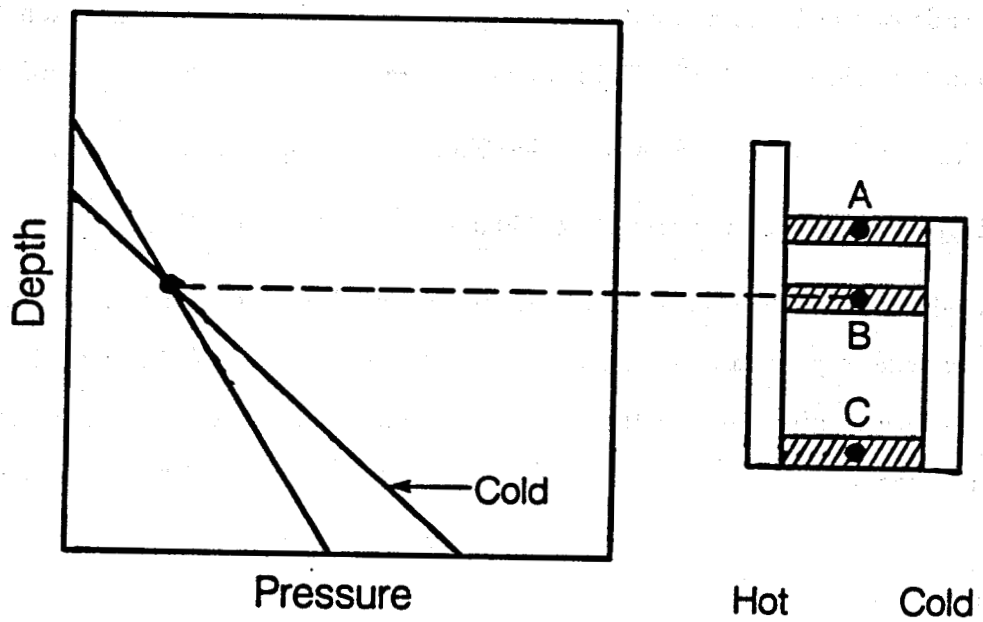

XBL 874-10063

Figure 33. Qualitative representation of convective flow induced by differences in temperature dependant densities. Two columns are shown on the right are dependant upon temperatures determined by a geothermal gradient.

towards the cold column, thereby creating a convective process. This is, of course, assuming that the two columns remain at their respective temperatures.

This basic concept was used in assigning initial estimates for the Bottom Boundary pressures. Figure 34a represents the final pressure distribution for the Bottom Boundary. The exact pressures and temperatures are shown in the appendix with corresponding locations of nodal points shown in Figure A2. The pressures in Figure 34a are less near the hot zone by approximately 1.5 bars. This pressure difference, nevertheless, allows for flow near the surface, from the fault to the cold region. Somewhat lower pressures in the Bottom Boundary are seen along the second subsidiary normal fault to allow for possible downflow of hot and cold waters (Figure 34a).

The most time consuming aspect of the three-dimensional simulations was in estimating the Bottom Boundary pressures. The temperature and pressure distribution in the geothermal reservoir appeared to be most sensitive to this parameter. By assigning bottom pressures too low, cold water downflow occured in all of the faults. If on the other hand these pressures were set too high, the system would experience excessive heat influx. If bottom pressures in the first subsidiary normal fault were set too high, downflow in the main normal fault would occur. If they were set too low, either cold water derived from the central graben or hot water from the main normal fault would cause unreasonably high downflows to occur in the first subsidiary normal fault. The magnitudes of these pressure changes were initially on the order of 1 bar and later after relatively stable conditions had been obtained, were on the order of .1 to .01 bars.

The Northwestern and Southeastern Boundaries were assigned pressures according to the measured water levels. A pressure based on the 12 meter head was imposed on the western portion of the Northwestern Boundary. It is assumed that this boundary supplies the majority of the cold regional groundwater flow to the system. The western portion of the Southeastern Boundary condition is believed to be the zone of primary discharge of water for the system.

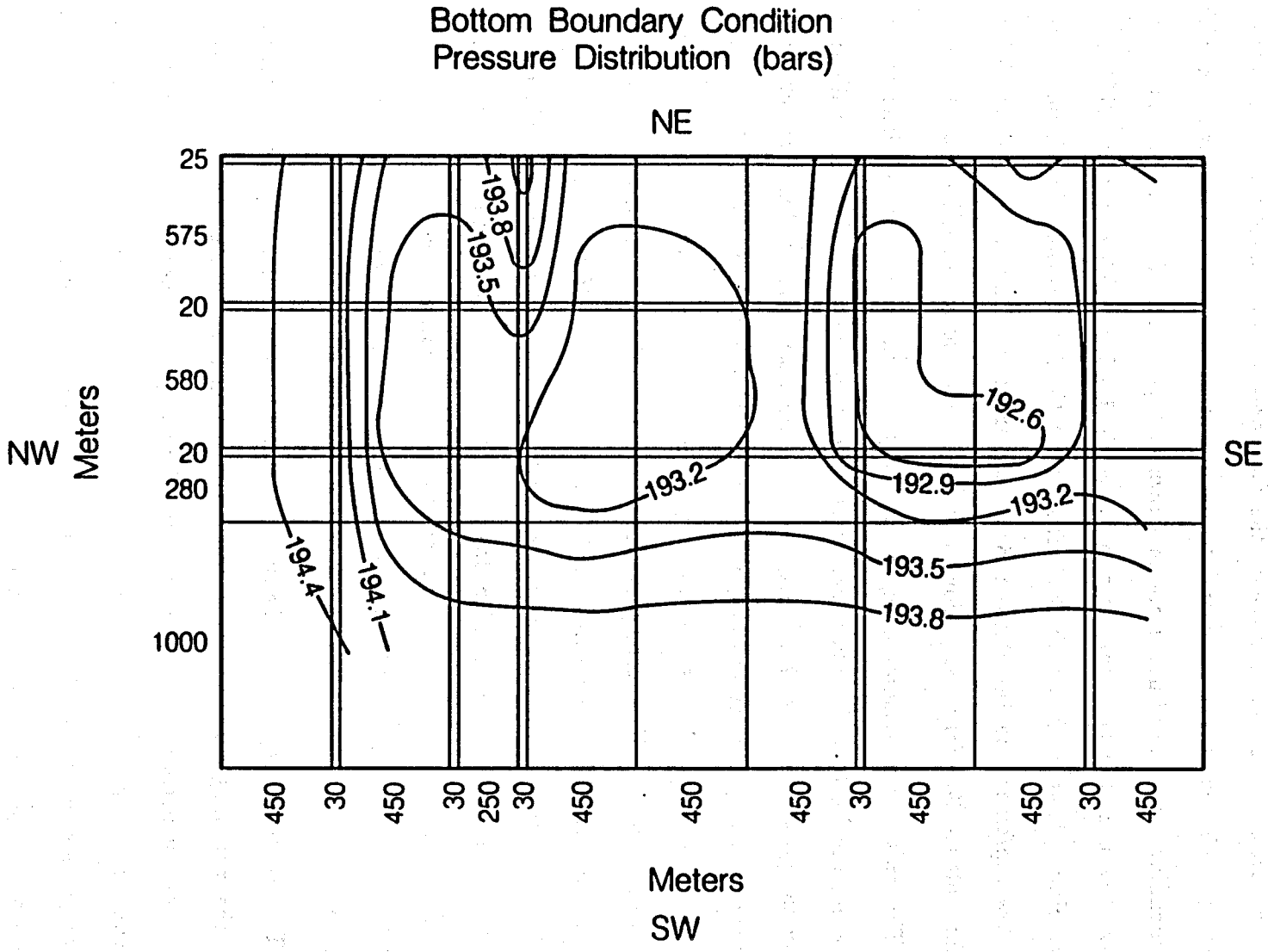

Figure 34a. Bottom Boundary pressure distribution (Bars).

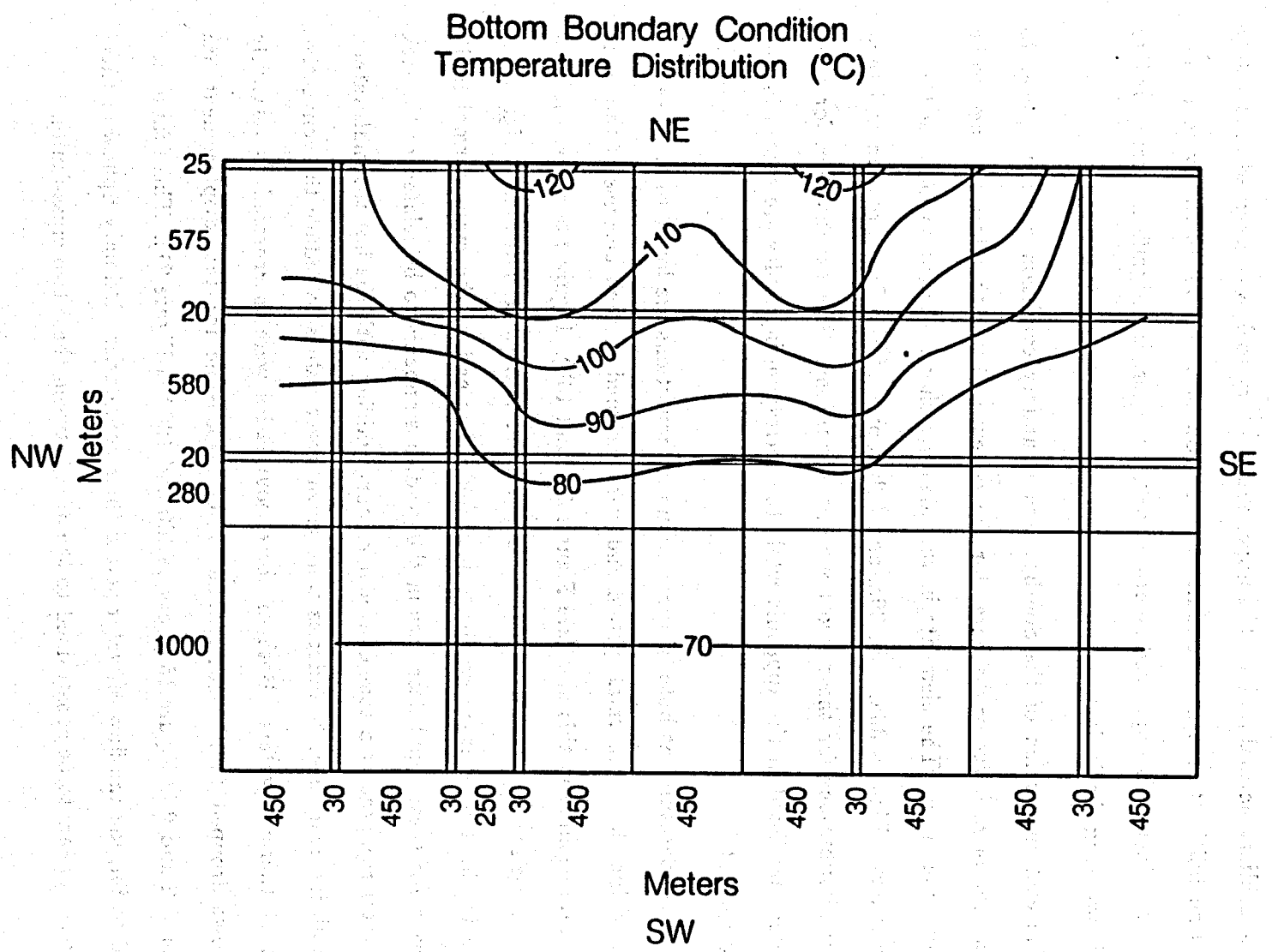

XBL 874-10108

Figure 34b. Bottom Boundary temperature distribution (°C).

The eastern portion of the Northwestern Boundary condition was assigned pressures which would allow hot water to flow from the main normal fault out of the system, and would also allow flow of colder waters into the system via the first and second subsidiary normal faults. The upper sedimentary rock was assigned moderately high permeabilities to act as a conduit for fluid flow into and out of the system. The surface flow from this upper sedimentary rock, however, is insignificant compared to the upflows along the faults.

The eastern portion of the Southeastern Boundary condition did not appear to act as a zone of recharge or discharge for the system and was therefore assumed to be a no flow boundary. The elements in this area are shown shaded to indicate the no flow boundary. Figures 35a, 35b, 36a, and 36b represent the final pressure and temperature distributions for these two boundary conditions. The exact values for these parameters are listed in the appendix while the corresponding nodes are shown in Figures A3 and A4.

The temperatures at both of these boundary conditions are lower than those that develop within the geothermal system and were assigned as such because of the rapid temperature declines in this area (see Figures 16a and 16b). Figure 14a shows the temperature cross-sections parallel to the main normal fault and indicates a significant decrease in the temperature gradients towards either end of the main normal fault. The reason for these rapid decreases in the gradients appears to be related to the lack of hot water recharge or a zone of colder recharge mixing with the hot thermal waters. Permeabilities near these boundaries were given lower values to reduce the convective transfer of thermal waters. Both of these boundaries were interpreted as relatively large down-dropped fault blocks. The faults responsible for this displacement are cross-faults 2 and 9 in Figure 15 (sections 100 and 1200 in Figure 27). These faults are assumed to impede the flow of water across their boundaries. Primary upflow of thermal waters appears to be constrained to the area between these two cross-faults.

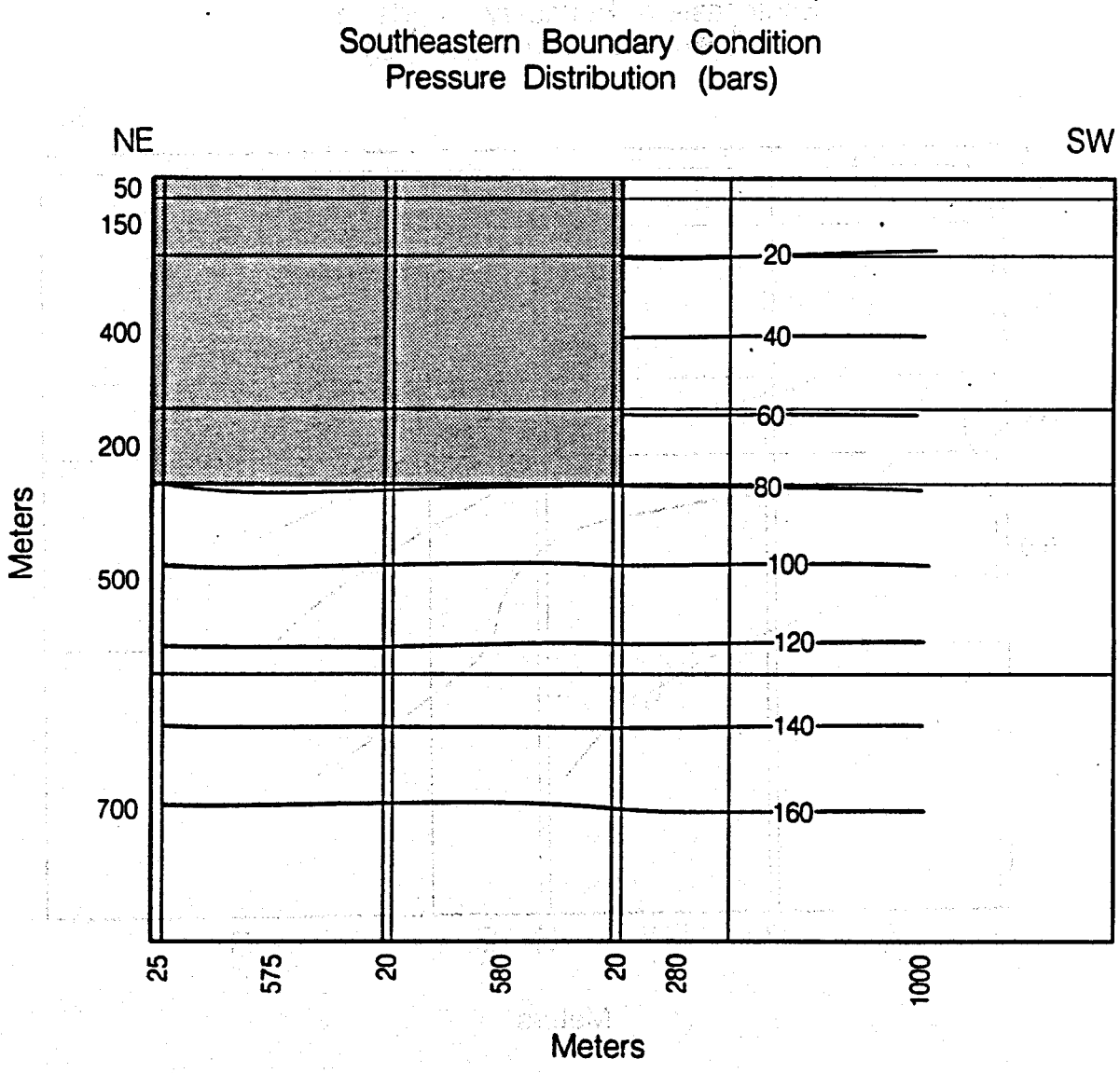

Figure 35a. Southeastern Boundary pressure distribution (Bars).

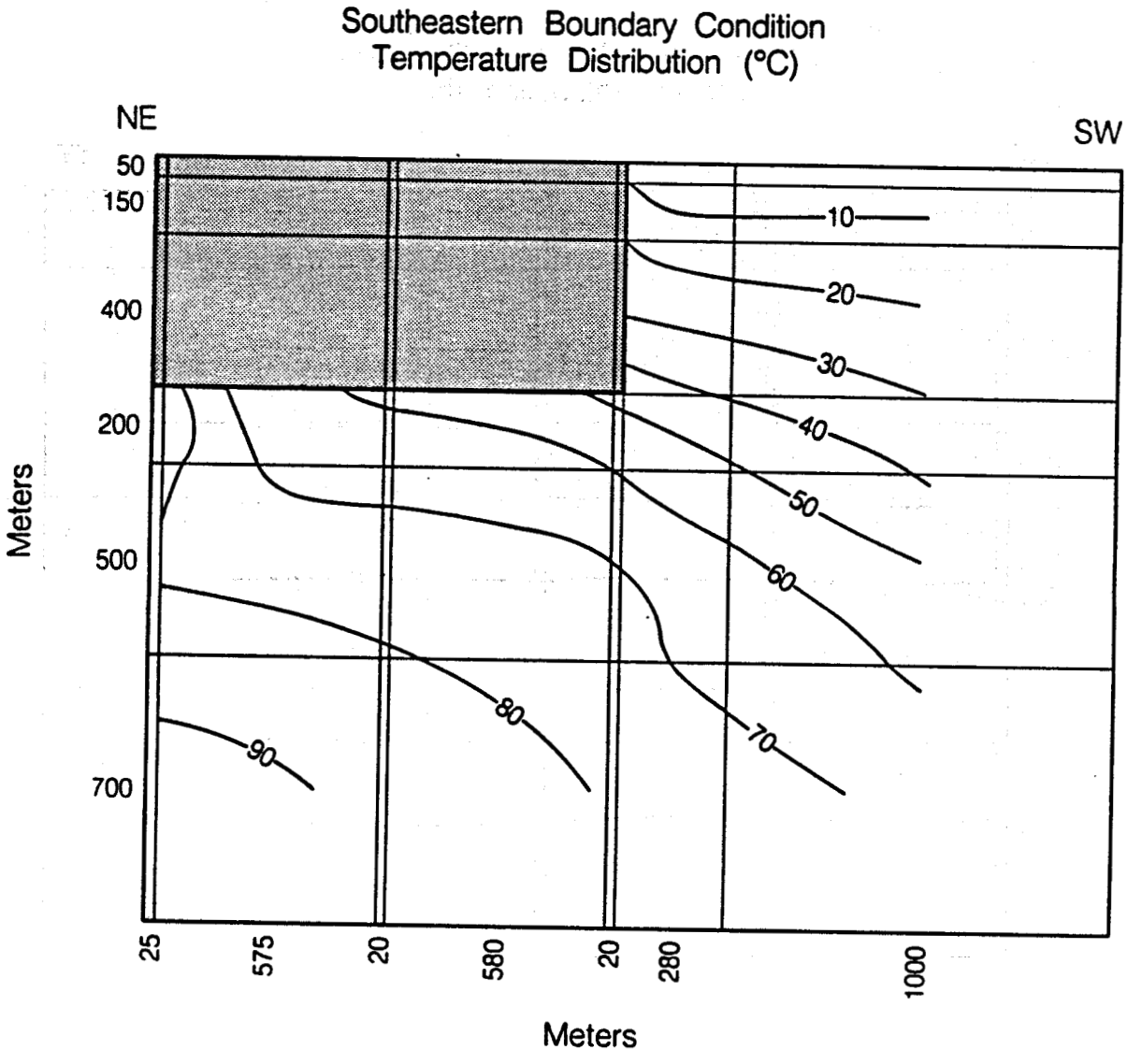

Figure 35b. Southeastern Boundary temperature distribution (°C).

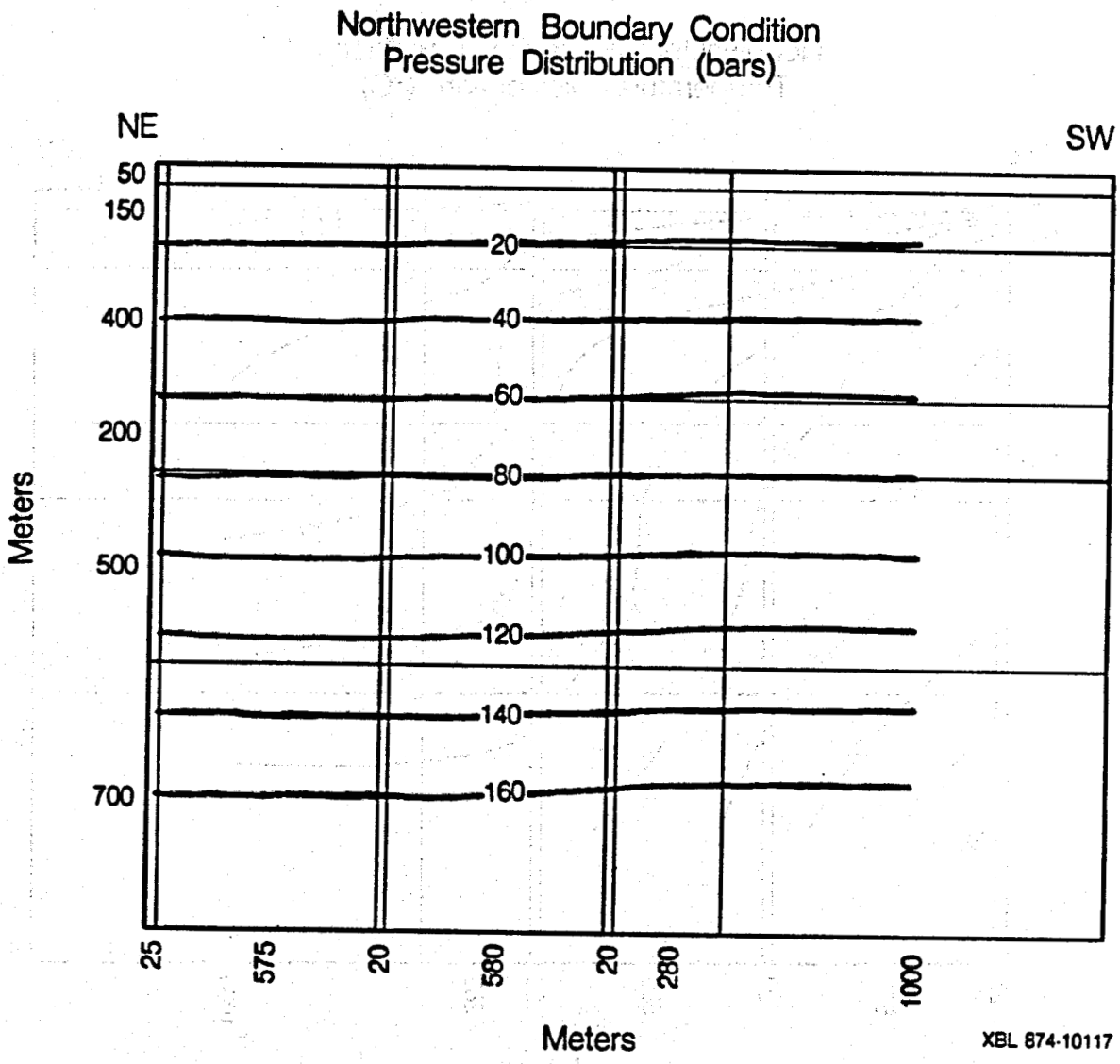

Figure 36a. Northwestern Boundary pressure distribution (Bars).

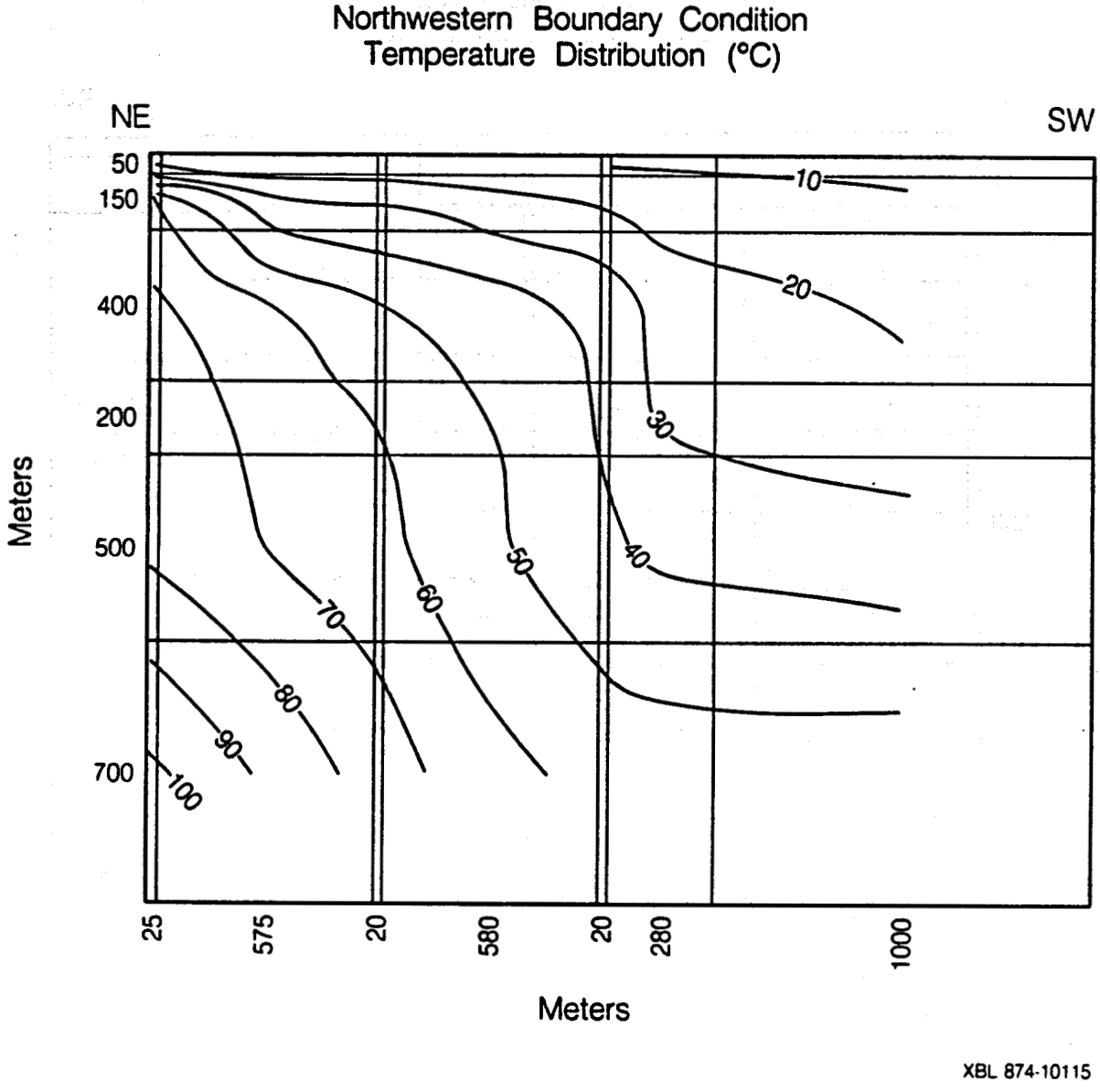

Figure 36b. Northwestern Boundary temperature distribution (°C).

5.4 Initial Conditions

At the start of the numerical simulations, the initial conditions for the internal elements in the three-dimensional mesh were set at temperatures and pressures determined by the 30°C1000 meter thermal gradient. It was soon apparent that numerical instabilities occurred if temperature and pressure changes were too large. This problem was resolved by assigning more appropriate material properties or boundary conditions. By setting temperatures and pressures, near the fault zone, closer to their final, anticipated temperatures and pressures, it was possible to obtain steady state conditions. The steady state temperatures and pressures from these initial simulations were then imposed as the initial conditions for each new successive simulation.

5.5 Results

The three dimensional numerical analysis incorporated all of the main features for the Klamath Falls geothermal system. These main features are summarized here, and were based upon inferences made from the three-dimensional conceptual model and the results from the three-dimensional numerical simulations.

The hot water recharge into the system occurs between two bounding cross-faults (2 and 9 in Figure 15). This hot water recharge enters the system through the main normal fault and flows upwards until it intersects near surface permeable strata. Initially the hot water flows towards the southwest. However, when the hot water recharge approaches the second subsidiary normal fault a large portion mixes with cold regional groundwater in the upper central graben sediments and flows towards the southeast. The remaining portion of hot water recharge flows down the second subsidiary normal fault to depth possibly recirculating into the convective system. The first subsidiary normal fault experiences both upflow and downflow. In general downflow along this fault occurs at the northern and southern extents of the study area, while upflow takes place only in the center region. This fault, in general, experiences much less flow compared to the other two normal faults.

It is very likely that hot waters flow along the lengths of the normal faults. This is due to their high permeabilities compared to surrounding rock material. The hot water also appears to be associated with flow along at least two of the cross-faults in the system (4 and 7 in Figure 15). The most significant hot water recharge occurs within the high permeability zones created by the intersection of the normal faults and these two cross-faults.

The main discharge from the system occurs through the Southeastern Boundary. Much smaller quantities of fluid ($\approx$ 1/4 that of the SB) from the NWB, SWB and BB. The main cold water recharge to the system is supplied from the Northwestern, Southwestern and the southern portion of the Fault Boundary. This cold water recharge mixes with the thermal waters and consequently produces the sharp declines in temperatures observed in Figures 16a and 16b.

The three-dimensional numerical model reproduces these features with reasonable accuracy. The calculated temperatures and pressures were compared to the measured temperature distributions and water levels for the area and appear to match well. This section focuses on this temperature/pressure comparison and also discusses the results from the three-dimensional numerical simulations for areas where no data has been collected. The results include temperature and pressure distributions from the three different planar sections of the 3-dimensional mesh (Figure 27). The associated mass fluxes are illustrated in vector plots. One heat flux diagram is also shown.

5.5.1 Temperature and Pressure Distributions

The final temperature and pressure distributions from the three-dimensional simulations are shown in Figures 37 to 50. These Figures include temperature and pressure distributions for horizontal sections, HZ17, HZ25, and HZ33 and for vertical sections perpendicular to the main normal fault, VS200, VS500, VS600, VS900, and VS1300, and also for vertical cross-sections parallel to the main normal fault, VSP1, VSP2, VSP5, and VSP6. All of these sections are referred to in Figure 37.

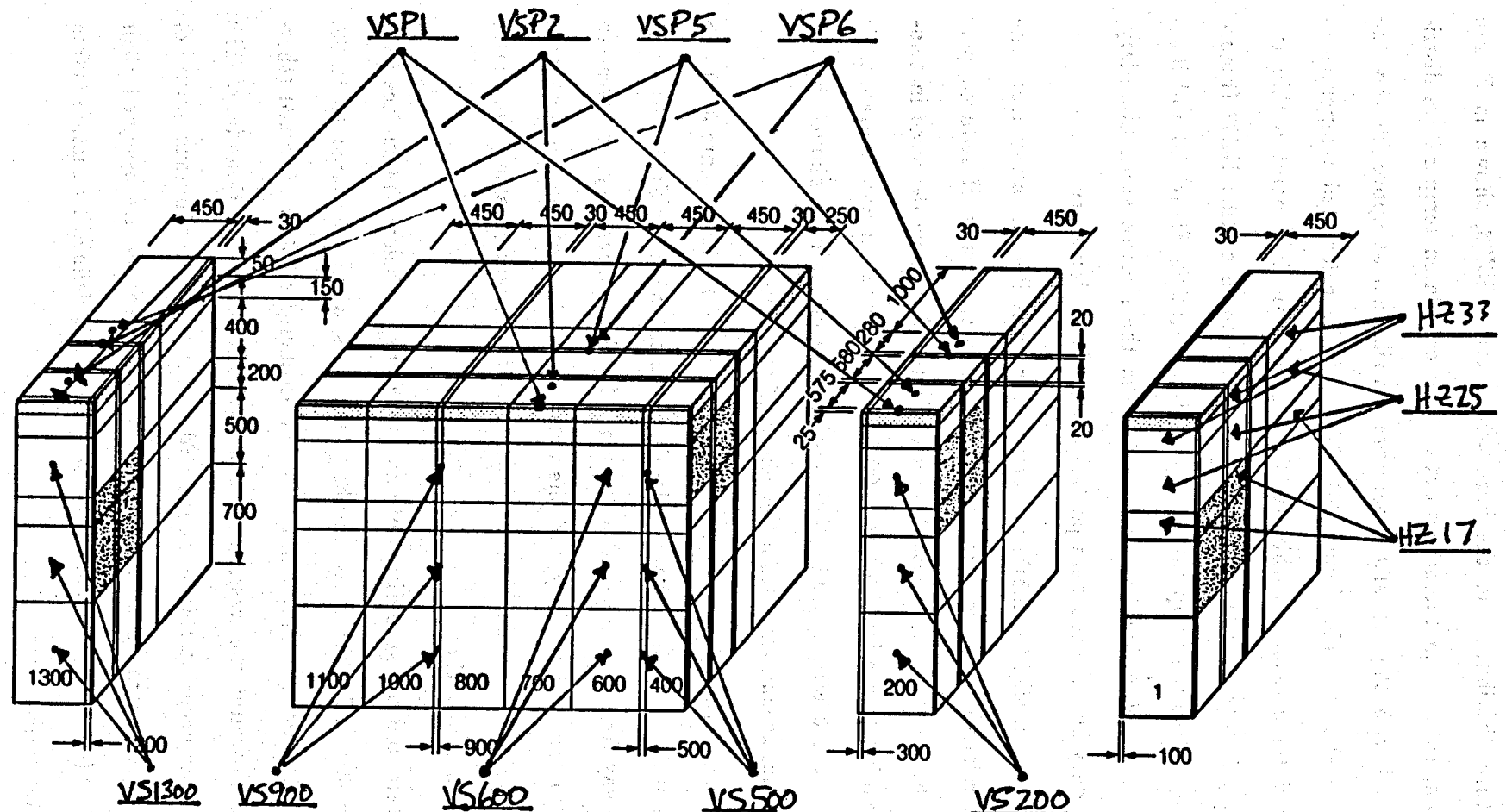

All dimensions in meters.

XBL 874-10042

Figure 37. Temperature and pressure distribution sections. Each section includes the entire set of connected nodes in the plane created by the arrows.

The temperature distribution in the horizontal section, HZ33, shown in Figure 39a, is used for comparison with the actual data. This calculated temperature distribution correlates well with the actual temperature distribution at approximately the same elevation (≈3800 feet a.s.l., Figure 38). Most of the calculated temperatures match the measured temperatures within 10°C at each individual point within the study region. The perimeter of the temperature distribution in section HZ33 (Figure 39a) also compares well to the temperature distribution found in Figure 38 and illustrates the cooling effects of regional groundwaters from the Northwestern Boundary, Southwestern Boundary and the southern portion of the Fault Boundary.

Section 700 shows a slightly inhibited temperature distribution away from the main normal fault relative to neighboring sections and is the result of reduced permeabilities within this section. The actual data indicates this same decrease in temperatures (corresponding to section 700) at 3800 feet a.s.l. elevation and is even more pronounced at 3700 and 3600 feet a.s.l.. This cooler zone might be explained by the influx of cooler regional groundwater from the center of the graben.

The hydraulic heads (based on the pressures calculated for HZ33 Figure 39b) also appear to compare well to the actual water levels found in the field (Figure 9). The pressures decline away from, the normal fault along the Fault Boundary, the western portion of the Northwestern Boundary and the northern portion of the Southwestern Boundary. The overall pressure distribution indicates flow of waters along the center of the graben towards the southeast.

The temperature and pressure distributions at 400 meters below the surface (section HZ25, Figures 40a and 40b) show notable differences when compared to HZ33. The temperature distribution in HZ25 is a result of an increased flow of mixed (thermal and cold) waters towards the western portion of the Southeastern Boundary. The greatest discharge rates occur at this elevation and is due to the continuous nature of permeable strata. The central graben elements at this elevation are assigned their highest permeabilities (4.0×10^{-13} m^2) south of the cross-fault defined by section 900 in the three-dimensional mesh (Figure 27).

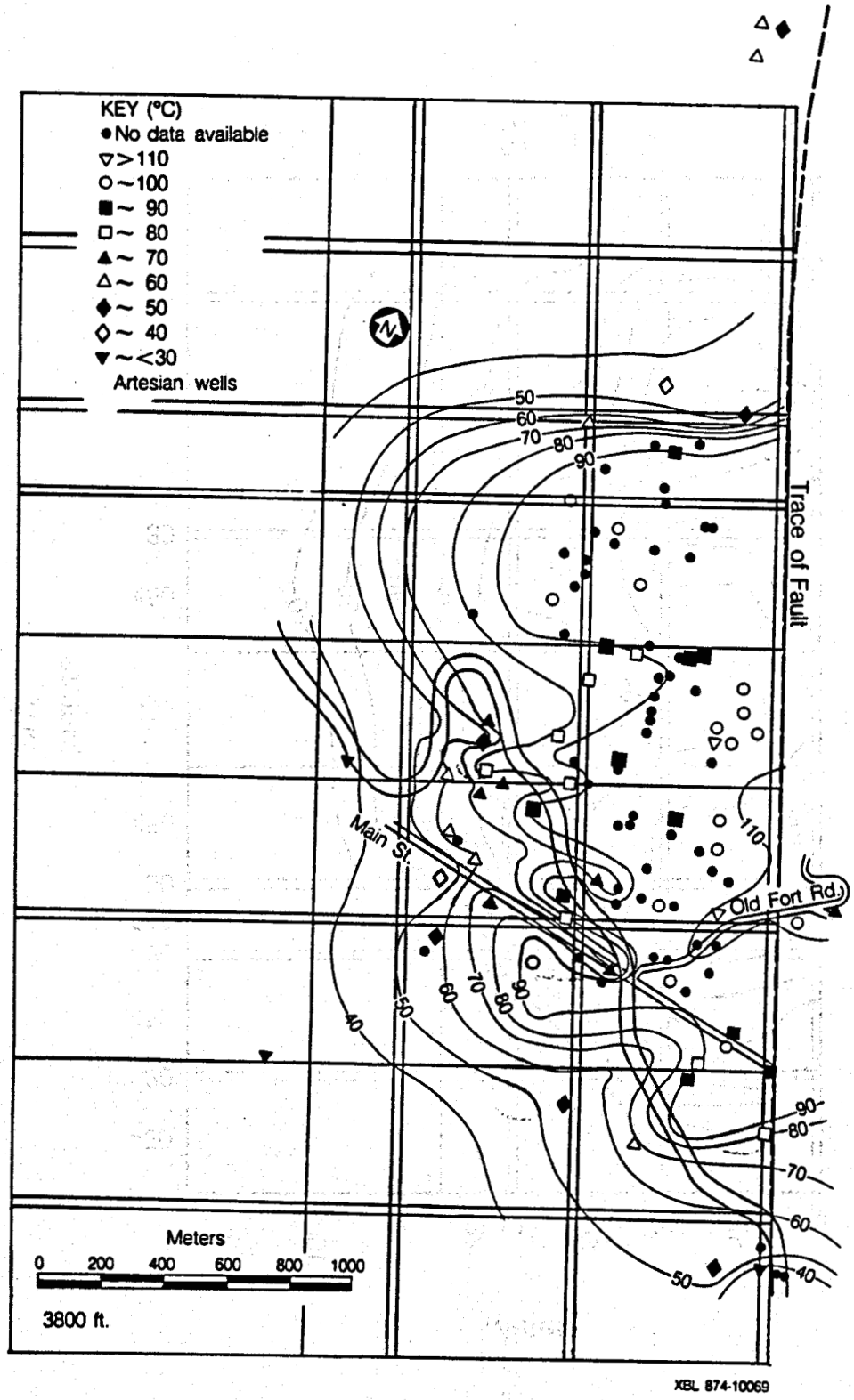

Figure 38. Actual temperature data at 3800 feet a.s.l. with horizontal grid overlay for comparison with the numerical results. Temperatures are in °C

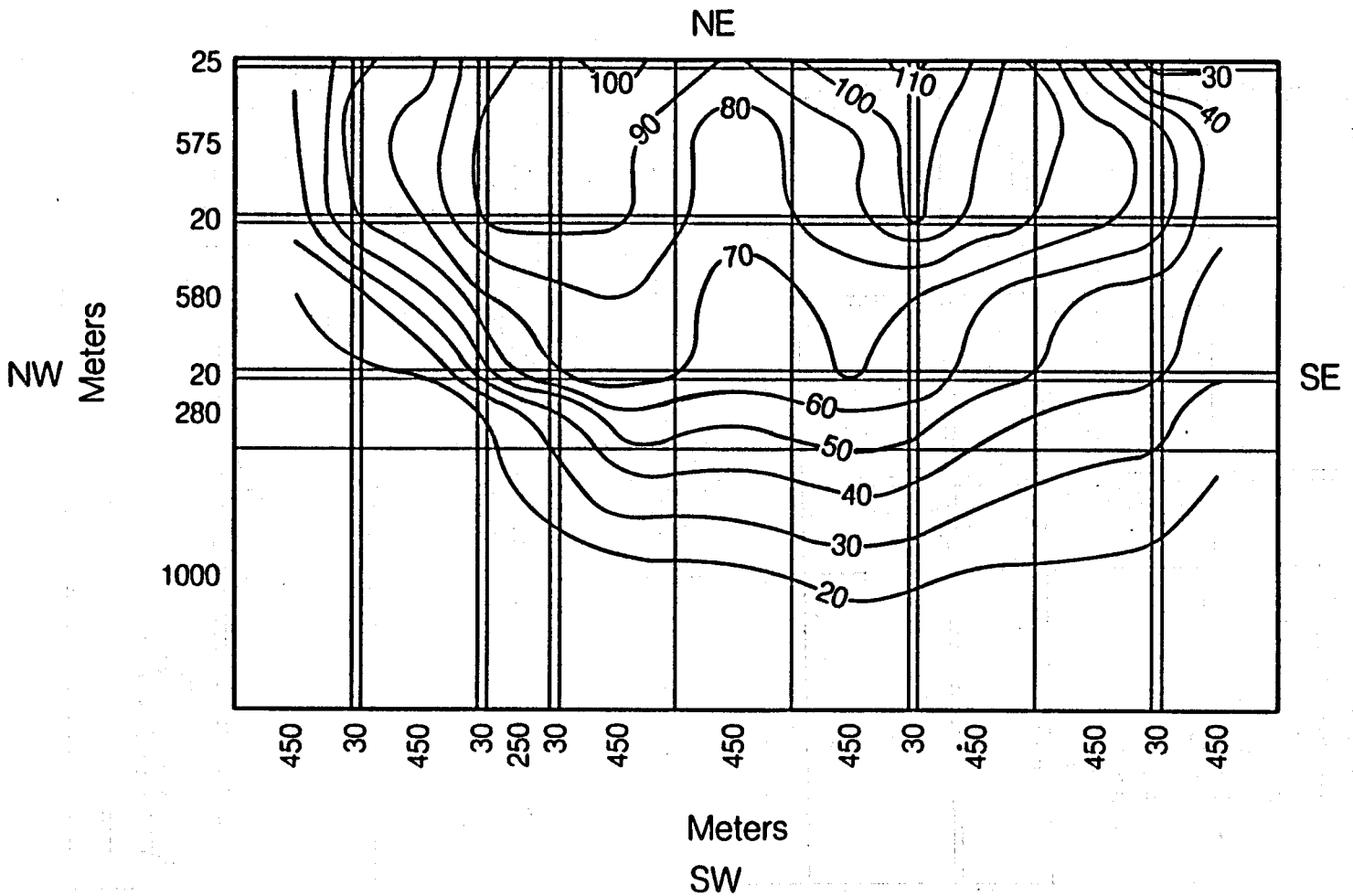

Figure 39a. Temperature distribution for horizontal section, HZ33. Temperatures are in (°C).

XBL 874-10104

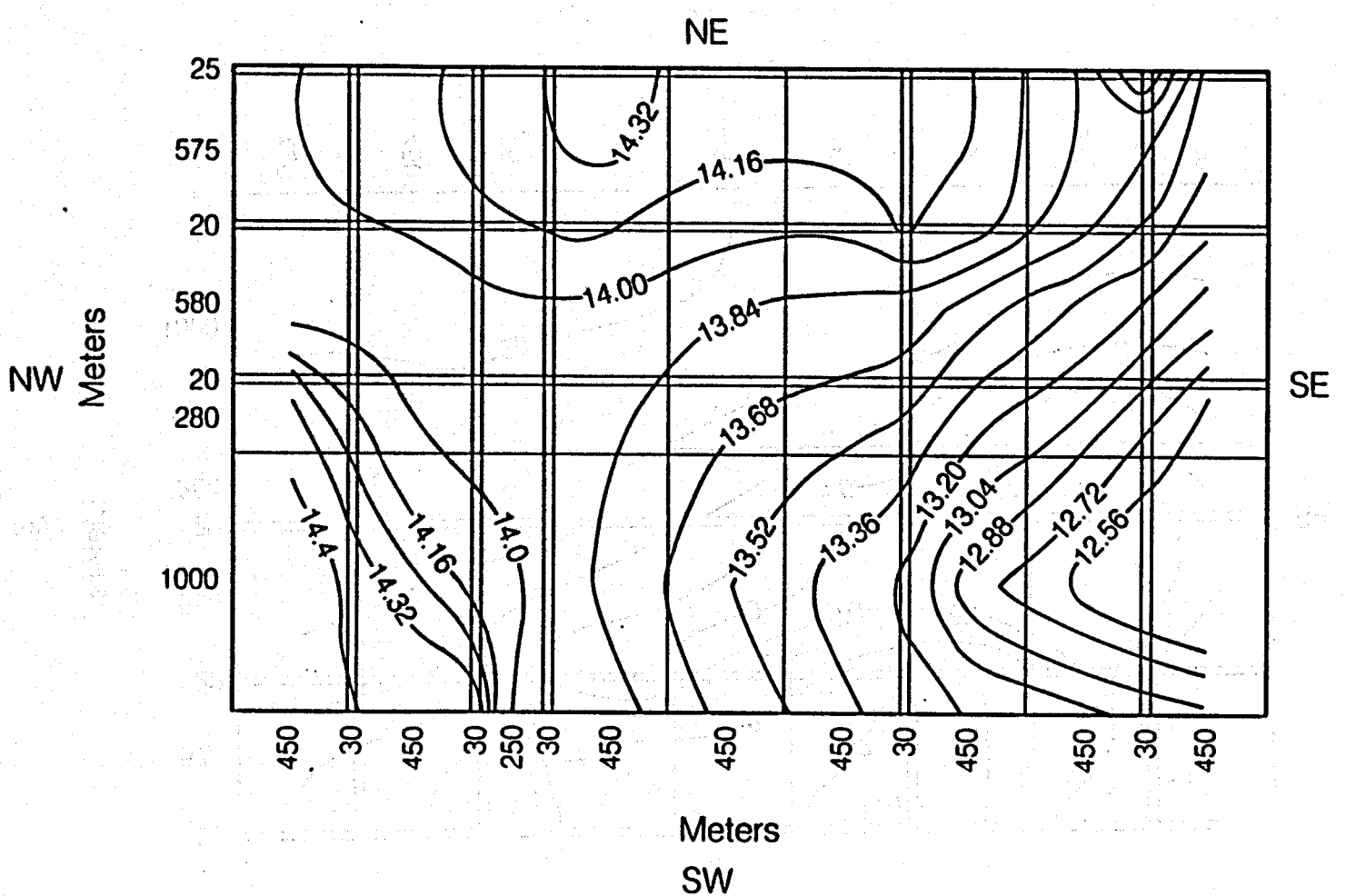

Figure 39b. Pressure distribution for horizontal section, HZ33. Pressures are in (Bars).

XBL 874-10101

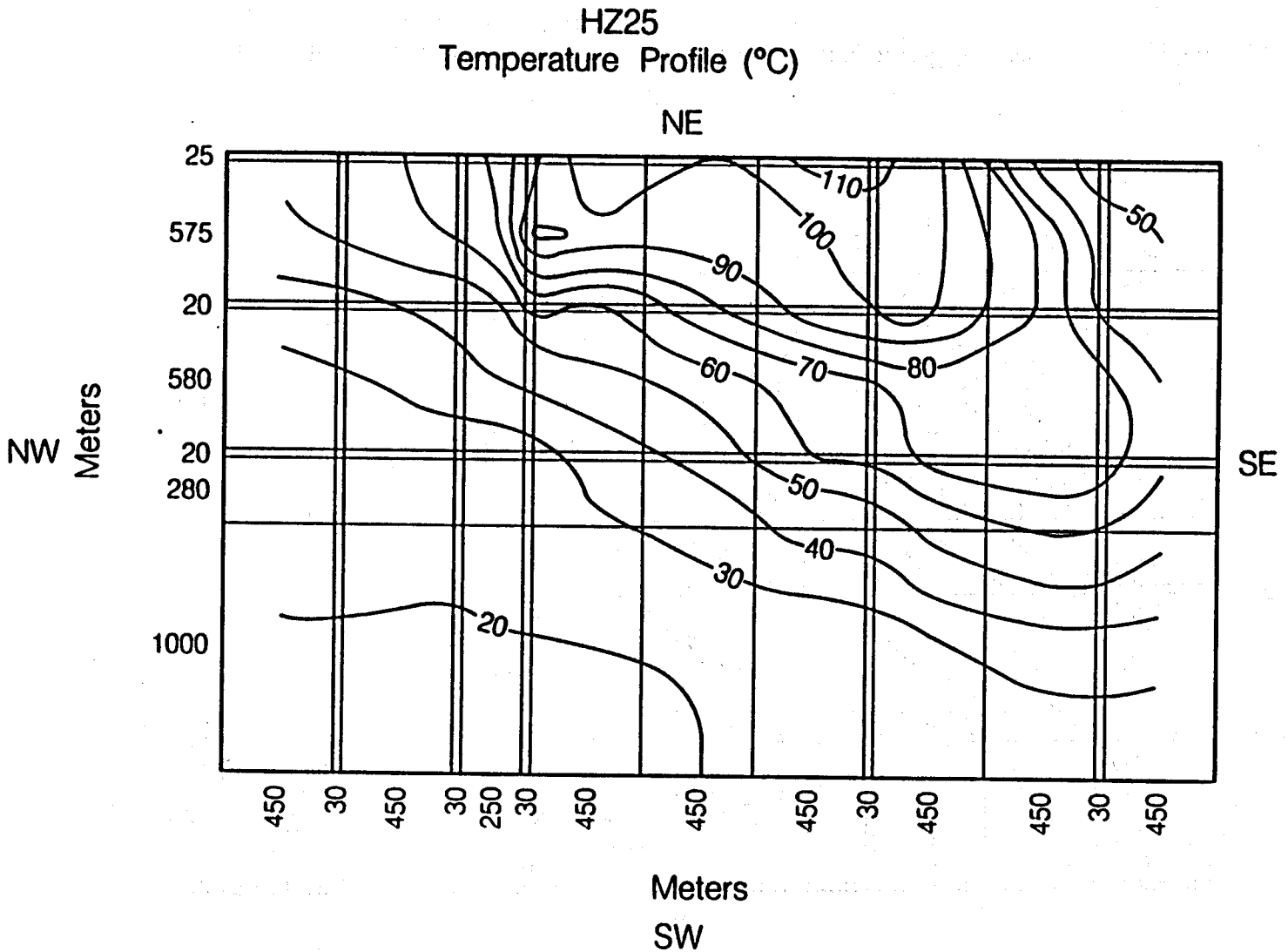

Figure 40a. Temperature distribution for horizontal section, HZ25. Temperatures are in (°C).

XBL 874-10105

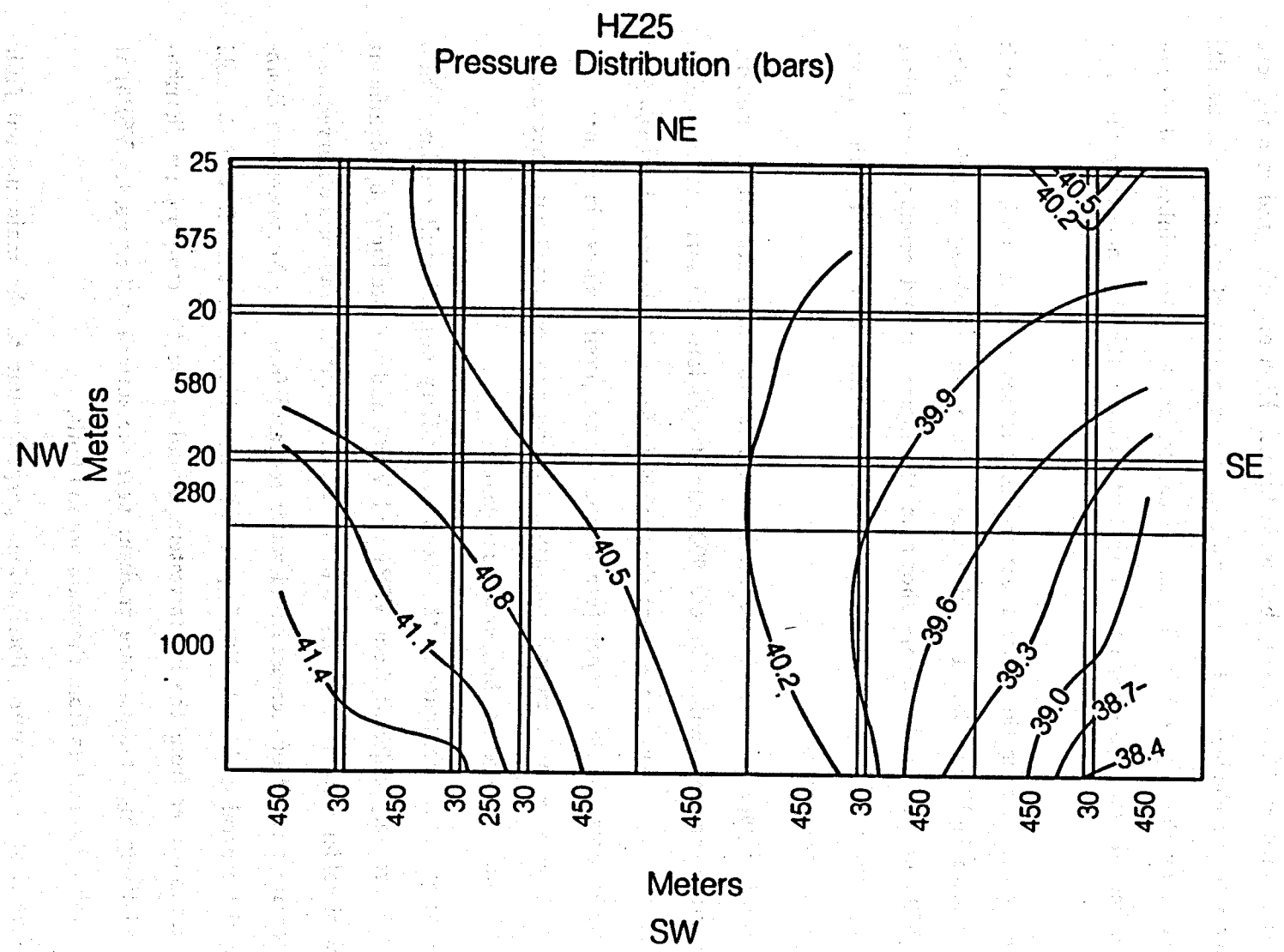

Figure 40b. Pressure distribution for horizontal section, HZ25. Pressures are in (Bars).

XBL 874-10102

The temperature and pressure distribution in the horizontal section at 700 meters (HZ17) below the surface is shown in Figures 41a and 41b. At this depth flow of thermal waters is constrained principally within the faults because of the occurrence of significant quantities of low density basement basalt. High pressure gradients are seen within each basalt element and are a result of the expansion of water in the basalts when heated by the adjacent faults (i.e. the basalts are low permeability and do not allow the heated water to escape faster than it expands thereby increasing the pressure).

The temperatures in the vertical section VSP1 representing the main normal fault zone are shown in Figure 42. Two high temperature plumes closely associated with sections 500 and 600, and 900 are shown in the figure. Rapid cooling takes place towards the outer ends of the section as a result of cold water recharge that mixes with the rising hot waters.

In VSP2 (Figure 43), the vertical section adjacent to VSP1, the 100°C temperature contours near cross-faults 500 and 900 extend well into the surrounding aquifer. High temperature gradients noted near the surface in Figure 43 do not exhibit the finer perturbations shown in the temperature cross-sectional profiles shown in Figures 14a, 14b and 14c, because the present 3-dimensional model was concerned with incorporating only the main features of the geothermal system.

The temperature contours in the second subsidiary normal fault section, VSP5 (Figure 44), are very different from VSP1 and VSP2 and are produced by significant downflow of colder waters along this fault. Lower temperature gradients observed near the surface are a result of increased cold water recharge from the Northwestern Boundary. In the central graben, VSP6 (Figure 45) better illustrates the effect of the cold regional groundwater from the Northwestern Boundary on the temperature distribution. A relatively high temperature gradient near the surface still exists, (in VSP6) at approximately 1360 meters from the main normal fault.

The vertical temperature distributions perpendicular to the main normal fault reveal several interesting features. They can account for the observed large scale, near

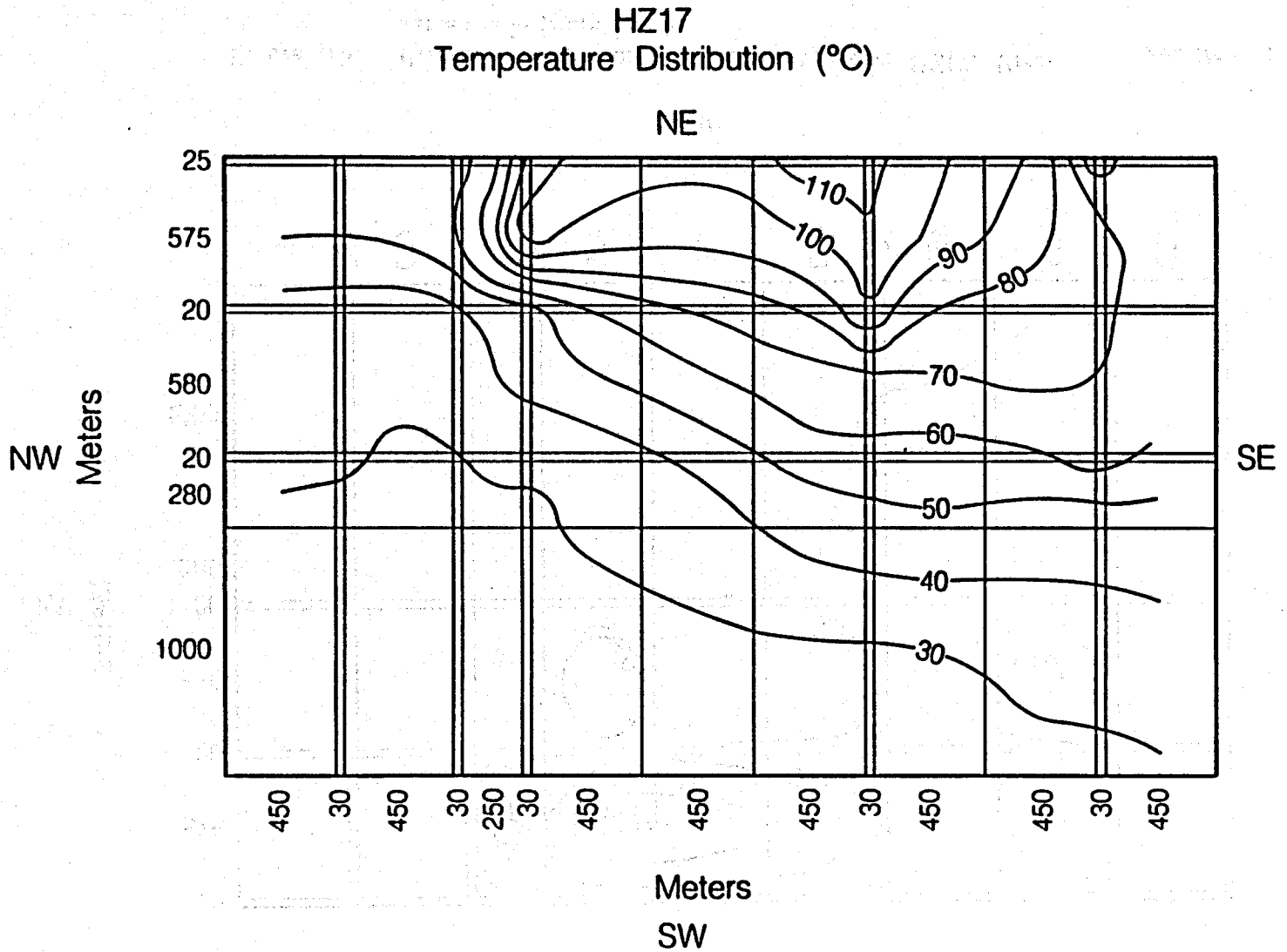

Figure 41a. Temperature distribution for horizontal section, HZ17. Temperatures are in (C).

XBL 874-10106

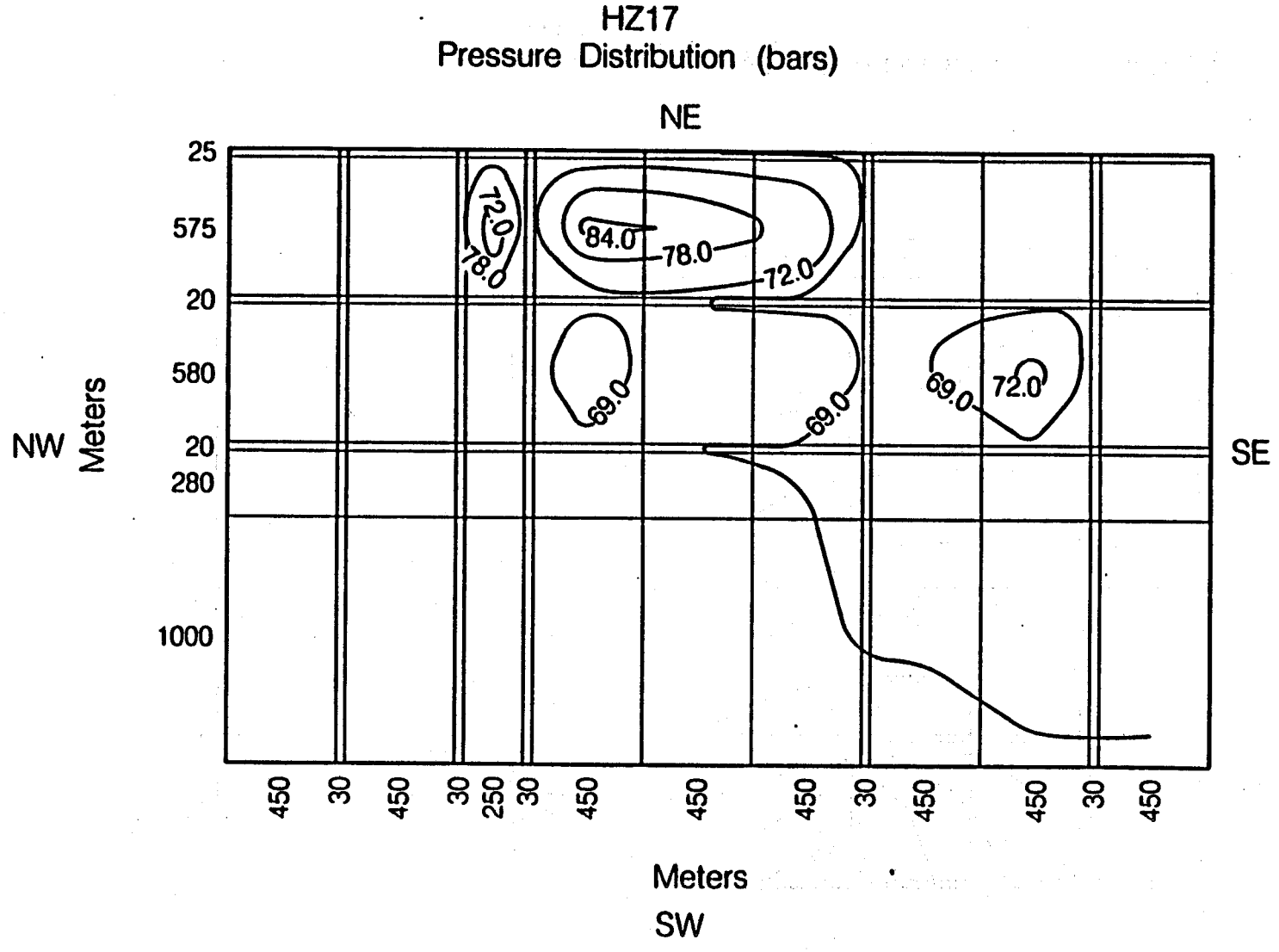

Figure 41b. Pressure distribution for horizontal section, HZ17. Pressures are in (Bars).

XBL 874-10103

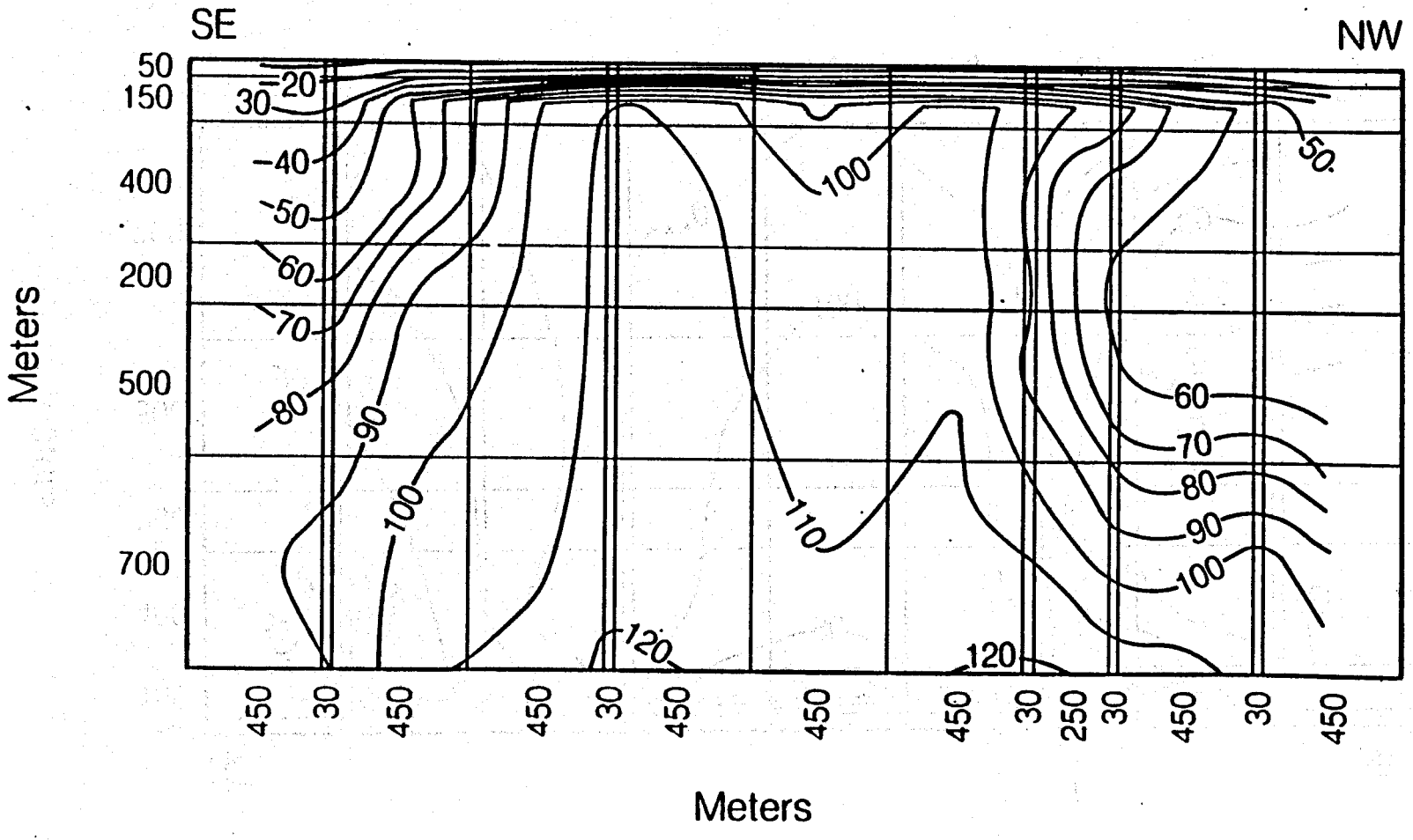

Figure 42. Temperature distribution for vertical sections VSP1, parallel to the main normal fault. Temperatures are in (°C).

XBL 874-10098

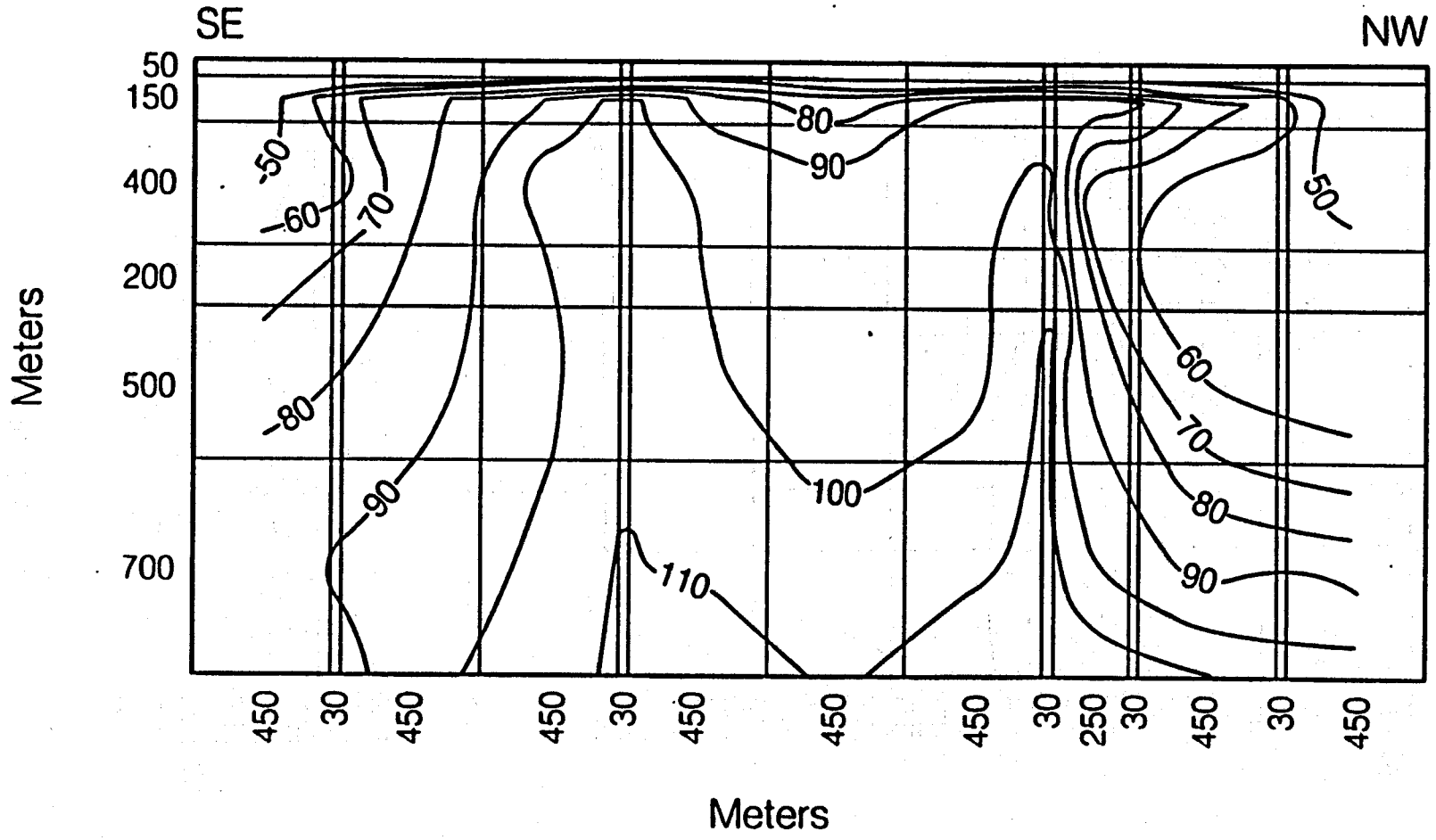

Figure 43. **Temperature distribution for vertical sections VSP2, parallel to the main normal fault. Temperatures are in (°C).**

XBL 874-10097

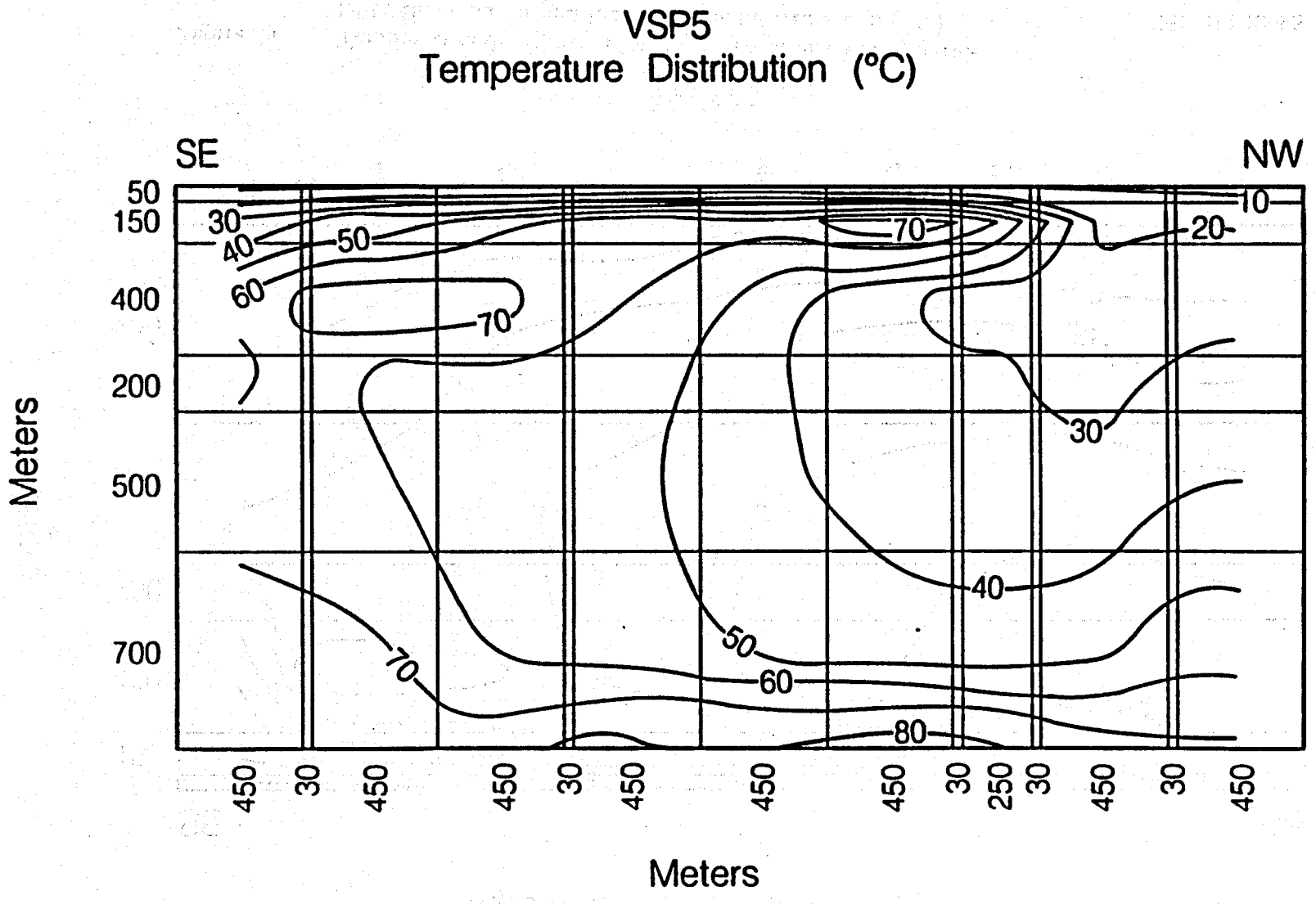

Figure 44. **Temperature distribution for vertical sections VSP5, parallel to the main normal fault. Temperatures are in (°C).**

XBL 874-10096

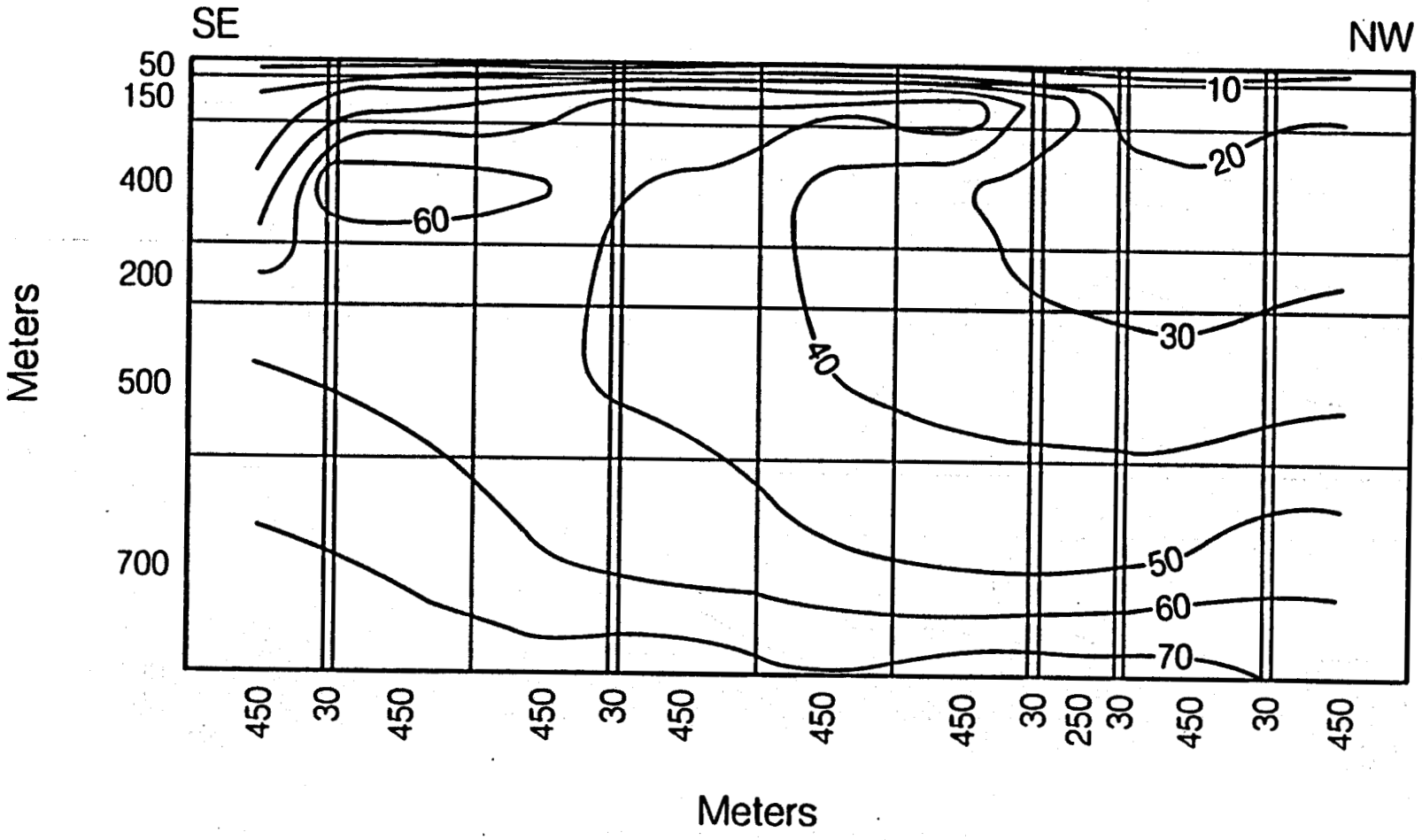

Figure 45. **Temperature distribution for vertical sections VSP6, parallel to the main normal fault. Temperatures are in (°C).**

XBL 874-10095

surface gradients seen in cross-sectional temperature profiles in Figure 14a, and also indicate that large temperature reversals probably exist at depth. Temperature profiles in areas of significant downflow or upflow, along the normal faults, might explain several of the isothermal temperature profiles measured in the hot well area.

The temperature contours in VS200 (Figure 46) show a significant temperature decrease in the second subsidiary normal fault caused by the downflow of cold water. High temperature, near surface gradients occur between the main normal fault and the second subsidiary normal fault. This seems to be reasonable in comparison to the cross-sectional temperature profiles perpendicular to the main normal fault (Figures 14b and 14c). Temperature profile reversals are noticeable near the first subsidiary normal fault. Near the second subsidiary normal fault, the temperature contours are more vertical caused by cold water downflow. In this particular section (VS200) the main normal fault is actually subdued by the influx of cold regional grounwaters from the Northwestern Boundary.

In general, overall temperatures increase in each vertical section towards the Southeastern Boundary. In VS500 and VS900 (Figures 47 and 48), a zone of higher temperatures is seen near the main normal fault and the first subsidiary normal fault. These two vertical sections represent cross-faults 4 and 7 in Figure 15 and supply a substantial quantity of the hot water recharge into the system. This is a result of the high permeabilities assigned to the intersections of these cross-faults and the normal faults. Their permeabilities range from 9.0×10^{-13} to 1.0×10^{-12} m^2. It is interesting to note that the temperature contours in VS900 are almost all vertical and might also help to explain some of the hotter isothermal temperature profiles found in the immediate area. The temperature distribution in VS600 (Figure 49) represents the typical temperature distribution found throughout the system and shows very noticeable temperature reversals. In VS1300 (Figure 50), temperatures are noticeably reduced as a result of the cold water recharge from the east, and because the faults do not supply hot water recharge at this particular section.

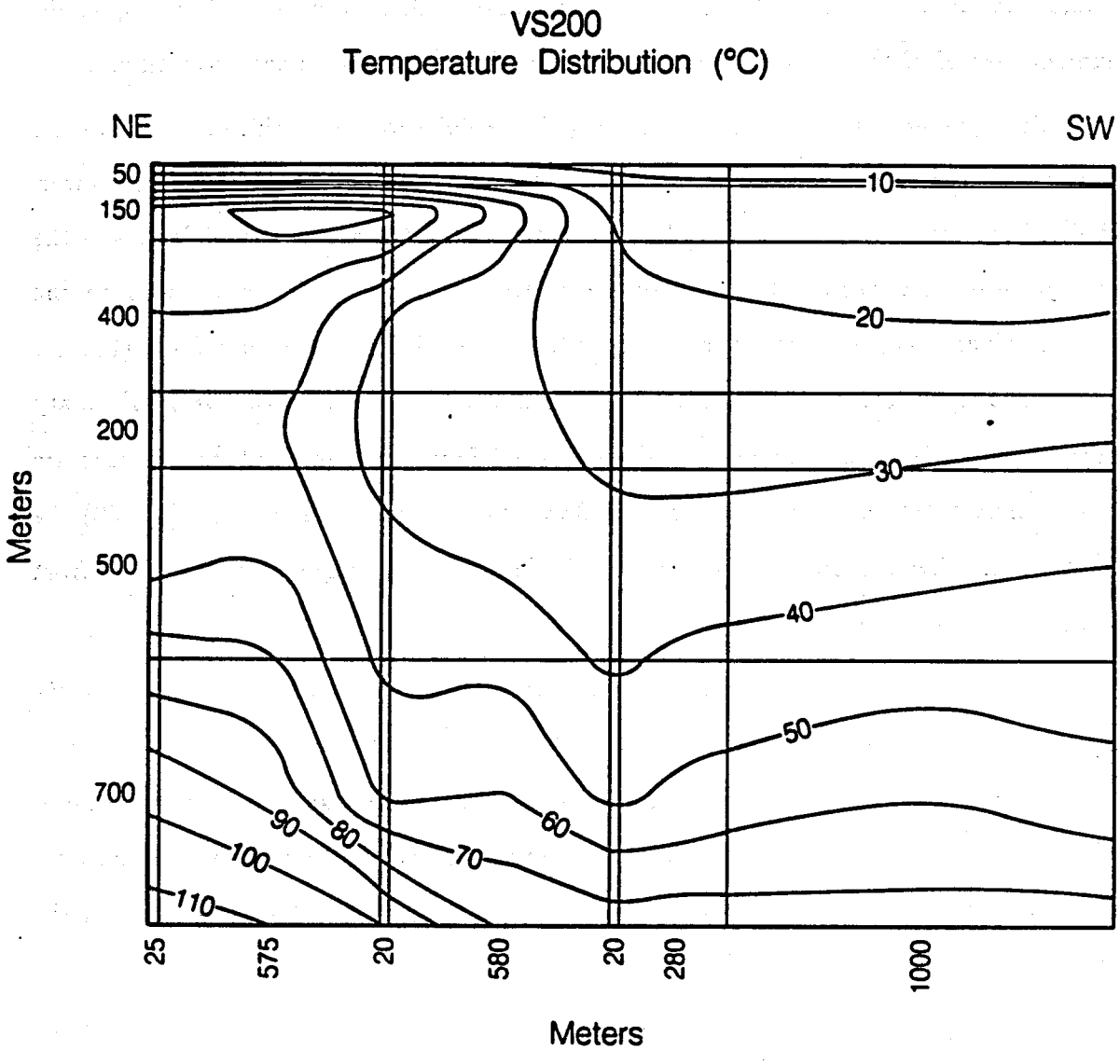

Figure 46. Temperature distribution for vertical section, VS200, perpendicular to the main normal fault. Temperatures are in (°C).

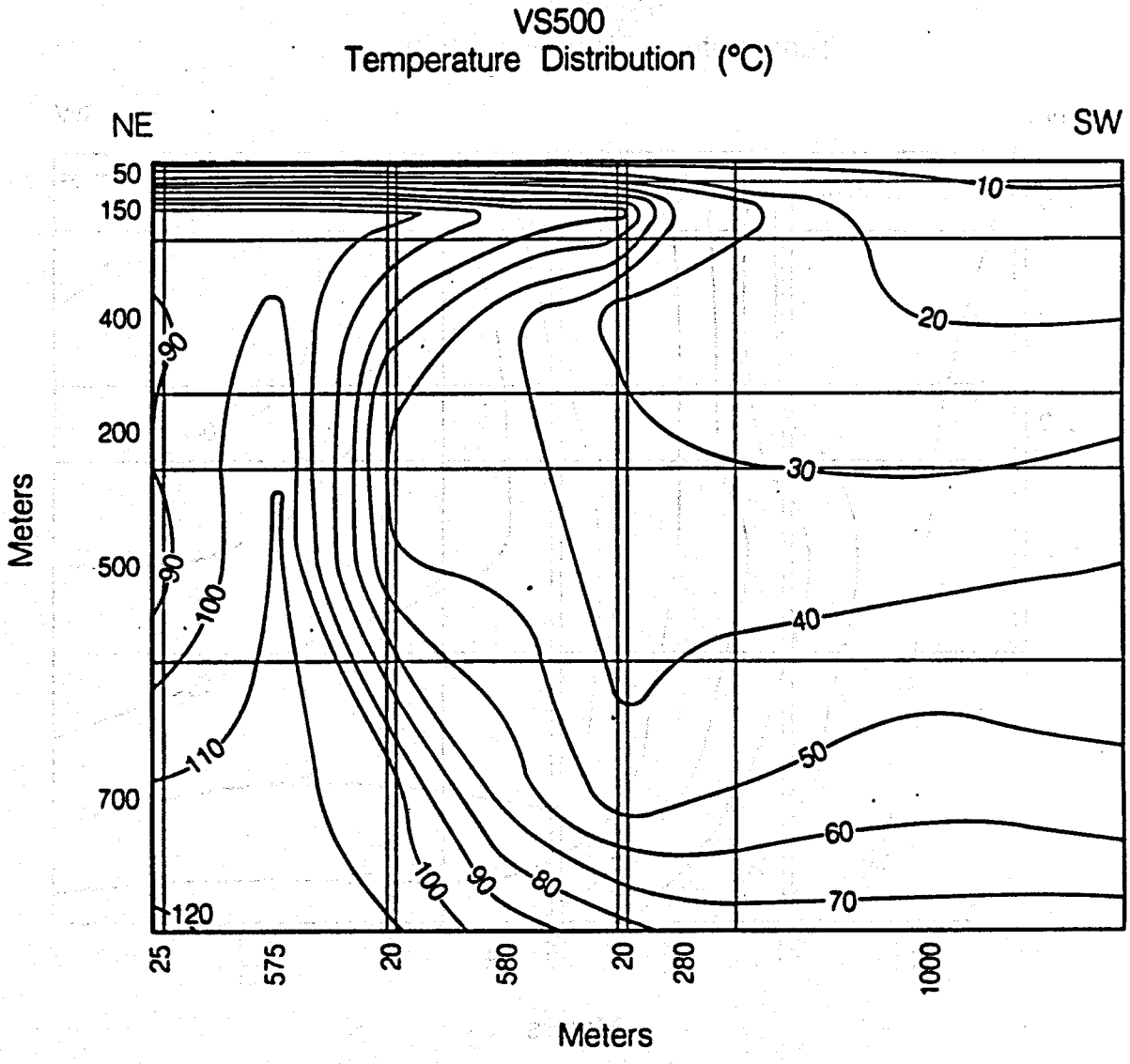

Figure 47. Temperature distribution for vertical section, VS500, perpendicular to the main normal fault. Temperatures are in (° C).

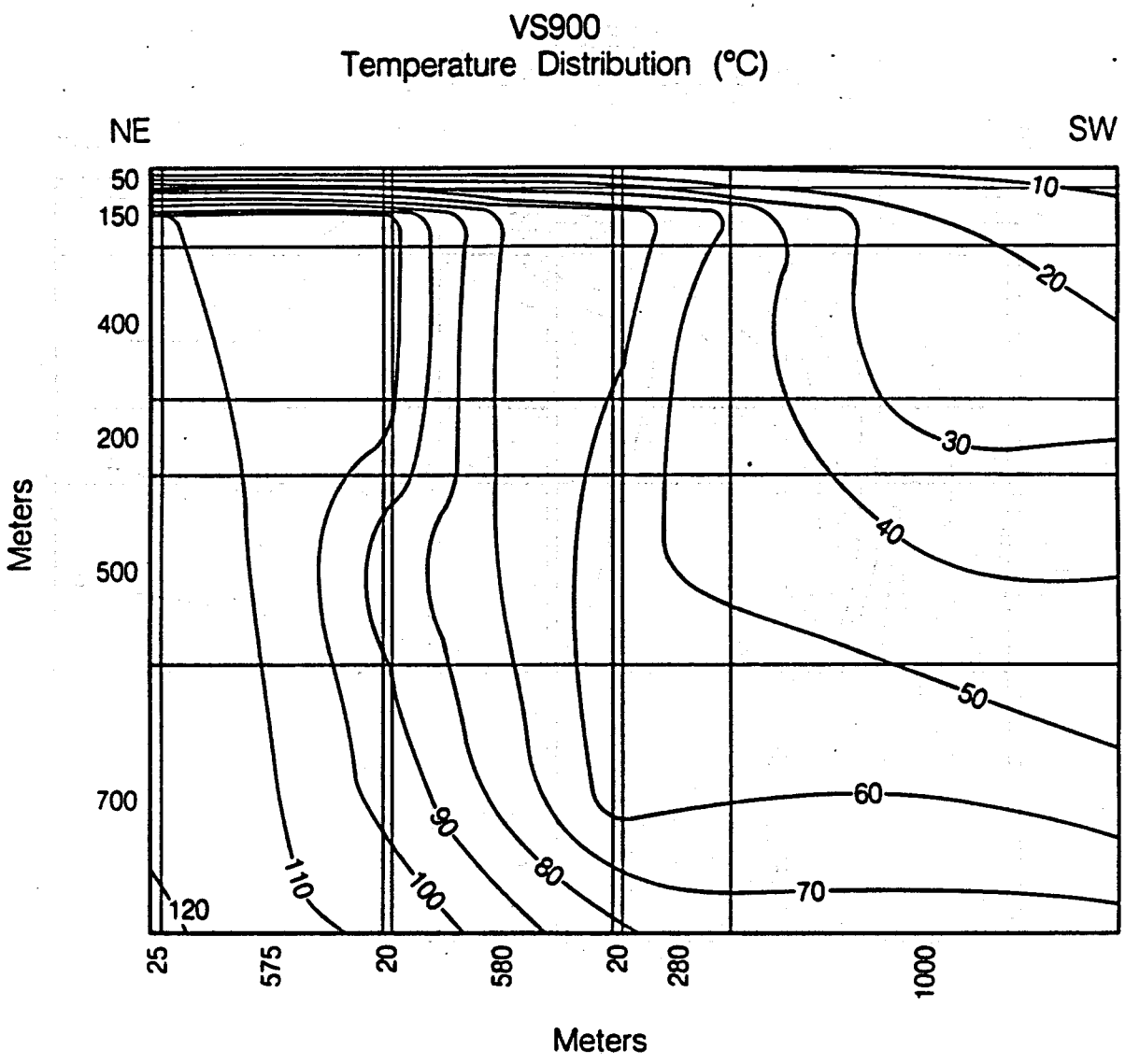

Figure 48. Temperature distribution for vertical section, VS900, perpendicular to the main normal fault. Temperatures are in (° C).

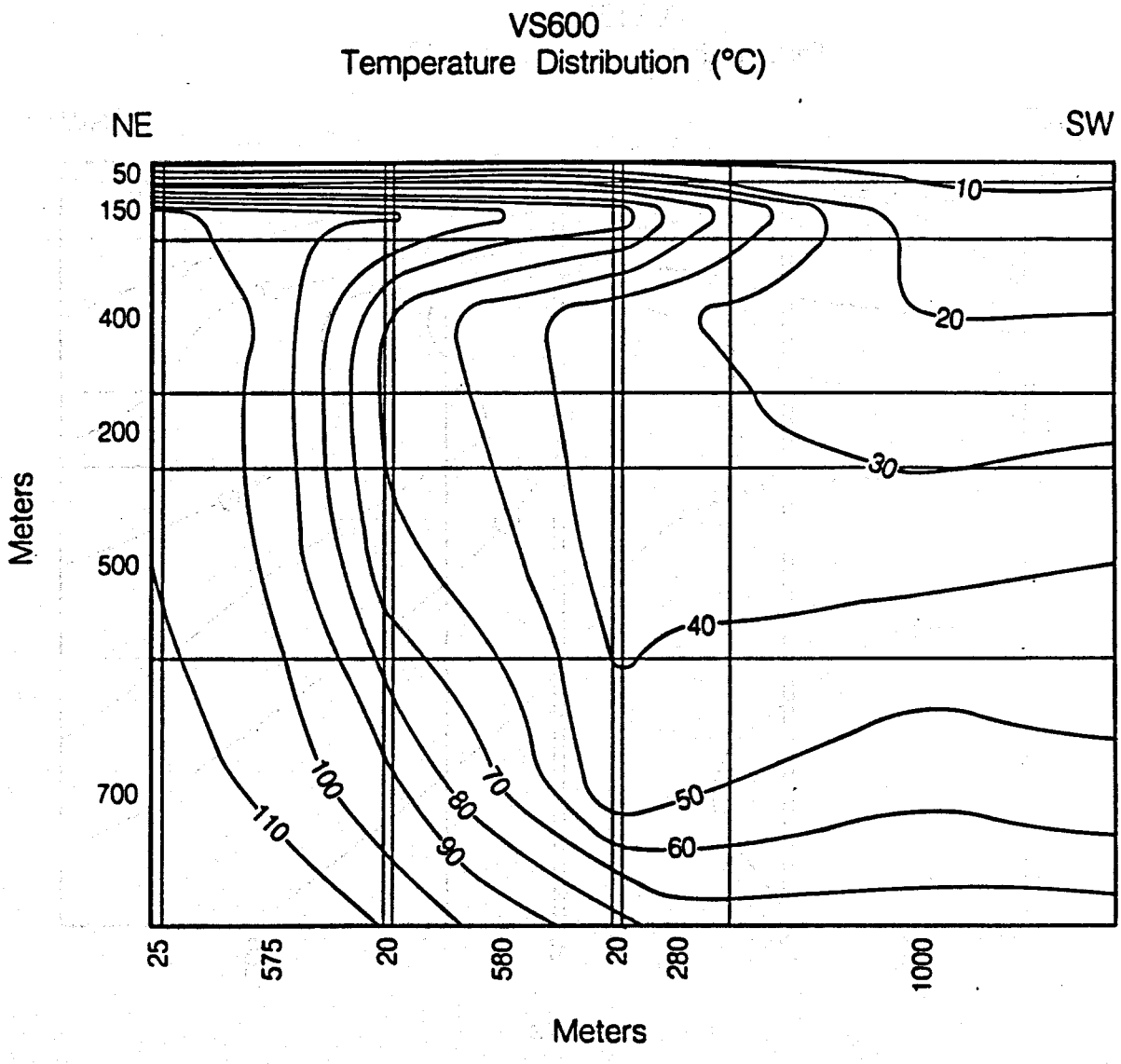

Figure 49. Temperature distribution for vertical section, VS600, perpendicular to the main normal fault. Temperatures are in (°C).

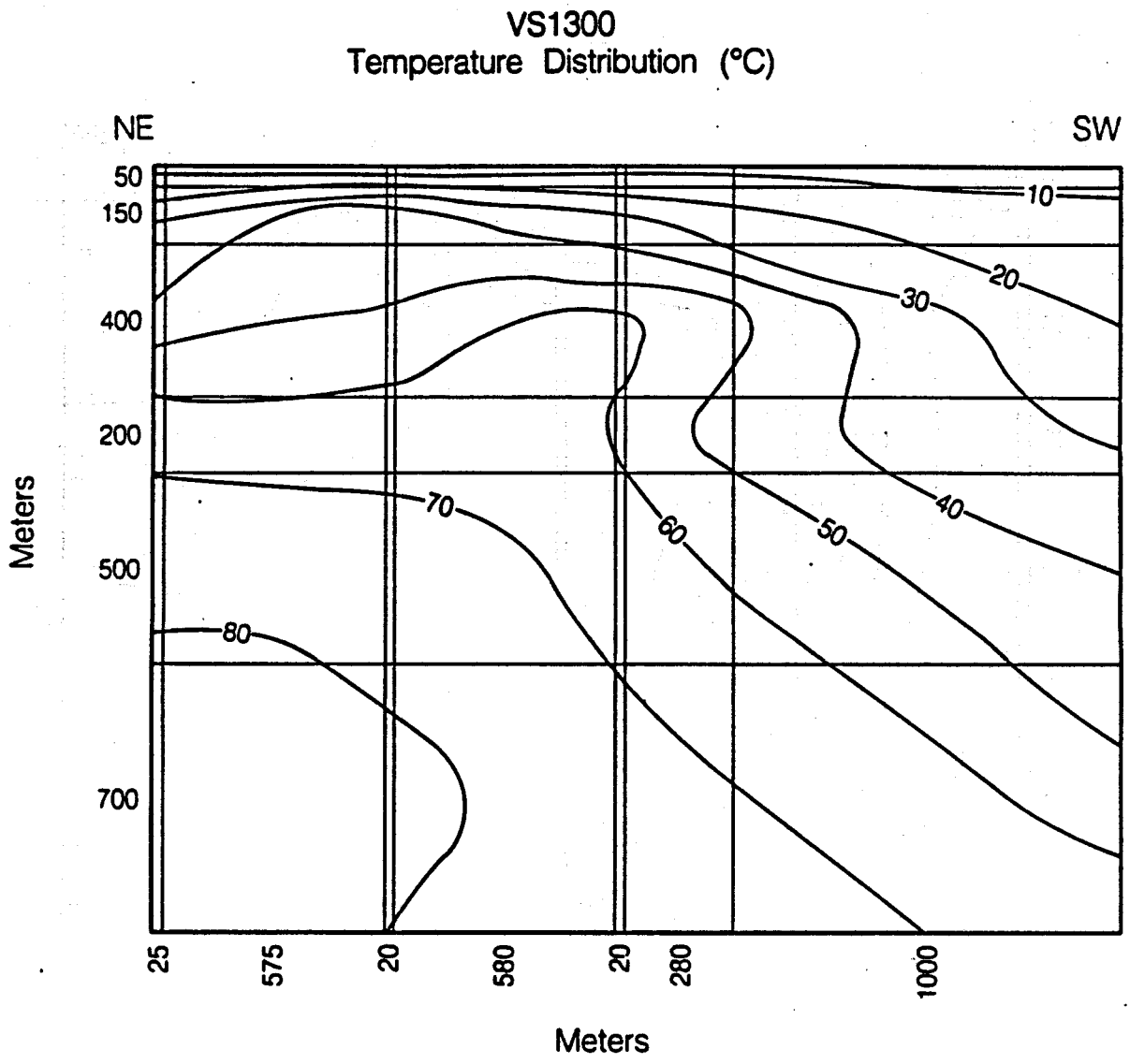

Figure 50. Temperature distribution for vertical section, VS1300, perpendicular to the main normal fault. Temperatures are in (°C).

5.5.2 Heat and Mass Recharge estimates

Mass flux plots are shown for horizontal sections at depths of 125 and 400 meters, corresponding to sections HZ33 and HZ25. Flux plots are also shown for vertical sections VS600, VS500 and VS900 perpendicular to the main normal fault. The sections VS500 and VS900 represent areas near the intersection of the normal fault and cross-faults 4 and 7 (Figure 15), and vertical cross-sections parallel to the main normal fault, VSP1 and VSP5. One horizontal heat flux plot is shown for the horizontal section, HZ33, at a 125 meter depth. Maximum flux values in the x and the y directions are shown for all of these plots.

Vertical cross-section VSP1 (Figure 51), representing the main normal fault, shows the major zones of hot water recharge occur along the intersections of cross-faults described by sections 500 and 900. Only a relatively small fraction of the hot water flows along the main normal fault from north to the south. The y-axis flux in VSP1 is twice as large as in the second subsidiary normal fault section, VSP5 (Figure 52). VSP5, however, indicates a larger fraction (2 times VSP1) of the flow directed along the x-axis. This is due to the flow of cold water from the Northwestern Boundary towards the Southeastern Boundary, along this permeable fault. The downflow along the second subsidiary normal fault is controlled by the permeability or the Bottom Boundary pressures. A certain amount of cold water must mix with the hot water discharge at the second subsidiary normal fault to produce the rapid temperature declines shown in Figures 16a and 16b.

Downflow along the second subsidiary normal fault is better illustrated in the vertical sections perpendicular to the main normal fault. VS600, in Figure 53, is representative of most of the flow patterns in sections along the main normal fault, and indicates a lateral flow of hot waters from the main normal fault, through the upper aquifer where it intersects the second subsidiary normal fault and begins to flow downward. In the northern part of the study area, more downflow is experienced along the second subsidiary normal fault than in the southern area. Some of this downflow flows laterally, towards the Southeastern Boundary as indicated by the

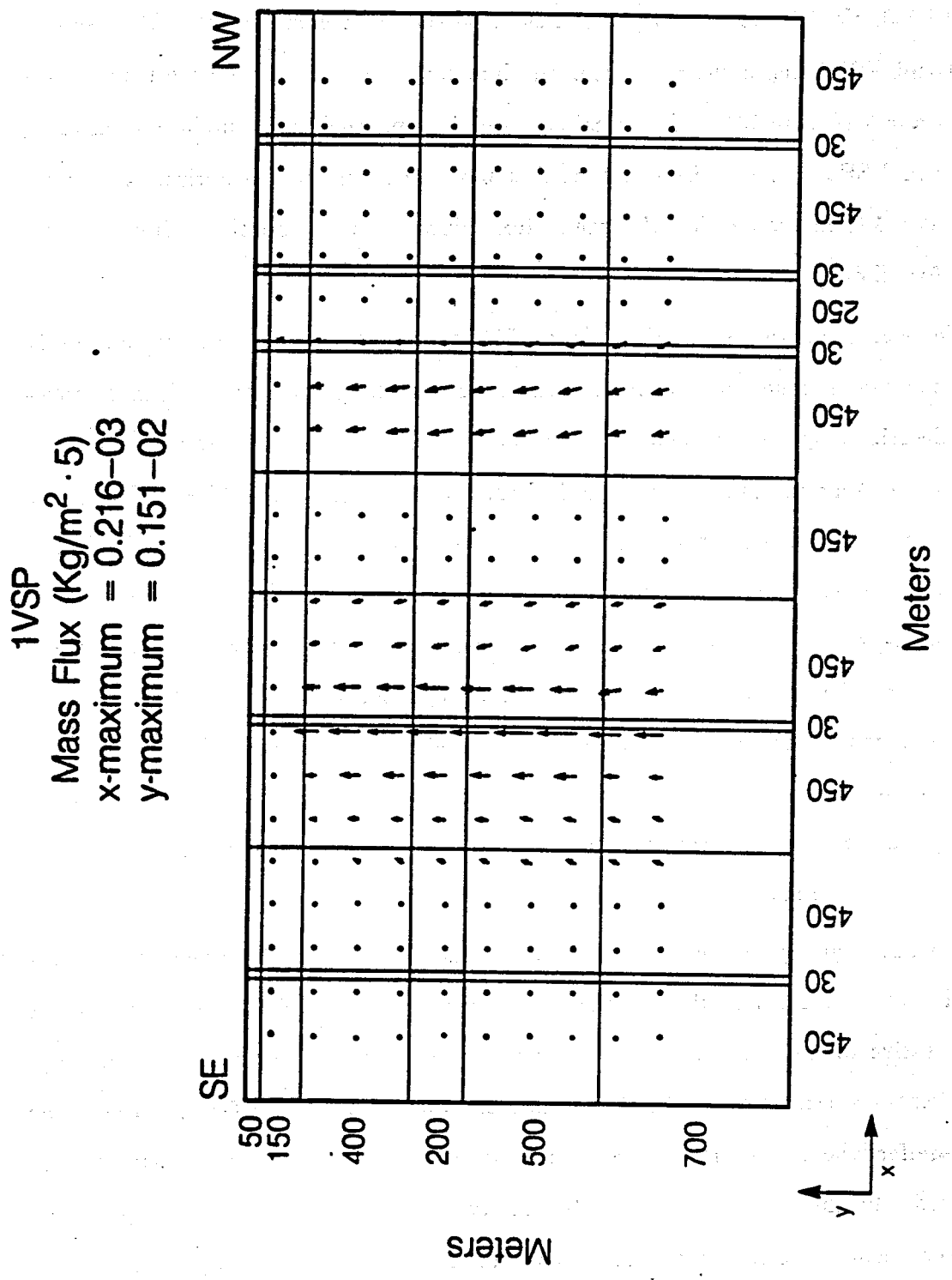

Figure 51. Mass flux plots for vertical section, VSP1, parallel to main normal fault. Mass flux is in (kg/m^2·s).

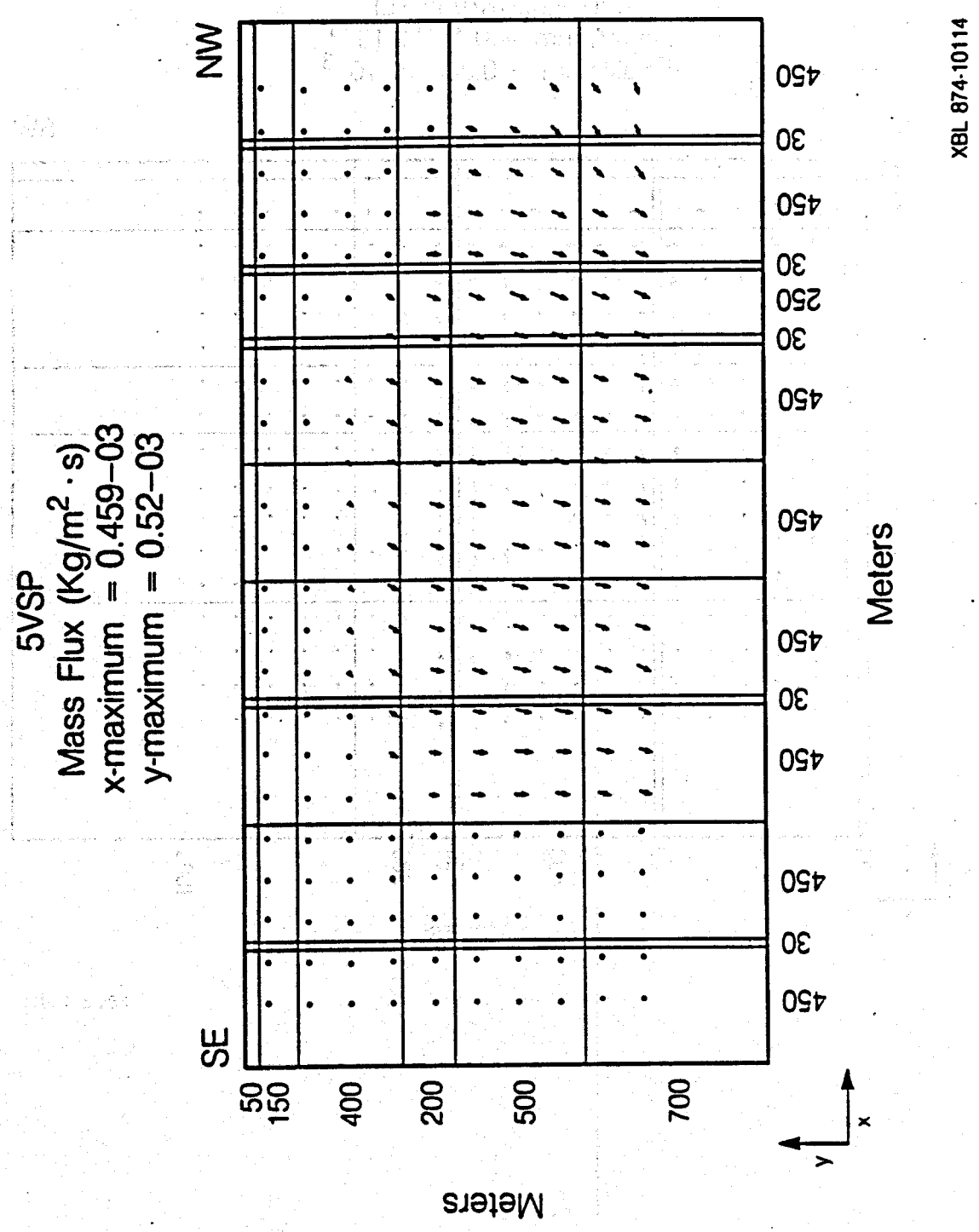

Figure 52. Mass flux plots for vertical section, VSP5, parallel to main normal fault. Mass flux is in (kg/m^2·s).

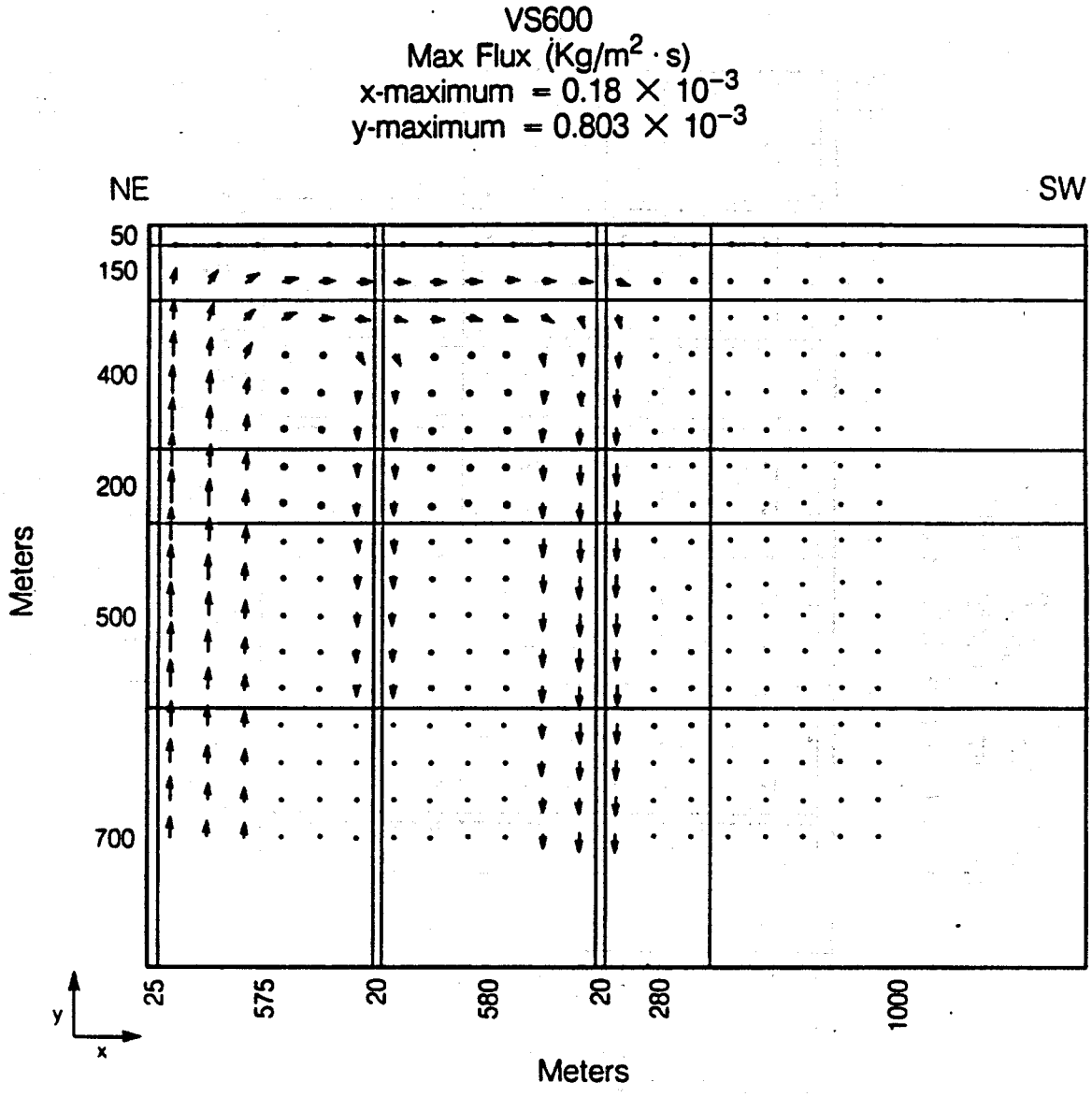

Figure 53. Mass flux plots for vertical section, VS600, perpendicular to main normal fault. Mass flux is in (kg/m^2·s).

direction of the flux vectors in Figure 53. VS600 shows only a small fraction of the recharge from the main normal fault flowing down the first subsidiary normal fault and a larger amount flowing down the second susidiary normal fault.

The first subsidiary normal fault, in general, does not significantly affect the flow pattern. It might have played a more dominant role in governing the flows if the Bottom Boundary pressures were increased or decreased in comparison to the main normal faults. However, this would cause the first subsidiary normal fault to be the primary zone of recharge or a main zone of discharge. This does not appear possible according to the field data.

Vertical sections VS500 and VS900 (Figures 54 and 55) show major upflow associated with the intersections of the two main cross-faults (4 and 7 in Figure 15) and the main normal fault. These sections provide the majority of the heat and mass flow into the system. Considerable flow occurs along each of these two cross-faults. Only small downflows are seen in the second subsidiary normal fault for these two vertical sections. From vertical sections 1-900, the primary hot water discharge is along the second subsidary normal fault, while discharge, in sections 1000-1300, is primarily towards the Southeastern and Southwestern Boundaries.

The mass fluxes in Figure 56, for the horizontal section HZ33, represent fluid flows at a depth of 125 meters. At this depth, the temperatures and pressures are known (from borehole data) and were compared to the calculated distributions in Figures (39a and 39b). Thermal waters flow in the aquifer away from the main normal fault and the two main recharge cross-faults (4 and 7, Figure 15). The mass fluxes are notably reduced after they reach the second subsidiary normal fault and begin to flow toward the south. Cold regional waters mix with the hot water discharge at the second subsidiary normal fault, resulting in both downflow and lateral flow towards the Southeastern Boundary. Cold waters from the southern end of the Fault Boundary force hot water discharge from the main normal fault (flowing towards the southeast), to flow towards the southwest.

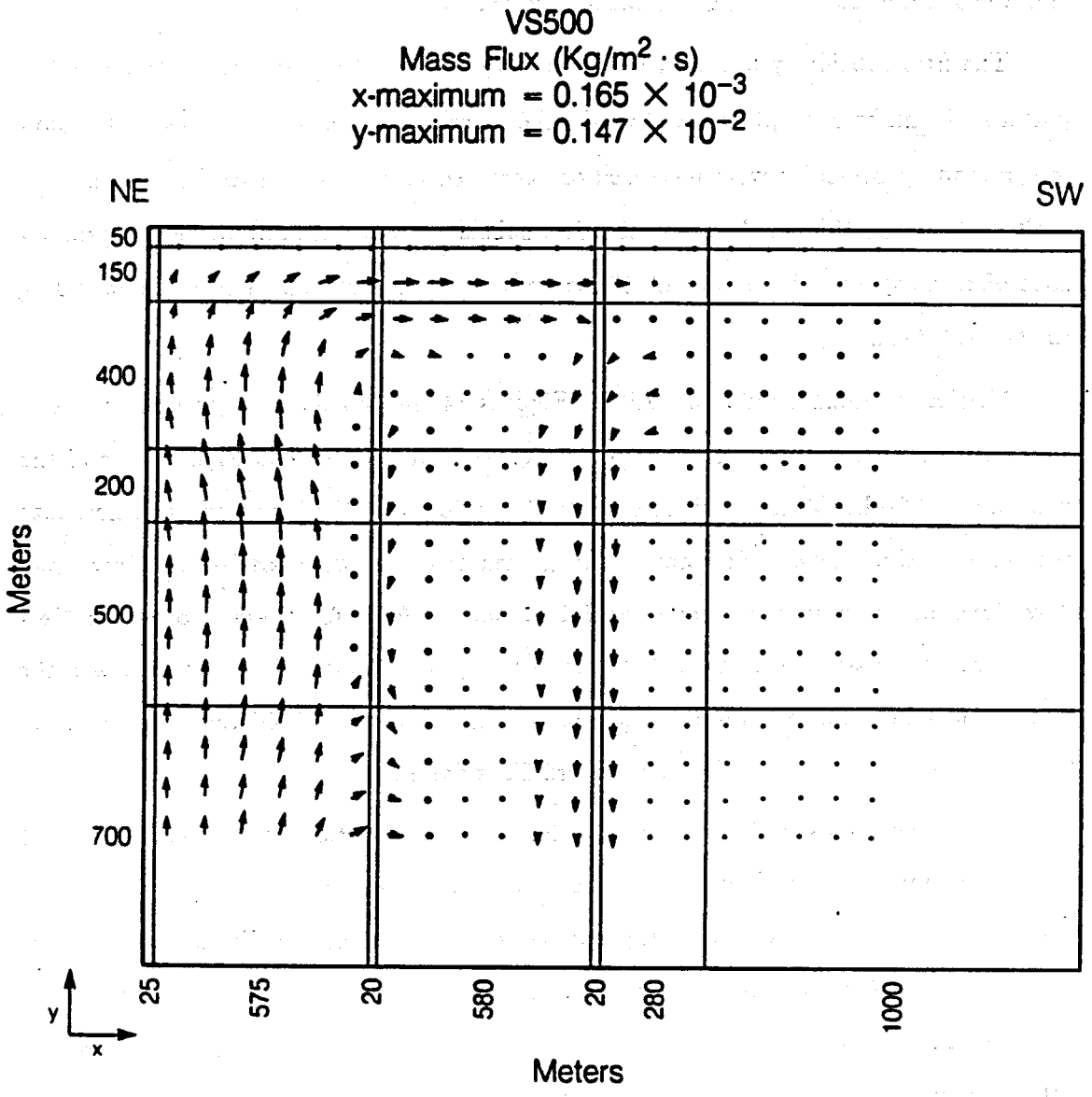

Figure 54. Mass flux plots for vertical section, VS500, perpendicular to main normal fault. Mass flux is in (kg/m^2·s).

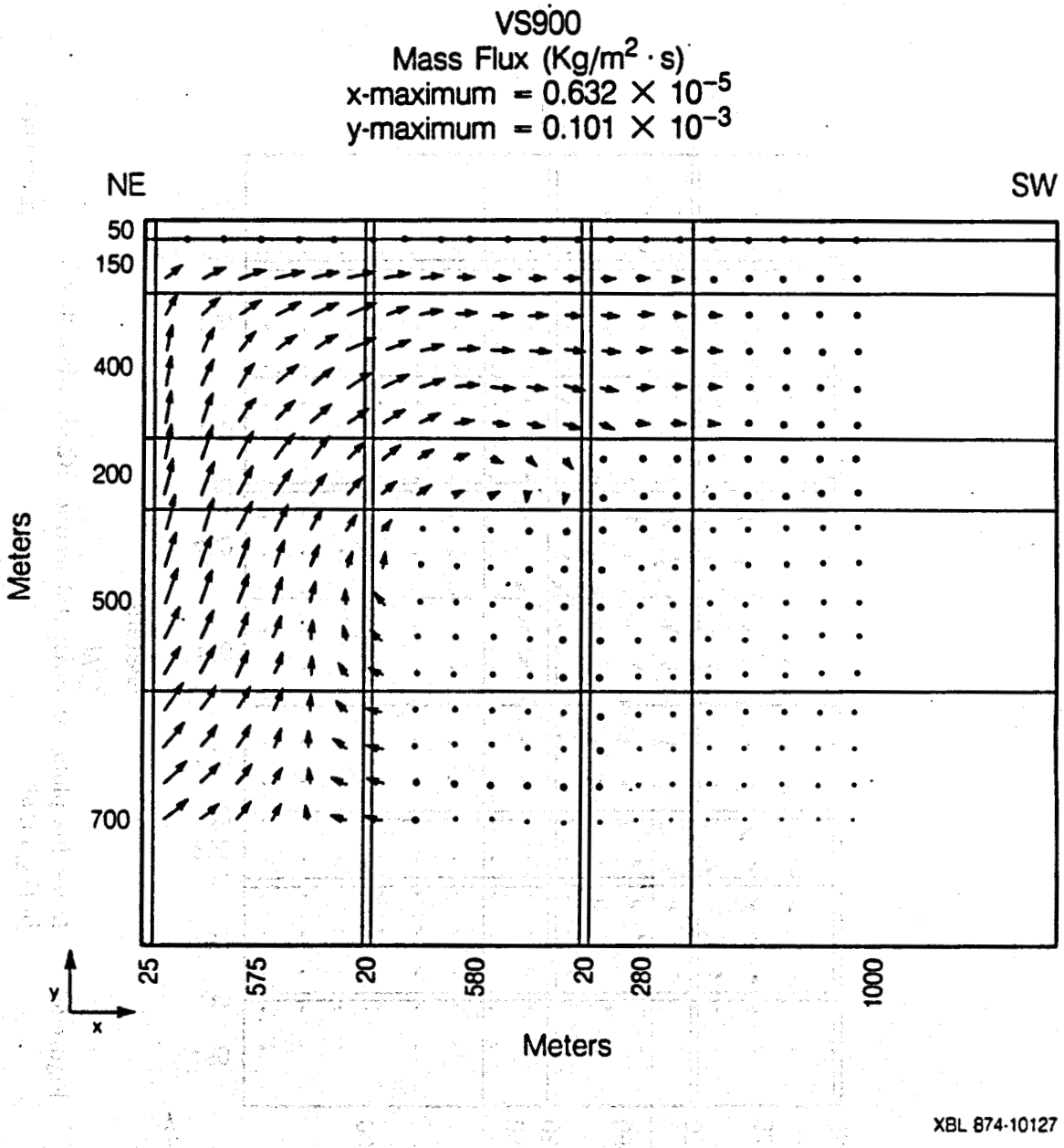

Figure 55. Mass flux plots for vertical section, VS900, perpendicular to main normal fault. Mass flux is in (kg/m^2·s).

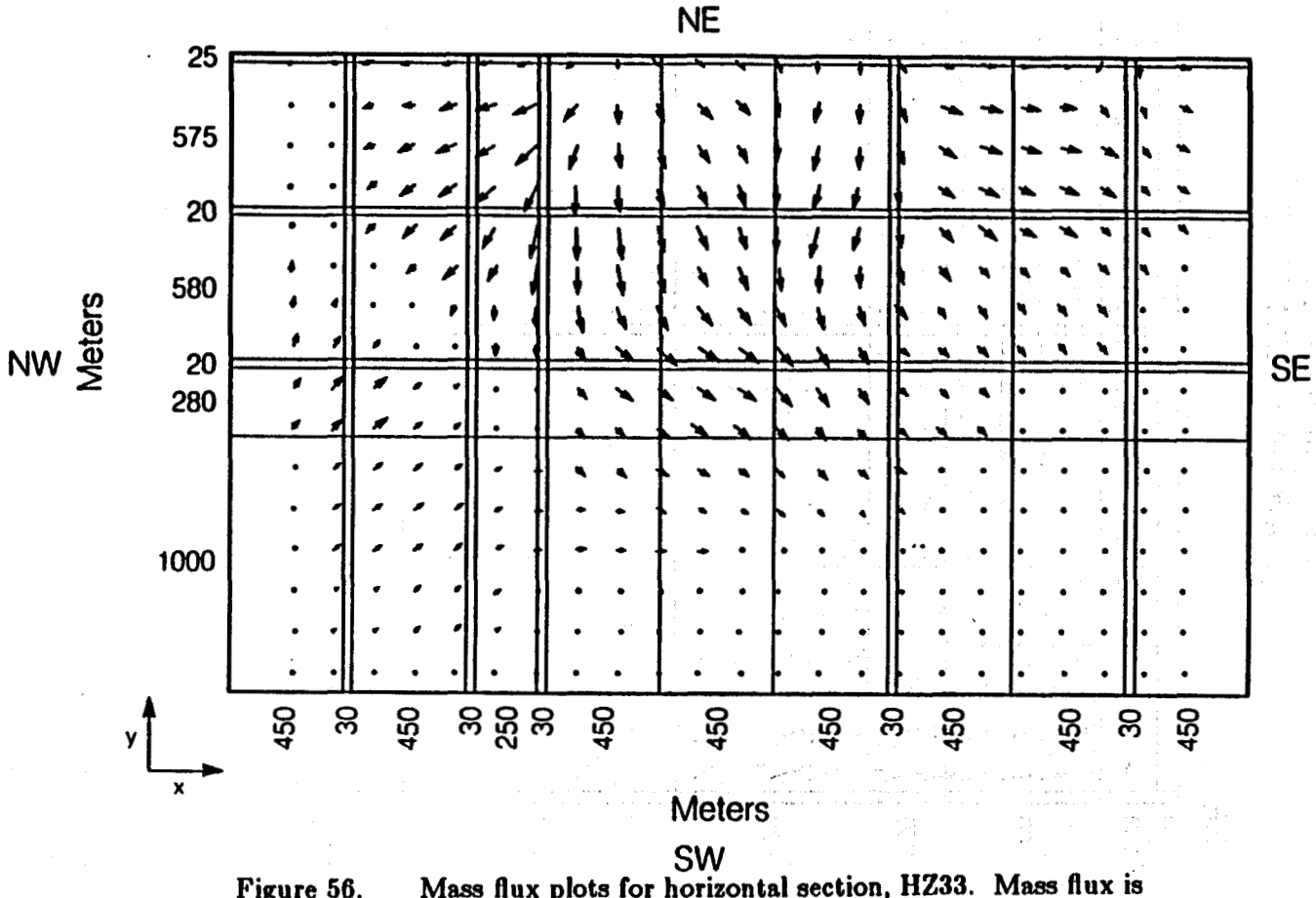

Figure 56. Mass flux plots for horizontal section, HZ33. Mass flux is in (kg/m^2·s).

3L 874-10109

In HZ25 (Figure 57), a significant quantity of water flows toward the western portion of the Southeastern Boundary and is responsible for the temperature and pressure distributions shown in Figures 40a and 40b. The Northwestern Boundary supplies the cold water recharge flowing down the center of the graben towards the Southeastern Boundary. The southern portion of the Fault boundary also supplies colder waters at this depth, towards the southwest. This large flux of cold water effectively controls the areal extent of the thermal front from the main normal fault. A significant flux of warm waters (mixed cold and thermal waters) is discharged into the southern part of the Southwestern Boundary (Lake Ewauna area).

Only one heat flux plot is shown for HZ33 (Figure 58), because the orientations of the heat flux vectors are very similar to the mass flux plots. The hot well area is dominated by convective heat flow, therefore the points of maximum heat flux correlate to the points of maximum mass flux.

The total mass and heat flow through each boundary are given in Tables 7 and 8.

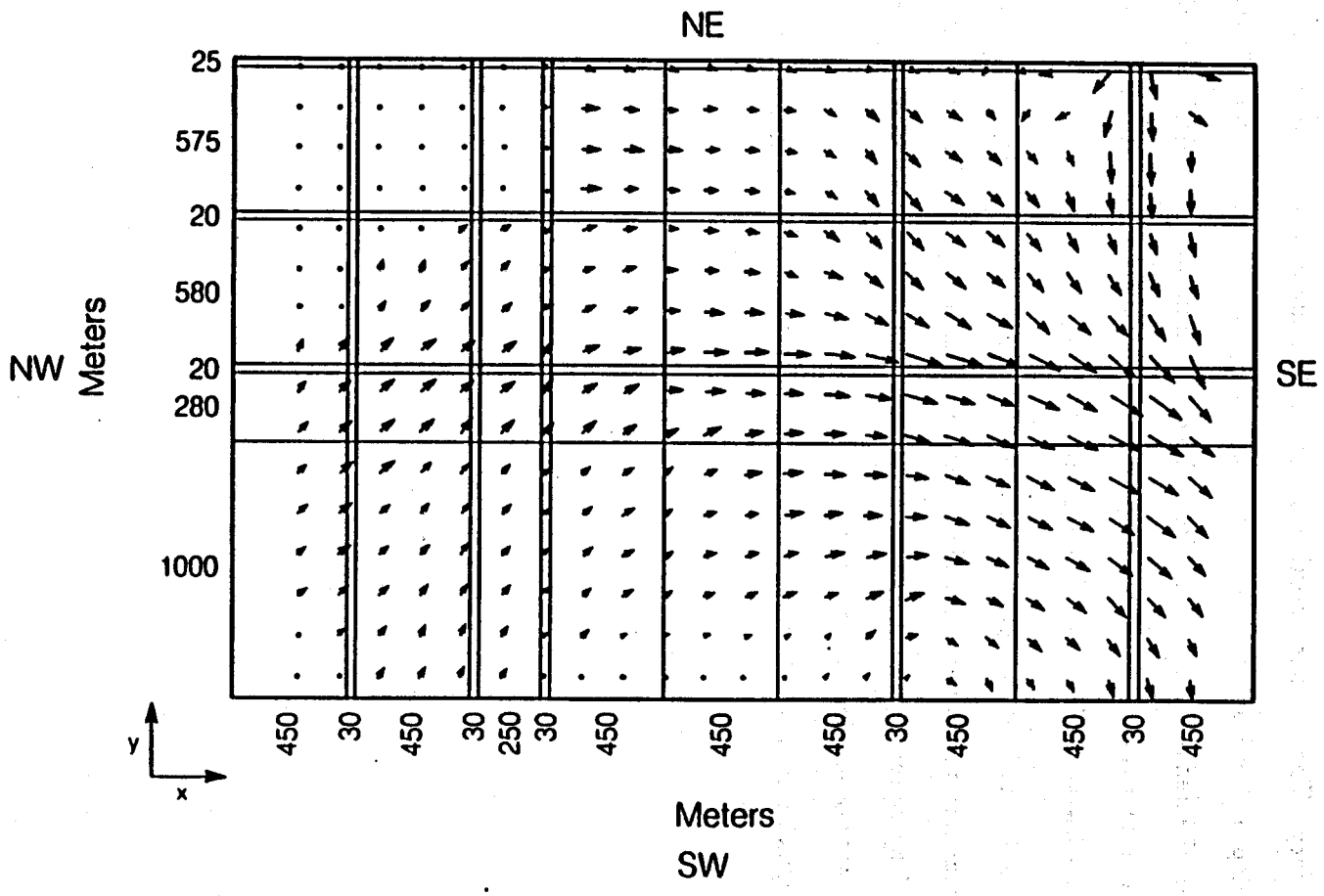

Figure 57. Mass flux plots for horizontal section, HZ25. Mass flux is in (kg/m^2·s). XBL 874-10111

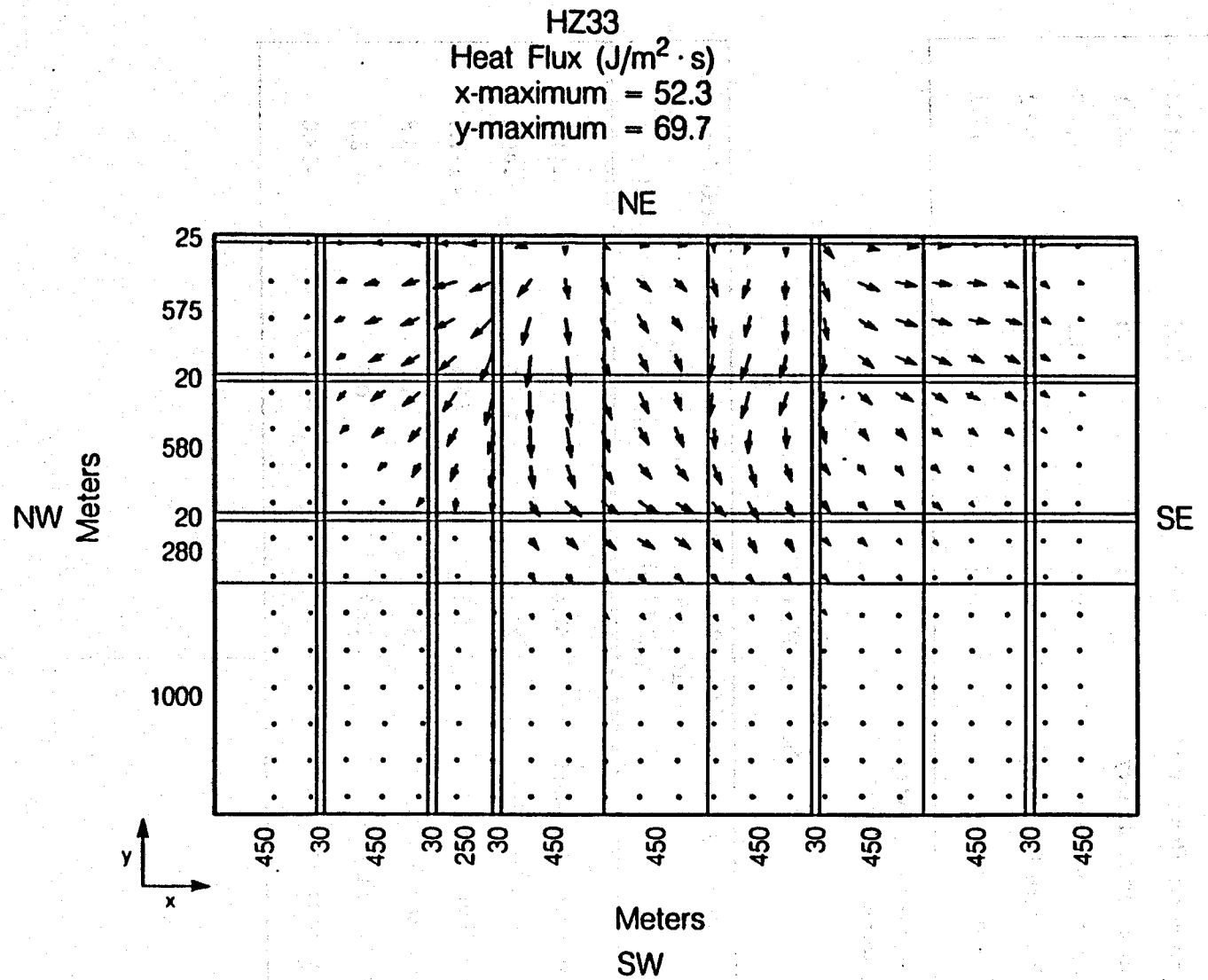

Figure 58. Heat flux plots for horizontal section, HZ33. Heat flux is in (J/m^2·s). XBL 874-10110

Table 7. Boundary mass flow rates

Boundary	Mass flow rate into system $\dot{m}_{in}$ (kg/s)	Mass flow rate out system $\dot{m}_{out}$ (kg/s)	Total flow rate (kg/s)
Northwestern Boundary*	41.6	23.3	+18.3
Southeastern Boundary*	43.1	90.2	-47.1
Bottom Boundary**	35.9	24.1	+11.8
Southwestern Boundary*	30.4	20.6	+9.2
Fault Boundary*	7.8	0.0	+7.8

* cold water ≈ 15-30 °C
** hot water ≈ 120 °C

Table 8. Boundary heat flow rates

Boundary	Heat flow rate into system $\dot{q}_{into}$ (J/s)	Heat flow rate out system $\dot{q}_{out}$ (J/s)	Total flow rate (J/s)
Northwestern Boundary	57.4	40.2	+17.2
Southeastern Boundary	72.2	171.5	-99.3
Bottom Boundary	176.5	59.1	+117.4
Southwestern Boundary	35.0	31.2	+3.8
Fault Boundary	13.9	0.0	+13.9
Atmospheric Boundary	0.0	53.0	-53.0

The total heat and mass flows into and out of the system, through each boundary, are indicated by the + and - signs, respectively. The main cold water recharge sources are from the Northwestern, the Southwestern Boundary and from part of the Southeastern Boundaries. The southern end of the Fault Boundary also supplies some cold water recharge to the system ($\approx$ 1/5 that of the other cold water recharge boundaries). Although the Southeastern Boundary indicates the highest cold water flow rates into the system, it also represents the major discharge zone for the geothermal system. The flow of cold waters at this boundary occur near the surface, while the warmer waters (mixed cold and thermal water discharge) exit the system through deeper sediments. The discharge of water across this boundary is twice the recharge which indicates a net discharge of water from the system. This net discharge (-47.1 kg/s) equals the sum total net flow rates from all of the other boundaries.

The Bottom Boundary is the primary source of hot water recharge to the system ($\approx$ 120°C). The discharge from the system to the Bottom Boundary occurs through the second subsidiary normal fault. This discharge is a mixture of hot water from the main normal fault and cold recharge from the Northwestern Boundary, and is about one third less than the hot water recharge into the system. The quantity of cold water flowing through the study area is approximately 3 times that of the hot water.

The principal source of heat convected into the system is through the Bottom Boundary from the main normal fault elements. Almost a third of the heat convected into the system from the Bottom Boundary is recirculated to depth along the second subsidiary normal fault as shown in Table 8. The heat supplied by other boundaries is relatively small in comparison to the quantity of heat supplied by the Bottom Boundary. Most of the heat lost by the system is through the Southeastern Boundary and the Atmospheric Boundary and through the second subsidiary normal fault elements in the Bottom Boundary.

5.5.3 Sensitivity Study

The relative sensitivity of the calculated hot water recharge rates to the imposed boundary conditions and permeabilities can be examined in several ways. The degree to which the boundary conditions and reservoir parameters affect the hot water recharge rates is one way to show the accuracy of the final three-dimensional numerical model. The relative sensitivity of the hot water recharge rate can be investigated by increasing or decreasing the Bottom Boundary pressures at various increments. The permeabilities for the upper central graben sediments control the effective flow of cold waters into the system and can also be used to study the sensitivity of the hot water recharge rate. The permeabilities can also be increased or decreased at various increments. If only small changes in these parameters are necessary to noticeably change the hot water recharge rate estimates, a higher degree of uniqueness is suggested for the numerical model.

Table 9 shows several cases used in this study to determine the sensitivities of the hot water recharge rates to the boundary conditions and the permeabilities. Since the Bottom Boundary supplies the major source of hot water recharge to the system, the flow rates shown in Table 9 reflect only this Boundary.

Table 9. Sensitivity Simulations

Parameter Varied	Mass flow rate into system $\dot{m}_{in}$ (kg/s)	Mass flow rate out system $\dot{m}_{out}$ (kg/s)	Total flow rate (kg/s)
Bottom pressure increase of 5 bars	108.4	21.8	+86.6
Bottom pressure increase of 1 bar	58.3	21.8	36.5
Decrease in Cold recharge permeability ($k=1.65 \times 10^{-13}$ m^2)	39.2	22.0	+17.2
Increase in Cold recharge permeability ($k=4.30 \times 10^{-13}$ m^2)	33.5	24.2	+9.3
Bottom pressure decrease of 1 bar	25.3	33.0	-7.7

It should be noted that pressures are changed only in the Bottom Boundary main normal fault elements because they control the system's internal pressures. The 5 bar increase in these main normal fault elements notably affect the hot water recharge for the system. They are increased by almost three times the original estimated value. This pressure increase however also results in a much greater flux of heat into the system causing temperatures and pressures to greatly increase. Increasing this Bottom Boundary pressure by 1 bar appears to increase the hot water recharge by $\approx$50%, while lowering it by 1 bar decreases the hot water recharge by $\approx$25%. The pressure increase by the 1 bar increase only moderately effects the temperature and pressure distributions. The 1 bar decrease in pressure, however, reduces the temperatures within the hot well significantly.

Decreasing or increasing the permeability of the upper sediments that control the cold water influx by the amount shown in Table 9, does not appear to affect the hot water recharge significantly. If, however, the permeabilities of the upper sediments are doubled, significant downflow occurs within the main normal fault. This does not

seem possible because it has not been observed in the field. Doubling these permeabilities would make the upper sediments in the central graben area more permeable than the aquifer in the hot well area, which also seems unlikely. The recharge rates therefore seem to be well constrained as far as the permeabilities are concerned.

Based on the hot water recharge sensitivities to the Bottom Boundary pressures, the recharge rates might be up to 25% greater than those shown in Table 7 (Bottom Boundary). Because of the significant changes in the temperature distribution caused by lowering the Bottom Boundary pressures by 1 bar, the recharge rates are probably not much lower than indicated in Table 7.

In a final crude simulation, 600 gal/min of hot water is produced from the hot well area to further demonstrate the reliability of the present three-dimensional numerical model. An actual estimate of the quantity of hot water being produced from the entire geothermal system is approximately 540 gal/min from 70 wells (Sammel, 1984). In the simulation, hot water is produced from elements 534, 634, 734, 834, 934 and 1034 (which can be seen by using Figures 26 and 27). These elements are found in the horizontal layer HZ33.

Results from the simulation indicated a steady state hydralic head drop in the hot well area of approximately 4.5 meters. This drop occurs within 100 to 120 days. Temperatures within the hot well area are reduced by approximately 10°C. Hot water recharge rates of 33.8 kg/s, and discharge rates of 25.0 kg/s were calculated which do not appear to change significantly. The seasonal water level changes in the aquifer are approximately 2-3 meters and are directly related to the production of thermal waters. However, as described before, the degree to which the production in the geothermal system affects this water variation in water levels has not been determined as of yet.

In any event, these results, although somewhat crude, seem to correlate well with the observed overall decline of the water levels in the area which suggests that the present 3-dimensional numerical model is reasonably reliable.

Summary and Conclusions

Based on the results from the three-dimensional numerical simulations, the proposed three-dimensional conceptual model appears to represent the Klamath Falls geothermal system reasonably well. The conceptual model includes all the major characteristics of the system. Upflow occurs along the main normal fault and is constrained the north and the south by bounding cross-faults (2 and 9, Figure 15). The hot waters intersect near surface permeable strata where they begin to flow towards the southwest until they reach the second subsidiary normal fault. At this point both downflow and lateral flow occur along this second subsidiary normal fault. Less downflow occurs along the first subsidiary normal fault because, it is associated more with the type of upflow observed in the main normal fault. The primary zone of discharge from the study area is through the western portion of the Southeastern Boundary and the southern part of the Southwestern Boundary (Figure 9).

Within the hot well area, thermal waters flow laterally through the main normal faults, most likely towards south. A considerable amount of hot water recharge is added to the system from the two principal cross-faults (4 and 7, Figure 15) and their intersections with the main normal fault. Once this hot water recharge has intersected the near surface permeable strata, it flows laterally, away from the cross-fault, in all directions.

Cold water recharge from the north flows down the center of the graben and cools the thermal discharge from the permeable aquifer. Most of this cooling takes place near the second subsidiary normal fault. Cold waters also mix with the thermal discharge at the southern end of the anomaly, near the main normal fault, and are derived from the hills immediately to the east. The model may respond slightly differently if the cold seasonal discharge from canal was considered.

From interpretations of the geochemical data, it was determined that the cold water recharge from the Northwestern Boundary was probably not derived from the nearby Upper Klamath Lake. This interpretation was based on the quantity tritium found in both the lake and the colder waters within the geothermal system. The

tritium in the Upper Klamath Lake is noticeably higher (bomb tritium water) at 25.7 TU whereas the cold end-member water is calculated to be 2.0 TU. If the maximum flow rates for the cold water recharge are used (0.3 - 20.0 m/year), the cold water would have only travelled about 1 kilometer into the system from the Northwestern Boundary, after 50 years (before advent of thermonuclear devices in atmosphere, 1953). This seems to imply that the cold water derived from the Northwestern Boundary (that mixes with the thermal waters), would be low in tritium near the hot well area, because the tritium rich waters (from the Upper Klamath Lake) would not have reached this point before the measurements were taken. It therefore, seems reasonable that significant cold water recharge from the Northwestern Boundary is derived from the Upper Klamath Lake. The hot water recharge into the system is only a point of speculation at present.

Several steps were necessary in performing a complete numerical analysis of the heat and mass transfer in the Klamath Falls, geothermal area. The first step required a re-evaluation of all current data collected to date, and the development of a 3-dimensional conceptual model which considered all of the fundamental dynamic and thermodynamic processes, and geohydrological characteristics associated with the geothermal system.

After an adequate conceptual model had been developed, quantitative estimates of the heat and mass recharge rates were calculated using a semi-analytic solution and a simple lumped parameter method. The major limitation in using the semi-analytic solution was that it neglected the spatial variation of heat and mass flows within the geothermal system. It did, however, offer reasonable, order of magnitude estimates for the heat and mass transfer in the system.

The next step was to develop a 3-dimensional numerical model capable of addressing the spatial variations of the heat and mass transfer within the system. Initially, several 2-dimensional models were used to determine the fundamental dynamics of the geothermal system and to develop a sufficiently discretized mesh arrangement to be used in the 3-dimensional model. Once a 3-dimensional mesh had been developed it

was possible to impose the boundary conditions and material properties and begin the numerical simulations.

Numerous simulations were performed using the final 3-dimensional mesh shown in Figure 27. Each run took approximately 20 minutes of CPU time at an average cost of 12.00 dollars. Costs add up quickly over time, because of the numerous simulations that are required to stabilize a complex system such as Klamath Falls.

The uniqueness of the solutions of the present 3-dimensional model are highly dependent on the boundary conditions imposed. The least known features of the geothermal system are the boundary conditions. The boundary conditions rely heavily on subsurface geological inferences. This is due to the lack of detailed borehole or geophyiscal data near the study area boundaries. The Northwestern, Southeastern and Bottom Boundaries required constant adjustments to equilibrate the system to the desired state. Initially, order of magnitude estimates for the temperatures and pressures were imposed at each boundary, however, this caused numerical instabilities to occur. Once semi-stable conditions were obtained, only small changes in the boundary conditions were needed.

After more stable boundary conditions were obtained, the permeabilities were allowed to vary for each new simulation. The basic geologic features (faults and bedding) acted as a basis for determining what values of permeabilities were assigned at each element. The permeability distribution, remained within a reasonable range for the system and was based on transmissivities obtained from several aquifer pump tests. From the transmissivities relatively high permeabilities were indicated for the aquifer, near the hotter areas. The aquifer permeabilities ranged from $1.0 - 9.0 \times 10^{-13}$ m/s, which is considered high for most geothermal systems. This might be explained by the high degree of faulting and fracturing within the geothermal area.

The numerical estimates for the mass recharge rates of hot water into the system per unit length of the main normal fault are compared to the results of the semi-analytic fault-charged solution and the lumped-parameter estimates and are shown in Table 9.

Table 9. Comparison of Mass Flow rates

Method used	Mass flow rate estimate (kg/m·s)
Semi-analytic solution	2.0×10^{-5} $m^3/m \cdot s$
Lumped parameter (heat conduction)	7.5×10^{-6} $m^3/m \cdot s$
Lumped parameter (Darcy velocity)	6.6×10^{-5} $m^3/m \cdot s$
Numerical solution	2.04×10^{-5} $m^3/m \cdot s$

The values compare well, however, it should be noted that neither the lumped parameter nor the semi-analytic method allow for additional upflow from cross-faults like the numerical model. The values for heat flow into the system associated with these mass flow rates is on the order of 12.0 - 118.0 HFU per meter length of fault and are calculated using the mass flow rates in Table 9, and an enthalpy of 492.0 KJ/kg (c_w = 4100 J/kg·°C and a recharge temperature of 120 °C).

The values shown in Table 9 represent the flow rates entering the system at the level where the upper aquifer intersects the main normal fault. Additional hot water recharge into the aquifer, indicated by the numerical results, is derived from the two major cross faults (4 and 7 in Figure 15) within the study area. If the hot water recharge from the cross-faults to the aquifer is neglected the numerical results are approximately one half the value indicated in Table 9. These results nevertheless demonstrate the value in using simple methods of estimating the rates of heat and mass into the system.

The numerical model assumes that the system has attained a steady state. Therefore the initial conditions used in the internal system only required order of magnitude estimates. All of the elements within the system were assigned initial temperatures determined by a 30 °C/1000 m temperature gradient. The pressures were determined according to the density variation with temperature and depths. The system required approximately 20,000 - 30,000 years to reach steady state conditions. This

was determined from the initial 3-dimensional simulations. The steady state conditions are reasonable because the geothermal system has been active for at least 30,000 years, as indicated by the hydrothermal alterations at elevations as great as 300 feet above the present water levels, and also because of the lack of any notable temperature declines in the past 50 years.

The need for better constraints on the data in all areas is essential for further validation and improvement of the present 3-dimensional model (both conceptual and numerical). As in most other geothermal reservoir models, the greatest concern is for greater information at depth (deep boreholes, geophysical data). A deep borehole would allow for better estimates of the pressures and temperatures for the bottom boundaries and would indicate if the present temperatures are reasonable. Deep boreholes might also give a better indication of the type of geology and type of flow patterns that occur at depth.

Only one quarter of the wells in the geothermal area actually provided temperatures which were used in the temperature data analysis. It would greatly increase the knowledge of the system and the accuracy of the model, if the remaining borehole data were measured and monitored. More temperature and pressure measurements are necessary over the entire field study area, including temperatures from colder wells. Better water level measurements in the study area are also needed to more accurately define the direction of groundwater flow. It is conventional in most geothermal modeling, to measure downhole pressures instead of hydraulic heads because these more accurately define the flow at depth. The hydraulic heads can give misleading indications of the relative flow patterns below the water table in geothermal systems because of the density variations with temperature.

The framework is now provided for future detailed numerical analysis of the Klamath Falls geothermal system. Exploitation strategies may now be investigated using the present 3-dimensional numerical model. Detailed 2-dimensional models may be studied which add or subtract water from each element to simulate cross-flows indicated by the three-dimensional model. Reservoir parameter sensitivities can be better

studied to define the heat and mass transfer within the system.

REFERENCES

Benson, S.M., 1982a, Klamath Falls (WP-1 and WP-2) system check, Sept. 29 through 30, 1981, unpublished report to the city of Klamath Falls, Oregon, 13 pp.

Benson, S.M., 1982b, Klamath Falls (WP-1, Supply and distribution network, Museum Well) system check, February 8 through 12, 1982, unpublished report to the city of Klamath Falls, Oregon, 8 pp.

Benson, S.M., 1983, Interpretation of interference data from the Klamath Falls, Oregon geothermal resource, Lawrence Berekeley Laboratory Report LBL-16671, 6 pp.

Benson, S.M., Goranson, C.B. and Schroeder, R.C., 1980, Evaluation of City Well 1, Klamath Falls, Oregon, Lawrence Berkeley Laboratory Report LBL-10848, 9 pp.

Benson, S.M. and Lai, C.H., 1986, Analysis of interference data in a highly heterogeneous and naturally fractured geothermal reservoir, Society of Petroleum Engineers Paper SPE-13252, pp. 236-248.

Bodvarsson, G.S, Benson, S.M., and Witherspoon, P.A., 1982, Theory of the development of geothermal systems charged by vertical faults, Journal of Geophy. Res., vol. 87, no.11, pp. 9317-9328.

Bodvarsson, G.S, 1982, Mathematical modeling of the behavior of geothermal systems under exploitation, Ph.D. Thesis, University of California, Berkeley, Lawrence Berkeley Laboratory Report LBL-13937, 353 pp.

Bodvarsson, G.S, Pruess, K. and Lippmann, M.J., 1985, Modeling of geothermal systems, Society of Petroleum Engineering, SPE-13613, 19 pp.

Bullard, E.C., 1947, The time necessary for a borehole to attain temperature equilibrium, Monthly Notices Roy. Astron. Soc., Geophys. Suppl. 5, pp. 127-130.

Buscheck, T.A., Doughty, C. and Tsang, C.F., Prediction and analysis of a field experiment on a multilayered aquifer thermal energy storage system with strong bouyancy flow, water resources research, vol. 19, no. 5, pp. 1307-1315.

Cheng, H.K., 1978, Heat-transfer in geothermal systems, Advances in Heat-Transfer, vol. 14.

Coats, K.H., 1977, Geothermal reservoir modeling, Dallas: Society of Petroleum Engineers Paper No. 6892.

Culver, G.G., Lund, J.W. and Svanevik, L.S., 1974, Klamath Falls hot water well study, report prepared for Lawrence Livermore Laboratory, Report No. UCRL-13614, 32 pp.

Donaldson, I.G., The simulation of geothermal systems with a simple convective model,

Geothermics, Special issue 2, U.N. Symposium on the Development and Utilization of Geothermal Resources, Pisa, Italy.

Donath, F.A., 1962, Analysis of basin-range structure, south-central Oregon, Geol. Soc. America Bull., v. 73, no. 1, pp. 1-16.

D.C. Long Energyman, Inc., 1984, Klamath Falls geothermal heating system data from four months of testing Klamath Falls, Oregon.

Faust, C.R. and Mercer, J.W., 1975, Mathematical modeling and geothermal systems, Proceedings 2nd U. N. Symposium on the Development and Use of Geothermal Resources, San Fransisco, California, vol. 3, pp. 1635-1641.

Freeze, R.A. and Cherry, J.A., 1979, Groundwater, Prentice-Hall, Inc., 604 pp.

Garg, S.K., Pritchett, J.W., and Brownell, D.H., 1975, Transport of mass and energy in porous media, Proceedings 2nd U.N. Symposium on the Development and Use of Geothermal Resources, San Fransisco, California, vol. 3., p. 1651.

Goyal, K.P., and Kassoy, D.R., 1981, A plausible two-dimensional vertical model of the East Mesa geothermal field, California., USA., J. Geophys. Res., 86, pp. 10719-10733.

Goyal, K.P. and Narasimhan, T.N., 1982, Heat and mass transfer in a fault controlled geothermal reservoir charged at constant pressure, Journal of geoph. Res., vol. 87, pp. 8581-8590.

Janik, C.J., Truesdell, A.H. Sammel, E.A. and White, A.F., 1985, Chemistry of low-temperature geothermal waters at Klamath Falls, Oregon, Transactions, Geothermal Resources Council, vol. 9, pp. 325-331.

Kassoy, D.R., and Zebib, A., 1978, Convection fluid dynamics in a model of a fault zone in the earth's crust, J. Fluid Mech., 88, pp. 769-802.

Kienle, C.F., Nelson, C.A. and Lawrence, R.D., 1981, Faults and lineaments of the Southern Cascades, Oregon, State of Oregon Dept. of Geol. and Min. Ind., Special Paper 13, 23 pp.

Kilty, K., et al., 1978, Aspects of forced convective heat transfer in geothermal systems, Dept. Geol. and Geophysics, Topical Report, Univ. of Utah, 61 pp.

Lauwerier, H.A., 1955, The transport of heat in an oil layer caused by the injection of hot fluid, Applied Science Research, Sec. A, vol. 5, pp. 145-151.

Lawrence, R.D., 1976, Strike-slip faulting terminates the Basin and Range province in Oregon: Geol. Soc. of America Bull., vol. 87, pp. 846-850.

Lippmann, M.J., C.F. Tsang and P. A. Witherspoon, 1977, Analysis of the response of geothermal reservoirs under injection and production procedures, presented at the 47th Annual California Regional Meeting of SPE-AIME, Bakersfield, Calif., Report

SPE-6537.

Lippmann, M.J. and Bodvarsson, G.S., 1983, A modeling study of the natural state of the Heber Geothermal Field, California, Geothermal Resources Council Transactions, Vol. 7, pp. 441-447.

Lund, J.W., Principal Investigator, 1978, Geothermal hydrology and geochemistry of Klamath Falls: Oregon, urban area, Oregon Institute of Technology, Geo-Heat Utilization Center, Final report to the U.S. Geological Survey, 123 pp.

Meyers, J.D. and Newcomb, R.C., 1952, Geology and ground-water resources of the Swan Lake-Yonna Valley area, Klamath county, Oregon., USGS, 151 pp.

Moore, B.N., 1937, Nonmetallic mineral resources of eastern Oregon, U.S. Geol. Survey Bull. 875, 180 pp.

Newcomb, R.C., 1958, Yonna Formation of the Klamath River Basin, Oregon, Northwest Sci., vol. 32, no. 2, pp. 41-48.

W.E. Nork, Inc., 1986, College Industrial Park Well No. 1 aquifer stress test results, prepared for Oregon Institute of Technology, 34 pp.

O'Brien, M.T. and Benson, S.M., 1980, Reservoir evaluation of Klamath Falls, Oregon, Annual Report, Earth Sciences Division, Lawrence Berkeley Laboratory, LBL-12100, pp. 140-147.

Peterson, N.V. and McIntrye, J.R., 1970, The reconnaissance geology and mineral resources of eastern Klamath County and western Lake County, Oregon, Portland, Oregon Department of Geology and Mineral Industries Bulletin 66, 70 pp.

Pritchett, J.W., and Garg, S.K., 1979, Flow in an aquifer charged with hot water from a fault-zone, Pure Appl. Geophys., Vol. 117, pp. 309-320,

Sammel, E.A. and Peterson, D.L., 1976, Hydrologic reconaissance of the geothermal area near Klamath Falls Oregon, USGS Water Resources Investigations No. 76-127, 129 pp.

Sammel, E.A., 1980, Hydrogeologic appraisal of the Klamath Falls geothermal area, Oregon, USGS Professional Paper 1044-G, 45 pp.

Sammel, E.A., Truesdell, A.H., Janik, C.J., Gudmundsson, J.S., Benson, S.M., Solbau, R.D. and Lai, C.H., 1984, Analysis and interpretation of data obtained in tests of the geothermal aquifer at Klamath Falls, Oregon, USGS Water Resources Investigations Report 84-4216.

Sass, J.H. and Sammel, E.A., 1976, Heat flow data and their relation to observed geothermal phenomena near Klamath Falls, Oregon, Journal of Geophysical research, vol. 81, no. 26, pp. 4863-4868.

Sorey, M. L., 1975, Numerical modeling of liquid geothermal systems, Ph.D. Thesis,

University of California, Berkeley.

Stark, M., Goldstein, N.E. and Wollenberg, H.A., 1980, Geothermal exploration assessment and interpretation, Upper Klamath Lake area, Klamath Basin, Oregon, Lawrence Berkeley Laboratory Report LBL-10140, 84 pp.

Stark, M. et al., 1979, Geothermal exploration assessment and interpretation, Upper Klamath Lake area, Klamath Basin, Oregon, Lawrence Berkeley Laboratory Report LBL-10140, 75 pp.

Stehfast, H., 1970, Numerical inversion of Laplace transforms, Communications ACM, vol. 13, pp. 44-49.

Stewart, J.H., 1978, Basin-range structure in western North America, A review, in Smith R.B. and Eaton, G.P., eds., 1978, Cenozoic tectonics and regional geophysics of the western Cordillera: Geological Society of America Memoir 152, pp. 1-32.

Stewart, J.H., 1983, Cenozoic structure and tectonics of the northern Basin and Range Province, California, Nevada, and Utah, Geothermal Resources Council, Special Report No. 13, pp. 25-40.

Tsang, C.H., Buscheck, T., Doughty, C., 1981, Aquifer thermal energy storage: A numerical simulation of Auburn University field experiments, Water Resources Research, vol. 17, no. 3, pp. 647-658.

Tsang, C.H. and Doughty, C., 1985, Detailed validation of a liquid and heat flow code against field performance, presented proceedings at the Eighth SPE Symposium on Reservoir Simulation, Dallas, Texas, 1985, pp. 16.

BOUNDARY CONDITIONS

BOTTOM BOUNDARY CONDITION

NODE	TEMPERATURE (C)	PRESSURE (Pa)
91	0.1050000000000D+03	0.194400000065D+08
89	0.1050000000000D+03	0.1944000000000D+08
92	0.9500000000000D+02	0.1944000000000D+08
90	0.7999999999999D+02	0.1944000000000D+08
93	0.7199999999977D+02	0.194400000009D+08
87	0.7000000000000D+02	0.1944000000000D+08
88	0.6999999999999D+02	0.1945000000000D+08
191	0.1060000000000D+03	0.1943000000000D+08
189	0.1050000000000D+03	0.1943000000000D+08
192	0.9500000000000D+02	0.1943000000000D+08
190	0.8000000000000D+02	0.1943000000000D+08
193	0.7199999999987D+02	0.1943000000000D+08
187	0.7000000000000D+02	0.1943000000000D+08
188	0.6999999999999D+02	0.1944000000000D+08
291	0.1150000000000D+03	0.1937000000000D+08
289	0.1100000000000D+03	0.1935000000000D+08
292	0.9999999999996D+02	0.1934000000000D+08
290	0.7999999999999D+02	0.1933000000000D+08
293	0.7499999999988D+02	0.1933000000000D+08
287	0.7500000000000D+02	0.1935000000000D+08
288	0.7499999999999D+02	0.1940000000000D+08
391	0.1170000000000D+03	0.1937000000000D+08
389	0.1150000000000D+03	0.1934000000000D+08
392	0.1050000000000D+03	0.193300000051D+08
390	0.8000000000000D+02	0.1933000000000D+08
393	0.7888799999997D+02	0.193300000120D+08
387	0.7500000000000D+02	0.1933000000000D+08
388	0.7500000000000D+02	0.1940000000000D+08
491	0.1200000000000D+03	0.1938000000000D+08
489	0.1170000000000D+03	0.1936000000000D+08
492	0.1080000000000D+03	0.193500000400+08
490	0.8500000000000D+02	0.1933000000000D+08
493	0.7999999999998D+02	0.193300000178D+08
487	0.7500000000000D+02	0.1933000000000D+08
488	0.7500000000000D+02	0.1940000000000D+08
591	0.1220000000000D+03	0.194200000001D+08
589	0.1160009999950+03	0.194000001983D+08
592	0.1110000000000D+03	0.193650000078D+08
590	0.9500000000000D+02	0.1933000000000D+08
593	0.8499999999998D+02	0.193200000066D+08
587	0.7500000000000D+02	0.1932000000000D+08
588	0.7500000000000D+02	0.1940000000000D+08
691	0.1200000000050+03	0.1933000000000D+08
689	0.1180000000000D+03	0.1932000000000D+08
692	0.109000000004D+03	0.1931000000000D+08
690	0.9499999999999D+02	0.193050099999D+08
693	0.8499999999860+02	0.193050001365D+08
687	0.7500000000000D+02	0.1931000000000D+08
688	0.7500999999980+02	0.1940000000000D+08
791	0.1140000000000D+03	0.193350999434D+08
789	0.1080000000000D+03	0.1932000000000D+08
792	0.9999999999980+02	0.193150000152D+08
790	0.8999999999990+02	0.193150000000D+08

793	0.799999999991D+02	0.193150001263D+08
787	0.700000000000D+02	0.193300000000D+08
788	0.700000999998D+02	0.194000000000D+08
891	0.120000000000D+03	0.193280000000D+08
889	0.118000000000D+03	0.193270000000D+08
892	0.109000000000D+03	0.193250000000D+08
890	0.919999999999D+02	0.193250000000D+08
893	0.799999999994D+02	0.193240001074D+08
887	0.750000000000D+02	0.193300000000D+08
888	0.750099999998D+02	0.194000000000D+08
991	0.122000000000D+03	0.192900000000D+08
989	0.112000000000D+03	0.192600000008D+08
992	0.109000000000D+03	0.192600000002D+08
990	0.950000000000D+02	0.192600000005D+08
993	0.820000000099D+02	0.192600000001D+08
987	0.750000000000D+02	0.193200000000D+08
988	0.750000000000D+02	0.194000000000D+08
1091	0.114000000008D+03	0.192700000021D+08
1089	0.105000000000D+03	0.192600000000D+08
1092	0.970000000009D+02	0.192600000000D+08
1090	0.850000000000D+02	0.192600000000D+08
1093	0.739999999997D+02	0.192500000889D+08
1087	0.740000000000D+02	0.193000000000D+08
1088	0.799999999998D+02	0.194000000000D+08
1191	0.107000000000D+03	0.193300000441D+08
1189	0.970000000000D+02	0.192800000000D+08
1192	0.880000000000D+02	0.192700000121D+08
1190	0.750000000000D+02	0.192650000000D+08
1193	0.749999999998D+02	0.192500000072D+08
1187	0.750000000000D+02	0.193100000000D+08
1188	0.750009999998D+02	0.194000000000D+08
1291	0.900000000000D+02	0.193100000951D+08
1289	0.850000000000D+02	0.192950000000D+08
1292	0.830000000000D+02	0.192950000000D+08
1290	0.750000000000D+02	0.192950000000D+08
1293	0.750000000000D+02	0.192950000025D+08
1287	0.750000000000D+02	0.193200000000D+08
1288	0.700000000000D+02	0.194000000000D+08
1391	0.850000000000D+02	0.193250000865D+08
1389	0.830000000000D+02	0.192960000000D+08
1392	0.800000000000D+02	0.192960000000D+08
1390	0.750000000000D+02	0.192960000000D+08
1393	0.749999999998D+02	0.192960000888D+08
1387	0.750000000000D+02	0.192960000000D+08
1388	0.699999999999D+02	0.194000000000D+08

SOUTHWESTERN BOUNDARY CONDITION

NODE	TEMPERATURE (C)	PRESSURE (Pa)
8	0.530000000000D+02	0.164000000000D+08
16	0.400000000000D+02	0.105000000991D+08
24	0.290000000000D+02	0.710000001007D+07
32	0.199999999994D+02	0.415000012684D+07
40	0.120000000000D+02	0.144000000000D+07
48	0.860000000000D+01	0.460000000000D+06
108	0.530000000000D+02	0.164000000000D+08
116	0.400000000000D+02	0.105000000007D+08
124	0.290000000000D+02	0.710000000997D+07
132	0.199999999999D+02	0.415000000004D+07

140	0.1200000000000+02	0.1440000000000+07
148	0.8600000000000+01	0.4600000000000+06
208	0.5300000000000+02	0.1640000000000+08
216	0.4000000000000+02	0.1050000000090+08
224	0.2900000000000+02	0.7100000000010+07
232	0.1999999999940+02	0.4150000000000+07
240	0.1200000000000+02	0.1440000000000+07
248	0.8600000000000+01	0.4600000000000+06
308	0.5300000000000+02	0.1640000000000+08
316	0.4000000000000+02	0.1050000000020+08
324	0.2900000000000+02	0.7100009000030+07
332	0.2000000000000+02	0.4150000000710+07
340	0.1200000000000+02	0.1440000000750+07
348	0.8600000000000+01	0.4500000000000+06
408	0.5550006769230+02	0.1635000000000+08
416	0.4000078181000+02	0.1048000999640+08
424	0.2900000005470+02	0.7090000007120+07
432	0.2000000000000+02	0.4120000008380+07
440	0.1200009585370+02	0.1400005999640+07
448	0.8600000000000+01	0.4500000000000+06
508	0.5300006769230+02	0.1630000000000+08
516	0.4000008181000+02	0.1045000999970+08
524	0.2900000375470+02	0.7070009000000+07
532	0.2000000000000+02	0.4100000000190+07
540	0.1200000005370+02	0.1400000000200+07
548	0.8600000000000+01	0.4450000000010+06
608	0.5300016769230+02	0.1600000000000+08
616	0.4000997818100+02	0.1041935999420+08
624	0.2900079375470+02	0.7011088999680+07
632	0.2000000000000+02	0.4081076979470+07
640	0.1200000585370+02	0.1391925998310+07
648	0.8600000000000+01	0.4138400000000+06
708	0.5300006769230+02	0.1600000000000+08
716	0.4000997818100+02	0.1039006999500+08
724	0.2900979375470+02	0.6981767999750+07
732	0.2000000000000+02	0.4051741988890+07
740	0.1200009585370+02	0.1362593999530+07
748	0.8600000000000+01	0.3845110000000+06
808	0.5300006769230+02	0.1600000000000+08
816	0.4000997818100+02	0.1037054999390+08
824	0.2900009375470+02	0.6962219999670+07
832	0.2000000000000+02	0.4032185976940+07
840	0.1200009585370+02	0.1343039999220+07
848	0.8600000000000+01	0.3649550000000+06
908	0.5300000000000+02	0.1614483000000+08
916	0.3939997818100+02	0.1035102999960+08
924	0.2889979375470+02	0.6942674999980+07
932	0.2000000000000+02	0.4012628999970+07
940	0.1164969585370+02	0.1323485000070+07
948	0.8600000000000+01	0.3454060000000+06
1008	0.5290016769230+02	0.1614483000000+08
1016	0.3939997818100+02	0.1035102999220+08
1024	0.2889979375470+02	0.6942674999600+07
1032	0.1990000000000+02	0.3940000000000+07
1040	0.1164969585370+02	0.1320000000070+07
1048	0.8600000000010+01	0.3454060009030+06
1108	0.5290016769230+02	0.1611565000000+08
1116	0.3939997818100+02	0.1032173999240+08
1124	0.2889979375470+02	0.6913354999780+07
1132	0.1990000000010+02	0.3900000000000+07

1140	0.116496958536D+02	0.1310000000000D+07
1148	0.8600000000000D+01	0.316077166244D+06
1208	0.529001676923D+02	0.1611565000000D+08
1216	0.3939997818100+02	0.103217399993D+08
1224	0.288997937547D+02	0.691335499998D+07
1232	0.1990000000000+02	0.3840000000000+07
1240	0.116496958537D+02	0.1300000000080+07
1248	0.8600000000000+01	0.316077101077D+06
1308	0.529001676923D+02	0.1611565000000+08
1316	0.3939997818100+02	0.103217399791D+08
1324	0.288997937547D+02	0.691335499872D+07
1332	0.1990000000000+02	0.3830000000030+07
1340	0.116496958537D+02	0.1298000000000+07
1348	0.8600000000000+01	0.316077104903D+06

SOUTHEASTERN BOUNDARY CONDITION

NODE		
2001	0.949999917984D+02	0.160119548450D+08
2002	0.920000868936D+02	0.160002288776D+08
2003	0.870084562688D+02	0.160001661270D+08
2004	0.840064542913D+02	0.159997579713D+08
2005	0.790005600343D+02	0.159121633418D+08
2006	0.750007711031D+02	0.159007593424D+08
2007	0.680000970242D+02	0.159011402333D+08
2009	0.780000000156D+02	0.103116287771D+08
2010	0.7700076279500+02	0.103124784259D+08
2011	0.760900433225D+02	0.103111279281D+08
2012	0.740002143817D+02	0.103097287143D+08
2013	0.709999546942D+02	0.103106245840D+08
2014	0.659999971074D+02	0.103160545673D+08
2015	0.508999987024D+02	0.103422204196D+08
2017	0.860754173861D+02	0.694714148890D+07
2018	0.630451658880D+02	0.694672514431D+07
2019	0.620083210365D+02	0.694082363712D+07
2020	0.610033941002D+02	0.693466118851D+07
2021	0.550008502038D+02	0.691320000019D+07
2022	0.5000766522250+02	0.691320098383D+07
2023	0.350008398911D+02	0.691330000005D+07
2029	0.300071799983D+02	0.381000000000D+07
2030	0.280007101800D+02	0.381000000000D+07
2031	0.220009417834D+02	0.383000000000D+07
2037	0.160002522250D+02	0.129200000119D+07
2038	0.100000910075D+02	0.129200000275D+07
2039	0.100000063567D+02	0.129800087476D+07
2045	0.900002612019D+01	0.320000000330D+06
2046	0.899997324282D+01	0.320000013821D+06
2047	0.899998095633D+01	0.321000000054D+06

NORTHWESTERN BOUNDARY CONDITIONS

NODE	TEMPERATURE (C)	PRESSURE (Pa)
3001	0.101902187212D+03	0.160659228474D+08
3002	0.886375729478D+02	0.160000000000D+08
3003	0.757371589925D+02	0.160000000000D+08
3004	0.630678164028D+02	0.161000000000D+08
3005	0.570093703413D+02	0.162699999323D+08
3006	0.560004436807D+02	0.164200000000D+08

3007	0.560006568639D+02	0.1642000000000D+08
3009	0.781075234176D+02	0.1032722567480+08
3010	0.700000443720D+02	0.1032759689270+08
3011	0.630079064270D+02	0.1032907501270+08
3012	0.520005339132D+02	0.1033068540190+08
3013	0.420008262990D+02	0.1045000058820+08
3014	0.380004939709D+02	0.1049999999790+08
3015	0.342746017872D+02	0.1050000000190+08
3017	0.767165172042D+02	0.695100964356D+07
3018	0.670004257958D+02	0.695045734511D+07
3019	0.600000009109D+02	0.694842984206D+07
3020	0.500003344785D+02	0.694593197799D+07
3021	0.388441938109D+02	0.709999990441D+07
3022	0.281723710435D+02	0.711999999515D+07
3023	0.242715294229D+02	0.711999999840D+07
3025	0.726503483565D+02	0.407054004647D+07
3026	0.607146617825D+02	0.406665118782D+07
3027	0.510000094348D+02	0.405940872892D+07
3028	0.475474039818D+02	0.405028618662D+07
3029	0.373309527059D+02	0.413999999179D+07
3030	0.264128748254D+02	0.416999990106D+07
3031	0.183605060274D+02	0.417000002497D+07
3033	0.601341156763D+02	0.142181652761D+07
3034	0.335071902953D+02	0.140870802199D+07
3035	0.308696394021D+02	0.139666884648D+07
3036	0.227833076611D+02	0.138058861681D+07
3037	0.196201990994D+02	0.184999993272D+07
3038	0.156961108794D+02	0.143999998375D+07
3039	0.112427090823D+02	0.144000001027D+07
3041	0.177432241733D+02	0.398909210357D+06
3042	0.130530171493D+02	0.389971201356D+06
3043	0.123684468268D+02	0.383562561768D+06
3044	0.108846694242D+02	0.375056601182D+06
3045	0.101456956040D+02	0.420000000000D+06
3046	0.947237174118D+01	0.463400000000D+06
3047	0.857086060455D+01	0.463400000003D+06

COLD INFLUX AT SOUTHEASTERN CORNER OF STUDY AREA

NODE	TEMPERATURE (C)	PRESSURE (Pa)
6025	0.450000000288D+02	0.410000244840D+07
6033	0.250000060423D+02	0.144000000009D+07
6041	0.180001828165D+02	0.445000000000D+06

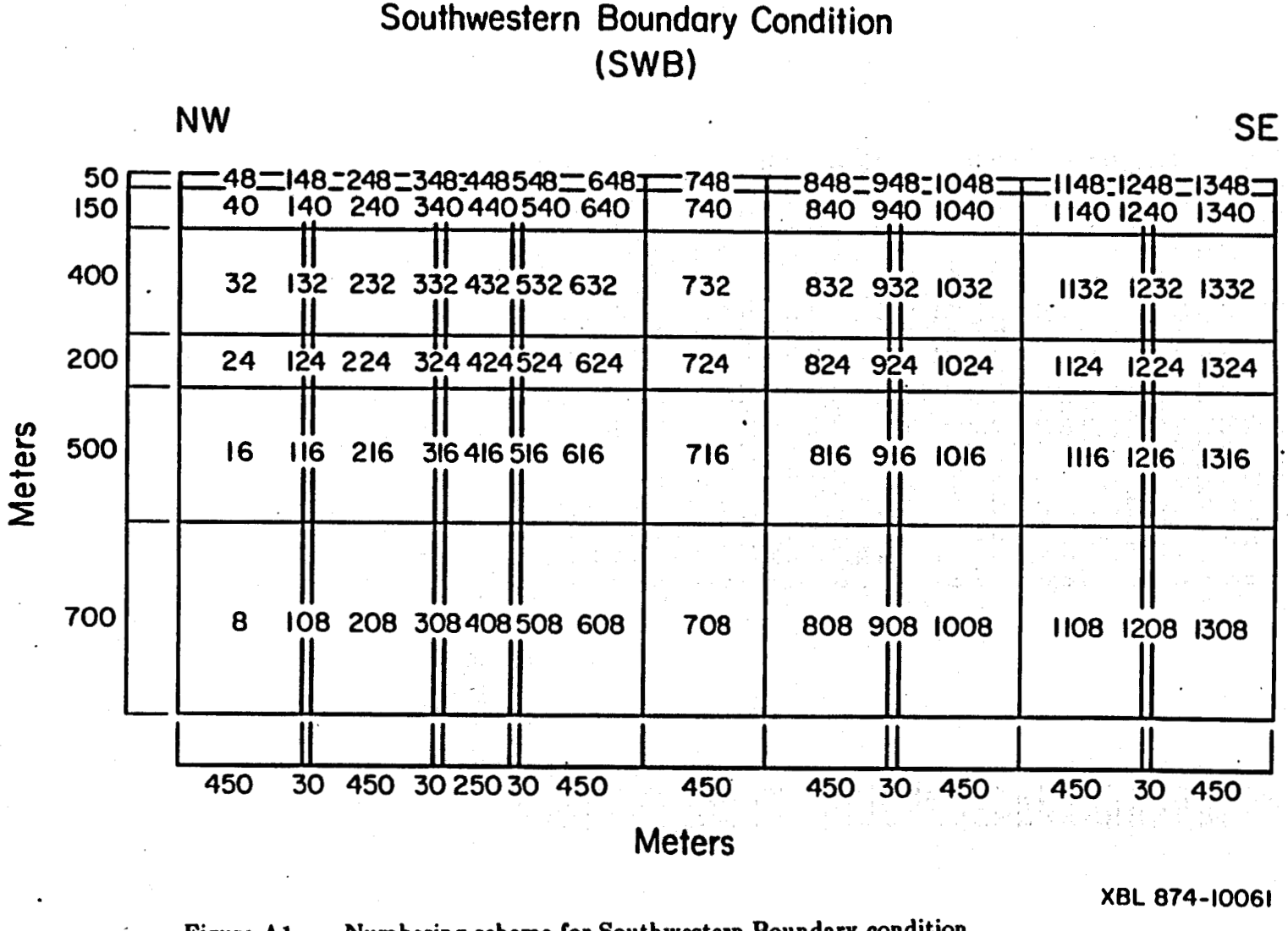

Figure A1. Numbering scheme for Southwestern Boundary condition.

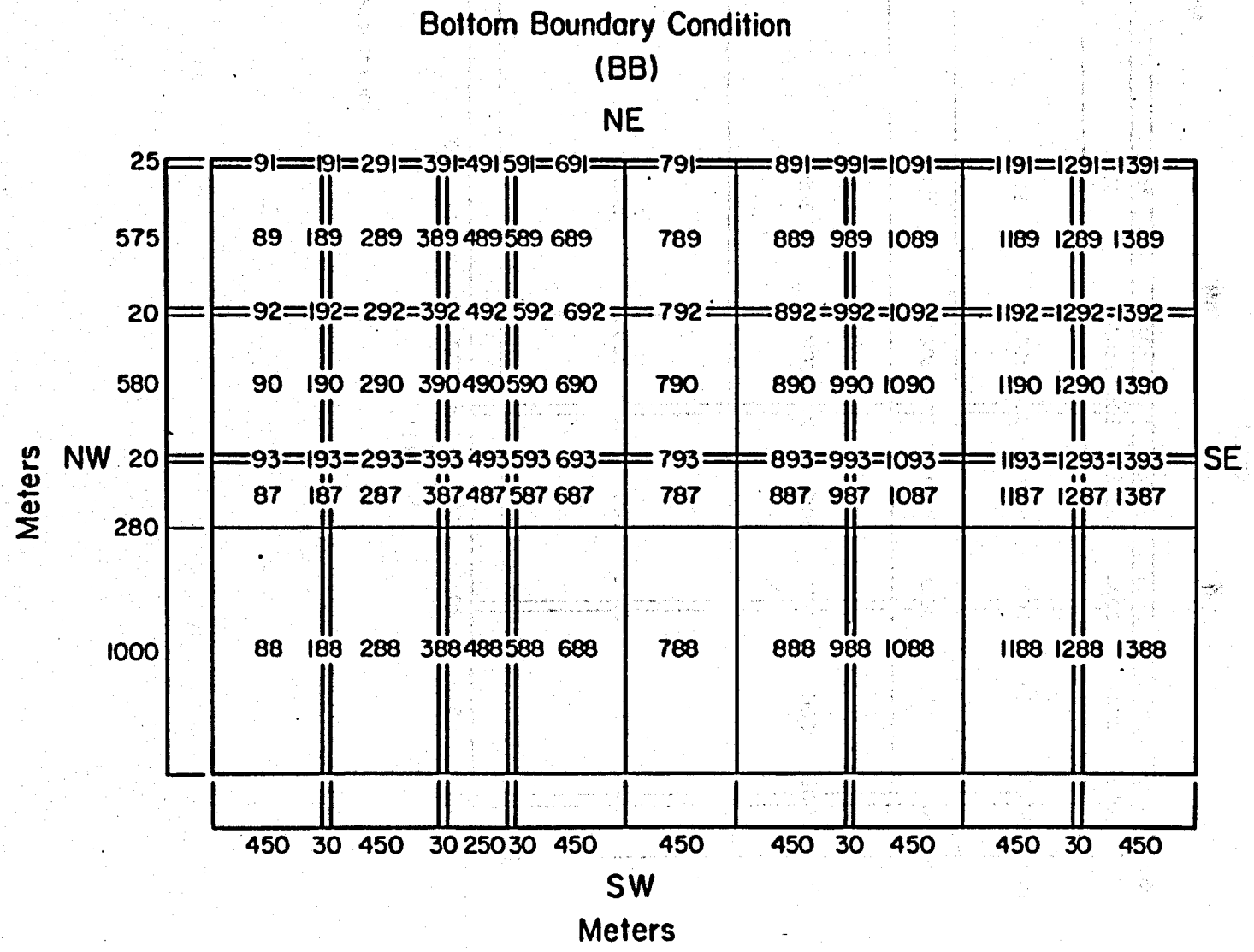

Figure A2. Numbering scheme for Bottom Boundary condition.

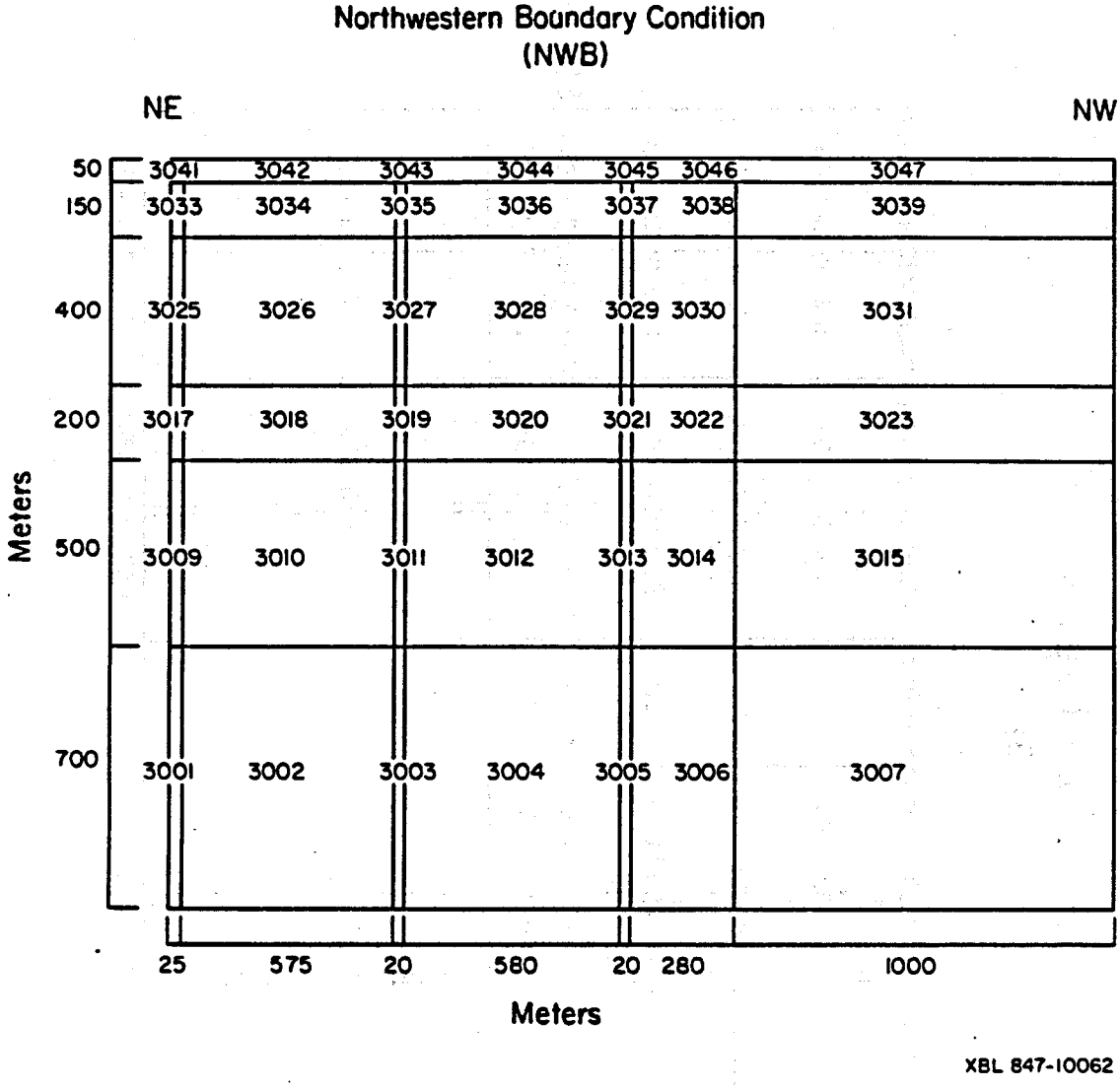

Figure A3. Numbering scheme for Northwestern Boundary condition.

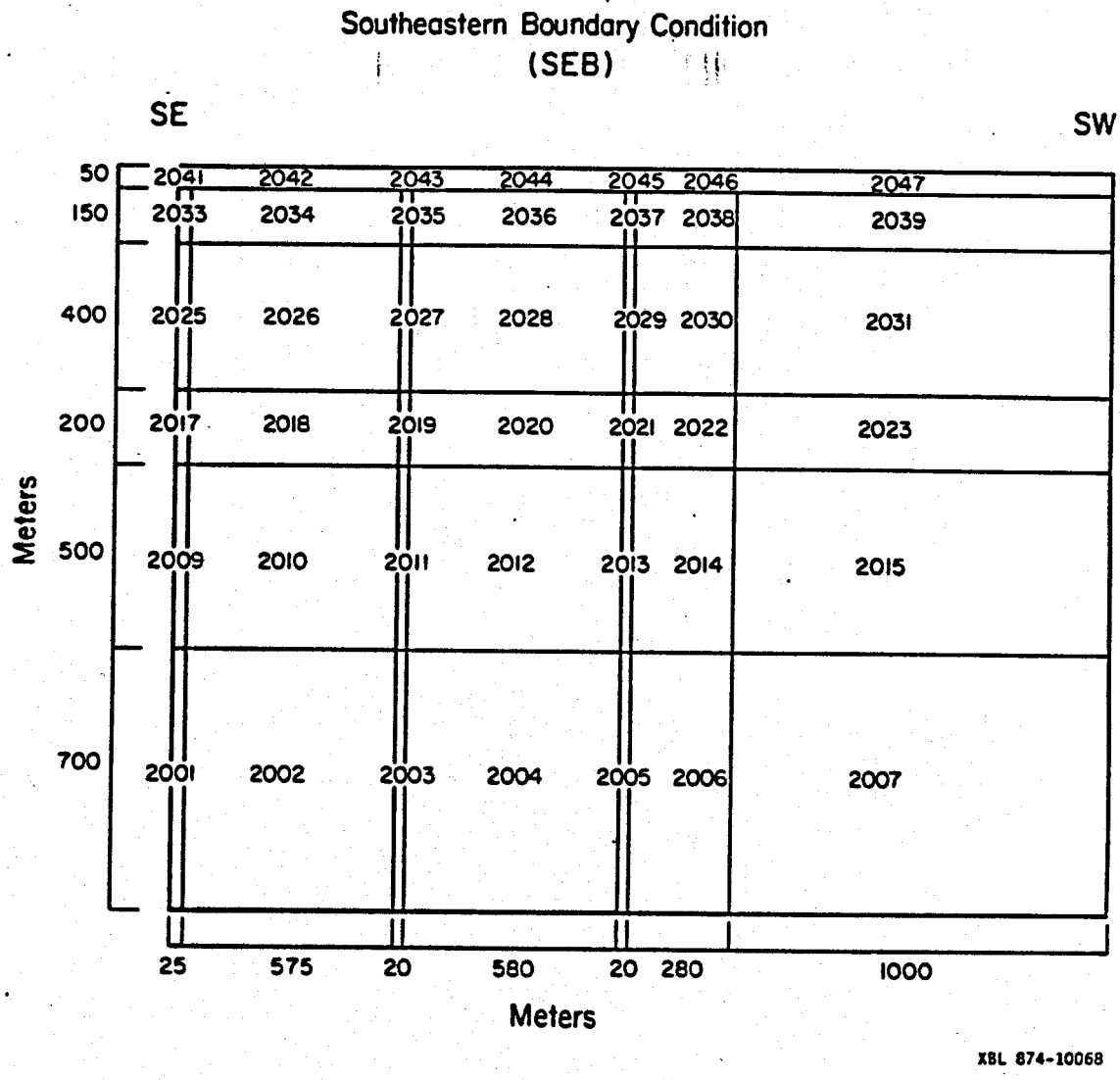

Figure A4. Numbering scheme for Southeastern Boundary condition.